Prove all things. Hold on to what is good.

1 Thessalonians 5:21

University of Alberta

Development of Platinum and Platinum-Nickel Catalysts for Fuel Cell Applications

by

Sonja Angelique Francis

A thesis submitted to the Faculty of Graduate Studies and Research
in partial fulfillment of the requirements for the degree of

Doctor of Philosophy

Department of Chemistry

Fall 2013
Edmonton, Alberta

Dedication

I dedicate this thesis to the memory of my sister who passed away suddenly on July 9th, 2011. The following is an excerpt of my eulogy to her:

"The second-to-last time I talked to Kerlene, she was asking about my Ph.D. progress. She said to me "Sonja, I hope you change the world cause I couldn't". How wrong she was. She did not know how many of her personal touches changed so many people's worlds. It was not just what she did; it was who she was. There's so much more I could say, but this is my tribute to my sister."

Kerlene Alicia Simone Scully

6th July 1981 – 9th July 2011

Abstract

This dissertation describes the use of a novel Pt deposition to prepare nickel- and carbon-supported platinum catalysts. The deposition is referred to herein as the *platinum counter electrode deposition.* The source of platinum is the sacrificial dissolution of a blacked platinum counter electrode under galvanostatic conditions that results in conformal, ultra-low loadings of platinum onto the substrates. It is shown that all or most of the platinum is located at the surface of the catalyst in the case where Pt is co-deposited with nickel from a solution of its salt. Furthermore, the deposition is self-limiting. Four major studies based on catalysts synthesized by this method are presented.

The opening study describes the deposition of platinum and co-deposition of platinum and nickel onto nickel foam substrates as well as the electronic and microscopic characteristics of the deposits. Further, the activity of the prepared catalysts towards 2-propanol oxidation in base was explored. Above 500 mV, the nickel and platinum co-deposit on nickel foam was 9 times more active than blackened Pt gauze, while the platinum deposit on nickel foam was 38 times more active.

The second study compares a conventional platinum deposition with the *platinum counter electrode deposition* on nickel nanopillar films prepared by Glancing Angle Deposition. The deposits prepared via our method were more active towards 2-propanol oxidation than both traditionally prepared deposits and commercially available state-of-the-art unsupported platinum nanoparticles.

The same nanopillar-supported platinum catalysts were prepared on glassy carbon disks for the third study. Activity towards oxygen reduction in base and acid was investigated. This is the first oxygen reduction study on nickel-

platinum glancing angle deposited structures and the first such study in basic media.

The ultimate study describes the modification of the *platinum counter electrode deposition* to accommodate particulate substrates. As a proof of concept, we deposited platinum onto Vulcan carbon to fabricate a carbon-supported platinum catalyst that was microscopically and electrochemically characterized and tested for oxygen reduction. The results of this study suggest the utility of this deposition for a variety of particulate conductive substrates.

Acknowledgements

"One grateful thought is a ray of sunshine. A hundred such thoughts paint a sunrise. A thousand will rival the glaring sky at noonday, for gratitude is light against the darkness." – Richelle E. Goodrich

I wish to extend my thanks to the many people who have contributed to the success of my Ph.D. program. First, I have the deepest sense of gratitude towards my Supervisor Steven Bergens for his guidance, support, discussion and encouragement over the past five years. I especially thank him for the many opportunities he provided for training and developing my skill set as a Chemist and his willingness to step out with me into the realm of Materials Chemistry. I am also deeply grateful to my supervisory and examining committee: Jon Veinot, Arthur Mar, Richard McCreery, Mike Brett and E. Bradley Easton for exemplary teaching, useful discussions, and succinct advice.

I sincerely thank the support staff in the Chemistry department. Specifically, I want to mention the technicians who provide Glass, Machine, Electronics and Information Technology Services, especially Dieter Starke, Paul Crothers and Allan Chilton for helping me to set up a hydrogen fuel cell test stand. I thank the superb administrative staff (past and present): Darryl McGee, Anita Weiler, Lynne Lechelt, Bonnie Gover, Joe Fiorillo, Corrine Chorney, Esther Moibi and Laura Pham. I also thank the staff in the Chemical Stores, Shipping and Receiving rooms, especially Bernie Hippel who always had the time to hold short, refreshing conversations with me.

I thank the technicians outside of the department of Chemistry who contributed to my research: Guangcheng Chen, who performed all of the Inductively Coupled Plasma Mass Spectrometry, De-Ann Rollings for Scanning Electron Microscopy, and Dimitre Karpusov, who performed the X-ray Photoelectron Spectroscopy.

I wholeheartedly express my appreciation to the many people who have trained me to perform and interpret the variety of experiments I have done. Firstly, I thank my dear friend Brent Rudyk for training me on his own time to perform powder X-ray Diffraction experiments, Peter Blanchard for a crash course in X-ray Photoelectron Spectroscopy, the staff at the Alberta Centre for Surface Engineering and Science for training in practical surface analysis, Dustin Banham, Hany El-Sayed, Samar Gharaibeh and Viola Birss, from the University of Calgary, for training in hydrodynamic voltammetry, Stanislav Stokyo for Scanning Electron Microscope Training and Greg Popowich of the Department of Physics, for Transmission Electron Microscopy training.

I thank my research group for the relentless support, advice, discussion and friendship they have provided over the years. Firstly, I thank Matthew Markiewicz who taught me the foundation of my practical electrochemistry and provided endless advice and discussion. Secondly, I thank Jeremy John who has been a friend to me for many years and an eternal source of encouragement and support. I thank Elizabeth Corkum for her advice and reassurance and for her silent company while writing this dissertation. I thank Sarah Sutherland and Guihua 'Jo' Zhou for their help in the Fuel Cell lab and for their continuing friendship even as they pursue other paths in life. I thank Satoshi Takebayashi and Suneth Kalapugama for being two of the most positive and upbeat people I have ever worked with, and I thank all the other peers I have worked with in the

past 5 years. Finally, I thank Ryan Tucker for being a gracious, helpful, humble and knowledgeable collaborator, and a supportive friend.

I must wholeheartedly and graciously thank my teaching mentor Jason Cooke. He has been a fantastic example of what I would like to aim for as an educator. His leadership, mentorship, patience, organization, professionalism, empathy, and sense of community and teamwork made him one of the most pleasant people to work for, and someone I continue to admire. I also thank Glen Loppnow and Charles Lucy for their commitment to high quality teaching and learning in the Chemistry Department, and Norman Gee for encouragement in pursuing professional development in Chemical Education.

I must thank my parents, Kenrick and Shirley Francis for their unlimited and unconditional support. I thank my siblings Keith, Kester and Kerlene, and in-laws, Antony and Ayana, and many other family and friends who form my support system, especially Edmay Francis, Willoughby Francis, Brenda John, Anne King, Dagmar Baker, Sharon Campbell, Karyn Chung, Sheila Beckles, Egbert Gould, Gary and Paulette Matthison and Pauline Bahnsen. I thank my friends, Ana-Michelle Broomes, Damali Cox, Monifa Graham, Kerron Joseph, Christopher Carter, Johann Hosein, Carla Roach, Kester Wilson and others who encouraged me to keep focused and studying especially when my sister passed away. I also thank the ladies of Delta Kappa Gamma chapters all over the world that called, emailed and posted messages of encouragement and support throughout the tenure of my Fellowship.

I wish to mention Lincoln Hall for suggesting that I apply to the University of Alberta to work with my supervisor, and the staff and students at the University of the West Indies Chemistry Department, specifically Anderson Maxwell, Roxanne Ali-Hassan, and Neisha Pennie-Douglas for continual support.

Of course, I would not have been able to complete my Ph.D. if it was not for the group of awesome friends I have made here, some of which I have mentioned before. I thank them for making my time away from family and home significantly more bearable, interesting and fun.

Finally, and most importantly, I thank my Lord and Savior Jesus Christ for sending all these people to be a blessing in my academic and personal life. I thank Him for the strength, wisdom, patience, guidance, comfort and grace to finally complete the journey to my doctoral degree.

Table of Contents

Chapter 1: Introduction

Chapter 2: Low Pt-loading Ni-Pt and Pt deposits on Ni: Preparation, activity and investigation of electronic properties

Chapter 3: Structural and activity comparison of self-limiting versus traditional Pt electro-deposits on glancing angle deposited nanopillar Ni films

Chapter 4: Oxygen reduction reaction activity of Pt electro-deposits on glancing angle deposited nanopillar Ni films

Chapter 5: Preparation, characterization and oxygen reduction reaction electrocatalytic activity on Vulcan carbon-supported Pt nanoparticles: First application of the Pt counter electrode deposition onto particulate substrates.

Chapter 6: Conclusions, future work and final remarks

Chapter 7: Appendices

List of Tables

Chapter 1: Introduction

Chapter 2: Low Pt-loading Ni-Pt and Pt deposits on Ni: Preparation, activity and investigation of electronic properties

Chapter 3: Structural and activity comparison of self-limiting versus traditional Pt electro-deposits on glancing angle deposited nanopillar Ni films

Chapter 4: Oxygen reduction reaction activity of Pt electro-deposits on glancing angle deposited nanopillar Ni films

List of Figures

Chapter 1: Introduction

Chapter 2: Low Pt-loading Ni-Pt and Pt deposits on Ni: Preparation, activity and investigation of electronic properties

Chapter 3: Structural and activity comparison of self-limiting versus traditional Pt electro-deposits on glancing angle deposited nanopillar Ni films

Chapter 4: Oxygen reduction reaction activity of Pt electro-deposits on glancing angle deposited nanopillar Ni films

Chapter 5: Preparation, characterization and oxygen reduction reaction electrocatalytic activity on Vulcan carbon-supported Pt nanoparticles: First application of the Pt counter electrode deposition onto particulate substrates.

Chapter 7: Appendices

List of Schemes

Chapter 1: Introduction

Chapter 4: Oxygen reduction reactivity of Pt electro-deposits on glancing angle deposited nanopillar films

List of Equations

Chapter 1: Introduction

Chapter 2: Low Pt-loading Ni-Pt and Pt deposits on Ni: Preparation, activity and investigation of electronic properties

Chapter 4: Oxygen reduction reaction activity of Pt electro-deposits on glancing angle deposited nanopillar Ni films

Chapter 5: Preparation, characterization and oxygen reduction reaction electrocatalytic activity on Vulcan carbon-supported Pt nanoparticles: First application of the Pt counter electrode deposition onto particulate substrates.

Chapter 7: Appendices

List of Abbreviations

® – registered trademark

ε_d – *d* band center

ε_i – intrinsic maximum efficiency

2POR – 2-propanol oxidation reaction

a.u. – arbitrary units

AA – acetic acid

acac – acetyl acetonate

$_{ads}$ – adsorbed on the catalyst surface

AEM – anion exchange membrane

AFC – alkaline fuel cell

AL – acetaldehyde

BDE – bond dissociation energy

BE – binding energy

CE – counter electrode

CTE – coefficient of thermal expansion

CV – cyclic voltammogram

CVD – chemical vapour deposition

D2PFC – direct 2-propanol fuel cell

DAFC – direct alcohol fuel cell

DEFC – direct ethanol fuel cell

DEMS – differential electrochemical mass spectrometry

DMFC – direct methanol fuel cell

DOE – Department of Energy

E^0 – standard electrode potential

E^0_{cell} – standard cell potential

E_{CE} – counter electrode potential

EOR – ethanol oxidation reaction

E_{peak} – peak potential

ESA – electro-active surface area

E_{WE} – working electrode potential

fcc – face centered cubic

FTIRS – Fourier Transform infrared spectroscopy

GDL – gas diffusion layer

GLAD – glancing angle deposition

hcp – hexagonal close packed

HOR – hydrogen oxidation reaction

HPLC – high pressure liquid chromatography

HUPD – hydrogen under potential deposited

ICP-MS – inductively coupled plasma mass spectrometry

KE – kinetic energy

LSM – strontium doped lanthanum manganite

MCFC – molten carbonate fuel cell

MEA – membrane electrode assembly

ML – monolayer

MOR – methanol oxidation reaction

MS – mass spectrometry

Ni-$Pt_{CE}Ni_{foam}$ – catalyst resulting from co-deposition of Ni from solution and Pt from dissolution of a Pt counter electrode onto a Ni foam

Ni-$Pt_{CE}Ni_{gauze}$ – catalyst resulting from co-deposition of Ni from solution and Pt from dissolution of a Pt counter electrode onto a Ni gauze

Ni_{black} – catalysts resulting from deposition of Ni from solution onto a Ni gauze

NSTF – nanostructured thin film formed by vacuum deposition of Pigment red 149

OCV – open circuit voltage

ORR – oxygen reduction reaction

PAFC – phosphoric acid fuel cell

PEM – polymer electrolyte membrane

PEMFC – polymer electrolyte membrane (proton exchange membrane) fuel cell

PSS – polystyrene sulfonate

Pt CE – a counter electrode prepared from deposition of Pt from solution unto a Pt gauze

Pt_{black} – catalyst resulting from deposition of Pt from solution onto a Pt gauze

$Pt_{CE}C$ – catalyst resulting from deposition of Pt from dissolution of a Pt CE onto carbon powder

$Pt_{CE}Ni_{foam}$ – catalyst resulting from deposition Pt from dissolution of a Pt counter electrode onto a Ni foam

$Pt_{CE}Ni_{NP}$ – catalyst resulting from deposition of Ni from solution and Pt from dissolution of a Pt counter electrode onto GLAD Ni nanopillars

PTFE – polytetrafluoroethylene

Pt_{foil} – a shiny Pt foil

$Pt_{Tr}Ni_{NP}$ – catalyst resulting from deposition of Pt from solution onto GLAD Ni nanopillars

PVD – physical vapour deposition

Q – charge

R.T. – room temperature

RDE – rotating disk electrode

RHE – reversible hydrogen electrode

SAD – small angle deposition

SCV – sampled current voltammogram

SERS – surface enhanced Raman spectroscopy

SHE – standard hydrogen electrode

SOFC – solid oxide fuel cell

$_{sol}$ – exists in bulk solution

SPAIRS – single potential alteration infrared spectroscopy

SPEEK – sulfonated polyether ether ketone

^{TM} – unregistered trademark

UHV – ultra-high vacuum

$V_{Ag/AgCl\ (4M\ KCl)}$ – potential versus the Ag/AgCl (4M KCl) reference electrode

V_{RHE} – potential versus the reversible hydrogen electrode

V_{SHE} – potential versus the standard hydrogen electrode

WE – working electrode

XPS – X-ray photoelectron spectroscopy

XRD – X-ray diffraction

YSZ – yttria-stabilised zirconia

Chapter 1: Introduction

1.1 Introduction to fuel cells

1.1.1 Definition and working principles

Fuel cells are electrochemical devices that continuously convert the chemical energy of a fuel into electrical energy at constant temperature. They consist of an electrolyte sandwiched between an anode where fuel is oxidised, and a cathode where an oxidant is reduced. The distinguishing feature between a battery and a fuel cell is that a battery stores the chemical reactants, and when they are used up the battery must be recharged or discarded. A fuel cell, however, should run indefinitely as long as it is supplied with reactants.

The working principles of all fuel cells can be demonstrated by the hydrogen-oxygen fuel cell represented in Figure 1-1. At the anode (negative electrode), hydrogen decomposes into hydrogen ions (protons) and electrons. At the cathode (positive electrode), electrons are collected from the external circuit where they combine with the incoming protons and O_2 to form water. The electric current travelling through the external circuit can be converted to heat, power or magnetism, for example, depending on the device positioned in the external circuit.

Figure 1-1 also shows the electrode half-reactions and overall equation of the processes occurring in the hydrogen-oxygen fuel cell. The standard cell potential, E^0_{cell}, gives the electrical potential difference between the two electrodes under standard conditions[1], and is equal to 1.23 V for the H_2-O_2 fuel cell[2]. For a fuel cell stack connected in series, the maximum voltage that can be

[1] Standard conditions are defined as 298.15 K (25°C) and 101.325 kPa (1 atm).

[2] The unit V (volt) in S.I. units is $J \cdot C^{-1}$ (Joules per Coulombs).

produced by the stack is the sum of the individual E^0_{cell} values. For a single fuel cell, E^0_{cell} is directly proportional to its *intrinsic maximum efficiency*, ε_i,(Equation 1-1):

Intrinsic Maximum Efficiency of a $H_2 - O_2$ fuel cell

$$\varepsilon_i = \frac{\Delta G^0}{\Delta H^0} \qquad 1-1$$

where ΔG^0 is the Gibbs Free Energy of the overall reaction

ΔH^0 is the standard enthalpy of the reaction

$$\Delta G^0 = -nFE^0_{cell} \qquad 1-2$$

where n is the number of electrons transferred

F is Faraday's constant

$$\Delta G^0 = -2 \times 96485\ C \bullet mol^{-1} \times 1.23\ J \bullet C^{-1} \times 10^{-3}\ kJ \bullet J^{-1}$$

$$\Delta G^0 = -237.35\ kJ \bullet mol^{-1}$$

$$\Delta H^0 = (\sum(\Delta H^0_{f,prod}) - (\sum(\Delta H^0_{f,reac}) \qquad 1-3$$

where $\Delta H^0_{f,prod}$ is the standard enthalpy of formation of the products

$\Delta H^0_{f,reac}$ is the standard enthalpy of formation of the reactants

$$\Delta H^0 = (\Delta H^0_{f,H_2O}) - (\Delta H^0_{f,H_2} + (\frac{1}{2})\Delta H^0_{f,O_2})$$

$$\Delta H^0 = (285.8) - (0 + (\frac{1}{2})0)$$

$$\Delta H^0 = -285.8\ kJ \bullet mol^{-1}$$

$$\therefore \varepsilon_i = \frac{-237.35}{-285.8}$$

$$\varepsilon_i = 83\ \%$$

A significant advantage of fuel cells as a power source is the theoretically minimal impact on the environment. Pollutants such as oxides of sulfur and

nitrogen are not formed. This is because zero sulfur fuels are typically used and also because the temperature required to form nitrogen oxides are way above the operating temperatures of most fuel cells. The case of carbon dioxide emission depends on the particular fuel source and application. For example, using a fuel cell vehicle running on hydrogen fuel from natural gas can lead to a 40% reduction in CO_2 emission compared to a traditional vehicle run on gasoline or diesel [1].

Figure 1-1 *Schematic of a typical hydrogen-oxygen fuel cell (not drawn to scale).*

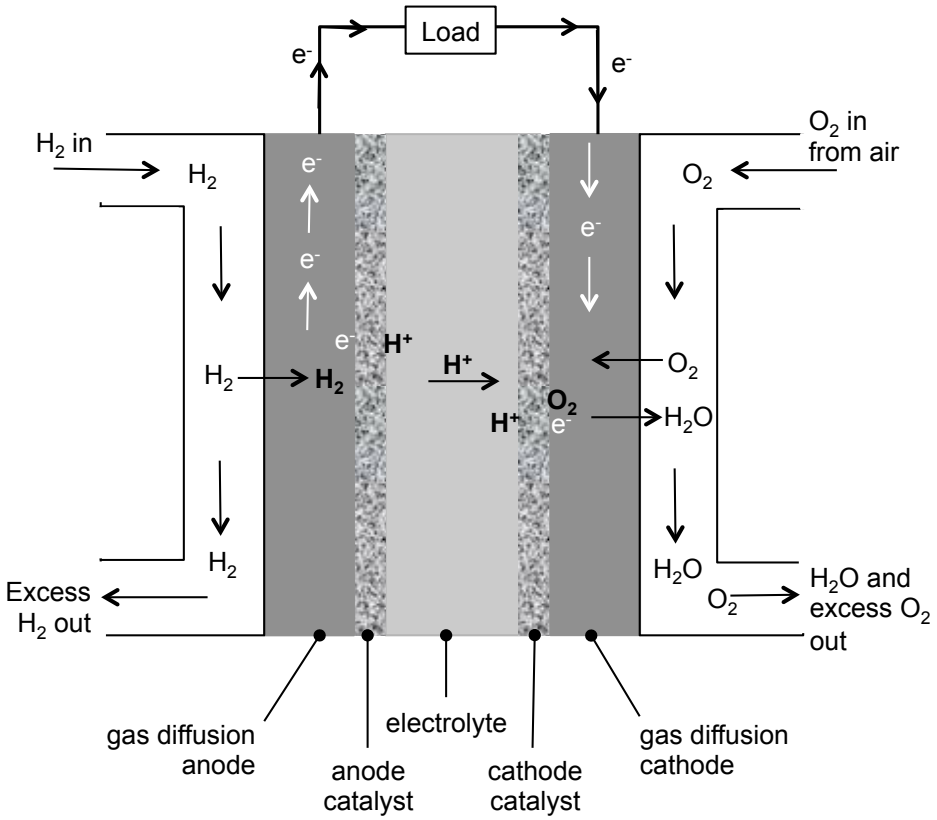

Anode: $H_2 \rightarrow 2\ H^+ + 2\ e^-$ **Cathode: $O_2 + 2\ H^+ + 2\ e^- \rightarrow H_2O$**

Overall: $2\ H_2 + O_2 \rightarrow 2\ H_2O$

1.1.2 History

Sir William Grove, a Welsh barrister, demonstrated the first fuel cell in 1839 [2]. He imagined that if water could be electrochemically decomposed by electricity into its component gases, hydrogen and oxygen, then the opposite could also be true. The device he eventually built to achieve this, aptly referred to as a gas battery, was later renamed the fuel cell.

The novel fuel cell technology was very attractive at the time of invention, as other power generating systems suffered from poor efficiency. For example, Thomas Edison's coal burning station built in Manhattan in 1882 only converted 2.5% of its energy input into usable energy output. In the 1920s, reciprocating steam engines only achieved about 14%, and steam turbines achieved almost 20% of their intrinsic maximum efficiency [3]. However, as the efficiencies of the former systems improved while remaining inexpensive, the interest in the development of fuel cells declined and research in the area was spasmodic or small scale. It is noted that at that time the fuel cell advantage of being pollution free was not as socially important, and did not outweigh the cheap, available and accessible nature of the other power producing technologies.

The first practical application of fuel cells was in the United States Space program (*Gemini* and *Apollo* missions) beginning in 1962, more than a century after their invention! For example, an *Apollo* lunar mission used a stack of alkaline hydrogen-oxygen fuel cells with a porous nickel anode and lithiated nickel oxide cathode in 70 to 85 wt. % potassium hydroxide electrolyte operating at near atmospheric pressure and > 200°C [3]. The stack was used to provide all power for life support, guidance, and communications, and as a source of potable

water. Fuel cells were most suitable for this purpose as no other power source was able to provide enough power (1 kW per day for 14 days) and simultaneously be within the weight allowance of the rocket propulsion units. For the interested reader, reference [4] is a very entertaining review of fuel cell development up to their use in space applications.

Interest in fuel cell research has been revived since its role in the missions to the Moon, with steady progress being made in the areas of the catalysts, electrolytes, structure of the electrodes, and system engineering, coupled with a better understanding of mass transport and diffusion of reactants and products within the device. Today potential applications for fuel cells include stationary power generation, replacements for batteries in portable consumer electronics, transport including automobiles, ships, scooters, trains, submarines and forklifts, cogeneration, and emergency power systems, the application typically being dependent on the type of fuel cell employed [3,5].

1.1.3 Components

Fundamentally, fuel cells are made up of several layers of various materials separated by insulating gaskets where necessary (Figure 1-2). Starting from the hypothetical center of the device, the electrolyte (ionic conductor) is sandwiched between the electronically conducting electrodes that are coated with a thin layer of the respective catalyst. For expediency, the electrolyte is shown as a solid ionic membrane in Figure 1-2. The electrolyte membrane together with the conducting electrodes is known as a membrane electrode assembly (MEA). Moving outward a gas diffusion layer (GDL), that also conducts electrons, exists next to each electrode. The GDL is typically made of a carbon cloth or paper, and is porous enough to allow diffusion of the fuel and oxidant

through it to the catalyst surface, or in some cases, water product away from the catalysts. Next to each GDL is a gas-impermeable bipolar plate. These plates typically comprise a flow field (channels etched into it that transport the fuel/oxidant from where it enters the cell to where it exists the cell), and are attached on the outer surface to a current collector that conducts electrons to an external circuit on the anode side and collects electrons at the cathode side.

Figure 1-2 *Exploded view of the components of a generic fuel cell.*

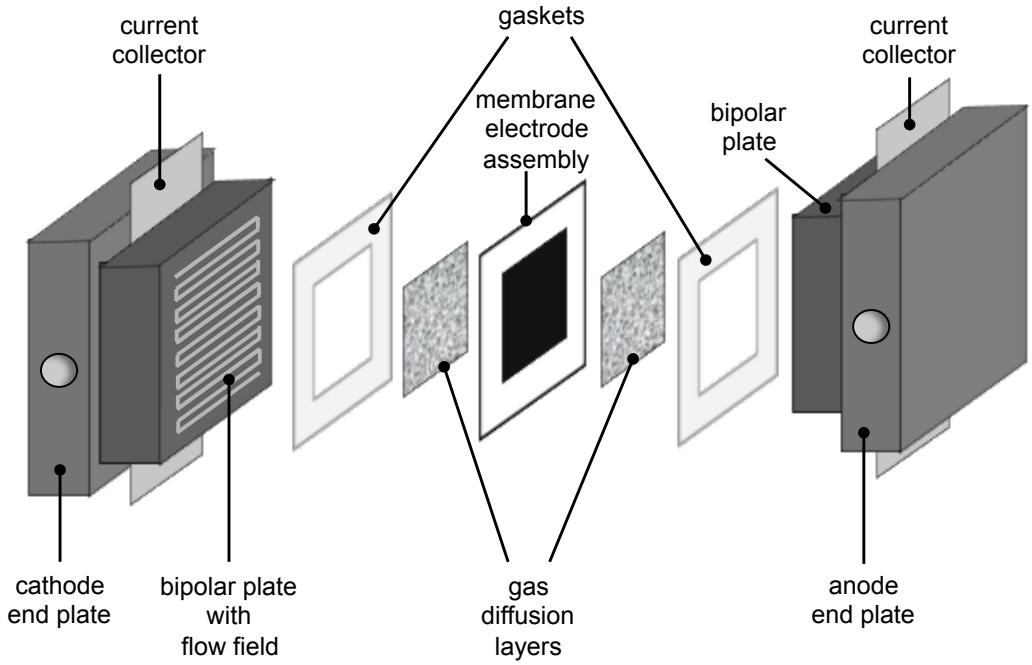

1.2 Types of Fuel Cells

Fuel cells are typically characterized by their electrolyte. In turn, the electrolyte dictates the operating temperature, catalysts, fuels, and materials used in the particular cell. Alternatively, fuel cells can be classified by their fuel, as they may operate with various electrolytes (for example, see Section 1.2.6 Direct Alcohol Fuel Cells). Naturally, each type of fuel cell technology has strengths and challenges making it suitable to its use and the features of the most studied types will be discussed in more detail presently. This information is also briefly summarized in Table 1-1 and Figure 1-3.

Figure 1-3 *Schematic of the principal types of fuel cells discussed in Section 1.2. Product species notated with * are consumed at the other electrode in the cell. Abbreviations are defined in the text, as well as in the List of Abbreviations (Prefatory pages).*

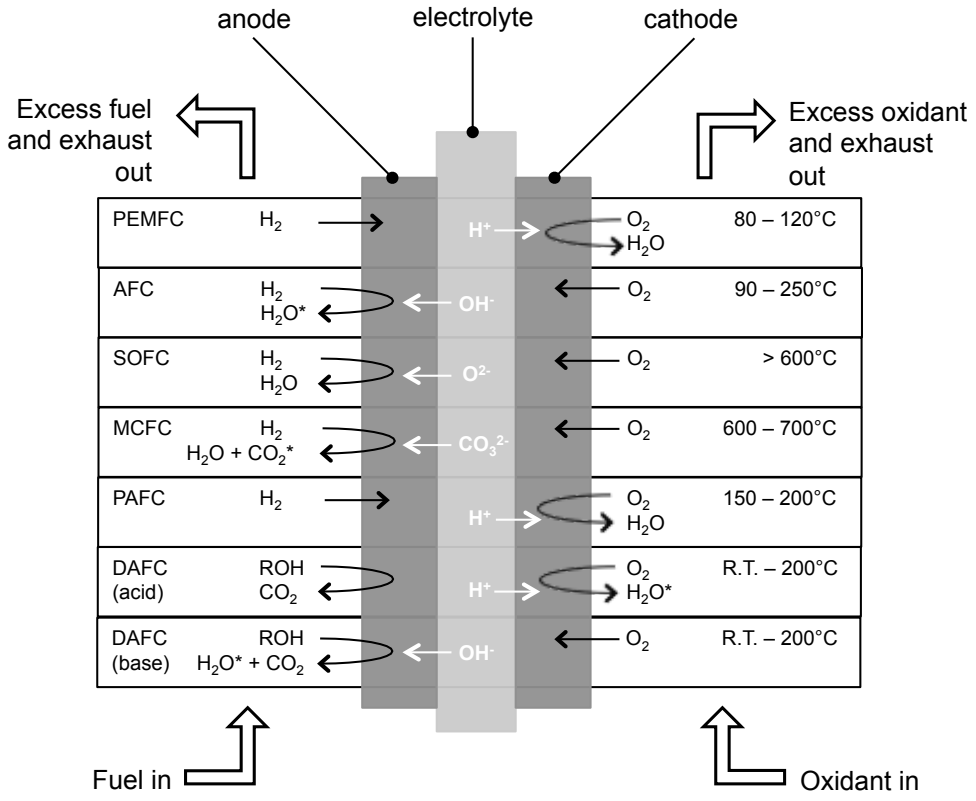

Table 1-1 *A comparison of Fuel Cell Technologies discussed in Section 1.2* [6,7]. *Abbreviations are defined in the text, as well as in the List of Abbreviations (Prefatory pages).*

Fuel cell type	*Electrolyte (Charge carrier)*	*Typical stack size*	*Efficiency*	*Operating temperature*	*Application*
PEMFC	Perfluorosulfonic acid (H^+)	< 1KW – 100 kW	60 % (transport) 35 % (stationary)	80 - 120°C	• Backup and portable power • Distributed generation • Transport
AFC	$KOH_{(aq)}$ soaked in a matrix or AEM/ (OH^-)	10 – 100 kW	60 %	< 120°C and 200 - 250°C	• Space, military and subsea power
SOFC	Yttria-stabilised zirconia (O^{2-})	1 kW – 2 MW	60 %	> 600°C	• Auxiliary power • Distributed generation • Electric utility
MCFC	Carbonates soaked in a matrix (CO_3^{2-})	200 kW – 3 MW	45 – 50 %	600 - 700°C	• Distributed generation • Electric utility
PAFC	> 85 % H_3PO_4 soaked in a matrix (H^+)	400 kW	40 %	150 - 200°C	• Distributed generation

1.2.1 Polymer Electrolyte Membrane Fuel Cell/Proton Exchange Membrane Fuel Cell (PEMFC)

PEMFCs feature a solid proton-conducting membrane as electrolyte. The *Gemini* mission fuel cells were of the PEMFC type where the membrane was polystyrene sulfonate (PSS)-based [8]. These PSS membranes suffered from instability, for example, localized melting during use. One major improvement in PEMFC technology is the development of the more stable polytetrafluroethylene (PTFE) based membrane, the most studied commercially available type being Nafion® by DuPont. In general, the fluorinated membranes are more resistant to degradation under the oxidizing and reducing conditions of the fuel cell because C-F bonds are more stable than C-H bonds (bond dissociation energy (BDE) of C-H 338.4 kJ mol^{-1} *versus* C-F 513.8 kJ mol^{-1} [9]). Figure 1-4 shows the general structure of the PSS and sulfonated PTFE (Nafion®) polymer membranes, while reference [10] is a recent review on different types of polymer electrolyte membranes designed for fuel cell applications.

Figure 1-4 *Structures of polystyrene sulfonate and sulfonated polytetrafluoroethylene polymers used in PEMFCs.*

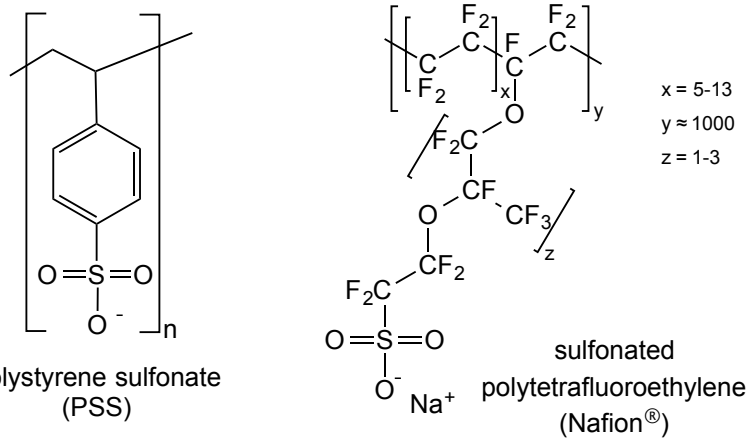

PEMFCs typically operate on hydrogen and oxygen (see Figure 1-1) between 80 and 120°C, and as such, they are classed as low temperature fuel

cells. Because water is necessary for proton conduction in the membrane, the upper limit of the operating temperature is strongly dependent on the humidification needs of the particular membrane employed. The humidity should also be optimally balanced to prevent flooding at the cathode, where water is a product, and dehydration of the fuel cell as a whole. Due to their high power density and rapid start up, typical applications of PEMFCs include transport, such as specialty vehicles like forklifts, distributed generation, and portable and backup power. For example, Ballard's FCgen®-1020ACS PEMFC stack for backup power is rated at 45 W/cell, 65 Amps and 683 mV/cell DC voltage, and achieves 80% of the rated power within 20 seconds of start up [11].

Typically, expensive Pt and Pt-based catalysts are used in PEMFCs. Conventionally, they have been hot-pressed onto the membrane. However, a significant improvement in PEMFC technology was the reduction of catalyst loadings by an order of magnitude to ~ 0.4 mg cm^{-2} by fabricating the electrodes using a catalyst ink instead [12]. This and many other developments came out of the Los Alamos National Laboratory and are discussed in reference [13]. Currently, more of the research related to PEMFC catalysts is geared towards developing cathode catalysts. This is because the oxygen reduction reaction (ORR) at the cathode is much slower than the hydrogen oxidation reaction (HOR) at the anode. For example, the ORR has several orders of magnitude lower exchange current density[3] than the HOR over Pt in acidic solution (10^{-7} to 10^{-9} versus 10^{-3} A cm^{-2}) [14]. Yet, Pt is still one of the most active materials for the

[3] Exchange current density reflects the intrinsic rate of electron transfer between the analyte (in this case, oxygen molecules) and the electrode. It is dependent on the identity, roughness and surface condition of the electrode, and the nature of the analyte.

ORR. A more in-depth discussion on the most active Pt-based ORR catalysts is left for Section 4.1.

One issue with the use of Pt-based catalysts is the intolerance to carbon monoxide. Small amounts of CO are often found in the anode fuel feed, especially when the source of hydrogen is reformed[4] hydrocarbons or alcohols. In order to improve the CO tolerance of Pt-based catalysts in PEMFCs, the Pt is often alloyed with two or three other oxophillic metals such as Ni, Ru, Co, and Sn. The oxophilic metals present a source of more adsorbed oxygenated species so that adsorbed CO can be easily oxidised off of the Pt active sites (a so-called bi-functional effect discussed in more detail in Section 2.1.2.1) [15-20]. Alternatively, depending on the structure of the catalyst, the additive metal can cause lattice contraction of the Pt, decreasing the affinity for adsorption of CO (a variably-named ligand/electronic/geometric effect) [16,21]. In general, features like the type, composition and atomic ratios in the catalysts, and the type and structure of support, as well as the synthetic method of the materials, will affect the degree of CO poisoning [22].

Developments in PEMFCs up to 2004 are provided in reference [23] and a recent review on the status of PEMFC technology and the major challenges toward future progress is provided in reference [24]. Reviews on contamination, durability and degradation in PEMFCs [25,26], and material challenges [27] are also available. Finally, we leave the discussion of PEMFCs run on alcohol oxidants for Section 1.2.6.

[4] Reforming is a method of producing hydrogen from hydrocarbon fuels by reacting the latter at high temperatures (700 to 1100°C) with steam.

1.2.2 Alkaline Fuel Cell (AFC)

AFCs are another type of low temperature fuel cell. As described in Section 1.1.1 above, the electrolyte in a typical AFC operating at 200 to 250°C is 85 wt. % potassium hydroxide solution, while at lower temperatures (< 120°C), concentrations of 35 to 50 wt. % are common. The oxygen reduction reaction (ORR) at the cathode produces hydroxide ions (Equation 1-4a), which migrate to the anode where they combine with hydrogen to form water (Equation 1-4b). Ionic conduction is therefore in the opposite direction to proton conduction in the PEMFC (see Figure 1-3). Water produced at the anode from the hydrogen oxidation reaction (HOR) diffuses to the cathode where it reacts with oxygen to form the hydroxide ions thus completing the circuit. As water is now consumed at the cathode (in contrast to PEMFCs), cathode flooding is avoided.

Anode: $H_2 + 2\ OH^- \rightarrow 2\ H_2O + 2\ e^-$ 1-4a

Cathode: $O_2 + 2\ H_2O + 4\ e^- \rightarrow 4\ OH^-$ 1-4b

Overall: $2H_2 + O_2 \rightarrow 2\ H_2O \quad (E^0_{cell} = 1.23\ V)$ 1-4c

Beyond space applications, AFCs were also the first type of fuel cells to be demonstrated for terrestrial vehicle applications. In the 1960s a farm tractor running on a 15 kW Allis Chalmers AFC was demonstrated, while in the 1970s an Austin A40 hybrid vehicle (AFC combined with a lead acid battery) was operated for 3 years in city traffic [28,29]. However, interest in AFC development declined with the advent of rapid improvements in PEMFCs discussed in Section 1.1.2.

Nevertheless, a review on the major developments of materials and systems in AFCs has recently been published [30].

Like the PEMFCs, platinum is one of the most studied catalysts. Hence, the problem of carbon monoxide poisoning is still apparent. On the other hand, the non-acidic conditions do allow for the use of less expensive, non-noble catalysts, some examples being those based on nickel, manganese oxide or cobalt and iron macrocycles ([30] and references therein), that may be more tolerant to CO than platinum. The use of CO-tolerant catalysts also opens up the variety of fuels that can be used in AFCs, for example, sugars [31-35] and alcohols [36,37], which can be incompletely oxidised to CO. (Alcohol fuels are further discussed in Section 1.2.6). Moreover, catalysts generally perform better in base than in acid [28,38-42].

A major issue for AFCs is that of carbonation of the electrolyte (Equations 1-5a and b). The source of carbon dioxide is either the reformed fuel at the anode and/or air at the cathode. Further, AFCs run on alcohols, instead of hydrogen, will produce carbon dioxide. Carbon dioxide will react with the potassium hydroxide electrolyte to precipitate potassium carbonate/bicarbonate, which can mechanically disrupt the catalyst layers, block catalyst pores and increase the ionic resistance of the electrolyte. (As an aside, alcohols could also be partially oxidised to acids that react with the alkaline electrolyte to potentially form insoluble salts). Moreover, consumption of hydroxide ions, via the carbonation reactions, decreases the pH of the system and can increase the ionic resistance of the electrolyte. In combination these effects lead to a reduction in fuel oxidation reactivity [43].

$$CO_2 + 2\ OH^- \rightarrow CO_3^{2-} + H_2O \qquad 1\text{-}5a$$

$$CO_2 + OH^- \rightarrow HCO_3^- \qquad 1\text{-}5b$$

Thus, traditional AFCs have required pure oxygen and hydrogen feeds. For this reason AFCs have been historically used in niche markets where the cost of pure pressurized oxygen and hydrogen is viable, for example, space, subsea and military applications. It should be noted, however, that it is suggested by some investigators that this disadvantage is severely overemphasized in the literature [29,44].

The development of anion exchange membranes (AEMs) analogous to proton exchange membranes has increased the opportunities for designing high performing AFCs. The use of a membrane instead of a liquid electrolyte simplifies the handling, sealing and assembly of the fuel cell. Further, it can improve AFC lifetime, as the highly caustic solutions tend to cause degradation of components and materials. There is a vast number of studies of design and applications of AEMs, but few reports of use in fuel cells.

Generally, fuel cell AEMs consist of a polymer backbone that confers mechanical and thermal stability, and ionic groups that allow ionic conductivity (≥ 100 x 10^{-3} S cm^{-1}) [45]. For example, Figure 1-5 shows the typical quaternary groups found in AEMs, that is, ammonium, sulfonium and phosphonium benzyl groups. Unfortunately, these cationic groups are susceptible to attack by the OH^- they are meant to transport.

Figure 1-5 *Structure of the quaternary ammonium, phosphonium and sulfonium groups typically used as cationic groups in anion exchange membranes.*

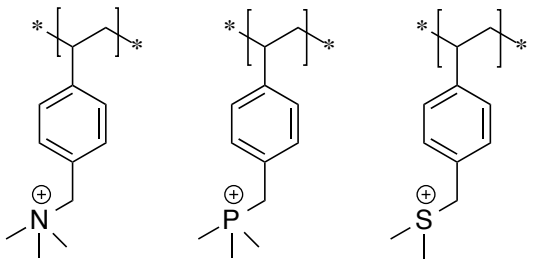

The principal degradation mechanisms are based on elimination (E1 and E2/Hoffmann degradation) and nucleophilic substitution (S_N2), as shown in Scheme 1-1 [46-49]. Degradation via the E1 route is rare and typically occurs with bulky substitutes. On the other hand, it is clear to see why the benzyl substituted quaternary group is present in so many stable configurations of AEMs, as it eliminates the possibility of at least the E2/Hoffmann degradation mechanism due to the lack of a β-H. Other degradation mechanisms such as rearrangements to ylides via alkyl shifts can occur, and these are shown in Scheme 1-2 [50]. The ammonium group has been found to be the most stable of the three benzyl substituted moieties under strongly alkaline conditions [51].

Scheme 1-1 *Elimination and substitution mechanisms of degradation of cationic groups in anion exchange membranes.*

Elimination:

E2/Hoffman degradation

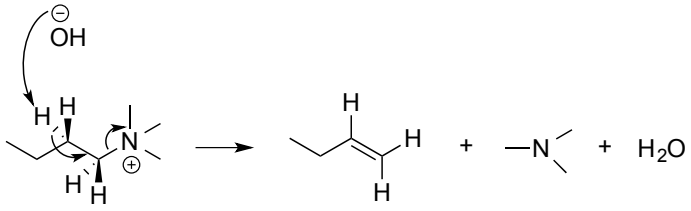

E1 (bulky substituents prevent E2)

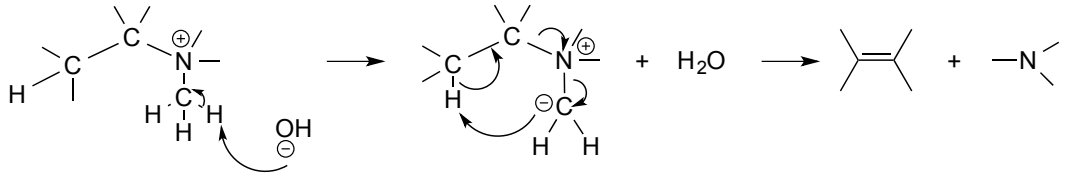

Substitution:

S_N2

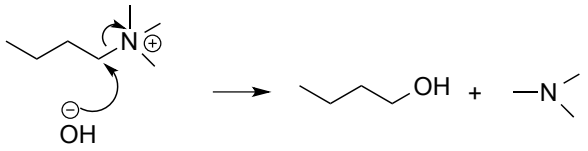

Scheme 1-2 *Proposed degradation mechanisms via rearrangement of alkyl groups to form ylides.*

Sommelet-Hauser rearrangement

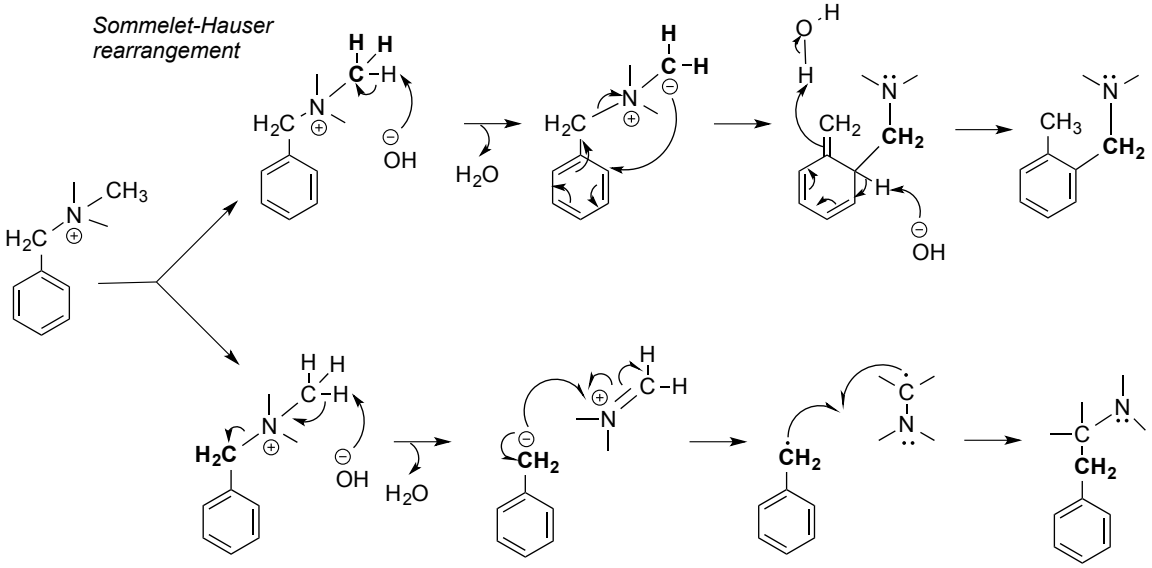

Stevens rearrangement

Merle *et al.* recently proposed a classification system for AEMs, as shown in Chart 1-1[45]. Three broad categories of AEMs have been proposed: heterogeneous membranes, interpenetrated polymer networks, and homogeneous membranes. The structures of the polymers discussed henceforth are shown in Figure 1-6.

Chart 1-1 *Classifications of anion exchange membranes in the literature according to Merle* et al*.* [45].

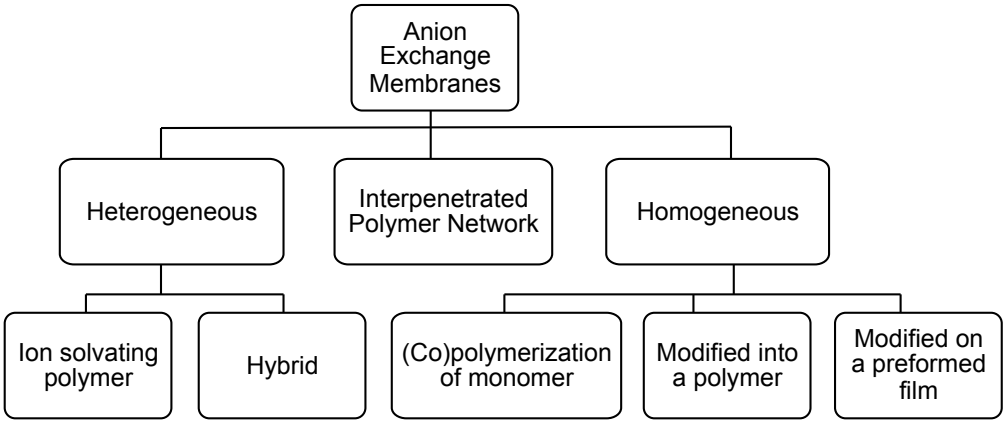

Heterogeneous AEMs describe an insulating polymer matrix combined with an inert compound. Polymers with inert salts are classified as ion solvating polymers, while those with inorganic segments are classified as hybrid membranes. An example of a well-studied ion solvating polymer is alkali-doped polybenzimidazole (PBI) [52-56]. For example KOH-doped PBI exhibits conductivity as high as 0.09 S cm^{-1} [56]. (As a comparison, Nafion® has a conductivity of 0.078 S cm^{-1} [57] under similar conditions.) PBI itself is stable in air up to 500°C and in inert atmosphere up to 600°C [58]. However, due to the hydroxide ions, issues related to carbonation (as seen with liquid electrolytes) can occur.

Figure 1-6 *Structures of various polymers reported for anion exchange membranes towards fuel cell applications.*

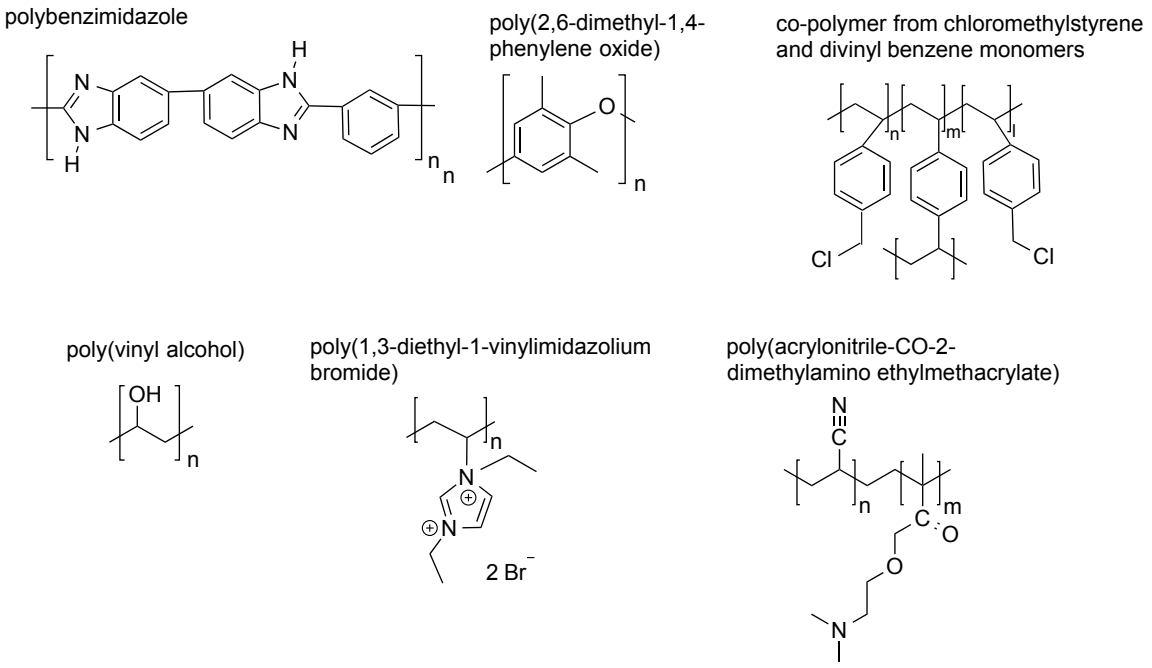

Hybrid membranes comprise an organic and an inorganic section, where the former acts as the ionic conductor and the latter confers mechanical properties. For example, Wu *et al.* prepared a poly(2,6-dimethyl-1,4-phenylene oxide)-silicon organic-inorganic hybrid AEM and investigated the performance in a fuel cell. The membrane displayed an ion-exchange capacity (IEC)[5] on the order of 2 mequiv g^{-1}, and hydroxide anion conductivities of 0.011 S cm^{-1} at room temperature [59]. (IEC of Nafion® = 0.91 mequiv g^{-1} [60])

The second class of AEMs, interpenetrated polymer networks, consists of distinct interlocking polymer chains that possess no covalent bonds between them. Interlocking is typically performed by the polymerization of one polymer in the presence of the other. One polymer usually acts as a source of thermal,

[5] Ionic exchange capacity describes the number of charges exchanged per gram of polymer. The units, milliequivalents per gram (mequiv g^{-1}) rather than millimoles per gram are used to take into account valency. In other words 1 equiv = 1 mole per valence charge.

chemical and mechanical stability, while the other serves to transport anions. Poly(vinyl alcohol) (PVA) has been interlocked with both poly(1,3-diethyl-1-vinylimidazolium bromide) [61] and poly(acrylonitrile-CO-2-dimethylamino ethylmethacrylate) [62]. These networks exhibited IEC values of ~1 mequiv g^{-1}, the latter having conductivity of 3.45 S cm^{-1}. However, in general, these interpenetrated polymer networks do not exhibit conductivities good enough for fuel cell applications [45].

Finally, a one-phase anion exchange polymeric material is referred to as a homogeneous AEM. The three classes of homogeneous AEMs describe their mode of synthesis, that is, via polymerization of a monomer with a functional group that can further form an anion exchange moiety, the grafting of a cationic species onto a preformed film, or the chemical modification of the polymer with cationic groups followed by casting into a film. Of the homogenous membranes, the best fuel cell performance was recorded for the quaternized copolymer of chloromethylstyrene cross-linked with divinylbenzene. To illustrate, IECs of 0.83 to 2.38 mequiv g^{-1} were recorded [63,64]. However, the cross-linking that was meant to improve solubility properties of the membrane also increased the electrical resistance [65]. Furthermore, divinylbenzene is expensive

For the interested reader, references [45,66] and [46] survey many of the AEMs designed and patented recently for fuel cell use. The development of new AEMs combined with the variety of possible non-noble catalysts and the faster catalysis of fuel cell reactions in alkaline media [38-40] means that alkaline AEMFC systems have great potential to be a low-cost and efficient alternative to PEMFCs in wider markets if the desired stability and conductivity parameters are met.

1.2.3 Solid Oxide Fuel Cell (SOFC)

SOFCs are a class of high temperature (> 600°C) fuel cells. They feature an entirely solid electrolyte and thus have no potential electrolyte leakage problems. However, due to the extreme operating temperatures, special materials that are chemically and thermally stable are required for the cell components [67]. The reactions occurring at the electrodes in a SOFC are shown in Equations 1-6a and 1-6b, the overall reaction being that between H_2 and O_2 to form water (Equation 1-4c).

Anode: $2\ H_2 + 2\ O^{2-} \rightarrow 2\ H_2O + 4\ e^-$ 1-6a

Cathode: $O_2 + 4\ e^- \rightarrow 2\ O^{2-}$ 1-6b

The typical electrolyte used in SOFCs operating above 800°C is the dense ceramic material Y_2O_3-stabilized ZrO_2 (YSZ). YSZ is an oxide ion conductor at high temperatures, the mechanism of ion conduction being migration via oxygen vacancies in the crystal structure [68]. YSZ is desirable because of its stability in the oxidizing and reducing environments in the SOFC. Because the electrolyte conductivity is dependent on the temperature, attempts to lower the operating temperature involve having to use thinner electrolyte layers [69] or doping the material. For example, thin layers of Gd_2O_3- and Sm_2O_3-doped CeO_2 have been used as electrolytes at lower temperatures [70]. Unfortunately, doped CeO_2 is inherently mechanically weak and may not withstand the harsh conditions within SOFCs [71].

In the SOFC literature, the bipolar plate (see Section 1.1.3) between the anode of one cell and the cathode of the adjacent cell is known as an interconnect. Typically, at temperatures below 800°C the interconnect is stainless

steel, whereas at higher temperatures chromium-based alloys or oxides, or calcium-doped lanthanum with yttria binders are used [1,68]. The interconnect and other components of SOFCs, need to possess similar coefficients of thermal expansion (CTEs) to avoid cracking of the cells during operation. Additionally, to alleviate thermal stress, SOFCs are not necessarily arranged in traditional sandwich-type (planar) stack designs such as that shown in Figure 1-2. Planar designs are more efficient as the path for current to flow is shorter, but thermally stable glass and glass-ceramic sealants are required to act as electrically insulating gaskets and prevent mixing of the fuel and oxidant between adjacent cells [72]. Tubular designs (Figure 1-7), however, do not require sealants as air flows on the inside of the tube, while the fuel flows on the outside of the tube. The cell components are typically layered in order via electrochemical vapour deposition onto an extruded tube of doped lanthanum manganite that serves as the cathode [68].

Figure 1-7 *Cut-away diagram of the layout of a tubular design solid oxide fuel cell.*

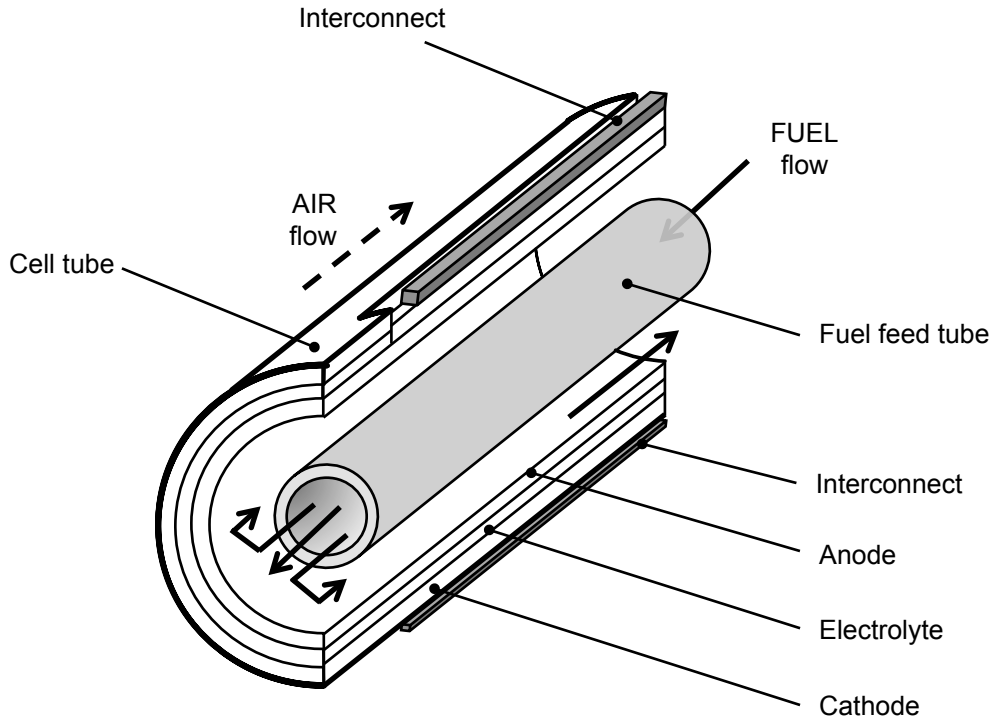

The catalysts used in SOFCs are porous ceramic-based materials. Historically, strontium-doped lanthanum manganite (LSM, $LaSrMnO_3$) has been used at the cathode due to its stability and high ORR selectivity and activity. Recently, perovskite materials, for example iron-doped cobaltates, have been investigated as they have shown higher ORR activity and a better match of the CTE to the YSZ electrolyte [3]. On the other hand, the anode is often a stabilized nickel *cermet* (*i.e.,* a composite made of *cer*amic and metal materials that have the characteristics of both) although zirconia-stabilised anodes have been investigated as well [1,68].

Because water is produced at the anode (Equation 1-4a), reforming of fuels *in situ* and/or direct oxidation of the fuel is possible. Though SOFC catalysts are not poisoned by carbon monoxide/dioxide formed during reformation, they

may be affected by coking, that is, the deleterious deposition of carbon on the catalyst surface [73,74].

Typical applications for SOFCs align with their high temperature operation. They are often used for large stationary, power plants. In addition, SOFCs are often parts of cogeneration systems (combined heat and power, or CHP) where the waste heat is used to produce steam for space heating in homes or for industrial processes, or is integrated with steam turbines to produce electricity [1,3].

1.2.4 Molten Carbonate Fuel Cell (MCFC)

MCFCs are a type of intermediate temperature fuel cell in that they operate at ~ 650°C (between that of a low temperature PEMFC (Section 1.2.1) and a high temperature SOFC (Section 1.2.3) [75]). The electrolyte consists of a molten carbonate salt mixture, mechanically stabilized by suspension in an inert, ceramic matrix of *β*-alumina [68,75]. Typical molten carbonates used are Li_2CO_3 and K_2CO_3. Essentially, carbonate ions are the ionic conductors in the MOFC, being generated at the cathode via reaction of carbon dioxide and oxygen (Equation 1-7a), and consumed at the anode through the oxidation of hydrogen (Equation 1-7b). It should be noted that MCFCs are prone to poisoning by carbon monoxide/dioxide. In fact, the fuel is often a humid mixture of hydrogen and carbon monoxide, although natural gas and light alcohols have also been utilized [68,75,76].

Cathode: $O_2 + 2\ CO_2 + 4\ e^- \rightarrow 2\ CO_3^{2-}$ 1-7a

Anode: $H_2 + CO_3^{2-} \rightarrow H_2O + CO_2 + 2\ e^-$ 1-7b

Typically, the anode catalyst is porous nickel stabilized by a dispersion of aluminum or chromium [76]. The cathode is typically a nickel oxide formed *in situ* by the oxidation of porous nickel. One issue with the cathode is the tendency of nickel to dissolve in the carbonate electrolyte and diffuse from the cathode to the anode; at the anode it can be reduced by the hydrogen and deposit as electronically conductive metallic nickel, thus forming a short circuit between the anode and cathode. To reduce the solubility of the cathode, it is typically doped with lithium or replaced by lithiated metal oxides such as $LiFeO_2$, Li_2MnO_3 or $LiCoO_2$ [68,76].

MCFCs have the same degradation, sealing and CTE matching challenges as SOFCs, and furthermore, tend to have lower power densities as well. They also have the same types of applications, that is CHP systems and stationary power generation [3,77]. Additional challenges with MCFCs, however, are electrolyte management and carbon dioxide recirculation [78].

On the other hand, an interesting application of MCFC technology is as a carbon dioxide removal system. Feasibility studies have been performed on MCFCs fed by the exhaust gases (flue gas) of existing power plants [79-82]. If the MCFC performs well in this role it would have the dual function of being a CO_2 separator/concentrator, as well as a source of more power.

1.2.5 Phosphoric Acid Fuel Cell (PAFC)

With an operating temperature of 150 to 200°C, the PAFC is classified as a low temperature fuel cell. The > 85% phosphoric acid electrolyte is typically supported in a matrix of silicon carbide and is a conductor of protons [1,68]. As such it undergoes the same reactions as shown in Figure 1-1 for a generic hydrogen-oxygen fuel cell. Most often, carbon-supported platinum-based

catalysts are used for both electrodes. Internal reforming is therefore atypical as the Pt catalysts can be easily poisoned. Further, the operating temperature is not high enough for an efficient reforming process. The fuel for PAFCs is therefore generally natural gas reformed in an external steam reformer. On the other hand, tungsten carbide has been investigated as a replacement cathode catalyst due to its resistance to carbon monoxide poisoning and its intrinsic stability [68].

The performance of the PAFC is inherently lower compared to an analogous PEMFC because of the low solubility of oxygen in phosphoric acid, the large Tafel slope[6] for the ORR (> 90 mV dec^{-1}) [83], and due to the strong interaction between phosphate anions and the Pt catalyst surface [3]. Further, because it operates at slightly higher temperature than the PEMFC (Section 1.1.2), it is more difficult to source stable materials.

Typical applications of PAFCs are as power sources for stationary power plants, especially for users who require constant, dependable energy (e.g. hospitals and army facilities) [68]. Also, waste heat can be collected for cogeneration similar to that seen for high temperature fuel cells like SOFCs and MCFCs.

1.2.6 Direct Alcohol Fuel Cell (DAFC)

DAFCs are low temperature fuel cells named for their alcohol fuels, and have been studied in both acid and alkaline electrolytes. Alcohols are attractive as liquid fuels as unlike hydrogen, they are easy to store, transport and handle using

[6] The Tafel slope is the gradient of the linear portion of an empirical plot of potential versus the logarithmic function of the current. Thus, a large slope indicates that a high potential must be applied to give a small change in current produced. Tafel slopes in context of the ORR are discussed in Appendix A.2.3.

current infrastructure. Alcohols also have higher volumetric energy densities than hydrogen assuming the fuels are stored as liquids [66,84]:

$$\text{Mass energy density of the fuel, } W_e^m = \frac{-\Delta G^0}{RMM} \qquad 1-8$$

where ΔG^0 is the standard Gibbs Free Energy of the combustion of 1 mole of liquid fuel

RMM is the relative molar mass of the liquid fuel

$$\text{Volumetric energy density of the fuel, } W_e^v = W_e^m \times \rho \qquad 1-9$$

where ρ is the density of the liquid fuel

For liquid H_2

$\Delta G^0 = -2 \times 96485\ C \bullet mol^{-1} \times 1.23\ J \bullet C^{-1} \times 10^{-3}\ kJ \bullet J^{-1} = -237.35\ kJ \bullet mol^{-1}$

$RMM = 2.02\ g \bullet mol^{-1}$;

$\rho = 0.0708\ kg \bullet L^{-1}$

$$\therefore W_e^m = \frac{237.35\ kJ \bullet mol^{-1}}{2.02\ g \bullet mol^{-1}} = 117.5\ MJ \bullet kg^{-1}$$

$W_e^v = 117.5\ MJ \bullet kg^{-1} \times 0.0708\ kg \bullet L^{-1} = 8.3\ MJ \bullet L^{-1}$

For liquid CH_3OH

$\Delta G^0 = -6 \times 96485\ C \bullet mol^{-1} \times 1.21\ J \bullet C^{-1} \times 10^{-3}\ kJ \bullet J^{-1} - 700.48\ kJ \bullet mol^{-1}$

$RMM = 32.04\ g \bullet mol^{-1}$

$\rho = 0.7918\ kg \bullet L^{-1}$

$$\therefore W_e^m = \frac{700.48\ kJ \bullet mol^{-1}}{32.04\ g \bullet mol^{-1}} = 21.86\ MJ \bullet kg^{-1}$$

$W_e^v = 21.86\ MJ \bullet kg^{-1} \times 0.7918\ kg \bullet L^{-1} = 17.3\ MJ \bullet L^{-1}$

Alcohols are also widely available from natural gas or biomass sources. Because the alcohol is directly oxidised at the anode, a reformer is not necessary and thus DAFCs also boast simple fuelling systems. Moreover, the cell voltage of DAFCs

is only slightly smaller (E^0_{cell} = 1.1 to 1.2 V) than H_2/O_2 cells (E^0_{cell} = 1.23 V). For example the methanol electro-oxidation reactions are shown below with their relative E^0 values.

In acidic media:

$$CH_3OH + H_2O \rightarrow CO_2 + 6H^+ + 6e^- \qquad (E^0 = 0.02\ V_{SHE}) \qquad 1\text{-}10a$$

$$O_2 + 4\ H^+ + 4e^- \rightarrow 2\ H_2O \qquad (E^0 = 1.23\ V_{SHE}) \qquad 1\text{-}10b$$

In basic media:

$$CH_3OH + 6\ OH^- \rightarrow CO_2 + 5\ H_2O + 6e^- \qquad (E^0 = -0.81\ V_{SHE}) \qquad 1\text{-}11a$$

$$O_2 + 2\ H_2O + 4e^- \rightarrow 4\ OH^- \qquad (E^0 = 0.4\ V_{SHE}) \qquad 1\text{-}11b$$

Overall:

$$2\ CH_3OH + 3\ O_2 \rightarrow 4\ H_2O + 2\ CO_2 \qquad (E^0_{cell} = 1.21\ V) \qquad 1\text{-}12$$

On the other hand, the kinetics of alcohol oxidation are more sluggish than hydrogen oxidation limiting their power output. Thus DAFCs are generally used for small portable electronics or smaller vehicles like forklifts. The most studied DAFC is the Direct Methanol Fuel Cell (DMFC), as methanol is the simplest alcohol, having no C-C bonds in its structure.

1.2.6.1 Direct Methanol Fuel Cells (DMFCs)

The first DMFCs were constructed in the 1960s and 1970s by Shell Research in England, and Exxon-Alsthom in France, respectively. The former used a sulfuric acid liquid electrolyte while the latter abandoned the acid route and investigated alkaline electrolytes [85]. Initially, the development of conductive acidic membranes (particularly the commercialization and availability of the acidic PEMs like Nafion®) led to numerous reports of methanol-fuelled PEMFCs. The

highest activities observed in the PEM-based DMFCs show a large dependence on Pt-based catalysts and this will be discussed in due course.

Many problems arose in PEM-based DMFCs because the PEMs (most often Nafion®-117 where 117 refers to a membrane with EW 1100 and is 0.007 inches thick [86]) were optimized for hydrogen fuel and not methanol. Methanol is a larger molecule than hydrogen, and is wetting in nature. Further, carbon dioxide must be removed from the catalyst sites and electrode pore system during methanol oxidation. Combined, these factors suggest that a PEM with a more 'open' structure may be essential [87]. Furthermore, Nafion® is permeable to methanol. This manifests in a phenomenon referred to as methanol crossover whereby methanol is transported via osmosis from the anode to the cathode where it can be oxidised. In turn, a mixed potential develops at the cathode and ultimately reduces the performance of the cell. Methanol crossover is exacerbated by electro-osmotic drag, that is, methanol associates as part of the hydration shell of protons conducted from the anode to the cathode because methanol possesses a similar dipole moment to water [68].

A few strategies have been used to counteract methanol crossover and its effects. For example, the fuel feed is typically limited to a 1 - 2 M aqueous solution (which in turn reduces the prospective power density), or a methanol vapor feed is used to lower the flux across the membrane. Modifications to the membrane have also been investigated. For instance, thicker membranes have been used, but this introduces other problems such as higher ionic resistance. Impregnation of membranes with caesium cations has been explored, as Cs^+ has a lower affinity to water than H^+ and should thus reduce electro-osmotic drag [68]. Pore-filling electrolyte membranes have also been synthesized by dispersing the membrane electrolyte in a porous substrate that is inert to the fuel

and gases. The substrate acts to restrict swelling of the membrane thereby minimizing crossover [88-90]. Mixed reactant DMFCs have also been developed where the oxidant and the methanol are delivered to the cell as a mixture, and very selective anode and cathode catalysts are used [91-94]. Obviously, this latter approach does not prevent methanol crossover, but aims to lessen its effects.

The use of alkaline electrolytes in DMFCs also mitigates the effects of methanol crossover because the direction of electro-osmotic drag is reversed in the alkaline electrolyte (see Section 1.2.2 and Figure 1-3). The alkaline system has other advantages as well. Firstly, lower catalyst loadings can be used as the methanol oxidation reaction (MOR) is faster in base than in acid [95]. This is likely because in alkaline solutions there is a lack of specifically adsorbed ions that block the surface from adsorbing active species such as OH (*vide infra*) [36,96]. Second, the propagation of these active OH moieties on catalyst surfaces occurs at lower potentials in base than in acid [36]. Further, non-noble catalysts are stable in alkaline conditions and therefore a precious metal free DMFC is conceivable [97,98]. Finally, alkaline membranes that are possibly cheaper than Nafion® could be developed for and used in the alkaline DMFCs [37,43,46,49,66,99] (See Section 1.2.2).

The mechanisms suggested in the literature for the MOR over Pt are summarized in Scheme 1-3. We note that many of the studies are not definitive so that the mechanisms represent the best proposals available for what is occurring. Over most transition metal catalysts, the mechanism of methanol electro-oxidation in acid occurs via a series of elementary C-H and O-H activations [100]. Based on empirical evidence and theoretical studies, it is believed that C-H activation occurs predominately below 0.35 V_{RHE} to form a

hydroxyl methylene (CHOH) intermediate that eventually forms carbon monoxide (CO). At higher potentials, O-H activation of methanol can occur as well, and accounts for the presence of formaldehyde ($H_2C=O$) in the bulk solution or adsorbed on the catalyst surface.

Solvated $H_2C=O$ can be hydrated to form methanediol ($CH_2(OH)_2$). Subsequently, $CH_2(OH)_2$ can dehydrogenate to formic acid (HCOOH) that in turn can be adsorbed as formate ($HCOO^-$). $HCOO^-$ presumably binds to the catalyst surface via a di-sigma interaction making conversion to CO_2 difficult. Interestingly, adsorbed formate has been observed by IR spectroscopy in a pathway that does not involve CO formation [101]. On the other hand, adsorbed $H_2C=O$ can react at these higher potentials to form CO [102]. It should be noted that CO acts as an electrocatalytic poison in the absence of adsorbed OH species, or as an active intermediate of CO_2 formation in their presence. In fact, CO poisoning is one of the challenges that limits the performance of DMFCs.

Scheme 1-3 *Proposed mechanism of the electro-oxidation of methanol by platinum in aqueous acidic media. The * notation indicates suggested atoms that bind to the Pt surface. The subscripts* sol *and* ads *indicate the species is in the solution or adsorbed on the Pt surface respectively.*

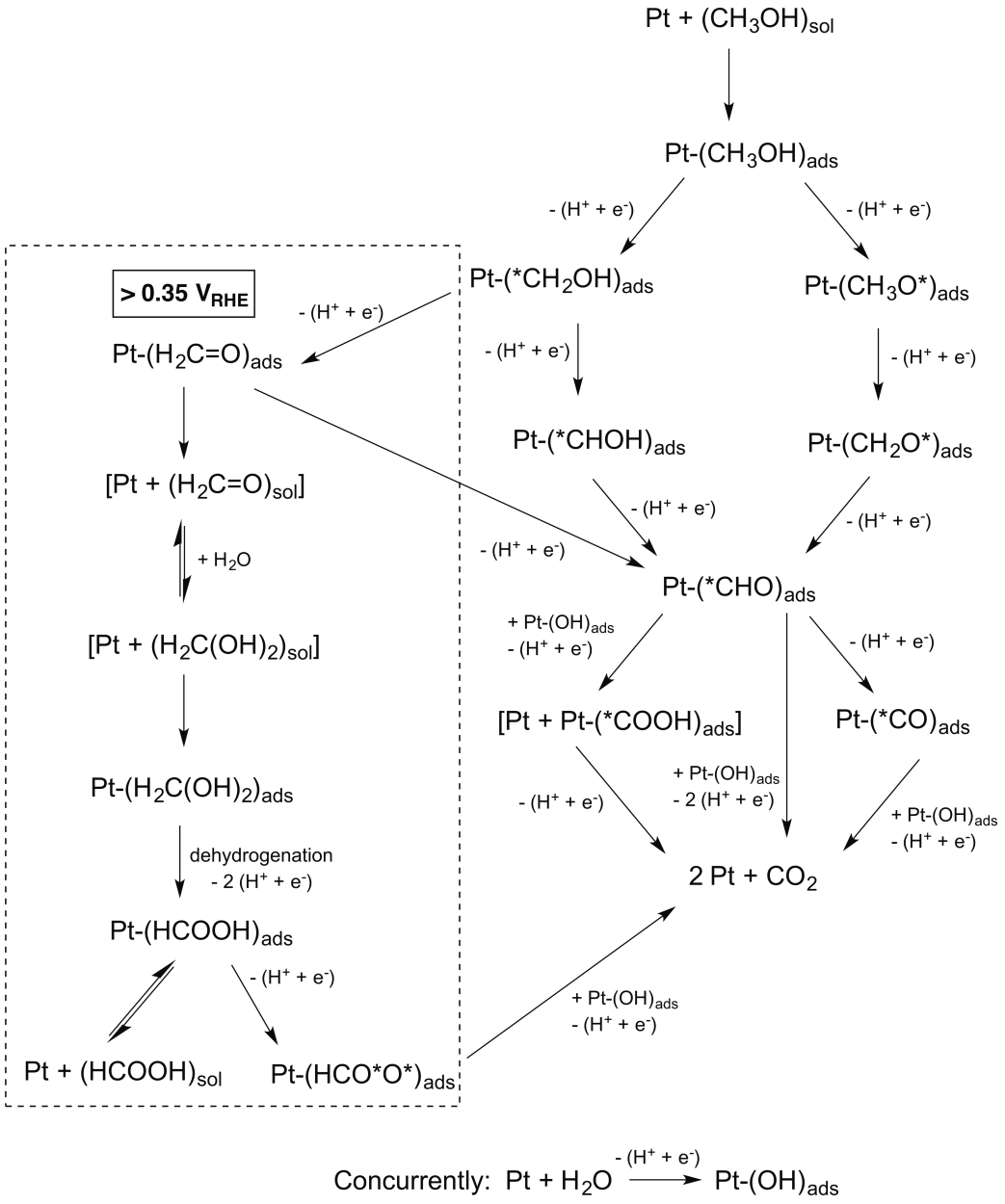

Similar intermediates (with a few exceptions like formic acid) are suggested or observed in the alkaline electro-oxidation of methanol. The

proposed mechanism for the alkaline MOR is shown in Scheme 1-4. Again, definitive evidence of binding modes of the adsorbates is not available.

Scheme 1-4 *Proposed mechanism of the electro-oxidation of methanol by platinum in aqueous alkaline media. The subscripts* sol *and* ads *indicate the species is in the solution or adsorbed on the Pt surface respectively.*

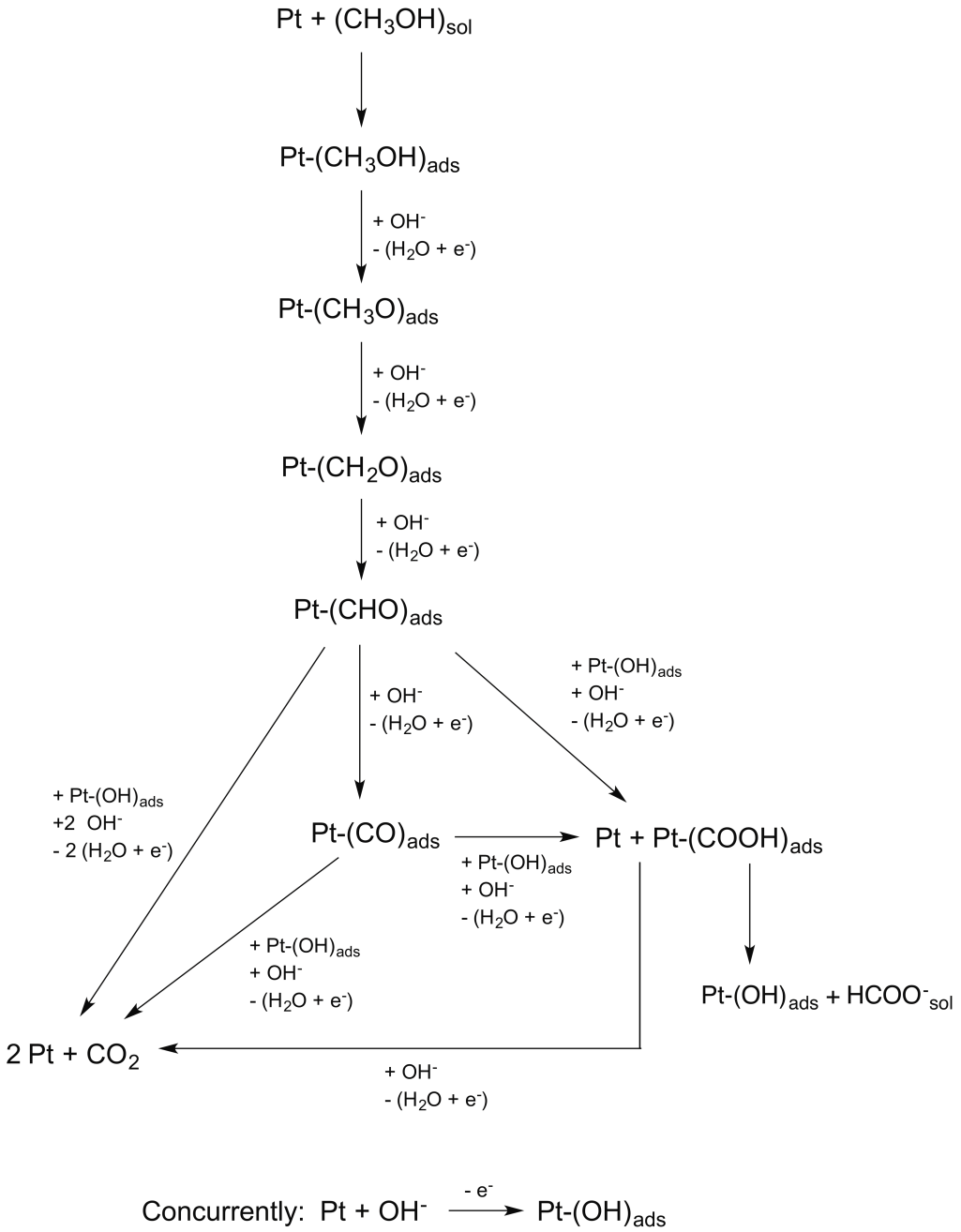

In both electrolytes, the formation of adsorbed OH on the catalyst surface is a vital step for the removal/oxidation of CO, and ultimately, the complete oxidation of methanol to CO_2. In fact, because the alcohol group only contains one oxygen atom, an extra oxygen atom must be provided by water or O-containing adsorbates. It follows that a catalyst that can not only efficiently dissociate alcohols, but can also form adsorbed OH species at low potentials, or prevent the build-up of adsorbed CO, can be highly active for alcohol oxidation. For example, the highest anode performance reported in a DMFC was a PtRu alloy catalyst supported on graphitic mesoporous carbon run under acidic conditions (210 mW cm^{-2}; 0.09 mW $\mu g_{Pt\ total}^{-1}$) [103]. In this case, the Pt sites act as efficient C-H/O-H activation catalysts, while Ru sites serve to adsorb OH in a lower potential range than on Pt sites, thus increasing the rate of oxidation of CO adsorbed on Pt sites compared to a pure Pt catalyst. These dual roles of Pt and Ru that enhance the activity observed for Pt alone are referred to as a bi-functional effect [15,16,104,105] (*vide infra*). It is also suggested that the presence of Ru alloyed to Pt could modify the electronic structure of the latter via an electronic/ligand effect and enhance its adsorption of OH species and/or desorption of CO [20,105,106]. As an aside the carbon support allows efficient mass transport of methanol, carbon dioxide, and electrons.

1.2.6.2 Direct Ethanol Fuel Cells (DEFCs)

Ethanol-fueled DAFCs have also been studied recently [107-109]. Ethanol has many advantages over methanol fuel including higher energy density, less toxic effects, higher boiling point, and availability as a renewable biofuel from the fermentation of biomass [84,98,107]. It also has a lower degree of permeability through Nafion® and other perfluorosulfonated ionomer membranes than

methanol, hence ethanol crossover is not as serious a problem in PEM-based DEFCs as in analogous DMFCs [107,110]. The complete electro-oxidation of ethanol, however, is slower and more difficult than methanol on account of the strong C-C bond (BDE = 618 kJ mol^{-1} [9]). Actually, the main products of ethanol electro-oxidation in both acid and base, over transition metals (Au, Pd, Pt), are those from partial oxidation, that is, acetaldehyde (AL) and acetic acid (AA). Only small amounts of the complete oxidation product CO_2 are usually detected [36,84,111,112]. Incomplete oxidation of ethanol to AL (Equations 1-13a and 1-14a) only provides one sixth of the current of complete oxidation reaction (Equations 1-13c and 1-14c), whereas formation of AA (Equations 1-13b and 1-14b) only accesses one third of the current. The amount of current produced worsens even further if the cell is run on diluted rather than neat ethanol.

$$CH_3CH_2OH \rightarrow CH_3CHO + 2\,H^+ + 2e^- \qquad 1\text{-}13a$$

$$CH_3CH_2OH + H_2O \rightarrow CH_3COOH + 4\,H^+ + 4e^- \qquad 1\text{-}13b$$

$$CH_3CH_2OH + 3\,H_2O \rightarrow 2\,CO_2 + 12\,H^+ + 12e^- \qquad 1\text{-}13c$$

$$CH_3CH_2OH + 2\,OH^- \rightarrow CH_3CHO + 2\,H_2O + 2e^- \qquad 1\text{-}14a$$

$$CH_3CH_2OH + 4\,OH^- \rightarrow CH_3COOH + 3\,H_2O + 4e^- \qquad 1\text{-}14b$$

$$CH_3CH_2OH + 12\,OH^- \rightarrow 2\,CO_2 + 9\,H_2O + 12e^- \qquad 1\text{-}14c$$

Initially, Pt catalysts were used in studies of the EOR, as Pt should facilitate the C-H, O-H and C-C activations required for complete oxidation of ethanol to CO_2. However, similar to the MOR, Pt suffers from self-inhibition: when the C-C bond is cleaved, CO and methyl fragment (CH_x) poisoning occurs [113]. Further, as implied above, when the C-C bond is not cleaved and the partial

oxidation products (AL and AA) form, they often desorb before they can be fully oxidised resulting in inefficient use of the fuel [102].

PtSn provides good results for ethanol oxidation in acid, with Sn performing a similar bi-functional role as that of Ru in methanol oxidation discussed above (Section 1.2.6.1) [114,115] but with higher activity towards the acid EOR than a comparable PtRu bimetallic catalyst. PtSn also outperformed analogous PtW and PtPd bimetallic catalysts [109,116]. The suggested mechanism for ethanol oxidation over PtSn in acid is shown in Scheme 1-5 below [109] where C_1 and C_2 adsorbates are unknown species with 1 and 2 carbons in their structures respectively.

Scheme 1-5 *Proposed mechanism of the electro-oxidation of ethanol by platinum-tin in acidic media. Dashed lines signify steps that are enhanced or allowed via the bi-functional effect of Sn on Pt. The subscripts* sol *and* ads *indicate the species is in the solution or adsorbed on the catalyst surface respectively.*

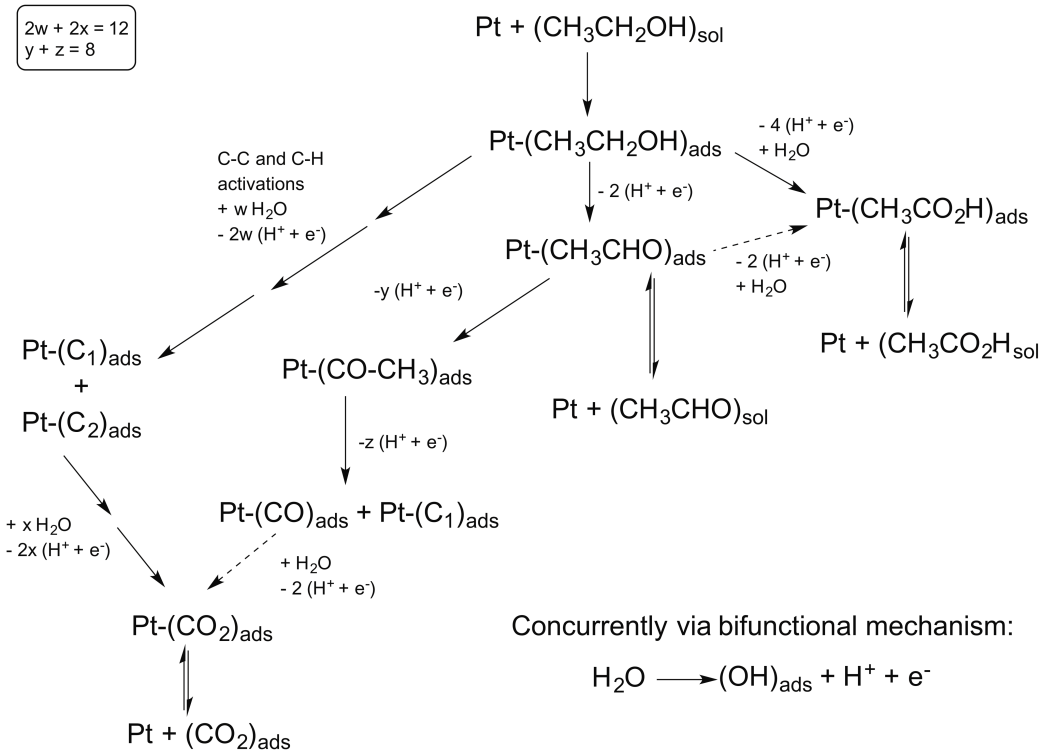

It was discovered that Pd also shows good activity for the acid EOR, and demonstrates markedly superior activity than Pt on the alkaline EOR [36,98]. The reason for the superior performance in base was attributed to the ease of continued dehydrogenation reactions in the presence of sufficient adsorbed OH moieties on the Pd surface as opposed to acid media where adsorbed OH species are less prevalent.

In 2007, the first DEFC vehicle was demonstrated at the European Shell Eco-marathon. The 50W fuel stack ran on biomass-derived ethanol and Acta Nanotech's Hypermec^{TM} electrodes and catalysts and an anion exchange membranes [117]. The Hypermec^{TM} catalysts are highly selective (mitigating the effects of ethanol crossover), tolerant to CO-poisoning, and based on non-noble metals [118,119]. Despite the success of the demonstration, the commercialization of DEFCs generally remains targeted at portable electronics applications. A recent review of DEFCs is provided in reference [120].

1.2.6.3 Direct 2-Propanol Fuel Cells (D2PFCs)

2-propanol is a viable alternative to methanol in DAFCs because of its higher energy density, lower toxicity [121], lower electro-oxidation onset potential over Pt and Pt-Ru [122,123], and lower degree of crossover [124,125]. Moreover, the 2-propanol oxidation reaction (2POR) is reversible [126,127], so in principle a rechargeable system is conceivable [123].

The first D2PFC was reported in 1995 by the Savinell research group [128]. The authors described a DAFC operating between 150 and 190°C with a commercial 4 mg_{met} cm^{-2} Pt-Ru alloy anode and 4 mg cm^{-2} Pt black cathode, separated by an acid-doped PBI membrane. Using on-line mass spectrometry (MS), they found that acetone was the main electro-oxidation product of 2-

propanol fuel. Moreover, no CO_2 was detected. However, in comparison to methanol, ethanol and 1-propanol fuels, the D2PFC had the poorest performance at 250 mA cm^{-2}, and the lowest open circuit voltage (OCV). In fact, the authors concluded that 2-propanol was not suitable as a fuel in DAFCs. Despite these discouraging results, the D2PFC was revisited in the early 2000s and these later results give a clue as to why this initial study was so unsuccessful.

In 2002, Umeda *et al* reported a room temperature acidic D2PFC, run on 0.5 M fuel with a Pt-Ru anode, showing better performance characteristics than the analogous DMFC at low power operation [129]. At higher power densities, the trend was reversed. The authors suggested that acetone accumulation on the anode catalyst (see Section 1.3) accounted for poor performance in the D2PFC. Interestingly, when the concentration of fuel was increased to 5 M, the D2PFC demonstrated better performance than the DMFC at both high and low power densities. With these promising results the interest in 2-propanol fuels piqued.

Qi and Kaufman reported a number of studies on acidic D2PFCs between 2002 and 2003. They found that D2PFCs demonstrate higher OCVs, lower activation voltages, and lower crossover currents than analogous DMFCs (alcohol concentration = 1 M, PtRu anode 4.8 mg_{met} cm^{-2}, Pt cathode 4.8 mg_{Pt} cm^{-2}, Nafion 117/112 membrane, air oxidant) [125,130,131]. As well, the authors noted that the D2PFC performance was not as sensitive to a decreasing air flow rate at the cathode. This is significant as the rate of air flow is critical to maintaining the water balance in the cell and preventing cathode flooding. In general, it was found that below 200 mA cm^{-2} D2PFCs demonstrate higher cell voltages than DMFCs and this was accounted for by faster oxidation kinetics and lower alcohol crossover. For example, a D2PFC produced a cell voltage of 690 mV at 20 mA cm^{-2} while a comparable DMFC only demonstrated 480 mV [131].

Above 200 mA cm^{-2}, it was found that the cell voltage in a D2PFC declined rapidly, not only due to mass transport limitations, but also due to poisons accumulating on the anode. A more recent study confirmed the results of Qi and Kaufman; a D2PFC with a Pt-Ru or Pt-Ru-Sn anode was found to outperform both a DMFC and DEFC at current densities < 200 mA cm^{-2} but the performance severely declines above that limit [132].

This trend of good performance at relatively low current densities and declining performance at high current densities is consistent with the first reports on D2PFCs by both Savinell and Umeda discussed prior. It is noted that the first report by Savinell and co-workers in 1995 disregarding the use of 2-propanol as a fuel, did not connect the *in situ* MS results, that is, acetone being the sole electro-oxidation product detected, with the poor performance of the D2PFC at *high* current densities [128]. This oversight was understandable as the MS only detected products in solution and the assumption that acetone could have also been adsorbed on the catalyst surface may have been deemed speculation at the time. Alternatively, the authors of reference [132] suggest that at current densities higher than 200 mA cm^{-2}, poor performance is a result of evolved hydrogen from the non-electrochemical oxidation of 2-propanol (Equation 1-15) impeding mass transport of fuel to the catalyst surfaces.

$$CH_3CHOHCH_3 \rightarrow CH_3COCH_3 + H_2 \qquad 1\text{-}15$$

Qi and Kaufman also demonstrated an acidic D2PFC run on neat 2-propanol and humidified air [131]. The 25 cm^2 cell was equipped with a Pt/Ru anode and Pt cathode catalysts (4.8 and 7.8 mg_{met} cm^{-2} respectively) and a sulfonated polyether ether ketone (SPEEK) membrane. The D2PFC exhibited a power density of 97 mW cm^{-2} (0.485 V at 200 mA cm^{-2}) at 60°C, 6.5 mL min^{-1} fuel rate and 920 mL min^{-1} air flow rate. This was the highest performance for a direct

oxidation liquid feed fuel cell at the time. At 30°C, the cell produced 48 mW cm^{-2} (0.598 V at 80 mA cm^{-2}). Further, the authors demonstrated that the cell could be refreshed during shut down by ceasing the fuel and oxidant flow, or especially by switching the polarity of the cell before restarting. The room temperature performance and the ability to refresh the cell demonstrated that D2PFCs were suitable for portable electronic applications that require high energy densities but not necessarily high current densities at room temperature.

Kobayashi *et al* demonstrated acidic D2PFCs using carbon supported base metal anode catalysts, Ni, Co, Cu and Mn [122]. They found that the D2PFC with a Ni/C anode showed the highest OCV (similar to over Pt/C), and compared to an analogous DMFC, displayed higher current densities at 25 and 80°C. Further, using stripping voltammetry, the authors found that the Ni/C catalyst had less adsorbates on its surface than a Pt/C catalyst during 2-propanol oxidation. Interestingly the authors did not mention catalyst stability problems despite the incompatibility of Ni and acid. Cao *et al* reported a Nafion®-based DAFC with a Pt-Ru anode catalyst operating on 2-propanol with ~200 mV higher cell voltage at 120 mA cm^{-2} than methanol [133]. The D2PFC, however, lost activity at higher current densities due to anode poisoning. Saravanan and collaborators reported similar results, that is, over a Pt-Ru anode, a 2-propanol fuelled DAFC performed better than an analogous one running on butanol, 1-propanol and methanol at low current densities (20 mA cm^{-2}), but methanol outperformed 2-propanol at higher current densities (44 mA cm^{-2}) [124]. Tapan and Öztürk reported a D2PFC with a Pt anode [134]. The highest performance was recorded at 1 M fuel concentration and 80°C operating temperature. However, the cell voltage was found to decline at short times due to acetone

build up on the anode. The cross over current was minimum at 0.5 M 2-propanol concentration and 40°C.

Few reports have been made on alkaline D2PFCs despite oxygen reduction and alcohol oxidation kinetics being faster in base than in acid [39,40], and the potential for using less expensive, non-noble catalysts that are intolerant to acidic media. Wang *et al* reported an alkaline DAFC with a poly(vinyl alcohol)/TiO_2 composite membrane, MnO_2/C air cathode and Pt/Ru anode [135]. The authors found that although 2-propanol demonstrated the lowest permeability through the membrane (i.e. lowest potential for alcohol crossover), the D2PFC had the poorest cell performance compared to an analogous DMFC and DEFC. The authors interestingly credited the poor performance of the D2PFC to low activity of Pt/Ru towards 2POR.

Our laboratory has reported a liquid electrolyte alkaline fuel cell operating on 2-propanol and methanol [136]. The cell featured commercial Pt/C catalysts at both the anode and the cathode with 5 M aqueous KOH as the electrolyte. When compared to the corresponding DMFC, the D2PFC had higher OCV and markedly higher power outputs and stability at cell voltages above 0.5 V. When the anode potential is kept below ~ 0.23 V_{RHE} the D2PFC is capable of producing relatively high power densities. This avoids the formation of strongly bound intermediates on the anode. To our knowledge, these are the only two reports of direct alkaline D2PFCs in the literature, although many reports of 3-electrode 2POR experiments in both base and acid exist. These will be discussed in the following section.

1.3 The 2-Propanol Electro-oxidation Reaction

1.3.1 Mechanistic studies of the 2-propanol electro-oxidation reaction

The 2POR over Pt catalysts was investigated as early as 1986 [137], yet Pt, modified Pt and/or Pt-group metals are still the most studied catalysts for both the acidic and alkaline 2POR. For example, blackened Pt [138], Pt/C [139-141], Pt nanoparticles (supported and unsupported) [123,137,142,143,143-146], AuPt [143], PtRh [147], PtRuSn [132], PtRu [123,145,148], PtNi [149,150], Au [143,151], Pd [143,146,152,153], AuPd [143,154,155], PdPt [156] and Pd/Ni foam [157] have been used in 3-electrode experiments.

The mechanism of 2-propanol oxidation has traditionally been investigated by infrared spectroscopy [137,144,148,158-164], mass spectrometry [132,144,147], and standard electrochemical experiments [84,139,140,145,165-168] (see Table 1-2). Recently a High Pressure Liquid Chromatography (HPLC) study has also been published [169]. The body of work, however, is far less than for the mechanism of methanol oxidation. Most of the studies agree on the following features of 2-propanol oxidation over Pt:

1. Based on DEMS, FTIRS and deuterium labeling experiments, 2-propanol bonds to the surface of Pt through dehydrogenation at the alpha carbon [144].
2. From mainly *in situ* FTIR [144,158-164] and one EQCM study [159], acetone is the main product in solution of the electro-oxidation of 2-propanol (and the only product detected in anhydrous solutions [137]), while little or no carbon dioxide has been detected, and only above at least 0.4 V_{RHE}. In other words, 2-propanol electro-oxidation to acetone

occurs at a lower potential than acetone electro-oxidation to carbon dioxide.

3. The electro-oxidation of 2-propanol to acetone occurs via low coverages of stable intermediates [147,170], while the electro-oxidation of acetone to carbon dioxide in acid does not involve strongly adsorbed species [144,169].
4. Unlike *n*-propanol [163] and glycerol [171], 2-propanol is the only C_3 alcohol that does not dissociate into CO at Pt surfaces in acid i.e. C-C bond dissociation is not favored.
5. Direct observation of adsorbed acetone is not available[7], but is inferred from a combination of DEMS and voltammetric results [144,159,164]. Propoxide may be a stable adsorbate but it cannot be detected due to overlapping 2-propanol/supporting electrolyte bands in FTIRS [147].
6. Propane is the only detected electro-reduction product of 2-propanol in acid [144].

[7] Recall that FTIR selection rules dictate that, for adsorbates on metal surfaces, only the vibrational modes that give rise to an oscillating dipole normal to the surface result in an observable IR absorption band. Acetone, if adsorbed, likely does so through an η^2 interaction involving the –C=O moiety positioned parallel to the metal surface, making it an IR inactive vibrational mode.

Table 1-2 *Typical experimental techniques used to probe alcohol electro-oxidation intermediates and products.*

Technique	*Analyte*	*Advantages*	*Disadvantages*
In situ Fourier Transform Infrared Spectroscopy (FTIRS)	Products and adsorbed species.	Detects volatile and non-volatile species; Adsorbed and non-adsorbed species can be differentiated.	Only works for smooth electrodes and liquid electrolytes; Only senses reversible potential-induced spectral events.
Single Potential Alteration Infrared Spectroscopy (SPAIRS)	Products and adsorbed species.	Same as FTIR and using potential steps or sweeps allows kinetics to be probed.	Only works for smooth electrodes and liquid electrolytes.
Differential Electrochemical Mass Spectroscopy (DEMS)	Volatile products.	Compatible with galvanostatic, potentiostatic or potentiodynamic methods; Can separate overlapping electrode processes.	Only works in liquid electrolytes; Cannot detect non-volatile species.
Surface Enhanced Raman Spectroscopy (SERS)	Adsorbed species.	Sensitive and surface selective.	Primarily works on Au, Ag and Cu surfaces; Analyte must be Raman active.
High Pressure Liquid Chromatography (HPLC)	Products in solution.	Complements voltammetric and spectroscopic findings.	Cannot detect volatile products or adsorbed species.

With the preceding information in mind, the mechanism of 2-propanol electro-oxidation over Pt in acidic media [163], and basic media [138] respectively, involves the following reactions:

$$(CH_3)_2CHOH \rightarrow (CH_3)_2CO + 2\,H^+ + 2e^- \qquad 1\text{-}16a$$

$$(CH_3)_2CO + 5\,H_2O \rightarrow 3\,CO_2 + 16\,H^+ + 16e^- \qquad 1\text{-}16b$$

$$(CH_3)_2CHOH + 5\,H_2O \rightarrow 3\,CO_2 + 18\,H^+ + 18e^- \qquad 1\text{-}16c$$

$$(CH_3)_2CHOH + 2\,OH^- \rightarrow (CH_3)_2CO + 2\,H_2O + 2e^- \qquad 1\text{-}17a$$

$$(CH_3)_2CO + 16\ OH^- \rightarrow 3\ CO_2 + 11\ H_2O + 16e^- \quad \text{1-17b}$$

$$(CH_3)_2CHOH + 18\ OH^- \rightarrow 3\ CO_2 + 13\ H_2O + 18e^- \quad \text{1-17c}$$

In both acid and base, the electro-oxidation of 2-propanol to acetone occurs at low potential ranges where Equation 1-16a occurs from 0.22 to 0.67 V_{RHE}, and 1-17a from 0.05 to 0.25 V_{RHE}. Above these potential ranges, both 2-propanol and acetone can be oxidised to carbon dioxide (Equations 1-16b and 1-17b, and 1-16c and 1-17c respectively). The literature does not provide definitive evidence of the relative rates of these pairs of reactions, but there is consensus that the oxidation of carbon dioxide to acetone is slow given the product ratio of acetone:carbon dioxide (approximately 8:1 according to reference [144]).

There are subtle differences between the mechanism in acid and base. First, it is noted that the dehydrogenation step (equation 1-16a and 1-17a) occurs at lower onset potentials in base than in acid. Further, contrary to in acid (point 3 above), the electro-oxidation of acetone occurs through strongly adsorbed intermediates in base [138]. This is manifested in chronoamperometry experiments as a low-potential current maximum. Sample data of this phenomenon is shown in Figure 1-8. At potentials between 50 and 150 mV_{RHE}, 2-propanol is rapidly oxidised to acetone, which is then strongly adsorbed to the catalyst's surface. This blocks further oxidation of 2-propanol so that the current observed decreases as the potential increases to 250 mV_{RHE}. Above this potential the adsorbed acetone can be oxidised to CO_2, clearing the surface for oxidation of 2-propanol and/or acetone resulting in an increase in current. Comparable data to Figure 1-8 is shown in Figure 3 in reference [172] but we note that the short times chosen for the chronoamperometry experiments therein

do not highlight the subsequent increase in current we see at higher potentials, presumably when acetone is oxidised off the surface of the catalyst.

Figure 1-8 *Sampled current voltammogram of 2-propanol electro-oxidation over a Pt blacked gauze. Conditions are 1M 2-$(CH_3)_2CHOH$ in 0.5 M NaOH at 60°C. The data points are the average stabilized current at the end of 15-minute potential steps, while the line is a guide for the eye.*

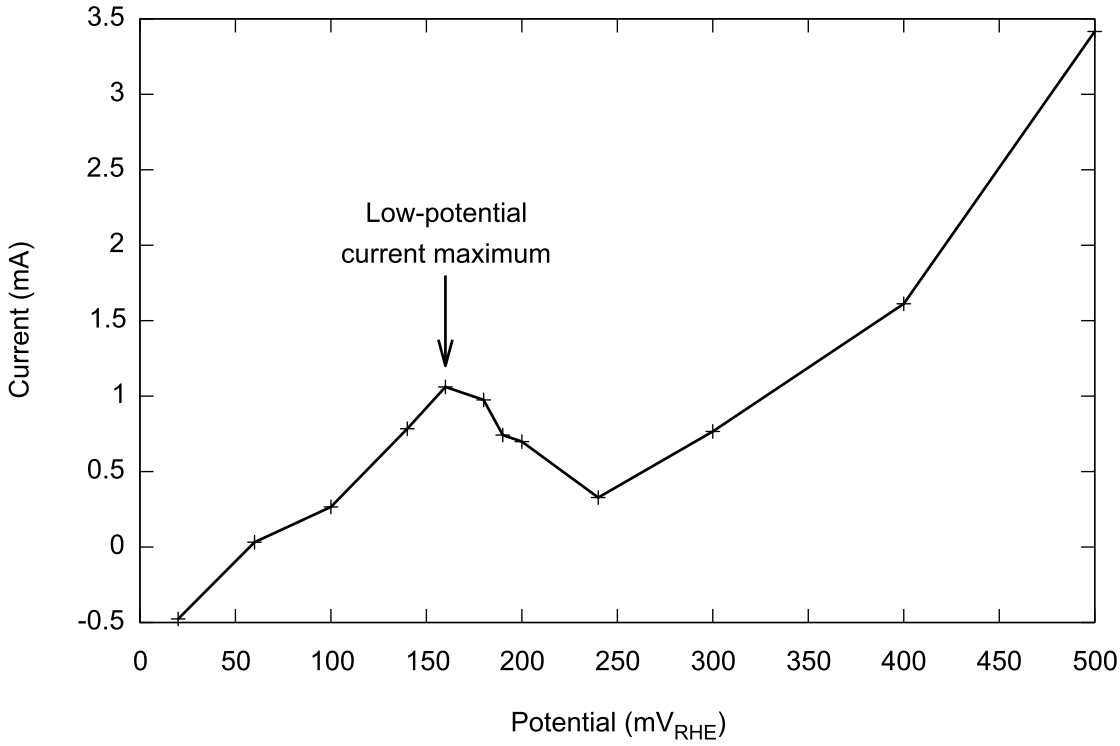

1.3.2 Electro-oxidation of 2-propanol over Pt-Ni catalysts

The Bergens group has demonstrated that Ni promotes the 2POR over Pt [150]. There are three main theories for the source of enhancement and these will be discussed in more detail in Chapter 2 (Section 2.1.2). Briefly, they are:

1. The bi-functional effect: surface oxides and hydroxides form at lower potential on Ni than on Pt surfaces. These species help to oxidise Pt active site-blocking adsorbates (for example, adsorbed CO in the MOR) [17,18,173].

2. The electronic effect: the presence of Ni can change the electronic structure of the *d* band of Pt and/or the energy of its electrons, in turn causing a change in the adsorption energy of species on Pt [174-178]
3. The geometric or composition effect: The presence and location of Ni changes the arrangement of the Pt atoms from what is found in bulk Pt [179,180].

These effects depend on the catalyst structure and composition, which in turn is dependent on the material's synthetic preparation. Therefore, the activity of these catalysts is strongly correlated to the mode of catalyst synthesis.

1.4 Synthesis of Pt-Ni catalysts

The chemical reduction of Pt and Ni salt precursors to afford Pt-Ni alloyed or bimetallic materials is common. Precursors such as $H_2PtCl_6 \cdot 6\ H_2O$ [181-184], $Pt(acac)_2$ (acac = acetyl acetonate) [185,186], $NiCl_2$ [181,183,184,186,187], $Ni(NO_3)_2 \cdot 6\ H_2O$ [182], and $Ni(acac)_2$ [185] are commonly employed, while reducing agents such as $NaBH_4$ [182-184,188-190], N_2H_4 [19,181,187], and H_2 [191] are typical. The process is considered to be autocatalytic [192]. When a core-shell material is desired, the reductions are usually performed stepwise to form a thin layer of Pt onto the Ni core [181,187], whereas, co-reductions most often yield more stochastic materials [183,191]. Further, the catalyst particles are often dispersed or stabilized by impregnation onto carbon powder (typically Vulcan XC-72) concurrent with, or subsequent to the reduction steps [182,184,191].

Pt-Ni materials are also prepared by organic solvothermal synthesis [193]. The method involves crystallizing Ni and Pt from a high temperature (usually 200°C) solution in a PTFE-lined furnace. Typical solvents are mixtures of diphenyl ether and long chain diols mixed with oleic acid and oleylamine surfactants that are removed after impregnating the materials onto high surface area carbon powders [185,194-197].

Electrolysis of an aqueous solution of Ni and Pt metal ions is another versatile technique to fabricate Pt-Ni catalysts [198,199]. For example, segmented Pt/Ni nanorods were synthesized by the stepwise galvanostatic deposition of a Pt from a solution having H_2PtCl_6 and potentiostatic deposition of Ni from a solution containing $NiSO_4 \cdot 6\ H_2O$ into an anodic aluminum oxide (AAO) membrane template [200]. Moreover, this dissertation centers on a unique

galvanostatic deposition of Pt (see Section 1.4.1 below). However, the simplest electrochemical deposition of Pt onto Ni is galvanic displacement (also referred to as transmetalation or immersion plating) [201]. This method involves the immersion of a pre-formed Ni electrode into an aqueous acid solution of H_2PtCl_6, K_2PtCl_6 or K_2PtCl_4 to result in a spontaneous oxidation of surface layers of the Ni and reduction of $[PtCl_6]^{2-}$ or $[PtCl_4]^{2-}$ ions. The resulting catalysts are unsupported Ni materials with sub-monolayer amounts of Pt on the surface, similar to core-shell structure [174,202-204].

Vacuum depositions are also quite common in the literature. Physical vapour deposition (PVD) techniques such as sputter deposition [205-208], electron beam deposition [209], and cathodic arc deposition [177] have been used. Atomic layer deposition (a chemical vapour deposition or CVD technique) has also been explored [210]. Our group has also used Glancing Angle Deposition (GLAD, a PVD method [211,212]) to fabricate Ni nanopillar substrates for Pt electro-deposition [213]. This will be discussed in Chapter 3.

1.4.1 The platinum counter electrode deposition

The platinum counter electrode deposition is a self-limiting, galvanostatic deposition of platinum. Its name stems from the source of platinum being the sacrificial dissolution of a blacked platinum counter electrode (Pt CE). The first reported instance of this unconventional deposition was performed in a solution of 0.2 M $NiCl_2$/ 2.0 M NH_4Cl, with a Ni gauze working electrode (WE) as the target of the deposition [150]. -0.1 A cm^{-2} was applied between the WE and Pt CE for 1 hour. Figure 1-9 shows the resulting potential profile during the deposition. The following observations and interpretations were made and are shown pictorially in Figure 1-10.

Figure 1-9 *a) Potential profiles of the Ni gauze WE and the blacked Pt CE during the platinum counter electrode deposition. The electrolyte is a sonicated/stirred solution of 30 mL of 2 M NH_4Cl/0.2 M $NiCl_2$ with a current of -0.1 A passing between the WE and CE for 1 hour. b) Concentration profile of Pt from the dissolution of the Pt CE during deposition.*

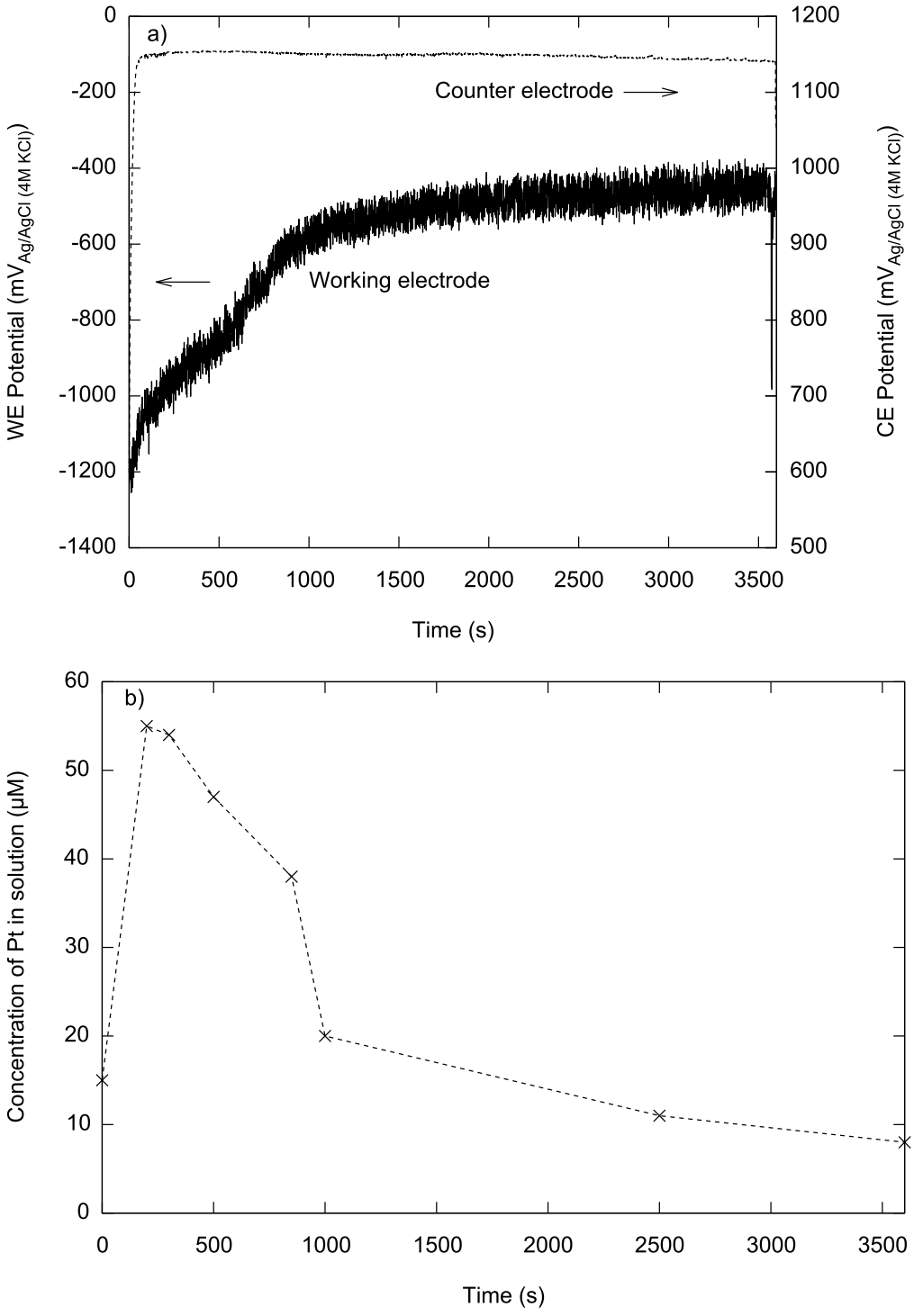

1. From t = 0 to 200 seconds,
    a. the potential of the CE (E_{CE}) instantaneously rises from ~ 0.6 to ~ 1.2 $V_{Ag/AgCl\ (4M\ KCl)}$. Under these conditions, Pt dissolution can occur. For example, the Pt/Pt^{2+} standard redox potential is E^0 = 0.85 $V_{Ag/AgCl\ (4M\ KCl)}$. The Pt CE dissolution is evident by observations that the concentration of solvated Pt in the electrolyte increased to a maximum of ~ 55 μM in this time frame.
    b. The potential of the WE (E_{WE}) is ~ -0.9 V At this potential, Ni can deposit onto the WE via reduction of the solvated Ni^{2+}. In fact, under similar conditions, the reduction/deposition of Ni is observed at E = -0.528 V [150].
    c. Finally, gas evolution was observed at the WE surface shortly after the current is applied. We believe that the gas is H_2, formed from the reduction of protons in the aqueous electrolyte ($2H^+_{(aq)} + 2e^- \rightarrow H_{2(g)}$, E^0 = -0.222 V).
2. From t = 200 to 800 seconds,
    a. E_{CE} plateaus at ~ 1.2 $V_{Ag/AgCl\ (4M\ KCl)}$. Under these conditions the platinum surface can become oxidised to the point of self-passivation [214]. As a result, the Pt CE stops dissolving, limiting the amount of Pt that can ultimately be deposited on the WE. The effects of surface passivation and concurrent Pt deposition are supported by the overall decrease in the concentration of Pt^{n+} in solution in this time frame.

b. E_{WE} rises gradually to ~ -0.1 V. This supports the development of the mixed potential system described above arising from the competing surface reactions that include H_2 evolution, Ni^{2+} reduction, and Pt^{n+} reduction. It is noted that H_2 evolution is exceedingly more facile over Pt sites than over Ni sites. Therefore, when Pt nucleates on the WE surface, the potential of the WE rises to reflect H_2 evolution preferentially occurring over Pt sites rather than Ni sites.

3. From t = 800 to 3600 seconds,

   a. E_{CE} remains at ~ 1.2 $V_{Ag/AgCl\ (4M\ KCl)}$ as surface oxides continue to build on the CE surface. As a result, the concentration of Pt^{n+} in solution continues decreasing as Pt deposits onto the WE surface but is not replenished in solution.

   b. E_{WE} stabilizes at ~ -0.1 V. At this potential we believe Ni^{2+} reduction is suppressed by H_2 evolution as the potential is now far above the observed potential of the Ni/Ni^{2+} couple. This limits the amount of Ni that is deposited on the WE surface. Furthermore, as H_2 continues to evolve preferentially over Pt surfaces, it physically impedes further deposition of Pt onto that particular Pt site. The result is that Pt can only nucleate on exposed Ni sites, culminating in a conformal deposit of Pt.

In summary, the procedure resulted in a self-limiting co-deposit of Ni and Pt onto a Ni gauze WE referred to herein as Ni-$Pt_{CE}Ni_{gauze}$, where most of the Ni is at the sub-surface of the deposit, and all or most of the Pt is at the surface of the deposit.

Figure 1-10 *Time-dependent pictorial representation of the Pt CE deposition used to co-deposit Ni and Pt onto a Ni gauze WE. Dashed circles highlight magnified views of the setup. At 800 seconds "PtO_x" represents the passivated surface of the Pt CE.*

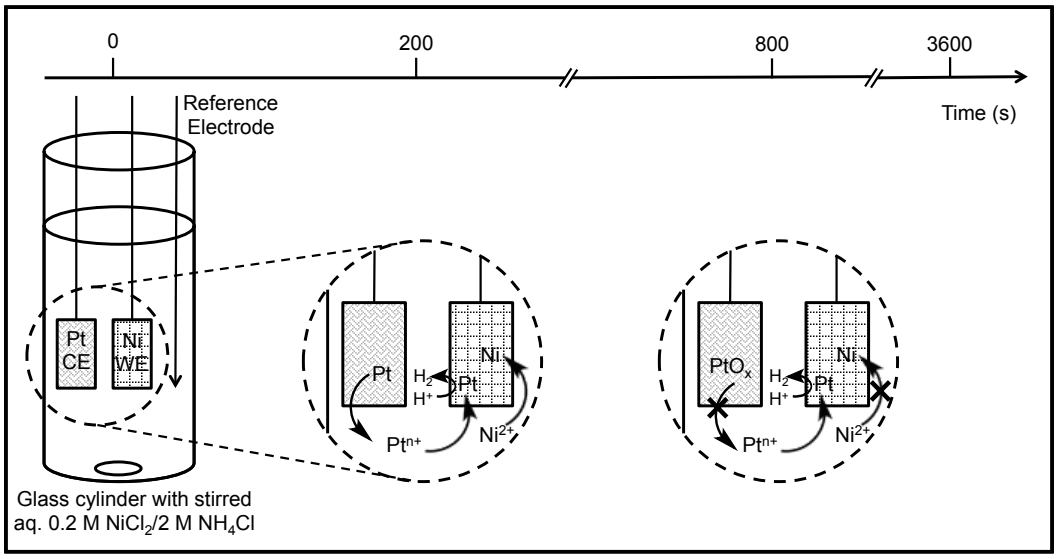

Attempts were made to replicate the result of the Pt CE deposition by the addition of H_2PtCl_6 or $K[PtCl_3(C_2H_4)]$, as the source of Pt to the deposition solution, and using a carbon CE. The deposition solution contained concentrations of Pt similar to the maximum concentration observed during the *Pt CE deposition.* Interestingly, in both cases the deposition behaved similar to that of pure Ni. There was no significant increase in the E_{WE} during the first 200 seconds and only traces of any gas (H_2) evolution were observed on the WE. Further, unlike Ni-$Pt_{CE}Ni_{gauze}$, these deposits did not visibly catalyze the decomposition of H_2O_2 despite having ten times higher masses of Pt deposited.[8] It was therefore suggested that the Pt deposited is presumably dispersed through the co-deposit rather than localized at the surface [150].

[8] A simple test for the presence of Pt is by immersing the electrode in dilute H_2O_2. An observation of bubbles of O_2 evolved on the electrode surface constitutes a positive test.

Since its first discovery, we have also shown that the *Pt CE deposition* proceeds even in the absence of $NiCl_2$ to afford Pt-only deposits onto various working electrode substrates (discussed in Chapter 2 and 3). Further, the mechanism of the Pt CE deposition has been mostly elucidated with the only unexplained component being the identity of the solvated platinum species. Due to the very low concentration of this species, identification via analytical techniques remains difficult. We hypothesize, however, that the species could be $Pt(NH_3)_2Cl_2$. This is consistent with the observation that E_{CE} during the deposition supports the formation of a Pt(II) species.

As an interesting aside, this Pt electrode dissolution phenomenon is not novel, the most noteworthy instance being a discovery in 1965 that eventually led to the exploration of the anti-cancer properties of *cis*-platin [215]. Rosenberg intended to investigate the effects of an electric field on the growth processes of *Escherichia Coli*. The experiments were performed in a special chamber equipped with Pt mesh electrodes and a nutrient medium whose components included NH_4Cl, the same supporting electrolyte that we have used. The authors note that Pt was chosen for its chemical inertness, but found that an electrolysis product of the Pt electrodes inhibited cell division under the voltage conditions (*f* = 1000 Hz, 2 A (peak to peak)). It was later suggested that this electrolysis product was $[PtCl_6]^{2-}$ [216,217] although both complexes *cis*-$Pt^{IV}(NH_3)_2Cl_4$ and *cis*-$Pt^{II}(NH_3)_2Cl_2$ were found to inhibit cell division in later studies [218].

1.5 Synopsis

This dissertation describes some of the applications of this Pt CE deposition towards the synthesis of novel platinum and platinum-nickel catalysts for fuel cell applications. Chapter 2 describes the preparation of Pt and Pt-Ni deposits on commercial nickel foam [219]. The move from nickel gauze to nickel foam was inspired by the high porosity (and therefore surface area) of foams versus gauzes, as well as the fact that foams have been used in prototype fuel cells [220-222]. This study also includes the first look into the microscopic characteristics and electronic effects manifested in deposits prepared by the Pt CE deposition method and their relation to the observed 2-propanol oxidation activity.

Chapter 3 explores further substrate development and comparisons to traditional Pt depositions. In this study a nickel nanopillar film, prepared by a physical vapour deposition technique referred to as glancing angle deposition (GLAD), was used as the substrate for Pt deposition [213]. The decision to use nanopillar films as substrates was motivated by the excellent results reported with GLAD and related nanostructured thin films in electrocatalysis [223-226]. The crystallographic features of the catalysts were probed, along with microscopic and electronic properties. The results of this study were particularly significant as we show that the catalyst prepared by the Pt CE deposition was more active towards alkaline 2-propanol oxidation than both traditionally prepared deposits and commercially available state-of-the-art unsupported Pt nanoparticles. Chapter 4 continues to discuss the nanopillar-supported Pt deposits, but with a focus on the oxygen reduction reaction.

Finally, Chapter 5 describes the first occurrence of the Pt CE deposition on particulate substrates. This was a significant advancement in the potential applications of this deposition method as we are now not limited to using heterogeneous bulk substrates. The substrate of choice was a commercially available microporous carbon black. The powder was characterized by microscopy and spectrometry and tested for oxygen reduction activity.

1.6 Bibliography

[1] N. Brandon, Fuel Cells In: Cleveland JC, (Ed), Encyclopedia of Energy, Elsevier, New York, 2004, pp. 749-758.

[2] W.R. Grove, The Correlation of Physical Forces, 6th ed., Longmans, Green, London; 1874, pp. 298.

[3] M.L. Perry, T.F. Fuller, J. Electrochem. Soc., 149 (2002) S59-S67.

[4] F.T. Bacon, Electrochim. Acta, 14 (1969) 569-585.

[5] C.K. Dyer, J. Power Sources, 106 (2002) 31-34.

[6] Comparison of Fuel Cell Technologies, U.S. Department of Energy. 2011; Available at: http://www1.eere.energy.gov/hydrogenandfuelcells/fuelcells/pdfs/fc_comparison_chart.pdf. Accessed May 20th, 2013.

[7] F. Bidault, P.H. Middleton, 4.07 - Alkaline Fuel Cells: Theory and Application In: A. Sayigh, (Ed), Comprehensive Renewable Energy, Elsevier, Oxford, 2012, pp. 179-202.

[8] A.J. Appleby, E.B. Yeager, Energy, 11 (1986) 137-152.

[9] Luo Y. Bond Dissociation Energies in CRC Handbook of Chemistry and Physics. 93rd Ed., 2012-2013; Available at: www.hbcpnetbase.com. Accessed May 7th, 2013.

[10] H. Zhang, P.K. Shen, Chem. Rev., 112 (2012) 2780-2832.

[11] Ballard Power Systems FCGen-1020ACS PEMFC. 2010; Available at: www.ballard.com/files/PDF/Backup_Power/1020ACS_v2.pdf. Accessed April 30th, 2013.

[12] I.D. Raistrick (Ed), Diaphragms, Separators and Ion-Exchange Membranes, The Electrochemical Society Proceedings Series, Pennington, NJ, 1986, pp. 172.

[13] S. Gottesfeld, T.A. Zawodzinski, Polymer Electrolyte Fuel Cells In: R.C. Alkire, H. Gerischer, D.M. Kolb, C.W. Tobias, (Eds), Advances in Electrochemical Science and Engineering, Volume 5, Wiley-VCH Verlag GmbH, Weinheim, Germany, 2008, pp. 195-301.

[14] A. Brouzgou, S.Q. Song, P. Tsiakaras, Appl. Catal. B-Environ., 127 (2012) 371-388.

[15] C. Roth, N. Benker, R. Theissmann, R.J. Nichols, D.J. Schiffrin, Langmuir, 24 (2008) 2191-2199.

[16] P. Liu, A. Logadottir, J.K. Nørskov, Electrochim. Acta, 48 (2003) 3731-3742.

[17] K.W. Park, J.H. Choi, Y.E. Sung, J. Phys. Chem. B, 107 (2003) 5851-5856.

[18] K.W. Park, J.H. Choi, B.K. Kwon, S.A. Lee, Y.E. Sung, H.Y. Ha, S.A. Hong, H. Kim, A. Wieckowski, J. Phys. Chem. B., 106 (2002) 1869-1877.

[19] Y. Hu, P. Wu, Y. Yin, H. Zhang, C. Cai, App. Cat. B-Environ., 111–112 (2012) 208-217.

[20] C. Roth, N. Benker, T. Buhrmester, M. Mazurek, M. Loster, H. Fuess, D.C. Koningsberger, D.E. Ramaker, J. Am. Chem. Soc., 127 (2005) 14607-14615.

[21] P. Waszczuk, G. Lu, A. Wieckowski, C. Lu, C. Rice, R.I. Masel, Electrochim. Acta, 47 (2002) 3637-3652.

[22] S.M.M. Ehteshami, S.H. Chan, Electrochim. Acta, 93 (2013) 334-345.

[23] E. Antolini, J. Appl. Electrochem., 34 (2004) 563-576.

[24] Y. Wang, K.S. Chen, J. Mishler, S.C. Cho, X.C. Adroher, Appl. Energy, 88 (2011) 981-1007.

[25] R. Borup, J. Meyers, B. Pivovar, Y.S. Kim, R. Mukundan, N. Garland, D. Myers, M. Wilson, F. Garzon, D. Wood, P. Zelenay, K. More, K. Stroh, T. Zawodzinski, J. Boncella, J.E. McGrath, M. Inaba, K. Miyatake, M. Hori, K. Ota,

Z. Ogumi, S. Miyata, A. Nishikata, Z. Siroma, Y. Uchimoto, K. Yasuda, K. Kimijima, N. Iwashita, Chem. Rev., 107 (2007) 3904-3951.

[26] X. Cheng, Z. Shi, N. Glass, L. Zhang, J. Zhang, D. Song, Z.-. Liu, H. Wang, J. Shen, J. Power Sources, 165 (2007) 739-756.

[27] Y. Shao, G. Yin, Z. Wang, Y. Gao, J. Power Sources, 167 (2007) 235-242.

[28] G.F. McLean, T. Niet, S. Prince-Richard, N. Djilali, Int. J. Hydrogen Energy, 27 (2002) 507-526.

[29] E. Guelzow, J.K. Nor, P.K. Nor, M. Schulze, Fuel Cell Review, 3 (2006) 19-25.

[30] E.H. Yu, X. Wang, U. Krewer, L. Li, K. Scott, Energy Environ. Sci., 5 (2012) 5668-5680.

[31] V. Ganesh, S. Farzana, S. Berchmans, J. Power Sources, 196 (2011) 9890-9899.

[32] P. Schechner, E. Bubis, L. Mor, Proceedings of the 3rd International Conference on Fuel Cell Science, Engineering, and Technology, 2005, (2005) 661-665.

[33] P. Schechner, E. Bubis, Z. Rubin, N. Sabag, L. Mor, Proceedings of the 1st European Fuel Cell Technology and Applications Conference 2005 - Book of Abstracts, 2005 (2005) 51.

[34] I. Taniguchi, Y. Nonaka, Z. Dursun, S. Ben Aoun, C. Jin, G.S. Bang, T. Koga, T. Sotomura, Electrochemistry, 72 (2004) 427-429.

[35] S. Ben Aoun, G.S. Bang, T. Koga, Y. Nonaka, T. Sotomura, I. Taniguchi, Electrochem. Commun., 5 (2003) 317-320.

[36] E. Antolini, E.R. Gonzalez, J. Power Sources, 195 (2010) 3431-3450.

[37] K. Matsuoka, Y. Iriyama, T. Abe, M. Matsuoka, Z. Ogumi, J. Power Sources, 150 (2005) 27-31.

[38] J.O. Bockris, J. Appleby, Energy, 11 (1986).

[39] K.F. Blurton, E. McMullin, Energy Conversion, 9 (1969) 141-144.

[40] P.A. Christensen, A. Hamnett, D. Linares-Moya, Phys. Chem. Chem. Phys., 13 (2011) 5206-5214.

[41] R.R. Adžić, M.I. Avramov-Ivić, A.V. Tripković, Electrochim. Acta, 29 (1984) 1353-1357.

[42] J. Taraszewska, G. Rosłonek, J. Electroanal. Chem., 364 (1994) 209-213.

[43] Y. Wang, L. Li, L. Hu, L. Zhuang, J. Lu, B. Xu, Electrochem. Commun., 5 (2003) 662-666.

[44] E. Gülzow, M. Schulze, J. Power Sources, 127 (2004) 243-251.

[45] G. Merle, M. Wessling, K. Nijmeijer, J. Membr. Sci., 377 (2011) 1-35.

[46] R. Zeng, J.R. Varcoe, Recent Patents on Chemical Engineering, 4 (2011) 99-115.

[47] A.C. Cope, A.S. Mehta, J. Am. Chem. Soc., 85 (1963) 1949-1952.

[48] S. Chempath, B.R. Einsla, L.R. Pratt, C.S. Macomber, J.M. Boncella, J.A. Rau, B.S. Pivovar, J. Phys. Chem. C, 112 (2008) 3179-3182.

[49] G. Couture, A. Alaaeddine, F. Boschet, B. Ameduri, Progress in Polymer Science, 36 (2011) 1521-1557.

[50] G. Ghigo, S. Cagnina, A. Maranzana, G. Tonachini, J. Org. Chem., 75 (2010) 3608-3617.

[51] B. Bauer, H. Strathmann, F. Effenberger, Desalination, 79 (1990) 125-144.

[52] H. Hou, G. Sun, R. He, Z. Wu, B. Sun, J. Power Sources, 182 (2008) 95-99.

[53] H. Hou, S. Wang, Q. Jiang, W. Jin, L. Jiang, G. Sun, J. Power Sources, 196 (2011) 3244-3248.

[54] A.D. Modestov, M.R. Tarasevich, A.Y. Leykin, V.Y. Filimonov, J. Power Sources, 188 (2009) 502-506.

[55] M.R. Tarasevich, Z.R. Karichev, V.A. Bogdanovskaya, L.N. Kuznetsova, B.N. Efremov, A.V. Kapustin, Russ. J. Electrochem., 40 (2004) 653-656.

[56] B. Xing, O. Savadogo, Electrochem. Commun., 2 (2000) 697-702.

[57] Y. Sone, P. Ekdunge, D. Simonsson, J. Electrochem. Soc., 143 (1996) 1254-1259.

[58] M. Jaffe, M.I. Haider, J. Mancel, J. Rafako, Polym. Eng. Sci., 32 (1992) 1236.

[59] Y. Wu, C. Wu, J.R. Varcoe, S.D. Poynton, T. Xu, Y. Fu, J. Power Sources, 195 (2010) 3069-3076.

[60] H. Dai, H. Zhang, Q. Luo, Y. Zhang, C. Bi, J. Power Sources, 185 (2008) 19-25.

[61] L. Lebrun, N. Follain, M. Metayer, Electrochim. Acta, 50 (2004) 985-993.

[62] M. Kumar, S. Singh, V.K. Shahi, J. Phys. Chem. B., 114 (2010) 198-206.

[63] M.S. Huda, R. Kiyono, M. Tasaka, T. Yamaguchi, T. Sata, Sep. Purif. Technol., 14 (1998) 95-106.

[64] T. Sata, Y. Yamane, K. Matsusaki, J. Polym. Sci. Part A, 36 (1998) 49-58.

[65] T. Sata, K. Teshima, T. Yamaguchi, J. Polym. Sci. Part A, 34 (1996) 1475-1482.

[66] J.R. Varcoe, R.C.T. Slade, Fuel Cells, 5 (2005) 187-200.

[67] A.J. Jacobson, Chem. Mater., 22 (2010) 660-674.

[68] L. Carrette, K.A. Friedrich, U. Stimming, ChemPhysChem, 1 (2000) 162-193.

[69] E.D. Wachsman, K.T. Lee, Science, 334 (2011) 935-939.

[70] A.S. Nesaraj, Journal of Scientific and Industrial Research, 69 (2010) 169-176.

[71] N. Sammes, G. Tompsett, Y. Zhang, A. Cartner, R. Torrens, Denki Kagaku, 64 (1996) 674-680.

[72] J.W. Fergus, J. Power Sources, 147 (2005) 46-57.

[73] N.M. Galea, D. Knapp, T. Ziegler, J. Catal., 247 (2007) 20-33.

[74] K.M. Walters, A.M. Dean, H. Zhu, R.J. Kee, J. Power Sources, 123 (2003) 182-189.

[75] A. Kulkarni, S. Giddey, Solid State Electr., 16 (2012) 3123-3146.

[76] E. Antolini, Appl. Energy, 88 (2011) 4274-4293.

[77] M.C. Williams, H.C. Maru, J. Power Sources, 160 (2006) 863-867.

[78] H.R. Kunz, J. Electrochem. Soc., 134 (1987) 105-113.

[79] U. Desideri, S. Proietti, G. Cinti, P. Sdringola, C. Rossi, Int. J. Greenh. Gas. Con., 5 (2011) 1663-1673.

[80] U. Desideri, S. Proietti, P. Sdringola, G. Cinti, F. Curbis, Int. J. Hydrogen Energy, 37 (2012) 19295-19303.

[81] G. Manzolini, S. Campanari, P. Chiesa, A. Giannotti, P. Bedont, F. Parodi, Journal of Fuel Cell Science and Technology, 9 (2012).

[82] K. Sugiura, K. Takei, K. Tanimoto, Y. Miyazaki, J. Power Sources, 118 (2003) 218-227.

[83] H.R. Kunz, G.A. Gruver, J. Electrochem. Soc., 122 (1975) 1279-1287.

[84] C. Lamy, E.M. Belgsir, J.-. Léger, J. Appl. Electrochem., 31 (2001) 799-809.

[85] B.D. McNicol, D.A.J. Rand, K.R. Williams, J. Power Sources, 83 (1999) 15-31.

[86] Sigma Aldrich Catalog. 2013; Available at: http://www.sigmaaldrich.com/catalog/product/aldrich/274674?lang=en&region=CA. Accessed June 27th, 2013.

[87] S. Wasmus, A. Küver, J. Electroanal. Chem., 461 (1999) 14-31.

[88] T. Yamaguchi, F. Miyata, S. Nakao, J. Membr. Sci., 214 (2003) 283-292.

[89] T. Yamaguchi, F. Miyata, S. Nakao, Adv. Mater., 15 (2003) 1198-1201.

[90] V. Saarinen, K.D. Kreuer, M. Schuster, R. Merkle, J. Maier, Solid State Ionics, 178 (2007) 533-537.

[91] A.K. Shukla, R.K. Raman, Annual Review of Materials Research, 33 (2003) 155-168.

[92] S.C. Barton, W. Deng, J. Gallaway, S. Levendovsky, T.S. Olson, P. Atanassov, M. Sorkin, A. Kaufman, H.F. Gibbard, ECS Transactions, 1 (2005) 315-322.

[93] E. Antolini, T. Lopes, E.R. Gonzalez, J. Alloys Compounds, 461 (2008) 253-262.

[94] B. Piela, T.S. Olson, P. Atanassov, P. Zelenay, Electrochim. Acta, 55 (2010) 7615-7621.

[95] J. Prabhuram, R. Manoharan, J. Power Sources, 74 (1998) 54-61.

[96] A.V. Tripković, K.D. Popović, B.N. Grgur, B. Blizanac, P.N. Ross, N.M. Marković, Electrochim. Acta, 47 (2002) 3707-3714.

[97] S. Lu, J. Pan, A. Huang, L. Zhuang, J. Lu, Proc. Natl. Acad. Sci. U.S.A., 105 (2008) 20611-20614.

[98] E.H. Yu, U. Krewer, K. Scott, Energies, 3 (2010) 1499-1528.

[99] N.W. Deluca, Y.A. Elabd, J. Polym. Sci. Part B, 44 (2006) 2201-2225.

[100] J. Léger, J. Appl. Electrochem., 31 (2001) 767-771.

[101] Y.X. Chen, A. Miki, S. Ye, H. Sakai, M. Osawa, J. Am. Chem. Soc., 125 (2003) 3680-3681.

[102] B. Braunchweig, D. Hibbitts, M. Neurock, A. Wieckowski, Catal. Today, 202 (2013) 197-209.

[103] J. Qi, L. Jiang, Q. Tang, S. Zhu, S. Wang, B. Yi, G. Sun, Carbon, 50 (2012) 2824-2831.

[104] C. Lu, R.I. Masel, J. Phys. Chem. B., 105 (2001) 9793-9797.

[105] T. Diemant, T. Hager, H.E. Hoster, H. Rauscher, R.J. Behm, Surf. Sci., 541 (2003) 137-146.

[106] M.T.M. Koper, Surf. Sci., 548 (2004) 1-3.

[107] E. Antolini, J. Power Sources, 170 (2007) 1-12.

[108] C. Bianchini, V. Bambagioni, J. Filippi, A. Marchionni, F. Vizza, P. Bert, A. Tampucci, Electrochem. Commun., 11 (2009) 1077-1080.

[109] S. Song, P. Tsiakaras, App. Cat. B-Environ., 63 (2006) 187-193.

[110] M. Saito, S. Tsuzuki, K. Hayamizu, T. Okada, J. Phys. Chem. B., 110 (2006) 24410-24417.

[111] S. Rousseau, C. Coutanceau, C. Lamy, J.-. Léger, J. Power Sources, 158 (2006) 18-24.

[112] K. Liu, A. Wang, T. Zhang, ACS Catalysis, 2 (2012) 1165-1178.

[113] R.B. Kutz, B. Braunschweig, P. Mukherjee, R.L. Behrens, D.D. Dlott, A. Wieckowski, J. Catal., 278 (2011) 181-188.

[114] S.Q. Song, W.J. Zhou, Z.H. Zhou, L.H. Jiang, G.Q. Sun, Q. Xin, V. Leontidis, S. Kontou, P. Tsiakaras, Int. J. Hydrogen Energy, 30 (2005) 995-1001.

[115] F. Vigier, C. Coutanceau, F. Hahn, E.M. Belgsir, C. Lamy, J. Electroanal. Chem., 563 (2004) 81-89.

[116] W.J. Zhou, W.Z. Li, S.Q. Song, Z.H. Zhou, L.H. Jiang, G.Q. Sun, Q. Xin, K. Poulianitis, S. Kontou, P. Tsiakaras, J. Power Sources, 131 (2004) 217-223.

[117] Offenberg students test world's first ethanol powered fuel cell vehicle. 2007; Available at: http://news.mongabay.com/bioenergy/2007/05/worlds-first-ethanol-powered-fuel-cell.html. Accessed May 13th, 2013.

[118] M. Zhiani, H.A. Gasteiger, M. Piana, S. Catanorchi, Int. J. Hydrogen Energy, 36 (2011) 5110-5116.

[119] B. Dumé, Fuel Cell Review, 3 (2006) 26-27.

[120] M.Z.F. Kamarudin, S.K. Kamarudin, M.S. Masdar, W.R.W. Daud, Int. J. Hydrogen Energy, 38 (2013) 9438-9453.

[121] E. Bingham, B. Cohrssen, Powell CH. Patty's Toxicology. Available at: http://knovel.com/web/portal/browse/display?_EXT_KNOVEL_DISPLAY_bookid=706&VerticalID=0. Accessed 11th Oct. 2011, 2011.

[122] T. Kobayashi, J. Otomo, C. Wen, H. Takahashi, J. Power Sources, 124 (2003) 34-39.

[123] M.E.P. Markiewicz, S.H. Bergens, J. Power Sources, 185 (2008) 222-225.

[124] J. Arun kumar, P. Kalyani, R. Saravanan, Int. J. Electrochem. Sci., 3 (2008) 961-969.

[125] Z. Qi, A. Kaufman, Fuel Cells Bulletin, (2002) 9-13.

[126] P.B.L. Chaurasia, Y. Ando, T. Tanaka, Energy Conversion and Management, 44 (2003) 611-628.

[127] Y. Ando, T. Tanaka, T. Doi, T. Takashima, Energy Conversion and Management, 42 (2001) 1807-1816.

[128] J. Wang, S. Wasmus, R.F. Savinell, J. Electrochem. Soc., 142 (1995) 4218-4224.

[129] M. Umeda, H. Sugii, M. Mohamedi, I. Uchida, Electrochemistry, 70 (2002) 961-963.

[130] Z. Qi, A. Kaufman, J. Power Sources, 112 (2002) 121-129.

[131] Z. Qi, M. Hollett, A. Attia, A. Kaufman, Electrochemical and Solid-State Letters, 5 (2002) A129-A130.

[132] Y.H. Chu, Y.G. Shul, Int. J. Hydrogen Energy, 35 (2010) 11261-11270.

[133] D. Cao, S.H. Bergens, J. Power Sources, 124 (2003) 12-17.

[134] N.A. Tapan, E. Öztürk, Turkish Journal of Chemistry, 33 (2009) 487-499.

[135] C. Yang, S. Chiu, K. Lee, W. Chien, C. Lin, C. Huang, J. Power Sources, 184 (2008) 44-51.

[136] M.E.P. Markiewicz, S.H. Bergens, J. Power Sources, 195 (2010) 7196-7201.

[137] P. Gao, S. Chang, Z. Zhou, M. J. Weaver, Journal of Electroanalytical Chemistry and Interfacial Electrochemistry, 272 (1989) 161-178.

[138] M.E.P. Markiewicz, D.M. Hebert, S.H. Bergens, J. Power Sources, 161 (2006) 761-767.

[139] S.S. Gupta, J. Datta, J. Chem. Sci., 117 (2005) 337-344.

[140] J. Otomo, X. Li, T. Kobayashi, C.-. Wen, H. Nagamoto, H. Takahashi, J. Electroanal. Chem., 573 (2004) 99-109.

[141] Y. Feng, Z. Li, C. Huang, Y. Wang, Ionics, 17 (2011) 617-625.

[142] S. Ertan, F. Şen, S. Şen, G. Gökağaç, Journal of Nanopart. Res., 14 (2012).

[143] M. Etesami, N. Mohamed, Chemija, 23 (2012) 171-179.

[144] E. Pastor, S. González, A.J. Arvia, J. Electroanal. Chem., 395 (1995) 233-242.

[145] M. Umeda, H. Sugii, I. Uchida, J. Power Sources, 179 (2008) 489-496.

[146] J. Ye, J. Liu, C. Xu, S.P. Jiang, Y. Tong, Electrochem. Commun., 9 (2007) 2760-2763.

[147] I.A. Rodrigues, F.C. Nart, J. Electroanal. Chem., 590 (2006) 145-151.

[148] I.D.A. Rodrigues, J.P.I. De Souza, E. Pastor, F.C. Nart, Langmuir, 13 (1997) 6829-6835.

[149] B. Habibi, E. Dadashpour, Electrochim. Acta, 88 (2013) 157-164.

[150] L.N. Menard, S.H. Bergens, J. Power Sources, 194 (2009) 298-302.

[151] I. Schwartz, A.P. Jonke, M. Josowicz, J. Janata, Catalysis Letters, 142 (2012) 1344-1351.

[152] Y. Su, C. Xu, J. Liu, Z. Liu, J. Power Sources, 194 (2009) 295-297.

[153] J. Liu, J. Ye, C. Xu, S.P. Jiang, Y. Tong, J. Power Sources, 177 (2008) 67-70.

[154] W. Zhou, C. Wang, J. Xu, Y. Du, P. Yang, Mater. Chem. Phys., 123 (2010) 390-395.

[155] C. Xu, Z. Tian, Z. Chen, S.P. Jiang, Electrochem. Commun., 10 (2008) 246-249.

[156] J. Lu, S. Lu, D. Wang, M. Yang, Z. Liu, C. Xu, S.P. Jiang, Electrochim. Acta, 54 (2009) 5486-5491.

[157] Y. Liu, Y. Zeng, R. Liu, H. Wu, G. Wang, D. Cao, Electrochim. Acta, 76 (2012) 174-178.

[158] A. Santasalo, F.J. Vidal-Iglesias, J. Solla-Gullón, A. Berná, T. Kallio, J.M. Feliu, Electrochim. Acta, 54 (2009) 6576-6583.

[159] H. Lin, G. Chen, Z. Zheng, J. Zhou, S. Chen, Z.-. Lin, Acta Phys.-Chem. Sin., 21 (2005) 1280-1284.

[160] S. Sun, Y. Lin, Electrochim. Acta, 44 (1998) 1153-1162.

[161] S. Sun, Y. Lin, Electrochim. Acta, 41 (1996) 693-700.

[162] S. Sun, Y. Lin, J. Electroanal. Chem., 375 (1994) 401-404.

[163] S. Sun, D. Yang, Z. Tian, Journal of Electroanalytical Chemistry and Interfacial Electrochemistry, 289 (1990) 177-187.

[164] L.H. Leung, S. Chang, M.J. Weaver, J. Electroanal. Chem., 266 (1989) 317-336.

[165] G. Fóti, C. Mousty, K. Novy, C. Comninellis, V. Reid, J. Appl. Electrochem., 30 (2000) 147-151.

[166] S.N. Raicheva, M.V. Christov, E.I. Sokolova, Electrochim. Acta, 26 (1981) 1669-1676.

[167] E.I. Sokolova, M.V. Christov, J. Electroanal. Chem., 175 (1984) 195-205.

[168] P.T.A. Sumodjo, E.J. da Silva, T. Rabockai, J. Electroanal. Chem., 271 (1989) 305-317.

[169] A. Santasalo-Aarnio, Y. Kwon, E. Ahlberg, K. Kontturi, T. Kallio, M.T.M. Koper, Electrochem. Commun., 13 (2011) 466-469.

[170] T. Iwasita, J. Braz. Chem. Soc., 13 (2002) 401-409.

[171] M. Simões, S. Baranton, C. Coutanceau, App. Cat. B-Environ., 93 (2010) 354-362.

[172] A. Santasalo-Aarnio, S. Tuomi, K. Jalkanen, K. Kontturi, T. Kallio, Electrochim. Acta, 87 (2013) 730-738.

[173] M. Watanabe, S. Motoo, J. Electroanal. Chem., 60 (1975) 267-273.

[174] S. Papadimitriou, S. Armyanov, E. Valova, A. Hubin, O. Steenhaut, E. Pavlidou, G. Kokkinidis, S. Sotiropoulos, J. Phys. Chem. C, 114 (2010) 5217-5223.

[175] V.R. Stamenkovic, B. Fowler, B.S. Mun, G. Wang, P.N. Ross, C.A. Lucas, N.M. Markovic, Science, 315 (2007) 493-497.

[176] J.R. Kitchin, J.K. Nørskov, M.A. Barteau, J.G. Chen, J. Chem. Phys., 120 (2004) 10240-10246.

[177] V.R. Stamenkovic, B.S. Mun, K.J.J. Mayrhofer, P.N. Ross, N.M. Markovic, J. Am. Chem. Soc., 128 (2006) 8813-8819.

[178] V. Stamenković, T.J. Schmidt, P.N. Ross, N.M. Marković, J. Phys. Chem. B., 106 (2002) 11970-11979.

[179] C. Wang, M. Chi, D. Li, D. Strmcnik, D. Van Der Vliet, G. Wang, V. Komanicky, K.-. Chang, A.P. Paulikas, D. Tripkovic, J. Pearson, K.L. More, N.M. Markovic, V.R. Stamenkovic, J. Am. Chem. Soc., 133 (2011) 14396-14403.

[180] H. Yang, C. Coutanceau, J. Léger, N. Alonso-Vante, C. Lamy, J. Electroanal. Chem., 576 (2005) 305-313.

[181] X. Fu, Y. Liang, S. Chen, J. Lin, D. Liao, Catalysis Communications, 10 (2009) 1893-1897.

[182] E. Antolini, J.R.C. Salgado, A.M. Dos Santos, E.R. Gonzalez, Electrochemical and Solid-State Letters, 8 (2005) A226-A230.

[183] Y. Xu, S. Hou, Y. Liu, Y. Zhang, H. Wang, B. Zhang, Chem. Comm., 48 (2012) 2665-2667.

[184] H. Wu, D. Wexler, G. Wang, J. Alloys Compounds, 488 (2009) 195-198.

[185] M.K. Carpenter, T.E. Moylan, R.S. Kukreja, M.H. Atwan, M.M. Tessema, J. Am. Chem. Soc., 134 (2012) 8535-8542.

[186] J. Zhang, J. Fang, J. Am. Chem. Soc., 131 (2009) 18543-18547.

[187] T.C. Deivaraj, W. Chen, J.Y. Lee, Journal of Materials Chemistry, 13 (2003) 2555-2560.

[188] T. Jeon, S.J. Yoo, Y. Cho, K. Lee, S.H. Kang, Y. Sung, J. Phys. Chem. C, 113 (2009) 19732-19739.

[189] S. Pokhrel, H. Zhao, S. Gao, L. Huo, J. Alloys Compounds, 480 (2009) 830-833.

[190] S. Bhlapibul, K. Pruksathorn, P. Piumsomboon, Renewable Energy, 41 (2012) 262-266.

[191] H. Yang, W. Vogel, C. Lamy, N. Alonso-Vante, J. Phys. Chem. B., 108 (2004) 11024-11034.

[192] C.R.K. Rao, D.C. Trivedi, Coord. Chem. Rev., 249 (2005) 613-631.

[193] C. Wang, N.M. Markovic, V.R. Stamenkovic, ACS Catalysis, 2 (2012) 891-898.

[194] K. Ahrenstorf, O. Albrecht, H. Heller, A. Kornowski, D. Görlitz, H. Weller, Small, 3 (2007) 271-274.

[195] K. Ahrenstorf, H. Heller, A. Kornowski, J.A.C. Broekaert, H. Weller, Adv. Funct. Mater., 18 (2008) 3850-3856.

[196] C. Wang, M. Chi, D. Li, D. van der Vliet, G. Wang, Q. Lin, J.F. Mitchell, K.L. More, N.M. Markovic, V.R. Stamenkovic, ACS Catal., 21 (2011) 1355-1359.

[197] C. Wang, M. Chi, G. Wang, D. van der Vliet, D. Li, K. More, H. Wang, J.A. Schlueter, N.M. Markovic, V.R. Stamenkovic, Adv. Funct. Mater., 21 (2011) 147-152.

[198] L. Ding, G. Li, Z. Wang, Z. Liu, H. Liu, Y. Tong, Chemistry - A European Journal, 18 (2012) 8386-8391.

[199] K. Yao, Y.F. Cheng, Int. J. Hydrogen Energy, 33 (2008) 6681-6686.

[200] F. Liu, J.Y. Lee, W.J. Zhou, Small, 2 (2006) 121-128.

[201] K. Sasaki, Y. Mo, J.X. Wang, M. Balasubramanian, F. Uribe, J. McBreen, R.R. Adzic, Electrochim. Acta, 48 (2003) 3841-3849.

[202] S. Papadimitriou, A. Tegou, E. Pavlidou, S. Armyanov, E. Valova, G. Kokkinidis, S. Sotiropoulos, Electrochim. Acta, 53 (2008) 6559-6567.

[203] A. Tegou, S. Papadimitriou, S. Armyanov, E. Valova, G. Kokkinidis, S. Sotiropoulos, J. Electroanal. Chem., 623 (2008) 187-196.

[204] A. Tegou, S. Papadimitriou, S. Armyanov, E. Valova, G. Kokkinidis, S. Sotiropoulos, J. Electroanal. Chem., 625 (2009) 175.

[205] D.A. Stevens, R. Mehrotra, R.J. Sanderson, G.D. Vernstrom, R.T. Atanasoski, M.K. Debe, J.R. Dahn, J. Electrochem. Soc., 158 (2011) B905-B909.

[206] M.K. Debe, A.J. Steinbach, G.D. Vernstrom, S.M. Hendricks, M.J. Kurkowski, R.T. Atanasoski, P. Kadera, D.A. Stevens, R.J. Sanderson, E. Marvel, J.R. Dahn, ECS Transactions, 33 (2010) 143-152.

[207] C.K.G. Liu, D.A. Stevens, J.C. Burns, R.J. Sanderson, G. Vernstrom, R.T. Atanasoski, M.K. Debe, J.R. Dahn, J. Electrochem. Soc., 158 (2011) B919-B926.

[208] T. Toda, H. Igarashi, H. Uchida, M. Watanabe, J. Electrochem. Soc., 146 (1999) 3750-3756.

[209] C. Chen, F. Pan, H. Yu, App. Cat. B-Environ., 104 (2011) 382-389.

[210] R.R. Hoover, Y.V. Tolmachev, J. Electrochem. Soc., 156 (2009) A37-A43.

[211] M.T. Taschuk, M.M. Hawkeye, M.J. Brett, Chapter 13 - Glancing Angle Deposition In: Peter M. Martin, (Ed), Handbook of Deposition Technologies for Films and Coatings (Third Edition), William Andrew Publishing, Boston, 2010, pp. 621-678.

[212] M.M. Hawkeye, M.J. Brett, J. Vac. Sci. Technol. A, 25 (2007) 1317-1335.

[213] S.A. Francis, R.T. Tucker, M.J. Brett, S.H. Bergens, J. Power Sources, 222 (2013) 533-541.

[214] Y. Xu, M. Shao, M. Mavrikakis, R.R. Adzic In: W. Wieckowski, M.T.M. Koper, (Eds), Fuel Cell Catalysis-A Surface Science Approach, John Wiley and Sons, New Jersey, 2009, pp. 271-315.

[215] B. Rosenberg, L. Van Camp, T. Kricas, Nature, 205 (1965) 698-699.

[216] B. Rosenberg, E. Renshaw, L. Vancamp, J. Hartwick, J. Drobnik, J. Bacteriol., 93 (1967) 716-721.

[217] B. Rosenberg, L. Van Camp, E.B. Grimley, A.J. Thomson, J. Biol. Chem., 242 (1967) 1347-1352.

[218] B. Rosenberg, L. Van Camp, J.E. Trosko, V.H. Mansour, Nature, 222 (1969) 385-386.

[219] S.A. Francis, S.H. Bergens, J. Power Sources, 196 (2011) 7470-7480.

[220] J.M. Skowroński, A. Wazny, Solid State Electr., 9 (2005) 890-899.

[221] D. Cao, D. Chen, J. Lan, G. Wang, J. Power Sources, 190 (2009) 346-350.

[222] W. Yang, S. Yang, W. Sun, G. Sun, Q. Xin, Electrochim. Acta, 52 (2006) 9-14.

[223] A. Bonakdarpour, M.D. Fleischauer, M.J. Brett, J.R. Dahn, Appl. Catal. A-Gen., 349 (2008) 110-115.

[224] M.D. Gasda, G.A. Eisman, D. Gall, J. Electrochem. Soc., 157 (2010) B437-B440.

[225] W.J. Khudhayer, N.N. Kariuki, X. Wang, D.J. Myers, A.U. Shaikh, T. Karabacak, J. Electrochem. Soc., 158 (2011) B1029-B1041.

[226] W.J. Khudhayer, N. Kariuki, D.J. Myers, A.U. Shaikh, T. Karabacak, J. Electrochem. Soc., 159 (2012) B729-B736.

Chapter 2: Low Pt-loading Ni-Pt and Pt deposits on Ni: Preparation, activity and investigation of electronic properties[1]

2.1 Introduction

2.1.1 Pt deposits on Ni gauze and Ni foam substrates for 2-propanol electro-oxidation

The Bergens group has reported the preparation of co-deposits of Ni and Pt onto a commercial Ni gauze working electrode (WE) using the *Pt CE deposition* [1] (Figure 1-10). The main findings were:

1. Galvanostatic co-deposition (at -0.1 A cm^{-2}) of Ni and Pt onto a Ni gauze can be achieved from solutions of 0.2 M $NiCl_2$ in 2.0 M NH_4Cl using a dissolving Pt CE as the source of Pt;
2. During the deposition, H_2 evolution over freshly deposited Pt on the WE suppresses the reduction of Ni^{2+} after short times and ultimately limits the Ni content in the deposit;
3. Self-passivation of the Pt CE limits the ultimate Pt content in the deposit;
4. Most of the Pt seems to be at the surface of the deposit;
5. The surface atom-normalized activity of the Ni-$Pt_{CE}Ni_{gauze}$ towards the alkaline 2-propanol electro-oxidation reaction (2POR) was comparable to that of a Pt blacked gauze (Pt_{black}).

[1] *A version of this chapter has been published. S.A. Francis, S.H. Bergens, J. Power Sources 196 (2011) 7470-7480.*

This chapter describes the use of the *Pt CE deposition* to prepare deposits on commercial 1 cm x 1 cm nickel foam substrates. The nickel foam substrate was chosen due to its high porosity (and therefore surface area). Moreover, foams have been successfully assembled as electrodes in prototype fuel cells [2-4]. This study also includes the first look into the microscopic and electronic properties of deposits prepared by the *Pt CE deposition*. Our objective was to confirm that most of the Pt in the co-deposits does indeed exist at the surface of the catalyst, as well as investigate possible electronic effects that contribute to the activity towards the alkaline 2POR. Further, by elimination of $NiCl_2$ from the deposition electrolyte, we achieved Pt-only deposits onto WE substrates. Thus, two new types of deposits on Ni_{foam} were investigated: Ni-$Pt_{CE}Ni_{foam}$, which is prepared with an unshielded Pt CE in 0.2 M $NiCl_2$/2 M NH_4Cl, and $Pt_{CE}Ni_{foam}$, which is prepared with an unshielded Pt CE in solely 2 M NH_4Cl. These are compared to the original deposit Ni-$Pt_{CE}Ni_{gauze}$.

Previous work in our group shows that incorporation of Ru [5] and Ni [1] increases the stabilized, potentiostatic currents for the 2POR over Pt (reproduced in Figure 2-1). The enhancement over Pt-Ru occurs over the entire potential range, whereas Ni promotes the reaction at potentials above 250 mV_{RHE}.

Figure 2-1 *Sampled current voltammograms of (a) Pt-Ru and Pt nanoparticles* [5]*), and (b) Ni-$Pt_{CE}Ni_{gauze}$ and Pt_{black} gauze* [1] *in 1 M $(CH_3)_2CH(OH)$ supported in 1 M KOH at 60°C. The current densities are averaged at the end of 15-minute potential steps, and are based on the estimated number of active surface atoms, 3.3 and 9.2 µmol for Ni-$Pt_{CE}Ni_{gauze}$ and Pt_{black} respectively. The values for Pt and Pt-Ru were not reported.*

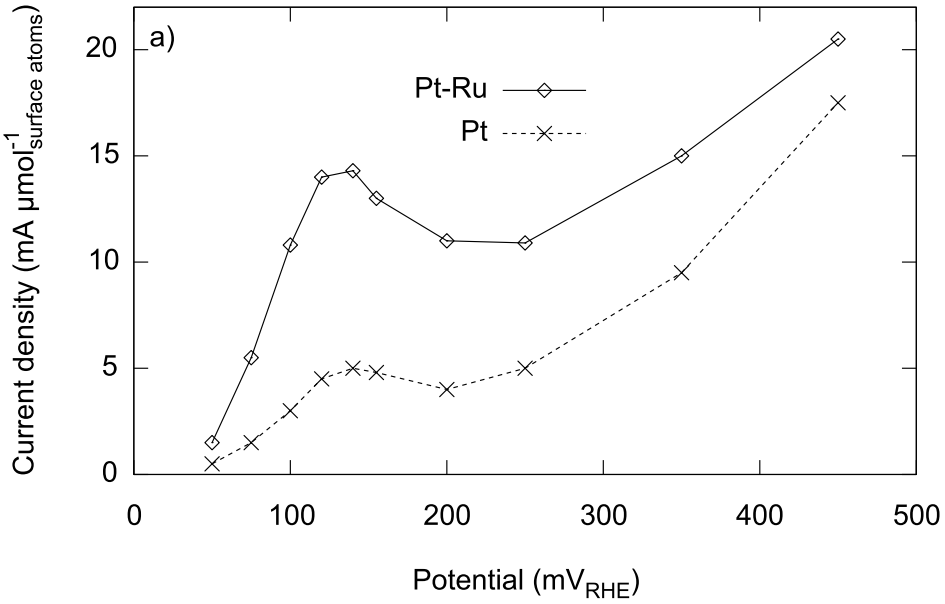

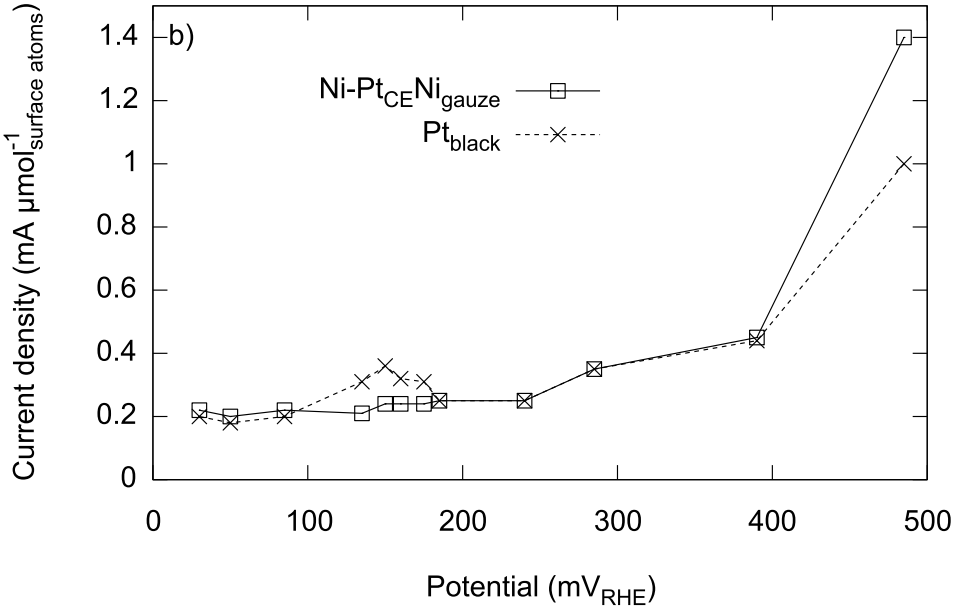

There are several models in the literature used to explain the enhancements to the intrinsic catalytic activity of Pt due to addition of an oxophilic element to platinum. These include the bi-functional effect, the electronic effect, and the geometric effect.

2.1.2 Origins of catalytic enhancement of Pt

The bi-functional, electronic and geometric effects are best explained by case study. Thus, the following sections will include a definition of each effect and a discussion supported by comprehensive literature examples. In general, the oxophilic element added to Pt will be referred to as metal M, although specific examples where M could be Ru, Ni, Sn, Mo, *etc.* will also be presented.

2.1.2.1 The bi-functional effect

The bi-functional effect occurs when a catalyst surface is considered to have two types of sites that have separate yet synergistic roles. Usually, comparative voltammetry, between Pt and M-modified Pt, reveals possible bi-functional features.

The bi-functional effect was first suggested by Watanabe and Motoo in 1975 to describe the enhanced electro-oxidation of methanol in acid over PtRu alloys or Pt with Ru adatoms compared to Pt [6]. According to the authors, Pt serves to dissociatively adsorb methanol, while Ru adsorbs OH radicals presumably from the aqueous solution[2]. The adsorbed OH radicals subsequently react with organic species (*i.e.,* poisons like CO) adsorbed on the Pt sites, in turn

[2] More modern interpretations of the bi-functional effect refer to “adsorbed hydroxyl” groups rather than hydroxyl radicals.

freeing the Pt sites for methanol adsorption. The enhanced activity manifests because the OH radicals adsorb on Ru at a lower potential (0.35 V_{RHE}) than they would on Pt (0.75 V_{RHE}), thus facilitating CO electro-oxidation at Pt sites at more negative potentials than on bulk Pt.

It is now widely accepted that the bi-functional effect is the principal mechanism for catalytic methanol electro-oxidation in acid over bimetallic and alloy surfaces [7]. In general, the activation of water at low potentials over the oxophilic metal M (M can be for example Ru, Sn or Mo) results in the formation of adsorbed hydroxyl:

$$H_2O + M^* \rightarrow M - OH_{ads} + H^+ + e^- \qquad 2-1$$

where * represents a free site and "ads" indicates the species is adsorbed.

Subsequently, CO adsorbed on Pt is oxidised to CO_2 by the M-adsorbed OH:

$$Pt - CO_{ads} + M - OH_{ads} \rightarrow CO_2 + H^+ + e^- + Pt^* + M^* \qquad 2-2$$

Conversely, in alkaline solution, the bi-functional effect usually occurs via conversion of M to M-hydroxide or oxide. For example, Chen *et al.* describe Pt nanoparticles supported on a Ni film that showed higher activity than Pt towards methanol oxidation in base [8]. The authors suggest that, compared to Pt, enhanced CO tolerance was observed due to a bi-functional mechanism via $Ni(OH)_2$ formation on the Ni substrate. Interestingly, Park *et al.* have described the bi-functional effect in acid in a similar manner. They refer to a surface redox process that removes CO poisons during methanol oxidation at long times via formation of nickel (hydro)oxides on Pt/Ni nanoparticles [9,10].

The bi-functional mechanism has also evolved to include phenomena such as “OH spillover”. In this interpretation, M is still the site for water activation (Equation 2-1) or hydroxide formation (in base), but the OH species formed on M

could spillover onto adjacent Pt sites and react with CO there. This spillover effect has been suggested by Davies *et al.* [11]. CO adsorbed onto Ru-modified Pt (111), was oxidised by voltammetry at lower potentials than on Pt (111). Two CO oxidation peaks were observed at ~ 0.6 and 0.7 V_{RHE}. The authors suggest that the first anodic peak represented CO oxidation via the traditional bi-functional effect as discussed above. The slower kinetics (*viz*. higher potential) of the second anodic peak was related to the rate of spillover and diffusion of OH species to sites at least one Pt atom away from the Ru site. Samjeské *et al.* have also described a spillover effect for CO oxidation over Ru deposited solely at the steps of Pt (110) [12]. The authors observed that oxidation of CO adsorbed at sites not in the vicinity of the Ru still occurred at lower potentials than over undecorated Pt (110). They concluded that the bi-functional effect via OH spillover accounts for this result. For Pt nanoparticles supported on a karst-like Ni film (that is, features sink holes and caverns), Chen *et al*. showed that alkaline CO electro-oxidation occurred at a much more negative potential than the formation of OH on the Pt surface, thus OH spillover from the Ni film contributed to CO electro-oxidation at low potentials [8].

2.1.2.2 The electronic effect

The electronic effect refers to modifications of the properties of a Pt site by nearby M sites. The interaction of these adjacent M atoms changes the electronic structure of Pt, in turn causing a change in the adsorption energy of species on Pt [13,14]. Many electrocatalytic reactions require adsorption of the active molecule to the surface (for example, O_2 in the ORR, CH_3OH in the MOR, *etc.*), while facilitating desorption of intermediates or products (for example OH in the ORR, CO in the MOR, *etc.*). If species are strongly adsorbed, activation may be easy,

but the accumulation of intermediates or products may block active sites. On the other hand, if species are weakly adsorbed, few reactant molecules can be activated. An optimal electronic effect would therefore result in a balance of moderate adsorption.

Typically, electronic effects are probed using photoelectron spectroscopy. Photoelectron spectroscopy directly measures the kinetic energy of electrons emitted from a sample irradiated with X-rays (X-ray photoelectron spectroscopy or XPS) or vacuum ultraviolet photons (Ultraviolet photoelectron spectroscopy or UPS) [15]. The experiments are shown pictorially in Figure 2-2.

Figure 2-2 *Scheme showing the electron transitions that describe ultraviolet and x-ray photoelectron spectroscopy. A valence or core electron is excited respectively by electromagnetic radiation and ejected into the vacuum in the spectrometer. E_F represents the Fermi level, shared by the metal sample and spectrometer as they are in physical contact. E_{vacuum} is the vacuum level at the surface of the sample where a perfect vacuum exists in the instrument. Other terms are explained in the text herein: BE_1 and KE_1 = binding and kinetic energy measured in UPS, BE_2 and KE_2 the same for the XPS experiment, φ_s is the work function of the spectrometer and φ_{sample} is the work function of the sample.*

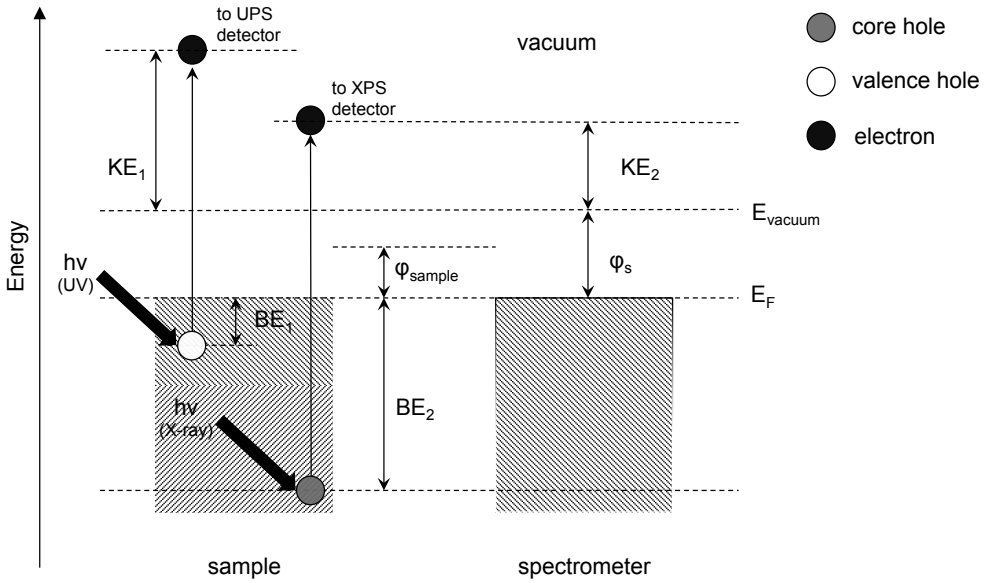

For probing electronic effects with XPS, the binding energy of the core-level electrons is the measure of interest.

$$BE = h\upsilon - (KE + \varphi_s) \qquad 2-3$$

where BE is the binding energy, that is the amount of energy required to move an electron from its ground state orbital to the Fermi edge

h is Planck's constant

υ is the frequency of the incident radiation

KE is the kinetic energy of the emitted photoelectrons

φ_s is the work function of the spectrometer

The core-level electron BE shifts provide an idea of the electronic structure of atoms in different environments in a solid. A simplified generalization is that relative to a neutral atom, increase of electron density around an atomic site would result in higher repulsion, causing a shift to lower BE and vice versa [16]. This simple explanation is based on *initial state effects*, that is, it assumes a *frozen-orbital approximation*, meaning that the remaining core electrons are the same in the final state as they were in the initial state (before the photoelectron ejection event) [17]. Alternatively, *final state effects* could be at play. For example, the BE could reflect relaxation of the remaining core electrons to minimize energy in the core-ionized final state. Said differently, the final state could experience a lower shielding effect. Thus, the BE would be lower as it is easier to remove the electron. Moreover, during the experiment, the reference level that the BE is measured against (Fermi edge or level, E_F) may change

position relative to the center of gravity of the band[3] that the ejected electron originated from, thereby contributing to observed shifts [16,17]. In fact, E_F is expected to shift during alloying when compared to the pure elements [17]. Even further, in principle a Pt-M alloy's core level energy could be very different to the core levels in Pt [17]. These factors lead to diverse and indefinite interpretations in the literature with respect to electronic effects.

For example, Pt core-line shifts to lower BE values have been reported for a variety of Ni-Pt systems [8-10,18-22]. This shift in BE was correlated to weaker surface Pt-CO adsorption for graphene supported Pt-Ni [18], Ni core:Pt shell catalysts [19], carbon supported Pt-Ni alloy [21], Pt/Ni thin film and nanoparticle alloys [9,10] and Pt-Ni alloys supported on multi-walled carbon nanotubes. In most cases, this negative shift was explained (in part or wholly) by Ni donating electron density to Pt according to the Pauling electronegativity (χ_P) values (1.91 and 2.28 respectively) [8-10,18,21]. Though a convenient argument, we point out that the Allred-Rochow electronegativity ($\chi_{A\text{-}R}$) scale is more appropriate to the nature of the XPS experiment ($\chi_{A\text{-}R}$ is 1.75 and 1.44 for Ni and Pt respectively). χ_P values are derived from bond dissociation energies, whereas $\chi_{A\text{-}R}$ values are derived based on the tendency of the atom to attract an electron [23].

To our knowledge, only one positive core line Pt BE shift has been reported for an electrocatalytic Ni-Pt system. Toda *et al.* used XPS to probe electronic effects in the oxygen reduction reaction (ORR) over Ni-Pt alloys with Pt-rich surfaces. They observed positive BE shifts for Pt 4*d* and 4*f* core lines with

[3] An energy level may contain numerous degenerate sublevels or *states*. The *density of states* reveals the number of states per band available to be occupied by electrons. An *energy band* therefore gives the range of energies the electron may have. The center of gravity of the band describes an average energy of the entire band, not to be confused with the average energy of the occupied states within the band.

respect to pure Pt [24,25]. The authors suggested, without explanation, that the origin of the positive shifts lies in a decrease in Fermi level of the alloy relative to that in Pt or an increase in Pt 5*d* vacancies. We presume that if the Fermi level is relatively lower in the alloy than pure Pt *due to* a depopulation of states in the Pt 5*d* band, then it would require more energy to eject a core photoelectron from the alloy than from the pure solid (based on *initial state effects*). Interestingly, the authors describe the increase in Pt 5*d* vacancies as a result of donation of Ni 5*d* vacancies as opposed to Pt donating electron density. This assumes that Pt is less electronegative than Ni (as the Allred-Rochow scale predicts), and that 5*d* - bands of Pt and Ni overlap in the alloy. While the increase in Pt 5*d* vacancies is not unfounded [26], the source of donation from the 5*d* Ni orbital is questionable. Subsequent calculations have shown that the Ni 3*d* and Pt 5*d* bands overlap in stable NiPt intermetallics [27], thus donation from Ni 3*d* orbitals may be a more likely explanation. Nevertheless, the authors suggested that with the addition of Ni up to 30-50 atomic %, the BE shift increased positively and the Pt 5*d* vacancies increased. They proposed a novel mechanism that explains enhanced adsorption of oxygen molecules during the ORR via increased 2π electron donation from O_2 to the $5d_{z^2}$ bonding orbital on Pt, concurrent with enhanced dissociation of the O-O bond via back-donation into the O_2 2π* anti-bonding orbital on the Pt surface. Above 50 atomic % Ni, they suggested that back donation becomes difficult thereby impeding O-O bond scission and slowing the rate of the ORR. Interestingly, the BE trend of increasing positive shift with atomic Ni composition became stochastic above 50 atomic %. Moreover, the BE shifts reported for the components of the 4*d* core lines (i.e. $4d_{5/2}$ and $4d_{3/2}$) were not the

same, indicating that the coupling constant was not *constant*. Thus, there is an essential flaw in the XPS data treatment therein.

On the other hand, UPS involves the excitation of valence electrons rather than core electrons. For metals like Pt, electrons in the *d* band are valence electrons [28]. Therefore, for probing electron effects on Pt-based catalysts with UPS, the energy shifts of the center of gravity of the *d* band, or more succinctly, the *d band center*, ε_d, is the metric of interest. Nørskov and co-workers have presented a model that predicts a correlation between ε_d and the adsorption of O, CO, H, *etc.* on a metal surface [29-31]. Simply put, the lower ε_d lies, the weaker the adsorbate binds to the metal surface.

Stamenkovic *et al*. performed UPS experiments on Pt_3Ni alloy (111) surfaces with a Pt skin surface [32]. They observed a downshift of the *d* band center compared to a surface of Pt (111). Comparative voltammograms also showed that both hydrogen adsorption and oxygen adsorption on Pt_3Ni was impeded compared to Pt. Thus, the theory that an adsorbate will bind more weakly the lower ε_d lies, was supported by this study.

Finally, we note that core-level shifts typically move in the same direction as *d* band center shifts for surface Pt [14]. Therefore, some reports use XPS experiments to probe core level shifts, yet discuss electronic effects in terms of *d* band center shifts. For example, both Park *et al*. [9,10] and Papadimitriou *et al.* [33] reported negative BE shifts of Pt core lines for Ni–Pt coatings and thin films/nanoparticles respectively. Park attributed the observed shift to the lowering of the *d* band center. All things being equal, this is in direct contrast to the understanding that core level shifts and *d* band center shifts should occur in the same direction [14]. Yet, Papadimitriou and co-workers came to the same conclusion. Both groups associated the lowering of the *d* band center with

lowered affinity of Pt for adsorbates such as CO. Additionally, Papadimitriou *et al*. did note that both methanol and CO adsorption was affected by the lowering of the energy of the *d* band center. At short times, when methanol activation was the major pathway, Pt was more active than Ni–Pt and at long times, when CO poisoning was prominent, Ni–Pt was more active than Pt.

Conversely, Jeon *et al*. observed Pt core line BE shifts to lower values for heat-treated carbon-supported Pt-Ni alloys, but suggested that the Pt *d* band center up-shifted. The reason given for this up-shift was that the Pt *d* band vacancy increased, causing the *d* band to narrow. As a result, to preserve the electron occupancy, the *d* band center had to shift up [20]. This concept is illustrated and further explained in the next section.

2.1.2.3 The geometric effect

The geometric or composition effect occurs due to the presence and/or location of M changing the arrangement of the Pt atoms from what is found in bulk Pt. In the literature, geometric effects typically refer to effects of strain in the surface Pt atoms. Herein, geometric effects will also encompass those that relate to surface composition as well.

Strain effects occur because of lattice mismatch between surface Pt and the M underlayers. Pt experiences expansive strain when its atomic radius is smaller than M's, thus having a reduced number of neighbouring atoms at the surface. Compressive strain occurs when M has the smaller atomic radius. All things being equal, calculations show that for metals like Pt with more than half-filled d bands, expansive strain results in a narrowing of the *d* band about its center due to less orbital overlap and less electronic repulsion (Figure 2-3a and b). It follows that the highest filled energy state will no longer coincide with the

metal's Fermi level. Electrons will either have to populate the empty states up to the Fermi level (an energetically unfavoured situation), or the energy bands will up-shift (Figure 2-3c). By an analogous process, compressive strain, which widens the surface *d* band, shifts the *d* band center down [17,34]. Evidently, strain can contribute to electronic effects.

Figure 2-3 *Density of states (DOS) for a metal with more than half-filled* d *bands under expansive strain. a) Energy levels and binding energy (BE) in the bulk of the material. b) Effect of strain on the with of the* d *band: surface band narrowing. c) The shift in the* d *band to preserve electron occupancy and match the material's Fermi level.*

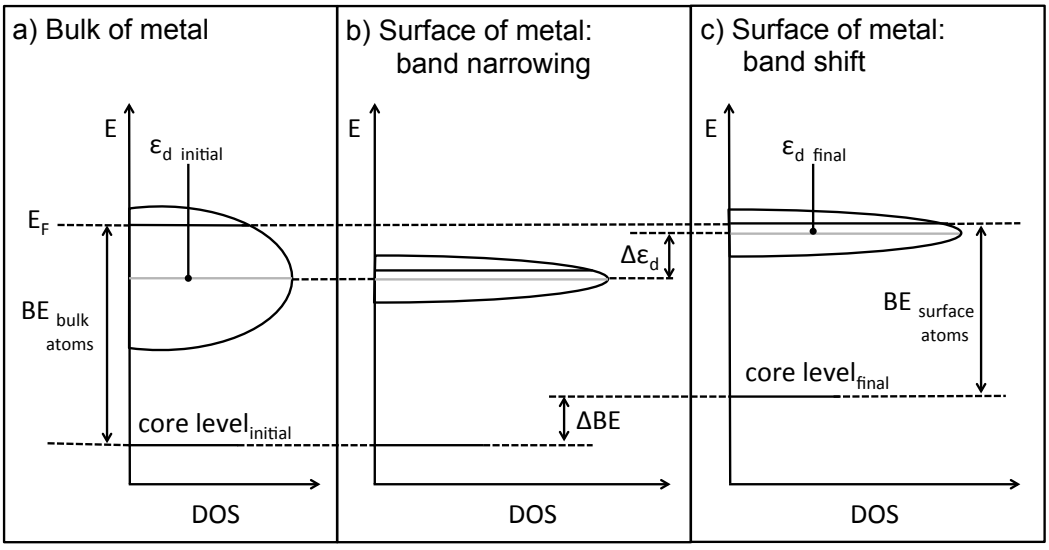

Gsell *et al*. have used Scanning Tunneling Microscopy to show direct evidence of the correlation between local strain at a surface and the bonding strength of adsorbates [35]. Using a Ru (0001) surface, they discovered that the adsorption of oxygen atoms is stronger at regions of expansive strain but weaker in regions of compression. Zhang *et al*. have shown that an expansive strain

effect occurs for a Pt monolayer (ML) on a Au (111) surface. An up-shift of the Pt surface *d* band center was suggested, leading to stronger Pt-O adsorption as predicted by Nørskov and co-workers [29-31]. On the other hand, Pt ML on Ir (111) experienced compressive strain, resulting in weaker Pt-O surface bonds. Strasser *et al*. have shown for dealloyed Pt-Cu core:Pt shell catalysts that strain in the Pt-enriched surface layers modifies the surface Pt band structure thereby weakening adsorption of ORR intermediates [36]. The authors demonstrated that the composition of Cu in the core could be adjusted to modify the expansive or compressive strain and control the strength of surface bonds. Adzic and co-workers reported a 2-fold enhancement of ORR specific activity for a Pt ML on Pd core catalyst. They attributed the enhancement to contraction of the Pt surface layer induced by lattice mismatch based on DFT calculations [37]. In general, the reports on interpretation of strain effects have been more consistent than those on electronic effects.

Another type of geometric effect is based on composition of the catalyst surface. References to such effects are rare in the literature. Gasteiger *et al.* has proposed a model for the MOR on Pt-Ru alloy surfaces where methanol adsorption and desorption occurs at 3-fold Pt sites adjacent to a Ru atom [38]. Statistically, they found that the maximum number of this arrangement of sites occurs in an alloy with 10 % Ru, which is the composition of the catalyst with the maximum methanol oxidation rate. Yang *et al.* described methanol tolerant ORR Ni-Pt alloy catalysts with no Pt surface enrichment. They propose that the alloy, with its disordered surface, had a low chance of having a 3-fold Pt site as described by Gasteiger and thus was not active towards methanol electro-oxidation [39].

In summary, the bi-functional, electronic and geometric effects, in principle, can occur simultaneously. The contribution of each effect to the overall observed activity likely depends on the preparation of the catalysts and their resulting structure and composition. Nevertheless, separating the effects and evaluating their comparative importance to the catalytic activity is quite difficult.

2.2 Results and Discussion

2.2.1 Comparison of the depositions of Ni–$Pt_{CE}Ni_{gauze}$, Ni–$Pt_{CE}Ni_{foam}$, and $Pt_{CE}Ni_{foam}$

Figure 2-3 shows the potential responses of the WE (E_{WE}) and Pt CE (E_{CE}) during the sonicated depositions of Ni–$Pt_{CE}Ni_{gauze}$, Ni–$Pt_{CE}Ni_{foam}$, and $Pt_{CE}Ni_{foam}$. Data for E_{WE} was collected by the potentiostat and its electrochemical software, while E_{CE} was simultaneously monitored and recorded using a multimeter and its corresponding software. As a brief reminder, the suggested mechanism (Figure 1-10) of the *Pt CE deposition* is that initially Pt is deposited on the WE via Equation 2-1. Once the Pt CE has begun dissolving, Pt begins to deposit on the WE as well (Equation 2-2). After a short time, Ni deposition stops concurrent with H_2 evolution commencing over freshly deposited Pt (Equation 2-3). This causes E_{WE} to rise as a mixed-potential system develops representing all three reactions. Finally, E_{WE} stabilizes as only Pt deposition and H_2 evolution occur until the deposition time is complete.

$$Ni^{2+}_{(aq)} + 2\,e^- \rightarrow Ni_{(s)} \qquad 2-1$$

$$Pt^{n+}_{(aq)} + n\,e^- \rightarrow Pt_{(s)} \qquad 2-2$$

$$2\,H^+_{(aq)} + 2\,e^- \xrightarrow{Pt} H_{2(g)} \qquad 2-3$$

The initial E_{WE} for both foam-based electrodes is similar to that of Ni–$Pt_{CE}Ni_{gauze}$. Comparing Ni–$Pt_{CE}Ni_{gauze}$ and Ni–$Pt_{CE}Ni_{foam}$, the rise in E_{WE} over foam was more delayed than over gauze. It is likely that these differences in E_{WE} between the gauze and foam substrates arise from either the higher real surface area of the foam and/or a longer induction period for Pt deposition on the foam. A longer induction period will result in a slower take-over of H_2 evolution over the WE and thus a delay in the sudden rise of E_{WE}. The $Pt_{CE}Ni_{foam}$ deposit also

showed this delayed rise of E_{WE}. Moreover, the rise was much steeper than in Ni–$Pt_{CE}Ni_{foam}$ and is likely because there is no contribution to the observed mixed-potential from Ni^{2+} reduction. For all of the depositions, the Pt_{CE} remained at a constant potential of 1340–1440 mV_{SHE}. For simplicity, only the E_{CE} during a Ni–$Pt_{CE}Ni_{foam}$ deposition was shown in Figure 2-4. Overall, based on the potential profiles we believe that the mechanism of the co-deposition (Section 1.4.1) does not change significantly with the type of Ni substrate. For the Pt–only deposition on Ni_{foam} the mechanism is slightly modified in that the sudden change in E_{WE} at ~ 1500 seconds is quite rapid as the potential only represents Equation 2-2 and 2-3. We note that the co-deposition and Pt deposition do differ in the concentration of chloride ions present in the deposition solution (2.4 M versus 2 M respectively). We do not know if this can affect the mechanism of the deposition.

Using an analytical balance, the mass of the substrate was recorded before and after deposition to determine the total mass of deposit. Further, inductively-coupled plasma mass spectrometry (ICP-MS) was used to determine the mass of Pt in the deposits. The average total mass of eight Ni–$Pt_{CE}Ni_{foam}$ deposits was 29.8 mg with ~ 0.56 mg_{Pt}. This equates to 0.6 atomic % Pt in Ni–$Pt_{CE}Ni_{foam}$, excluding the portion of Ni that is Ni_{foam}. Six $Pt_{CE}Ni_{foam}$ deposits had an average mass of 0.23 mg, which is consistent with the ~0.21 mg_{Pt} detected by ICP-MS. These low masses are expected given the self-limiting nature of the depositions. As a comparison, the mass of the deposit in Ni-$Pt_{CE}Ni_{gauze}$ was reported as 6.5 mg, with the amount of Pt being 0.37 mg_{Pt} or 1.8 atomic % Pt [1]. The difference in the mass of Ni between Ni–$Pt_{CE}Ni_{foam}$ (29.2 mg_{Ni}) and Ni-$Pt_{CE}Ni_{gauze}$ (6.1 mg_{Ni}) is consistent with the deposition profiles in Figure 2-4. The delayed rise in E_{WE} over the foam substrate meant a longer time for Ni deposition and ultimately more Ni deposited on foam than on gauze.

Figure 2-4 *Potential profiles of the electrodes during the galvanostatic Pt CE deposition at -0.1 A for 1 hour in sonicated solution. The Ni-$Pt_{CE}Ni_{gauze}$ and Ni-$Pt_{CE}Ni_{foam}$ electrodes were deposited from 0.2 M $NiCl_2$ in 2.0 M NH_4Cl while the $Pt_{CE}Ni_{foam}$ was deposited from 2.0 M NH_4Cl. The Pt_{CE} shown was for a deposition of Ni-$Pt_{CE}Ni_{foam}$ and is representative of the E_{CE} of all three depositions.*

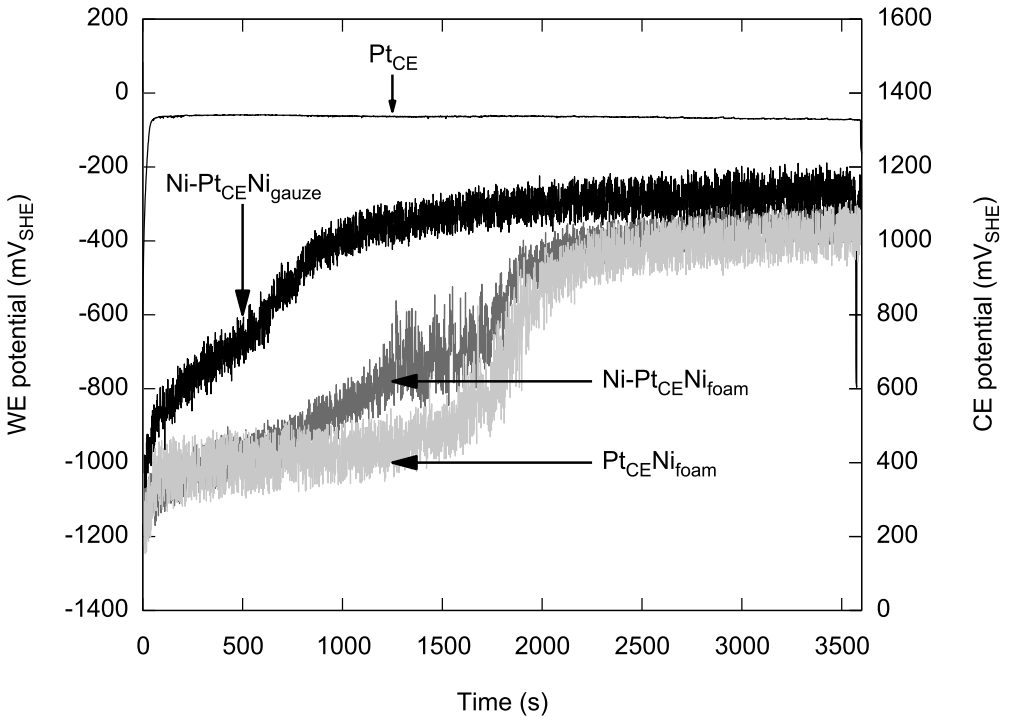

2.2.2 Microscopic comparison of substrates and deposits

Scanning electron microscopy (SEM) was used to compare the surface morphology of the pristine substrates and deposits. Figure 2-5 shows the resulting images of Ni_{gauze}, Ni_{foam}, Ni–$Pt_{CE}Ni_{gauze}$, Ni–$Pt_{CE}Ni_{foam}$ and $Pt_{CE}Ni_{foam}$. The Ni_{gauze} substrate is not perfectly smooth and appears to have lightly textured lines on its surface. The Ni_{foam} appears to have a scale like surface. The surface of Ni–$Pt_{CE}Ni_{gauze}$ (Figure 2-5a) consists of globular deposits while Ni–$Pt_{CE}Ni_{foam}$ (Figure 2-5b) appears to comprise multiple layers. $Pt_{CE}Ni_{foam}$ has the thinnest deposit with

the surface features of the foam substrate still visible (Inset of Figure 2-5b versus 2-4c). The relative roughness of the Ni–Pt deposits to the Pt only deposit is accordant with their relative masses (29.8 mg and 6.5 mg, versus 0.23 mg).

It was previously shown that Ni-Pt deposits on Ni gauze, prepared conventionally in the presence of a carbon CE and H_2PtCl_6 or $K[PtCl_3(C_2H_4)]$ in the deposition solution, did not visibly catalyze the decomposition of aqueous H_2O_2 despite containing ten times higher masses of Pt than those prepared by the *Pt CE deposition* [1]. It was concluded that the Pt deposited in the conventional way is dispersed throughout the co-deposit whereas Pt in Ni-$Pt_{CE}Ni_{gauze}$ is localized at the surface. To probe the distribution of Pt in the catalysts, composition analysis with Energy Dispersive X-ray Spectroscopy (EDX) was performed. Figure 2-6 shows EDX mapping of Ni–$Pt_{CE}Ni_{foam}$ and $Pt_{CE}Ni_{foam}$. The EDX sampling depth is ~ 1 μm. At this scale, the distribution of Pt (red regions) appears uniform. ~ 10 atomic % Pt was found in Ni–$Pt_{CE}Ni_{foam}$ (Figure 2-6a). Given that the ICP-MS results for the entire deposit of Ni–$Pt_{CE}Ni_{foam}$ (0.6 atomic % Pt) is much less than that detected by EDX, then most of the Pt is at the surface of the co-deposit. The proportion of Pt detected in $Pt_{CE}Ni_{foam}$ was less than 2 atomic % (Figure 2-6b). Furthermore, Ni was detected. This indicates that the thickness of the deposit is less than the sampling depth (1 μm) and the Ni detected was part of the foam substrate. This is consistent with the thin deposit viewed in the SEM results (Figure 2-5c). On the other hand, parts of the Ni foam substrate could also have remained uncovered by Pt. For both deposits, a large amount, ~20–50 atomic % of oxygen is present after exposure to air.

Figure 2-5 *Scanning electron micrographs of (a) Ni-$Pt_{CE}Ni_{gauze}$, inset: Ni_{gauze}, (b) Ni-$Pt_{CE}Ni_{foam}$, inset: Ni_{foam}, (c) $Pt_{CE}Ni_{foam}$. The scale bar is 10 µm in both insets.*

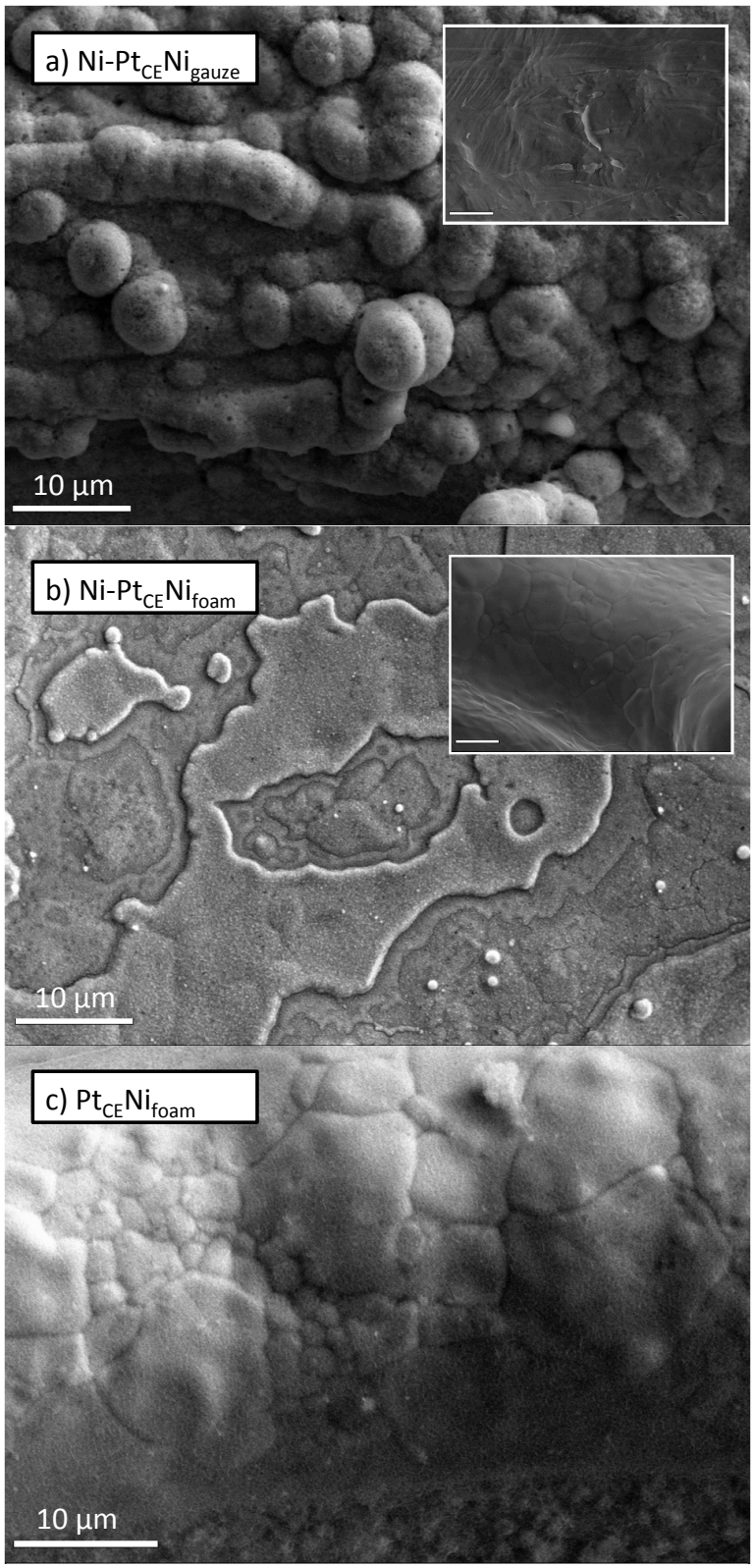

Figure 2-6 *EDX mapping of Pt (red) on the surface of the deposits: (a) Ni–$Pt_{CE}Ni_{foam}$ and (b) $Pt_{CE}Ni_{foam}$.*

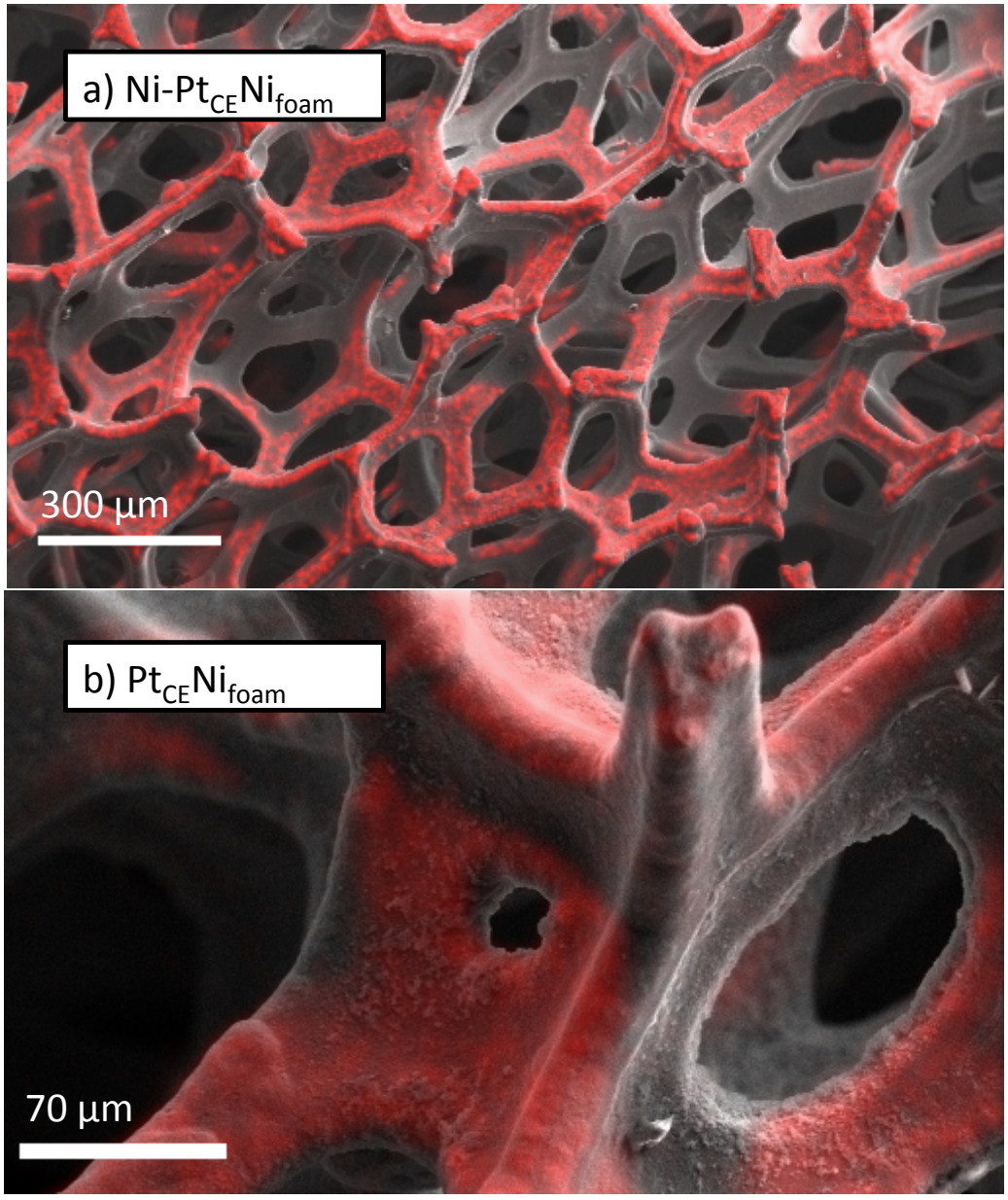

2.2.3 Cyclic voltammetry

We used cyclic voltammetry as a characterization tool to probe the electrochemically active surface of the deposits. Moreover, the charge (*viz.* the definite integral) of a CV is a measure of the real or electro-active surface area (ESA) of the electrodes (*vide infra)*. We therefore were able to compare the substrates and deposits to each other and to pure Pt and pure Ni electrodes. A Pt_{black} electrode was prepared by blackening Pt gauze in 0.02 M K_2PtCl_6 in 1 M $HClO_4$ or 0.04 M H_2PtCl_6 in 1 M HCl at -0.1 $V_{Ag/AgCl\ (4M\ KCl)}$. A Ni_{black} electrode was similarly prepared by blackening a Ni gauze in 0.2 M $NiCl_2$ in 2.0 M NH_4Cl at -0.1 A for 1 hour. Figures 2-7 and 2-8 show the CVs of Pt_{black} and Ni_{black} control electrodes.

Figure 2-7 *Cyclic voltammogram of Pt_{black} in 1 M KOH at 22°C with a scan rate of 10 mV s^{-1} showing the relevant surface processes occurring.*

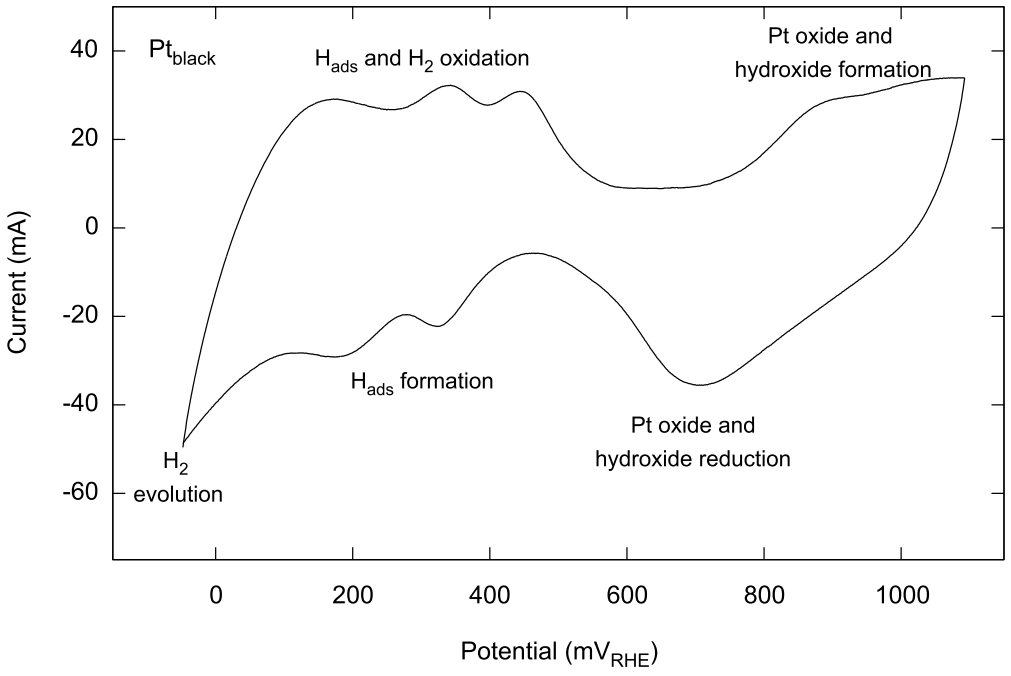

The CV of Pt_{black} has three regions: the hydrogen region from ~ 50 to 400 mV_{RHE}, the double layer region from ~400 to 500 mV and the oxygen region above 500 mV [40,41].

In the negative going (cathodic) sweep of the hydrogen region, protons from the aqueous electrolyte are reduced to form a (sub)monolayer of surface adsorbed hydrogen (H_{ads}) until $H_{2(g)}$ evolution occurs at ~ 0 V. The formation of H_{ads} is understood to be a one-electron reaction:

$$H^{+}_{(aq)} + e^{-} \xrightarrow{Pt} H_{ads} \qquad 2\text{-}4$$

During the positive going (anodic) sweep of the hydrogen region, H_{ads} and a portion of excess $H_{2(g)}$ are oxidised to protons. Multiple peaks are observed in this region due to the formation of strongly and weakly bound H_{ads} on the different crystal faces of the polycrystalline Pt surface. The number, shape, and size of the peaks depend on the crystal faces exposed to the electrolyte.

In the cathodic sweep of the oxygen region, the oxidation of H_2O occurs at ~ 800 mV_{RHE} causing the formation of platinum oxides and/or adsorbed oxygen, while in the reverse direction these species are reduced with a peak current at ~ 700 mV_{RHE}.

Finally, in the double layer region, no surface chemical reactions occur. The charge observed is due to double layer capacitance associated with the adsorption of anions and cations present in the electrolyte.

Figure 2-8 *Cyclic voltammogram of Ni_{black} in 0.5 M NaOH at 22°C with a scan rate of 10 mV s^{-1}.*

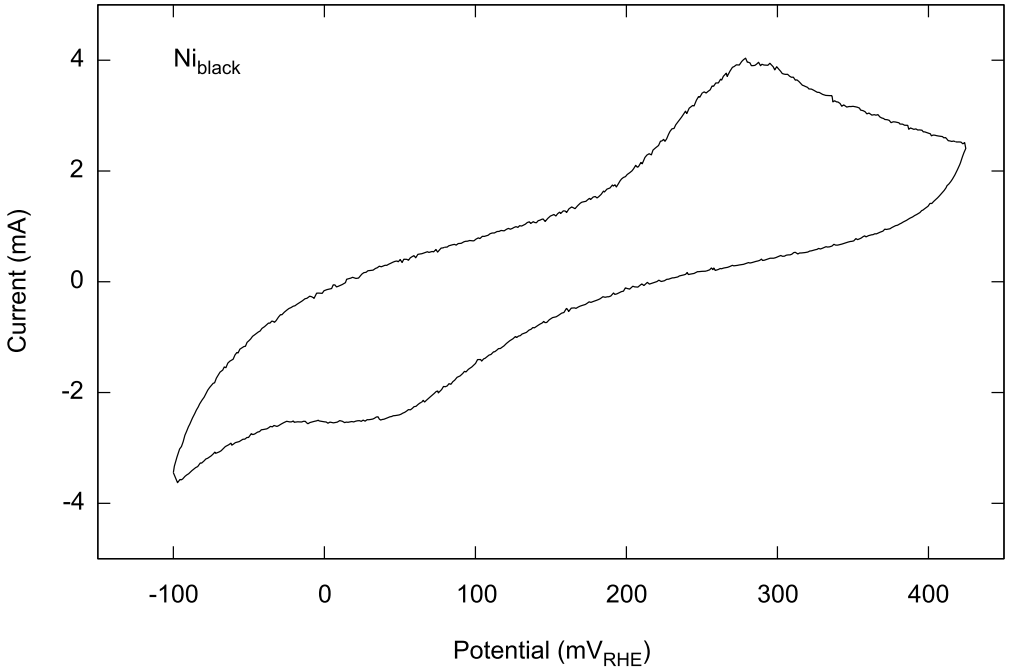

In contrast, the CV of Ni_{black} (Figure 2-8) involves mainly one reversible couple:

$$Ni + 2\,OH^- \rightarrow Ni(OH)_2 + 2\,e^- \qquad 2\text{-}5$$

In the positive going sweep, Ni is oxidised to α-$Ni(OH)_2$, while on the negative going sweep, α-$Ni(OH)_2$ is reduced to metallic Ni. The CV potential limits here are not as wide as that for Pt_{black} in Figure 2-8 because, above 450 mV_{RHE}, oxidation of Ni to β-$Ni(OH)_2$ (a phase of 2 or more monolayers) can occur. β-$Ni(OH)_2$ reversibly oxidises to NiOOH but does not readily reduce to zero-valent nickel (Equation 2-6) [8,42]. As an aside, β-$Ni(OH)_2$ has also been associated with a passivated surface that could inhibit methanol oxidation in base [43].

$$Ni(OH)_2 + OH^- \rightarrow NiOOH + H_2O + e^- \qquad 2-6$$

The CV of Ni-$Pt_{CE}Ni_{foam}$ and the Ni_{foam} substrate is shown in Figure 2-9. The CV of Ni_{foam} is featureless with no discernible reduction and oxidation peaks. The superlative increase in charge upon comparison of the substrate and the deposit indicates the ESA of Ni-$Pt_{CE}Ni_{foam}$ is higher than the ESA of Ni_{foam}. The CV features two broad anodic peaks between 0 and 200 mV_{RHE}. We believe that the broad peak at ~ 250 mV is due to the reversible oxidation of *deposited* Ni to α-$Ni(OH)_2$ (Equation 2-5). In contrast, the equivalent peak appears at about 280 mV_{RHE} in Ni_{black} (Figure 2-8). We believe that this lower potential for the onset of reaction 2-5 over Ni–$Pt_{CE}Ni_{foam}$ is due to the presence of Pt in the deposit, that is, Pt promotes the transformation of Ni to *α*-$Ni(OH)_2$. Moreover, with respect to the CV of Ni–$Pt_{CE}Ni_{foam}$, if we assign the peak potential for the reverse reaction at ~100 mV, then the separation of the redox peaks is about ΔE_{peak} = 200 mV. For Ni_{black} this separation is larger at 230 mV (ΔE_{peak} = 280 – 50 mV), indicating the apparent reaction rate must be higher in Ni–$Pt_{CE}Ni_{foam}$ than over Ni_{black}. Promoter activity of small amounts of Pt in Ni–Pt catalysts is known. For example, Pt is thought to catalyze the reduction of nickel oxide surfaces [44,45].

Figure 2-9 *Cyclic voltammogram of Ni-$Pt_{CE}Ni_{foam}$ in 0.5 M NaOH at 22°C with a scan rate of 10 mV s^{-1}.*

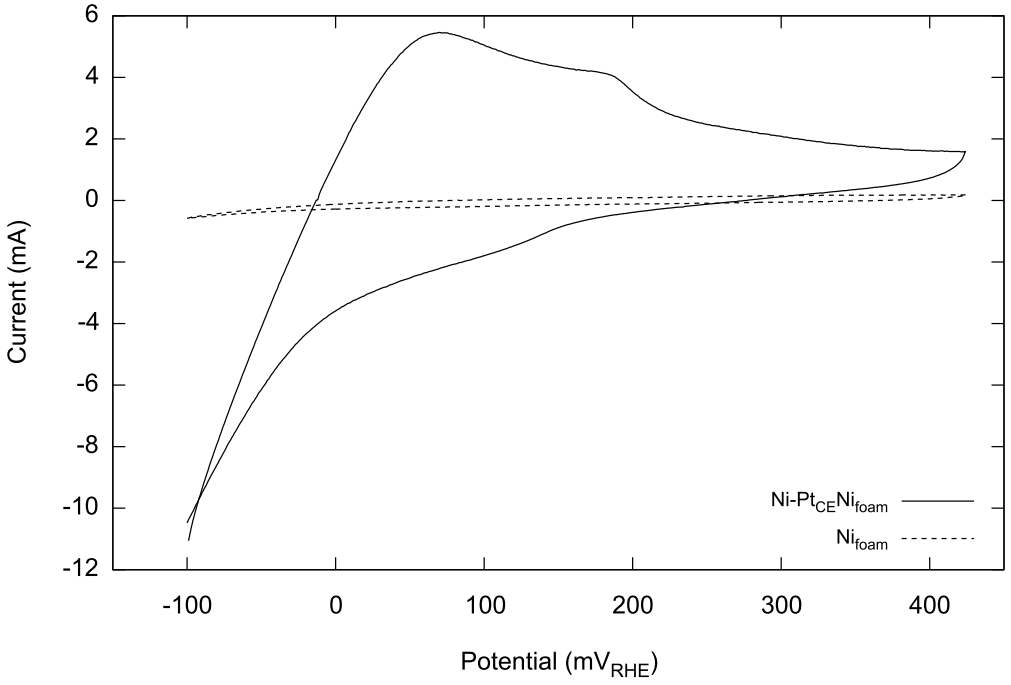

The second broad anodic peak at ~ 50 mV is also present in the CV of $Pt_{CE}Ni_{foam}$ (Figure 2-10). We attribute this peak to hydrogen desorption over Pt sites, but we cannot discern between weakly and strongly adsorbed hydrogen desorption peaks. Intriguingly, a similar peak was observed by Hu and Liu [46] in CVs of "Type-I" Pt deposits onto titanium substrates. Like our deposits, they are prepared under conditions of H_2 evolution. Hu and Liu attributed their broad anodic peak between 0 and 200 mV to the hydrogen desorption peaks as well. The $Pt_{CE}Ni_{foam}$ CV also showed an enhancement in ESA compared to the foam substrate. No Ni peaks were observed in $Pt_{CE}Ni_{foam}$. This is consistent with the absence of voltammetric peaks in the Ni_{foam} CV.

Figure 2-10 *Cyclic voltammogram of $Pt_{CE}Ni_{foam}$ in 0.5 M NaOH at 22°C with a scan rate of 10 mV s^{-1}.*

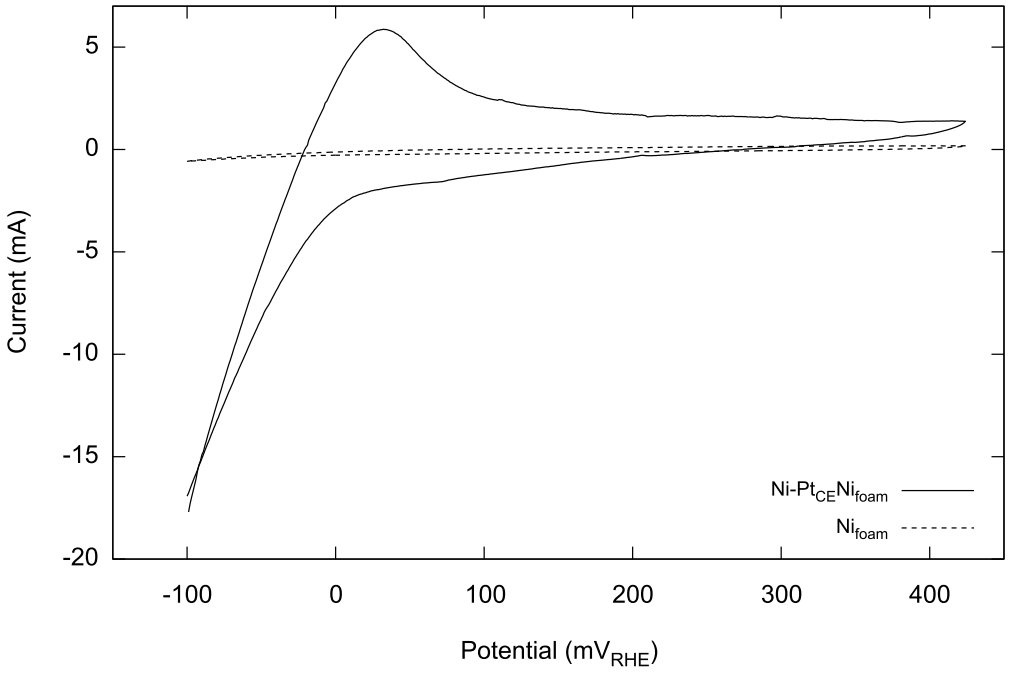

2.2.4 Evaluation of 2-propanol electro-oxidation activity

Sampled current voltammetry was used to evaluate the catalytic activity of the deposits towards the electro-oxidation of 2-propanol. This experiment involves invoking a potential step on the WE, and recording the average steady state current in the presence of 2-propanol for 15 minutes. Before each potential step, the WE was held at a reducing potential for 5 minutes (between -0.4 to 0 mV_{RHE}) to "reset" the electrode surface to its original state before proceeding to the next step. We believe the original state is oxidised as the electrodes have been exposed to air while transferring from deposition cells to activity cells.

Figure 2-11 shows the un-normalized sampled current voltammograms (SCVs) for Ni-$Pt_{CE}Ni_{gauze}$ [1], Ni-$Pt_{CE}Ni_{foam}$, $Pt_{CE}Ni_{foam}$ and Pt_{black} in 0.5 M NaOH/1 M $(CH_3)_2CH(OH)$. The Pt_{black} SCV features an activity maximum between 100 and

250 mV_{RHE} indicative of acetone inhibition. However, this low-potential current maximum was minor for the $Pt_{CE}Ni_{foam}$ and absent for both Ni–$Pt_{CE}Ni_{foam}$ and Ni-$Pt_{CE}Ni_{gauze}$. On the other hand, at potentials above 300 mV the deposits were very active towards the electro-oxidation.

Figure 2-11 *Un-normalized sampled current voltammograms in 0.5 M NaOH/1 M $(CH_3)_2CH(OH)$ at 60°C for Ni-$Pt_{CE}Ni_{gauze}$ Ni-$Pt_{CE}Ni_{foam}$, $Pt_{CE}Ni_{foam}$ and Pt_{black}.*

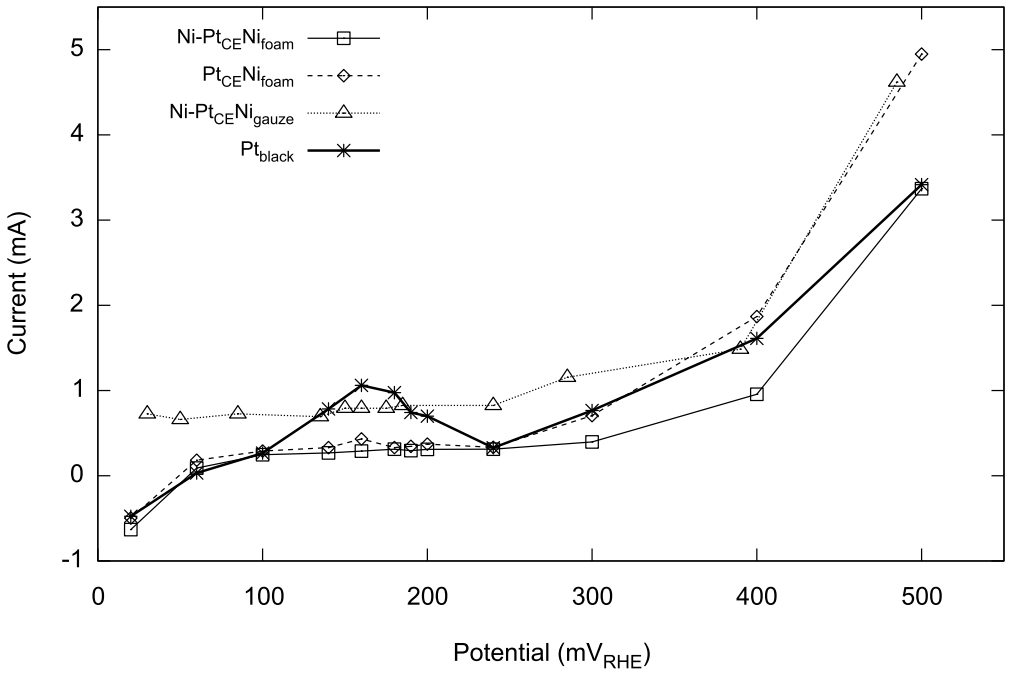

Specific activity of the deposits was determined by using the ICP-MS data discussed prior in Section 2.2.1. The Pt mass-normalized currents are shown in Figure 2-12. Pt_{black} was not included in this plot as the mass of the electrode excluding the mass of the Pt gauze substrate was not available. The results show that, all three deposits had similar activity up to 240 mV. Above 240 mV, $Pt_{CE}Ni_{foam}$ displays the highest current density, and therefore utilizes the mass of Pt the most efficiently in this potential range.

Figure 2-12 *Pt mass-normalized sampled current voltammograms in 0.5 M NaOH/1 M $(CH_3)_2CH(OH)$ at 60°C for Ni-$Pt_{CE}Ni_{foam}$, and Ni-$Pt_{CE}Ni_{foam}$, $Pt_{CE}Ni_{foam}$.*

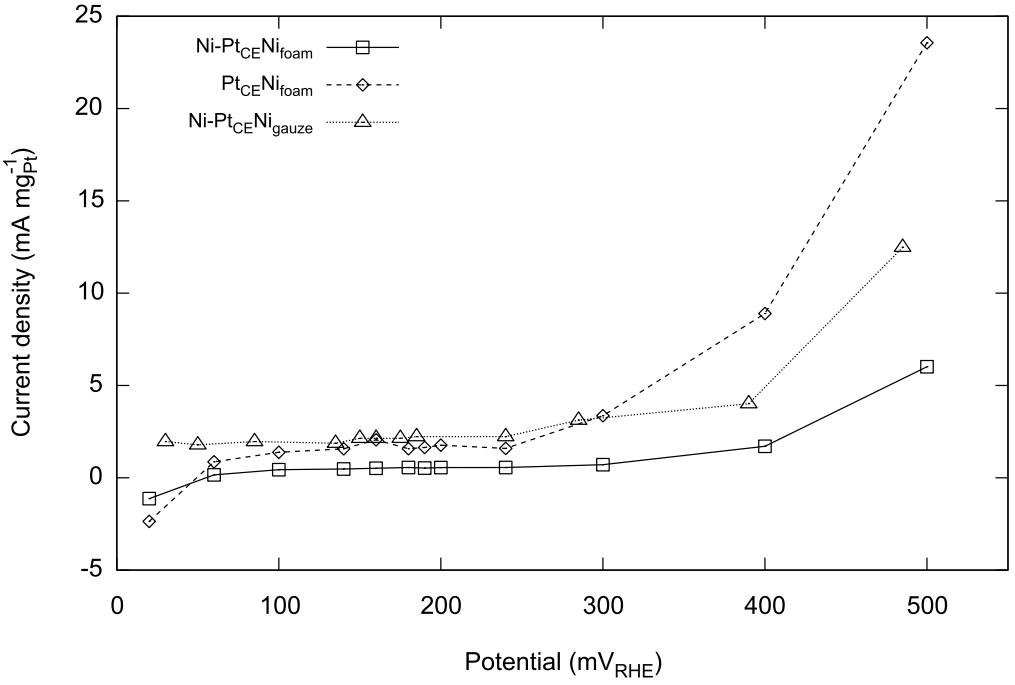

Normalization of the current by the number of surface atoms (n_{surf}) was also attempted. n_{surf} for Pt_{black} was calculated using the standard method of hydrogen underpotential deposition (H_{UPD}) [41,47]. H_{UPD} describes the formation of a single monolayer of hydrogen (Equation 2-4) onto the Pt surface at a more positive potential than that for formation of a layer of hydrogen onto hydrogen (that is, formation of H multi-layers). Because this process is limited to monolayer coverage under these conditions, the charge associated with the reaction (Q_{HUPD}) is proportional to the number of moles of Pt surface atoms, assuming each Pt site can only adsorb one hydrogen atom (Equation 2-7). Figure 2-13 shows the region chosen to measure Q_{HUPD}. The charge associated with double layer charging is carefully omitted and the potential of the minimum cathodic current before H_2 evolution occurs is chosen as the lower potential cut-off.

$$n_{surf} = \frac{Q_{HUPD}}{f_s \bullet n F} \qquad 2\text{-}7$$

where Q_{HUPD} is the charge due to the formation of a single monolayer of hydrogen on the Pt electrode (shown in Figure 2-12)

f_s accounts for incomplete monolayer formation and overlap with the charge due to H_2 evolution and is equal to 77%

n is the number of electrons transferred

F is Faraday's constant

Figure 2-13 *Cyclic voltammogram of Pt_{black} in 1 M KOH at 22°C with a scan rate of 10 mV s^{-1} showing the double layer charge between the dashed lines and the charge associated with hydrogen adsorption shaded in grey.*

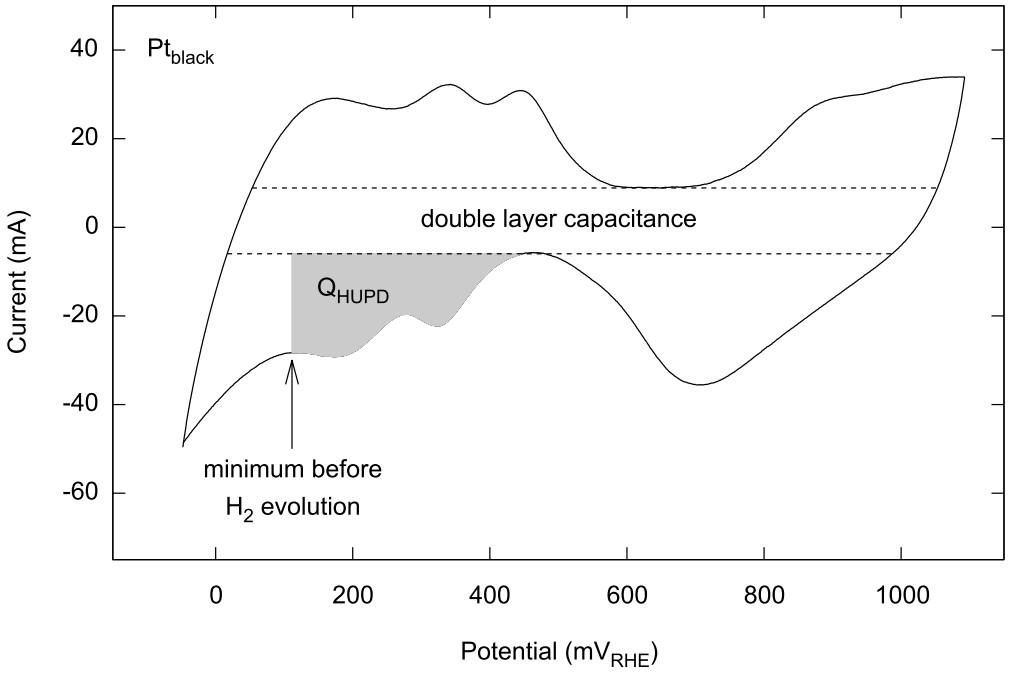

The Pt_{black} electrode has a Q_{HUPD} value of 0.332 C giving 4.47 µmol surface atoms. The determination of the n_{surf} for the prepared deposits is more complex as the Ni and Pt features in the CVs cannot be easily deconvoluted or are not

clearly expressed in the CVs. We therefore used CO adsorption and stripping to estimate this value.

CO adsorption and stripping is based on the principle of adsorptive stripping voltammetry [48]. In this experiment, the WE is held at a potential where CO can be adsorbed onto the electrode surface from a CO-purged electrolyte. The adsorbed monolayer of CO is subsequently oxidised off the WE surface using cyclic voltammetry via the reverse of Equation 2-8 [49]:

$$CO_2 + 2H^+ + 2e^- \leftrightarrow CO + H_2O \qquad (E^0 = -0.12\ V_{SHE}) \qquad 2-8$$

The charge associated with this process can thus be used to estimate the surface area of the WE.

CO adsorption and stripping in 0.5 M NaOH was performed by bubbling CO vigorously over the WE electrolyte while holding the potential at -0.4 V_{RHE} for 30 minutes. At this potential, the Pt surface can be reduced, removing oxides and allowing optimum coverage of strongly adsorbing CO. The solution was then purged with N_2 at 0.05 V_{RHE} for 5 minutes, immediately followed by cycling under N_2 between -0.1 and 1.1 V_{RHE} for seven complete cycles. Figure 2-14 shows the first, second and seventh CO stripping cycles for the deposits. For clarity, we did not include cycles 3 to 6 because they overlap with cycle 7. We propose that the charge of each cycle represents the processes described in Table 2-1.

Figure 2-14 *Carbon monoxide stripping voltammograms in 0.5 M NaOH at 10 mVs^{-1} for a) Ni-$Pt_{CE}Ni_{foam}$ and b) $Pt_{CE}Ni_{foam}$. Prior to stripping, carbon monoxide was adsorbed at -400 mV_{RHE} for 30 minutes, followed by purging the electrolyte with N_2 at 50 mV for 5 minutes.*

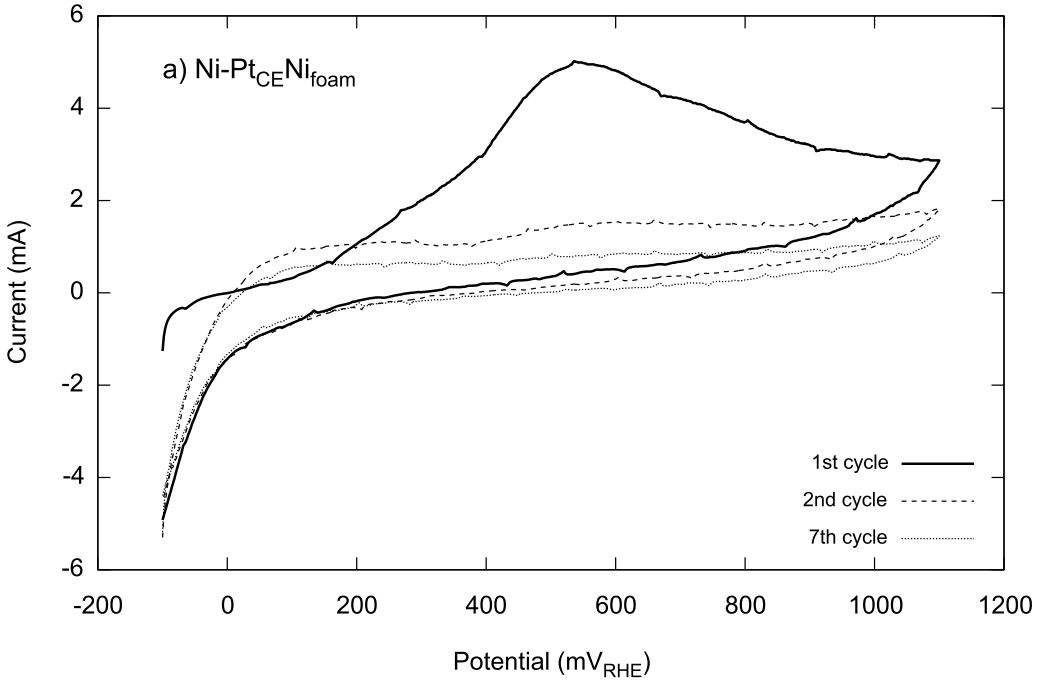

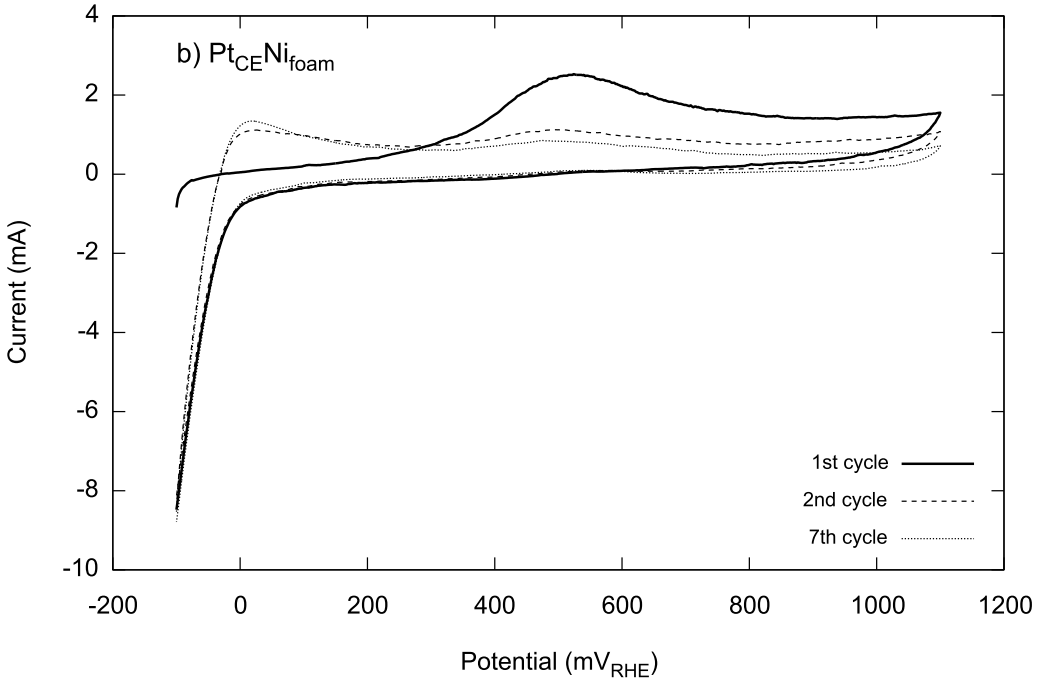

Table 2-1 *Processes occurring during the CO adsorption and stripping cycles for the Ni-$Pt_{CE}Ni_{foam}$ and $Pt_{CE}Ni_{foam}$ deposits.*

Cycle	Processes occurring
1	$CO + H_2O \xrightarrow{Pt} CO_2 + 2\,H^+ + 2e^-$ $Ni + 2\,OH^- \rightarrow \beta\text{-}Ni(OH)_2 + 2e^-$ Double layer charging (capacitance)
2	$Ni + 2\,OH^- \rightarrow \beta\text{-}Ni(OH)_2 + 2e^-$ Double layer charging (capacitance)
7	Double layer charging (capacitance)

Recall that the oxidation of Ni to β-$Ni(OH)_2$ is irreversible, thus, the combined charge of cycles 1 and 2 represent the total CO stripping charge, the total Ni surface oxidation charge and double the total capacitance charge. Therefore, the combined charge due to CO stripping and Ni surface oxidation, Q_{Tot}, can be calculated:

$$Q_{Tot} = Q_{CO} + Q_{Ni} \qquad 2\text{-}9$$
$$= (Q_1 + Q_2) - 2\,(Q_7)$$

where Q_{Tot} is the total charge due to CO stripping and Ni surface oxidation

Q_{CO} is the charge due to CO stripping

Q_{Ni} is the charge due to Ni surface oxidation

Q_1 is the anodic charge of cycle 1

Q_2 is the anodic charge of cycle 2

Q_7 is the anodic charge of cycle 7

The number of surface atoms can therefore be estimated:

$$n_{surf} = \frac{Q_{Tot}}{n \bullet F} \qquad 2\text{-}10$$

where n is the combined number of electrons for CO stripping and Ni oxidation reactions, that is, 4

We recognize that the calculated value for n_{surf} could be grossly overestimated if CO adsorbs on both Pt and oxidised Ni sites, although to our knowledge there are no reports of electro-chemical CO adsorption and stripping on Ni surfaces. Further, after the first sweep that removes CO, the newly clean Pt surfaces contribute to double layer charging. Therefore the double layer charging in step 2 may not be exactly equal to that in cycle 1 or 7. Finally, the oxidation of the Ni surface occurs over many surface layers *viz*. the number of Ni sites will be counted multiple times. Thus, the surface atom-normalized activity data will be underestimated.

An additional challenge with the CO stripping experiment is that one cannot use a particular WE for both CO stripping and for 2-propanol oxidation. The CO stripping experiment can permanently change the surface of the catalyst (*viz.* formation of *β*-$Ni(OH)_2$) if it is performed before activity experiments. Therefore, we assumed that two of the same type of WE with similar anodic charge in their baseline voltammograms, Q_{CV} (Figure 2-9 and 2-10), should have similar activity towards the electro-oxidation of 2-propanol. As a result, we used activity data from one WE (denoted A), and CO stripping data from another WE (denoted B) to standardize Equation 2-10 and account for any changes in surface area between A and B:

$$n_{\text{surface atoms}} = f \bullet \frac{Q_{Tot}}{nF} \qquad 2\text{-}11$$

$$= \frac{Q^{B}_{CV}}{Q^{A}_{CV}} \bullet \frac{Q_{Tot}}{nF}$$

where the standardization factor, $f = \frac{Q^{B}_{CV}}{Q^{A}_{CV}}$ 2-12

and Q^{A}_{CV} is the anodic charge in the baseline CV of the WE used for 2-propanol activity determination

Q^{B}_{CV} is the anodic charge in the baseline CV of the WE used for CO adsorption and stripping

Thus, Table 2-2 summarizes the data used to produce the surface atom-normalized SCVs shown in Figure 2-15.

Figure 2-15 shows that the normalized activities of Ni-$Pt_{CE}Ni_{foam}$ and $Pt_{CE}Ni_{foam}$ were not significantly greater than that of Pt_{black} or Ni-$Pt_{CE}Ni_{gauze}$ between 50 and 250 mV_{RHE}. However, the foam-based deposits were markedly more active than Pt_{black} at potentials above 250 mV. At 500 mV, Ni-$Pt_{CE}Ni_{foam}$ was 5 times more active than Ni-$Pt_{CE}Ni_{gauze}$ and 9 times more active than Pt_{black}. Moreover, $Pt_{CE}Ni_{foam}$ was 20 times more active than Ni-$Pt_{CE}Ni_{gauze}$ and a remarkable 38 times more active than Pt_{black}. Over the entire potential range, the catalysts can be ranked in order of activity $Pt_{CE}Ni_{foam}$ > Ni-$Pt_{CE}Ni_{foam}$ > Ni-$Pt_{CE}Ni_{gauze}$ > Pt_{black}. These results confirm that Ni promotes the 2-propanol electro-oxidation over Pt particularly at high potentials where acetone oxidation also occurs. The reasons for these enhancements are discussed presently.

Table 2-2 *Summary of surface atom calculations for normalization of activity data by the number of surface atoms.*

Electrode	$\frac{Q_{CV}^{B}(C)}{Q_{CV}^{A}(C)}$	$Q_{Tot}(C)$	n_{surf} (μmol)
Ni-$Pt_{CE}Ni_{foam}$	$\frac{0.087}{0.134}$	0.286	0.480
$Pt_{CE}Ni_{foam}$	$\frac{0.074}{0.100}$	0.090	0.173

Figure 2-15 *Surface atom-normalized sampled current voltammograms in 0.5 M NaOH/1 M $(CH_3)_2CH(OH)$ at 60°C for a) Pt_{black}, Ni-$Pt_{CE}Ni_{gauze}$, Ni-$Pt_{CE}Ni_{foam}$ and $Pt_{CE}Ni_{foam}$ and b) the same within the range 100 to 100 mV_{RHE}.*

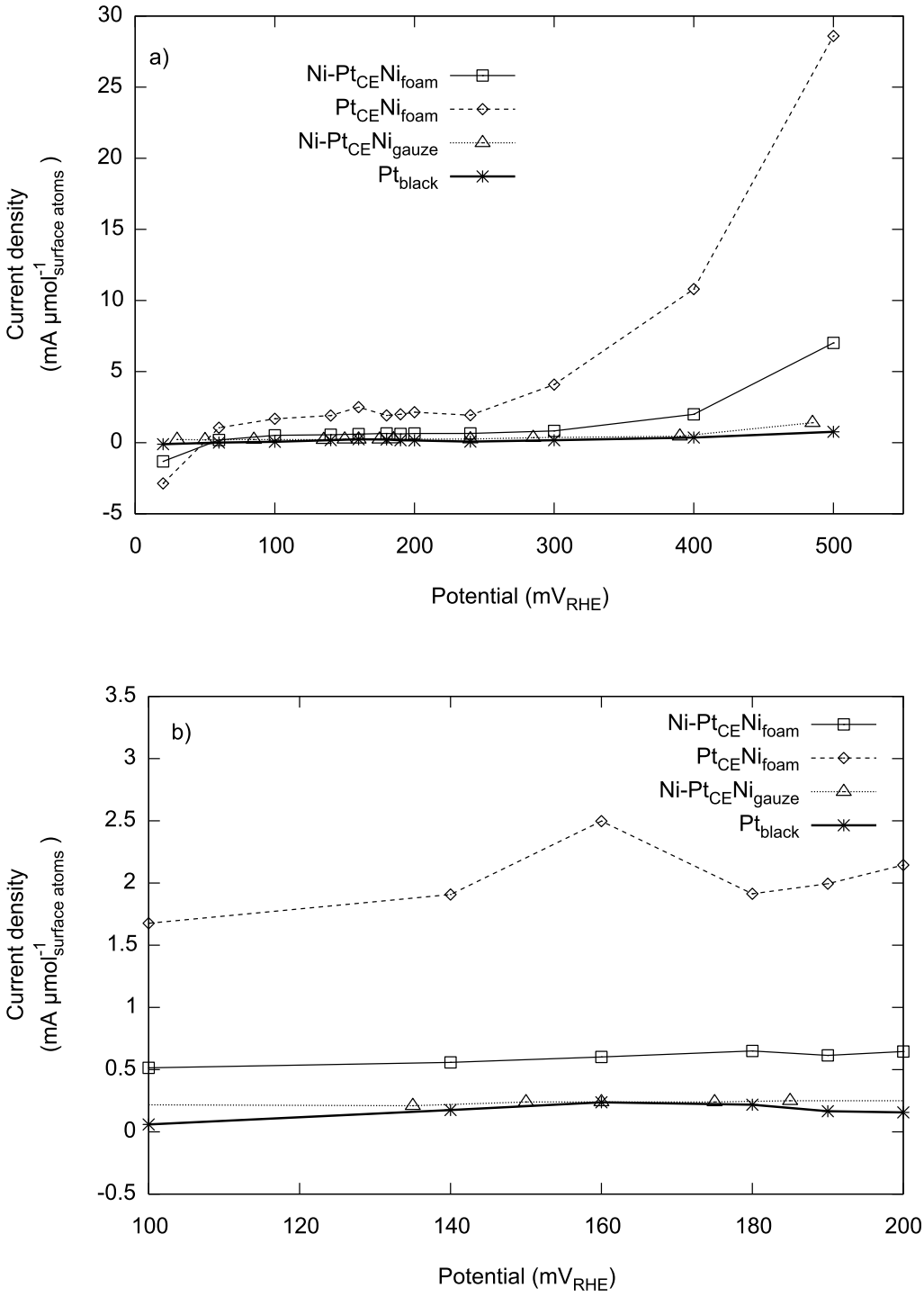

2.2.5 X-ray photoelectron spectroscopy

X-ray photoelectron spectroscopy (XPS) was performed to probe the spectroscopic and electronic characteristics of our deposits. Figure 2-16 shows the Pt 4*f* XPS spectra of Ni–$Pt_{CE}Ni_{foam}$ and $Pt_{CE}Ni_{foam}$. The general shape of both spectra have the following features: (i) a Pt 4*f* doublet with peaks at ~71 and 74 eV, (ii) asymmetric tails[4] on these doublets at higher binding energies, and (iii) a large Ni 3*p* shoulder at ~69 eV. To fit these features we used four pairs of peaks representing metallic Pt, $Pt(OH)_2$, NiO and $Ni(OH)_2$ based on reported data [50]. More details on the fitting procedure are provided in Section 2.4.1. The choice of these species is based on the position of the experimental peaks (Table 2-3) and upon the presence of a large amount of oxygen on the surface of our catalysts as seen in a survey spectrum.

[4] Metals like Pt have a significant density of occupied states near the Fermi level. When the electron is ejected, it excites these valence electrons by losing KE, creating a number of closely spaced satellites towards higher BE and resulting in an asymmetric tail in the main peak [55]. This is an example of a *final state effect*.

Figure 2-16 *X-ray photoelectron spectra of a) Ni-$Pt_{CE}Ni_{foam}$ and b) $Pt_{CE}Ni_{foam}$. Dashed lines are experimental data, solid lines are calculated fits and solid grey lines are component peaks of the calculated fits.*

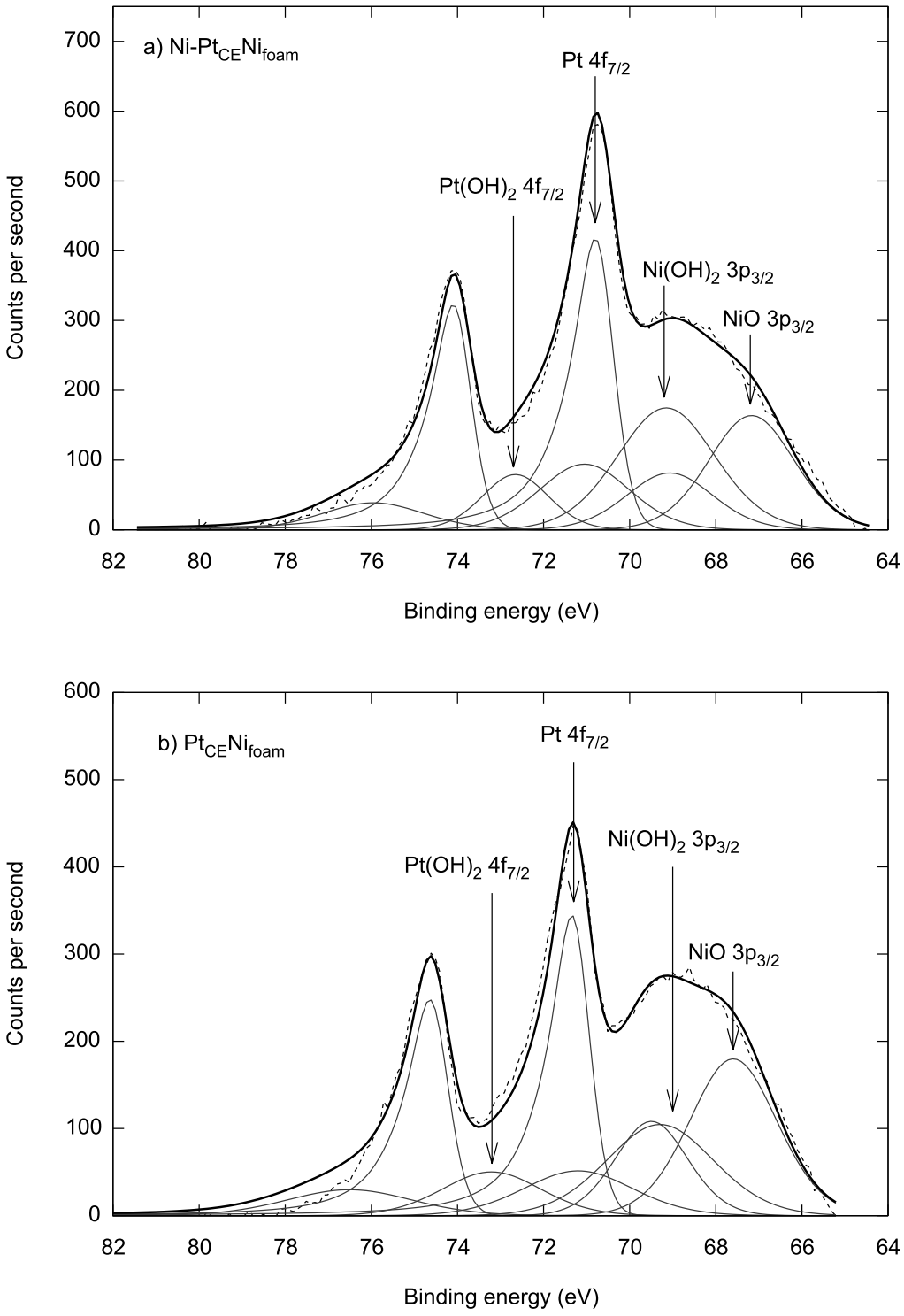

Table 2-3 *Calculated average and experimental binding energies and standard deviations.*

Chemical state and spectral line	Binding energy (eV)		
	Reference	Ni-Pt_{CE} Ni_{foam}	Pt_{CE} Ni_{foam}
Pt[a] $4f_{7/2}$	71.1 (0.1)[b]	70.8	71.3
$Pt(OH)_2$ $4f_{7/2}$	72.7 (0.1)	72.7	73.2
Pt(II) $4f_{7/2}$	73.8	-	-
Pt(IV) $4f_{7/2}$	74.6	-	-
NiO[c] $3p_{3/2}$	68.0 (-)	67.2	67.6
$Ni(OH)_2$ $3p_{3/2}$	69.0 (-)	69.2	69.3

[a] Specimens were either Pt crystals or sputtered platinum samples.

[b] Numbers in brackets denote the standard deviation of the data set for values in the reference column. In all other columns experimental error was ±0.1 eV. Dashes in brackets signify that no standard deviation has been recorded as only one value for the spectral line has been reported in the database.

[c] Specimens were pelletized crystals or films.

The XPS area ratios compiled in Table 2-4 indicate that Ni–$Pt_{CE}Ni_{foam}$ contains > 30% Pt at its surface. XPS probes depths of 3 to 9 nm, EDX probes up to 1 μm, and ICP-MS results reveal the atomic % Pt in the entire deposit. Given that the atomic % Pt determined by XPS was much more than that showed by EDX (10 atomic % Pt), and ICP-MS (0.6 atomic % Pt), then most of the deposited Pt is on or near the catalyst surface. With this in mind, we believe the best model for the Ni–$Pt_{CE}Ni_{foam}$ catalyst is a bimetallic Pt and Ni shell with gradually decreasing proportions of platinum leading down to a nickel foam core. A representative structure is provided in Figure 2-17a.

Figure 2-17 *Diagram showing the proposed structure of Ni-$Pt_{CE}Ni_{foam}$ and $Pt_{CE}Ni_{foam}$.*

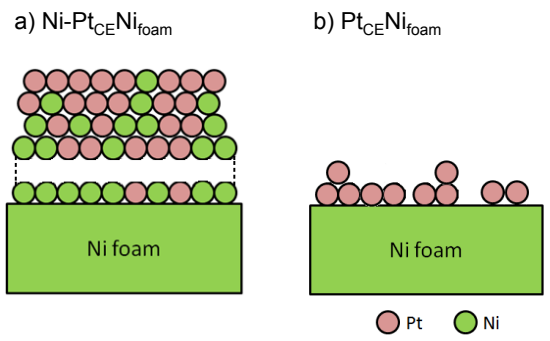

Table 2-4 *Chemical states and area ratios of Ni-$Pt_{CE}Ni_{foam}$ and $Pt_{CE}Ni_{foam}$ catalysts by XPS.*

Chemical state	XPS area ratio (%)	
	Ni-Pt_{CE} Ni_{foam}	Pt_{CE} Ni_{foam}
Pt	32.08	29.96
NiO	25.65	33.61
$Ni(OH)_2$	31.12	24.04
$Pt(OH)_2$	11.13	12.40

The Pt metal $4f_{7/2}$ peak in Ni–$Pt_{CE}Ni_{foam}$ appears at 70.8 ± 0.1 eV. This is a slight shift to lower binding energy (BE) compared to the expected BE for Pt bulk (71.1 eV, given in the reference column of Table 2-3). The magnitude of the shift is within the range of 3 standard deviations of the bulk value, making the effect observed very small. Additionally, the majority of the Pt exists in an oxidation state closer to 0 than to +2 (32 % Pt versus 11% $Pt(OH)_2$).

In the case of the $Pt_{CE}Ni_{foam}$ catalysts, the XPS area ratios in Table 2-4 do not reveal any significant additional information and the proposed structure still stands as either a < 1 μm deposit of Pt on the Ni foam or areas of foam are exposed (determined by EDX and discussed in Section 2.2.2; Figure 2-17b). The

Pt metal $4f_{7/2}$ peak appeared at 71.3 ± 0.1 eV, a slight positive shift with respect to bulk Pt and opposite in direction of the Ni–$Pt_{CE}Ni_{foam}$. However, we point out that the shift is within 2 standard deviations of the Pt bulk value, so it is either very small or inconsequential.

2.2.6 Origins of enhanced activity

As discussed in Section 2.1.1, there are three main effects in the literature used to explain the enhancements in catalytic activity observed due to addition of a nickel to platinum. At this point, it is imperative to note that the activity enhancements we observe over $Pt_{CE}Ni_{foam}$ and Ni-$Pt_{CE}Ni_{foam}$ are not just a summative effect of Ni catalysis and Pt catalysis of the 2-propanol oxidation. Firstly, neither Ni_{gauze} nor Ni_{foam} nor Ni_{black} catalyze the 2-propanol electro-oxidation reaction between 0 and 500 mV_{RHE}. Moreover, Tafel plots above 200 mV generated from the raw SCV data in Figure 2-11 gave slopes of 260, 224 and 241 mV dec^{-1} over Pt_{black}, $Pt_{CE}Ni_{foam}$ and Ni-$Pt_{CE}Ni_{foam}$ respectively.[5] These values are quite similar indicating the 2-propanol/acetone electro-oxidation mechanisms over the two foam-based electrodes are similar to Pt, further confirming the non-activity of the Ni component.

The XPS data for Ni-$Pt_{CE}Ni_{foam}$ showed a slight negative shift in BE for the Pt 4*f* core spectral lines. According to the Allred-Rochow electronegativity scale, Pt is less electronegative than Ni [23]. Therefore, we suggest that this shift is

[5] A Tafel plot is an empirical plot of potential versus the logarithmic function of the current for an electrochemical process and is relevant at high potentials relative to the Nernst potential for the reaction. In principle, the Tafel slope is viewed as a mechanistic parameter. Tafel plots are discussed in Section A.2.3.

related to Ni donating *d* vacancies to Pt as suggested by Toda *et al.* [24,25]. However, we take a different approach in explaining our observed BE shift.

It has been shown by Wetzig and co-workers that p-doping of SnO_2 results in the lowering of the Fermi level on the semiconductor because of additional hole states near the valence band [51]. Compared to the intrinsic semiconductor, the observed BE shifts to lower values. If we treat the donation of *d* vacancies to Pt as "p-doping", we would expect the Fermi level in our catalyst to lie closer to the core electrons than it does in bulk Pt, resulting in a shift of the BE to lower values. The shift to lower BE is correlated to weaker surface Pt-adsorbate bond strength as suggested in general by Nørskov and co-workers [29]. This is assuming there is no narrowing of the *d* bands as shown in Figure 2-3.

Alternatively, if the surface Pt in Ni-$Pt_{CE}Ni_{foam}$ does experience band narrowing due to the *d* vacancy donation to Pt, then the *d* band center is expected to up-shift as suggested by Jeon *et al.* [20] for carbon supported Pt-Ni alloys, and in general by Egelhoff [17] and Nørskov and co-workers [34]. In this case, stronger surface Pt-adsorbate bonds will form on Ni-$Pt_{CE}Ni_{foam}$.

We believe that the first alternative fits our experimental observations, that is, the Fermi level in Ni-$Pt_{CE}Ni_{foam}$ lies closer to the core electrons than it does in bulk Pt, resulting in a shift of the BE to lower values. This would imply that the adsorption of species onto Ni–$Pt_{CE}Ni_{foam}$ is weaker than onto $Pt_{CE}Ni_{foam}$ or Pt_{black}. We did find that CO might be more weakly adsorbed on Ni–$Pt_{CE}Ni_{foam}$ than $Pt_{CE}Ni_{foam}$ as it had a lower CO stripping onset potential than the latter (Figure 2-14). Furthermore, the onset potential of CO stripping on Pt (1 0 0) and Pt (1 1 1) is at least ~200 and 450 mV higher than on Ni–$Pt_{CE}Ni_{foam}$ [52,53]. On a similar

notion, this trend in BE could account for the low-potential current maximum attributed to acetone inhibition seen in the SCVs (Figures 2-10, 2-11 and especially the Figure 2-15b). This feature was almost absent for Ni–$Pt_{CE}Ni_{foam}$. At these potentials, the activation of 2-propanol as well as acetone inhibition would rely on the autonomous adsorption of the two molecules on the catalyst surface. Ni–$Pt_{CE}Ni_{foam}$ should therefore have the weakest adsorption properties according to the XPS data and this is consistent with the lowest low-potential current maximum (that is the absolute difference between the current at 100 and 160 mV).

If the positive XPS shift observed in $Pt_{CE}Ni_{foam}$ is not real, then the Pt in this deposit is electronically similar to bulk Pt. Consequently, electronic effects would not sufficiently explain the activity enhancement of this catalyst especially at potentials above 250 mV where Pt_{black} is the worst performer and $Pt_{CE}Ni_{foam}$ is the best performer.

Given that Ni itself is not active towards 2-propanol electro-oxidation, we believe that the activity enhancement of both catalysts at high potentials compared to Pt, is mainly via the bi-functional mechanism and less by an electronic effect. The mechanism of 2-propanol oxidation discussed in Sections 1.3.1 and 1.3.2 is such that addition of Ni to Pt enhances the current observed only at potentials above 250 mV [1]. The SCVs of Ni-$Pt_{CE}Ni_{foam}$ and $Pt_{CE}Ni_{foam}$ (Figures 2-11 and 2-14) confirm this result. According to the CV of Ni-$Pt_{CE}Ni_{foam}$ electrode (Figure 2-9), the conversion of Ni to $Ni(OH)_2$ occurs close to 200 mV_{RHE}. For $Pt_{CE}Ni_{foam}$ we presume that the exposed regions of the Ni foam substrate form $Ni(OH)_2$ at similar potentials. It is therefore apparent that Ni promotes the electro-oxidation only after the formation of $Ni(OH)_2$, thereby providing OH at low potentials to commence the bi-functional mechanism. This is

consistent with the results of Chen *et al.* for a Pt deposition on a Ni film discussed in Section 2.1.2.1 [8]. Moreover, we reiterate that the onset potentials in our CO stripping experiments were lower than that observed for Pt [52,53]. The bi-functional mechanism could readily explain these observations, as well as act in conjunction with the electronic effect on the relative CO adsorption strength, *vide supra*.

It is interesting that $Pt_{CE}Ni_{foam}$ is more active than Ni–$Pt_{CE}Ni_{foam}$ at potentials above 250 mV despite the latter having a higher Ni content and likely a greater bi-functional effect, and the former having inconsequential electronic effects. Perhaps a geometric effect similar to the one described by Gasteiger *et al.* and Yang *et al.* for methanol electro-oxidation is existent for $Pt_{CE}Ni_{foam}$ [38,39]. Assuming similar mechanisms for activation of 2-propanol and methanol and given that $Pt_{CE}Ni_{foam}$ is not co-deposited, the probability of having enough Pt sites in the correct orientation for 2-propanol adsorption is much higher than in Ni–$Pt_{CE}Ni_{foam}$. It is therefore probable that this additional geometric effect makes $Pt_{CE}Ni_{foam}$ so much more active than Ni–$Pt_{CE}Ni_{foam}$, while the combination with the bi-functional effect makes it superior to Pt_{black}. We also should not discount the possibility that the deposition itself creates a highly active form of Pt.

.

2.3 Conclusions

We have shown that the *Pt CE deposition* is not exclusive to Ni gauze substrates, and that Pt deposition can occur regardless of the presence of $NiCl_2$ in the deposition solution. As such, we prepared two new catalysts, Ni-$Pt_{CE}Ni_{foam}$ and $Pt_{CE}Ni_{foam.}$ Novel results of the microscopic and spectroscopic characteristics of the catalysts were presented. Combined data (SEM, ICP-MS, EDX and XPS) helped to determine a likely structure of the catalysts. Ni-$Pt_{CE}Ni_{foam}$ possibly exists as a bimetallic Pt and Ni shell with gradually decreasing proportions of platinum leading down to a nickel foam core. On the other hand, $Pt_{CE}Ni_{foam}$ is either a conformal deposit of Pt with depth < 1 μm on the Ni foam substrate, or exists as an incomplete thin layer of Pt with areas of Ni foam exposed.

SEM showed that the co-deposits, Ni-$Pt_{CE}Ni_{gauze}$ and Ni-$Pt_{CE}Ni_{foam}$, had rougher surfaces than $Pt_{CE}Ni_{foam}$. This reflected the relative masses of the deposits as determined by ICP-MS. CVs revealed that Ni-$Pt_{CE}Ni_{foam}$, like Ni-$Pt_{CE}Ni_{gauze}$, had both nickel and platinum characteristics, while only Pt peaks were identified in the CV of $Pt_{CE}Ni_{foam}$.

The surface atom normalized activity of the catalysts towards 2-propanol electro-oxidation in alkaline media between 0 and 500 mV_{RHE} were ranked as follows: $Pt_{CE}Ni_{foam}$ > Ni-$Pt_{CE}Ni_{foam}$ > Ni-$Pt_{CE}Ni_{gauze}$ > Pt_{black} (Table 2-5). Ni-$Pt_{CE}Ni_{foam}$ and $Pt_{CE}Ni_{foam}$ activities were not significantly greater than that of Pt_{black} or Ni-$Pt_{CE}Ni_{gauze}$ between 50 and 250 mV_{RHE}. However, the foam-based deposits were markedly more active than Pt_{black} at potentials above 250 mV. At 500 mV, Ni-$Pt_{CE}Ni_{foam}$ was 5 times more active than Ni-$Pt_{CE}Ni_{gauze}$ and 9 times more active than Pt_{black}. Moreover, $Pt_{CE}Ni_{foam}$ was 20 times more active than Ni-$Pt_{CE}Ni_{gauze}$ and a remarkable 38 times more active than Pt_{black}.

Table 2-5 *Summary of the relative activity enhancements of the Ni-$Pt_{CE}Ni_{foam}$ and $Pt_{CE}Ni_{foam}$ catalysts compared to Pt_{black} for 2-propanol oxidation in 1M $(CH_3)_2CHOH$/0.5 M NaOH at 60°C.*

	Ni-$Pt_{CE}Ni_{foam}$		$Pt_{CE}Ni_{foam}$	
Potential (mV vs. RHE)	Low	High	Low	High
Enhancement compared to Pt (mA surf. atoms^{-1})	None	2.3 x	2.6 x	9.4 x
Effects proposed	Electronic and bi-functional	Bi-functional	Bi-functional	Geometric and bi-functional

Electronic effects based on XPS analysis were more apparent for Ni-$Pt_{CE}Ni_{foam}$, while the Pt 4*f* peak shifts for $Pt_{CE}Ni_{foam}$ was negligible. The observed activity at potentials between 50 and 250 mV_{RHE} were therefore attributed to slight electronic effects in the Ni – $Pt_{CE}Ni_{foam}$ catalysts. We believe that the enhanced activity at potentials > 250 mV for Ni–$Pt_{CE}Ni_{foam}$ was a combination of electronic and bi-functional effects and for $Pt_{CE}Ni_{foam}$ a combination of geometric and bi-functional effects.

Given that by simply changing the WE for the *Pt CE deposition* from Ni gauze to a high porosity Ni foam, we made significant gains in the observed activity of the catalysts, the next study sought to investigate the effect of an even higher surface area Ni film as the substrate. Chapter 3 therefore discusses Pt deposits on a glancing angle deposited Ni nanopillar film and its activity towards 2-propanol electro-oxidation in alkaline media.

2.4 Experimental

2.4.1 General

The following reagents were used as received from the supplier: Nitrogen (Praxair, pre-purified), Carbon monoxide (Praxair, technical grade), concentrated sulfuric acid (Caledon), hydrochloric acid (EMD chemicals), nitric acid (EMD chemicals), and perchloric acid (Anachemia Corporation), potassium permanganate (Fischer Scientific), 30% hydrogen peroxide (Fischer Scientific), sodium hydroxide (Alfa Aesar, 99.9% semiconductor grade), ammonium chloride (Caledon Laboratory chemicals), 2-propanol (Fischer Scientific, ACS plus grade), ethanol (Greenfield Ethanol Incorporated) potassium hexachloroplatinate (Aithica Chemical Corporation), hexachloroplatinic acid (Alfa Aesar), and nickel chloride (Baker & Adamson). The following materials were used as received from the supplier: platinum gauze (Alfa Aesar, 52 mesh woven from 0.1 mm wire, 99.9% metals basis), nickel gauze (Alfa Aesar, 100 mesh woven from 0.1 mm wire, 99.9% metals basis), and nickel foam (Goodfellow Cambridge Limited, 95% porosity, 95% purity).

Triply distilled H_2O was used to prepare all aqueous solutions and was itself prepared by distilling a mixture of alkaline $KMnO_4$ and doubly distilled water. Analytical grade reagents were used to prepare all electrolyte solutions. Electrolytes were purged with N_2 before use, and all voltammetric and chronoamperometric experiments were carried out under N_2 unless otherwise specified. All glassware was rinsed with *Piranha* solution (5:1 by volume concentrated H_2SO_4 and 30% H_2O_2) followed by thorough rinsing with triply distilled water, and drying in an oven at 80°C.

Electrochemical experiments were performed on either an EG&G Princeton Applied Research Potentiostat/Galvanostat Model 273 using the corresponding M270 software or a Solartron SI 1287 Electrochemical Interface controlled by CorrWare for Windows Version 2-3d software and using a conventional three-electrode cell configuration. During electrochemical depositions, the potential of the platinum counter electrode was recorded using a Radio Shack multimeter and Scope View version 1.08 software.

Scanning electron microscopy (SEM) was performed on a Zeiss EVO MA 15 scanning electron microscope equipped with a Bruker silicon drift detector for energy dispersive X-ray spectroscopy. A Kratos Analytical Axis X-ray imaging photoelectron spectrometer was used to perform X-ray photoelectron spectroscopy (XPS). Both techniques were executed on freshly prepared samples rinsed with triply distilled H_2O and C_2H_5OH, and then dried overnight in a desiccator under vacuum. XPS data was fit using CASA XPS Software File version 1.0.0.1 and the spectra were calibrated to adventitious carbon at 284.8 eV. The binding energies of the peaks were calculated from the background-subtracted spectra using an applied Shirley background. The intensity ratios of the Pt $4f_{7/2}$ and $4f_{5/2}$ peaks were set to the theoretical value of 4:3 and spin-orbit coupling was 3.3 eV. Similarly, the Ni $3p_{3/2}$ and $3p_{1/2}$ peaks were set to have intensity ratios of 2:1 and separation of 1.9 eV [50]. The Pt peaks were assigned 10% asymmetry to account for the experimental line shape, while all other peaks were fitted with 30% Gaussian-Lorentzian curves.

Inductively coupled plasma mass spectrometry was performed on an Elan 6000 spectroscope from Perkin Elmer. Samples were prepared by dissolving in *aqua regia*, evaporating to dryness on a hot plate and making up the residue quantitatively in 0.3 M HNO_3.

2.4.2 Preparation of platinum black counter electrodes

The platinum black electrode used as a source of platinum in the platinum counter electrode deposition (see below) consisted of a 2.5 cm x 2.5 cm platinum gauze blacked with 0.02 M K_2PtCl_6/1 M $HClO_4$ or 0.04 M H_2PtCl_6/1 M HCl. No difference in results was observed with the different plating solutions. A typical blackening experiment would be performed at -0.1 $V_{Ag/AgCl\ (4M\ KCl)}$ until the observed current decayed to ~ 0 mA. The real surface area of the platinum black electrode was determined from the hydrogen under potential deposition (H_{UPD}) peak of a stabilized cyclic voltammogram recorded in 0.5 M H_2SO_4 assuming the charge associated with a monolayer of hydrides on polycrystalline Pt is 210 μC cm^{-2} [54] with 77% efficiency. Typical estimations were more than 25,000 cm^2.

The platinum black electrode used as a counter electrode in voltammetry, or as a working electrode for the electro-oxidation of 2-propanol, was prepared in the manner described above.

2.4.3 Preparation of working electrodes

The substrate used for deposition was either a 1 cm x 1 cm nickel gauze or a 1 cm x 1 cm nickel foam with a 3 mm x 3 mm tab for affixing to a graphite rod handle with Teflon tape. The substrates were cleaned with 1% H_2O_2 and triply distilled H_2O before being used as working electrodes.

2.4.4 Platinum counter electrode deposition

The electrolyte comprised 30 mL of 2.0 M NH_4Cl prepared in a glass cylinder of dimensions 10 cm x 2.5 cm inner diameter. The cylinder was then lowered into a sonic bath (Cole-Parmer Model 8890) up to the level of the electrolyte. A current

of -0.1 A was applied between the Ni (gauze or foam) working electrode and the Pt black counter electrode in the presence of a Ag/AgCl (4M KCl) reference electrode for 1 hour with sonication to afford Pt deposits on the working electrodes. These materials are denoted $Pt_{CE}Ni_{gauze}$ in the case of deposition onto the gauze substrate, and $Pt_{CE}Ni_{foam}$ where the foam substrate was utilized.

Alternatively, the deposition electrolyte comprised 30 mL of 2.0 M NH_4Cl/0.2 M $NiCl_2$ (Baker & Adamson) to afford Ni-Pt co-deposits. These deposits are referred to as Ni-$Pt_{CE}Ni_{gauze}$ in the case of co-deposition onto the gauze substrate, and Ni-$Pt_{CE}Ni_{foam}$ where the foam substrate was utilized.

2.4.5 Electrochemical methods

Cyclic voltammetry and chronoamperometry were performed in 0.5 M NaOH at 22°C, or 0.5 M NaOH/1.0 M $(CH_3)_2CH(OH)$ at 60°C, in which case the cell was equipped with a dry ice/acetone condenser to minimize evaporation of the 2-propanol. The Pt black counter electrode was isolated in a glass tube with a 10 μm porous glass frit. A static reversible hydrogen electrode (RHE) was used as a reference point and all potentials are versus this reference unless otherwise stated (denoted V_{RHE}). The working electrode was rinsed with triply distilled water and then conditioned for 5 minutes at -0.4 V_{RHE} prior to collecting each voltammogram or chronoamperometric measurement.

Stabilized cyclic voltammograms were recorded between -0.1 and 0.425 V_{RHE} at 10 mV s^{-1}. Chronoamperometry was performed by stepping to the desired potential for 15 minutes. Sampled current voltammograms were constructed by calculating the average current in the last 5 seconds of the chronoamperometric step and plotting against the relevant potential.

Carbon monoxide adsorption and stripping experiments were performed by bubbling CO vigorously over the working electrode in 0.5 M NaOH electrolyte while holding the potential at -0.4 V_{RHE} for 30 minutes. The solution was then purged with nitrogen at 0.05 V_{RHE} for 5 minutes, followed by immediate cycling under nitrogen between -0.1 and 1.1 V_{RHE} for 7 complete cycles at 10 mV s^{-1} and 22°C.

2.5 Bibliography

[1] L.N. Menard, S.H. Bergens, J. Power Sources, 194 (2009) 298-302.

[2] J.M. Skowroński, A. Wazny, Solid State Electr., 9 (2005) 890-899.

[3] D. Cao, D. Chen, J. Lan, G. Wang, J. Power Sources, 190 (2009) 346-350.

[4] W. Yang, S. Yang, W. Sun, G. Sun, Q. Xin, Electrochim. Acta, 52 (2006) 9-14.

[5] M.E.P. Markiewicz, S.H. Bergens, J. Power Sources, 185 (2008) 222-225.

[6] M. Watanabe, S. Motoo, J. Electroanal. Chem., 60 (1975) 267-273.

[7] M.T.M. Koper, Surf. Sci., 548 (2004) 1-3.

[8] C.S. Chen, F.M. Pan, H.J. Yu, App. Cat. B-Environ., 104 (2011) 382-389.

[9] K.W. Park, J.H. Choi, B.K. Kwon, S.A. Lee, Y.E. Sung, H.Y. Ha, S.A. Hong, H. Kim, A. Wieckowski, J. Phys. Chem. B., 106 (2002) 1869-1877.

[10] K.W. Park, J.H. Choi, Y.E. Sung, J. Phys. Chem. B., 107 (2003) 5851-5856.

[11] J.C. Davies, B.E. Hayden, D.J. Pegg, M.E. Rendall, Surf. Sci., 496 (2002) 110-120.

[12] G. Samjeské, X.Y. Xiao, H. Baltruschat, Langmuir, 18 (2002) 4659-4666.

[13] B. Hammer, J.K. Nørskov, Surf. Sci., 343 (1995) 211-220.

[14] B. Hammer, J.K. Nørskov, Advances in Catalysis, 45 (2000) 71-129.

[15] T.L. James, J. Chem. Educ., 48 (1971) 712-718.

[16] M. Weinert, R.E. Watson, Physical Review B, 51 (1995) 17168-17180.

[17] W.F. Egelhoff Jr., Surface Science Reports, 6 (1987) 253-415.

[18] Y. Hu, P. Wu, Y. Yin, H. Zhang, C. Cai, App. Cat. B-Environ., 111–112 (2012) 208-217.

[19] X. Fu, Y. Liang, S. Chen, J. Lin, D. Liao, Catalysis Communications, 10 (2009) 1893-1897.

[20] T. Jeon, S.J. Yoo, Y. Cho, K. Lee, S.H. Kang, Y. Sung, J. Phys. Chem. C, 113 (2009) 19732-19739.

[21] D.B. Kim, H.J. Chun, Y.K. Lee, H.H. Kwon, H.I. Lee, Int. J. Hydrogen Energy, 35 (2010) 313-320.

[22] Y. Zhao, Y. E, L. Fan, Y. Qiu, S. Yang, Electrochim. Acta, 52 (2007) 5873-5878.

[23] A.L. Allred, E.G. Rochow, Journal of Inorganic and Nuclear Chemistry, 5 (1958) 264-268.

[24] T. Toda, H. Igarashi, M. Watanabe, J. Electrochem. Soc., 145 (1998) 4185-4188.

[25] T. Toda, H. Igarashi, H. Uchida, M. Watanabe, J. Electrochem. Soc., 146 (1999) 3750-3756.

[26] S. Mukerjee, S. Srinivasan, M.P. Soriaga, J. Electrochem. Soc., 142 (1995) 1409-1422.

[27] L.G. Wang, A. Zunger, Physical Review B - Condensed Matter and Materials Physics, 67 (2003) 921031-921034.

[28] N.J. Shevchik, D. Bloch, Journal of Physics F: Metal Physics, 7 (1977) 543-550.

[29] J.R. Kitchin, J.K. Nørskov, M.A. Barteau, J.G. Chen, J. Chem. Phys., 120 (2004) 10240-10246.

[30] J.R. Kitchin, J.K. Nørskov, M.A. Barteau, J.G. Chen, Phys. Rev. Lett., 93 (2004) 156801-1-156801-4.

[31] A. Ruban, B. Hammer, P. Stoltze, H.L. Skriver, J.K. Nørskov, J. Mol. Cat. A-Chem., 115 (1997) 421-429.

[32] V.R. Stamenkovic, B. Fowler, B.S. Mun, G. Wang, P.N. Ross, C.A. Lucas, N.M. Markovic, Science, 315 (2007) 493-497.

[33] S. Papadimitriou, S. Armyanov, E. Valova, A. Hubin, O. Steenhaut, E. Pavlidou, G. Kokkinidis, S. Sotiropoulos, J. Phys. Chem. C, 114 (2010) 5217-5223.

[34] M. Mavrikakis, B. Hammer, J.K. Nørskov, Phys. Rev. Lett., 81 (1998) 2819-2822.

[35] M. Gsell, P. Jakob, D. Menzel, Science, 280 (1998) 717-720.

[36] P. Strasser, S. Koh, J. Anniyev, J. Greeley, K. More, C. Yu, Z. Liu, S. Kaya, D. Nordlund, H. Ogasawara, M.F. Toney, A. Nilsson, Nat. Chem., 2 (2010) 454-460.

[37] J.X. Wang, H. Inada, L. Wu, Y. Zhu, Y. Choi, P. Liu, W.-. Zhou, R.R. Adzic, J. Am. Chem. Soc., 131 (2009) 17298-17302.

[38] H.A. Gasteiger, N. Markovic, P.N. Ross Jr., E.J. Cairns, J. Electrochem. Soc., 141 (1994) 1795-1803.

[39] H. Yang, C. Coutanceau, J. Léger, N. Alonso-Vante, C. Lamy, J. Electroanal. Chem., 576 (2005) 305-313.

[40] A.J. Bard, L.R. Faulkner, Double-Layer Structure and Adsorption, Electrochemical Methods Fundamentals and Applications, 2nd ed., 2001, pp. 534-579.

[41] J.M. Doña Rodríguez, J.A.H. Melián, J.P. Peña, J. Chem. Educ., 77 (2000) 1195-1197.

[42] B. Beden, D. Floner, J.M. Léger, C. Lamy, Surf. Sci., 162 (1985) 822-829.

[43] M.A. Abdel Rahim, H.B. Hassan, R.M. Abdel Hameed, Fuel Cells, 7 (2007) 298-305.

[44] E.J. Nowak, R.M. Koros, J. Catal., 7 (1967) 50-56.

[45] N.V. Parizotto, D. Zanchet, K.O. Rocha, C.M.P. Marques, J.M.C. Bueno, Appl. Catal. A-Gen., 366 (2009) 122-129.

[46] C.C. Hu, K.Y. Liu, Electrochim. Acta, 44 (1999) 2727-2738.

[47] T.J. Schmidt, H.A. Gasteiger, G.D. Stäb, P.M. Urban, D.M. Kolb, R.J. Behm, J. Electrochem. Soc., 145 (1998) 2354-2358.

[48] A.J. Bard, L.R. Faulkner, Bulk Electrolysis Methods, Electrochemical Methods Fundamentals and Applications, 2nd ed., 2001, pp. 417-464.

[49] P.C. Hayes, Sources of Data on Chemical Physical Systems, Process principles in minerals and materials production, 3rd ed., Hayes Publishing Co., Queensland, Australia, 1993, pp. 637-671.

[50] C.D. Wagner, A.V. Naumkin, A. Kraut-Vass, J.W. Allison, C.J. Powell, J.R. Rumble Jr., NIST X-ray Photoelectron Spectroscopy Database, Version 3.5 (Web Version). 2003; Available at: srdata.nist.gov/xps. Accessed March 1st, 2012.

[51] D. Dobler, S. Oswald, K. Wetzig, Analytical and Bioanalytical Chemistry, 374 (2002) 646-649.

[52] G. García, M.T.M. Koper, Phys. Chem. Chem. Phys., 10 (2008) 3802-3811.

[53] D.F. Van Der Vliet, M.T.M. Koper, Surf. Sci., 604 (2010) 1912-1918.

[54] B.E. Conway, H. Angerstein-Kozlowska, Acc. Chem. Res., 14 (1981) 49-56.

[55] N.J. Shevchik, Phys. Rev. Lett., 33 (1974) 1336-1339.

Chapter 3: Structural and activity comparison of self-limiting versus traditional Pt electro-deposits on glancing angle deposited nanopillar Ni films[1]

3.1 Introduction

The gains from using porous commercial Ni foam as a substrate for *Pt CE deposition* inspired us to collaborate with researchers that could construct high surface area, porous Ni substrates with well-controlled surface morphology. Naturally, we teamed up with the Brett Research group of the Department of Electrical and Computer Engineering at this University. The Brett group specializes in the fabrication of nanostructured films using a PVD technique known as Glancing Angle Deposition (GLAD). In this chapter, we report the comparison of the *Pt CE deposition* and a more conventional Pt deposition on GLAD nanopillar Ni films.

Comprehensive reviews of the GLAD technique have been reported previously [1,2]. Briefly, GLAD is performed *in vacuo*, and is achieved by the precise motion of the substrate relative to the incoming vapour flux. A schematic of a typical GLAD apparatus in a PVD system can be found in Figure 1.6 of Ref. [2], while Figure 3-1 shows the relevant angles defined in the GLAD process. The oblique deposition angle, α, is the angle between the incident vapour flux and substrate normal, and the angle of rotation about the substrate normal is denoted as φ.

[1] *A version of this chapter has been published. S.A. Francis, R.T. Tucker, M.J. Brett, J. S.H. Bergens, J. Power Sources 222 (2013) 533-541.*

During GLAD, the obliquely incident atoms are only capable of nucleating onto the highest points of the substrate surface due to a self-shadowing effect. With increasing flux deposition, this self-shadowing effect extends to pillar-shaped growth where the average width of the pillar increases with its height (see Figure 3-1). It follows that porosity and nanopillar spacing can be controlled by changing the deposition angle α. Modulation of substrate rotation in φ adds further morphology control and access to various structures (e.g. vertical columns, slanted posts, chevrons, square spirals, helices, and combinations thereof). Therefore, the GLAD technique has been used for advanced nanostructuring in a variety of applications that require strict control of component shape and dimension. These components include nanoengineered optical thin films [3-5], ordered small molecule organic photovoltaic bulk heterojunctions [6,7]; columnar microbattery electrodes [8]; and anisotropic ultrathin-layer chromatography plates [9].

Figure 3-1 *(a) Schematic of the oblique deposition angle, α, and rotation angle about the substrate normal, φ, as defined in the GLAD process. Dashed lines emphasize the self-shadowing effect of the growing pillars. (b) Self-shadowing effect resulting in pillar-shaped growth where average width increases with pillar height.*

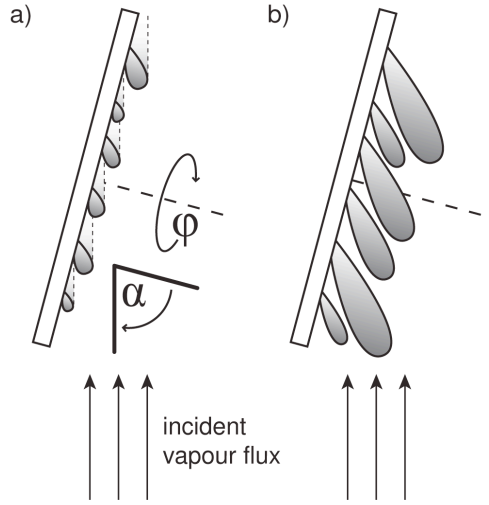

GLAD-based nanostructures have also been studied as electro-catalysts in fuel cells and related systems. For example, Khudhayer *et al.* reported GLAD-fabricated nanostructures as catalysts for the ORR [10]. Their nanorod arrays of Pt on glassy carbon substrates have higher area-specific activity towards the ORR, as well as higher stability towards potential cycling in acid than conventional Pt/C catalysts. In fact, the reported specific activity was similar to bulk polycrystalline Pt. This high area-specific activity was attributed to the large crystallite size and to the results of a crystallographic analysis, which concluded that the nanorod sidewalls were dominated by Pt (110) planes. The mass-specific activity of the GLAD Pt deposits was lower than that of Pt/C. The same group also recently reported a small angle deposition (SAD) of Pt (α = 45°) onto GLAD Cr nanorod arrays for ORR [11].

The Gall group reported the deposition of GLAD Pt onto carbon-based GDL substrates (Sigracet 35DC) and evaluated their performance in fuel cells [12]. They demonstrated that the porosity control provided by the GLAD process

allowed improvements to mass transport. As a result, electrodes made form GLAD Pt deposits had higher mass-specific activities than electrodes made from conventional Pt black at high current densities. Cathodes comprising Pt-coated GLAD CrN deposited on similar GDLs (Sigracet 35BC) have also been studied by this group [13]. Finally, the Gall research group has described Pt-coated GLAD carbon film supported on flat or patterned Si substrates. After fabrication, the film was bonded to a Nafion® membrane at 126°C and 350 psi (2.4 MPa) and the Si substrate simply peeled off and discarded [14,15]. Both studies showed that the pore structure of the cathode catalysts have a positive effect on mass transport of oxygen to the catalytic sites.

Recently, the Wilkinson group, in collaboration with researchers in the Brett lab, has described Pt deposited on GLAD nanopillar niobium oxides as ORR catalysts [16]. The Nb-O supports were found to withstand aggressive electrochemical degradation protocols and temperatures up to 1000°C without degrading their high surface area morphology.

The Dahn group has sputtered Pt onto high-surface area GLAD columnar Ti to prepare oxygen reduction electro-catalysts with a 10 to 15 times increase in electro-active surface area (ESA) compared to smooth Pt [17]. Although there were no reports of Pt-Ni electro-catalysts prepared by GLAD, the same Dahn group has reported related systems comprised of Pt and Ni co-deposits prepared by sputter deposition onto a nanostructured thin film (NSTF) fabricated by 3M [18-22]. The NSTF comprises high surface area, closely-packed crystalline 500 to 1000 nm long whiskers of vacuum annealed N,N-di(3,5-xylyl)perylene-3,4:9,10-bis(dicarboximide) (also known as Pigment red 149 and drawn in Figure 3-2). It has been shown for related Pt-based deposits that the equilibrium shape and faceting of such deposits are whiskerettes on the sides of the whiskers,

comprising polycrystalline layers with highly oriented crystallites with the (111) face predominantly exposed [23].

Figure 3-2 *Chemical structure of the NSTF precursor Pigment red 149.*

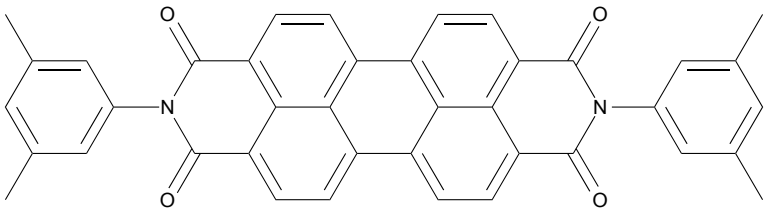

Pigment red 149
N,N-di(3,5-xylyl)perylene-3,4:9,10-bis(dicarboximide)

The ORR activity of a range of $Pt_{1-x}Ni_x$ ($0 \leq x \leq 1$) alloy deposits on NSTF was studied with rotating disk voltammetry in perchloric acid electrolytes and in a membrane electrode assembly (MEA). The predominant features of these systems are that Ni dealloys by dissolution during the ORR in acid, the dissolution initially increases the ORR activity of these catalysts to quite high levels by increasing the number of exposed Pt sites and by increasing the intrinsic activity of the exposed Pt, and systems with $x = 0.69 \pm 0.02$ have an extraordinarily sharp activity maximum upon dealloying of Ni. The dissolution of Ni into the membrane electrolyte, however, impedes the activity of H_2/air fuel cells operating with these cathode catalysts.

Our GLAD Ni substrate consists of 500 nm GLAD Ni nanopillars (Ni_{NP}) deposited onto a planar Ni film. We electrochemically deposited low-mass loadings of Pt onto the Ni_{NP} working electrode via the *Pt CE deposition* to give $Pt_{CE}Ni_{NP}$, and a more traditional Pt deposition [24] from K_2PtCl_6 in aqueous $HClO_4$, to prepare a deposit we denote as $Pt_{Tr}Ni_{NP}$. The pristine Ni_{NP} substrates, and $Pt_{CE}Ni_{NP}$ and $Pt_{Tr}Ni_{NP}$ catalysts were all characterised by SEM, powder XRD,

XPS, ICP-MS and voltammetric methods. The potential of all materials were kept below ~0.5 V_{RHE}, and the electrochemical studies were carried out in base in order to minimize dissolution of Ni and to obtain information about the surface as made by the deposition. Finally, the catalytic activities towards 2-propanol electro-oxidation are measured and compared to $Pt_{CE}Ni_{foam}$ (see Chapter 2), a shiny Pt foil (Pt_{foil}), and two commercial noble metal nanoparticle catalysts, Pt-Ru and Pt. This is the first reported study of GLAD-based Pt-Ni catalysts, and alcohol oxidation over GLAD-based electro-catalysts.

3.2 Results and discussion

3.2.1 Comparison of the depositions of $Pt_{CE}Ni_{NP}$ and $Pt_{Tr}Ni_{NP}$

Figures 3-3 and 3-4 show the voltage and current responses recorded during representative depositions of $Pt_{CE}Ni_{NP}$ and $Pt_{Tr}Ni_{NP}$, respectively. The main differences in the conditions of these depositions are outlined in Table 3-1. Compared to our previous reports [25,26], the *Pt CE deposition* behaved as expected, that is, H_2 evolution was observed with a rise in the potential of the WE, though the rise in E_{WE} was not as dramatic as that seen for the gauze and foam substrates. As explained in Section 1.4.1, this behaviour occurs because the overpotential for H_2 evolution over Ni is high under these conditions, but not over Pt, causing the potential of the electrode and the amount of H_2 evolution to increase as Pt is deposited on the Ni surface. The E_{WE} observed therefore represents a mixed-potential condition at the Ni and newly deposited Pt surfaces. The counter electrode potential was steady at ~1.1 $V_{Ag/AgCl\ (4M\ KCl)}$ for the duration of the experiment. The amount of Pt dissolved into solution is limited by self-passivation of the counter electrode under these conditions [27]. The traditional deposition also occurred as expected [24]. The pale yellow colour of the solution faded and the current remained constant at ~ -1 mA for the duration of the experiment.

Table 3-1 *Comparison of the conditions of the Pt CE deposition and traditional Pt depositions.*

	Pt CE deposition	*Traditional Pt deposition*
Type of deposition	Galvanostatic -100 mA cm^{-2}	Potentiostatic -100 $mV_{Ag/AgCl\ (4M\ KCl)}$
Electrolyte	2 M NH_4Cl bulk pH ~5	0.01 M $HClO_4$ bulk pH ~2
Source of Pt	Dissolution of blacked Pt gauze counter electrode	Added to solution as K_2PtCl_6
Conditions at working electrode	Reducing conditions ~-1.2 $V_{Ag/AgCl\ (4M\ KCl)}$	Less reducing conditions – 0.1 $V_{Ag/AgCl\ (4M\ KCl)}$

Figure 3-3 *Potential profile of the electrodes during the* Pt CE deposition *of* $Pt_{CE}Ni_{NP}$ *at -100 mA for 1 hour in 2.0 M* NH_4Cl*.*

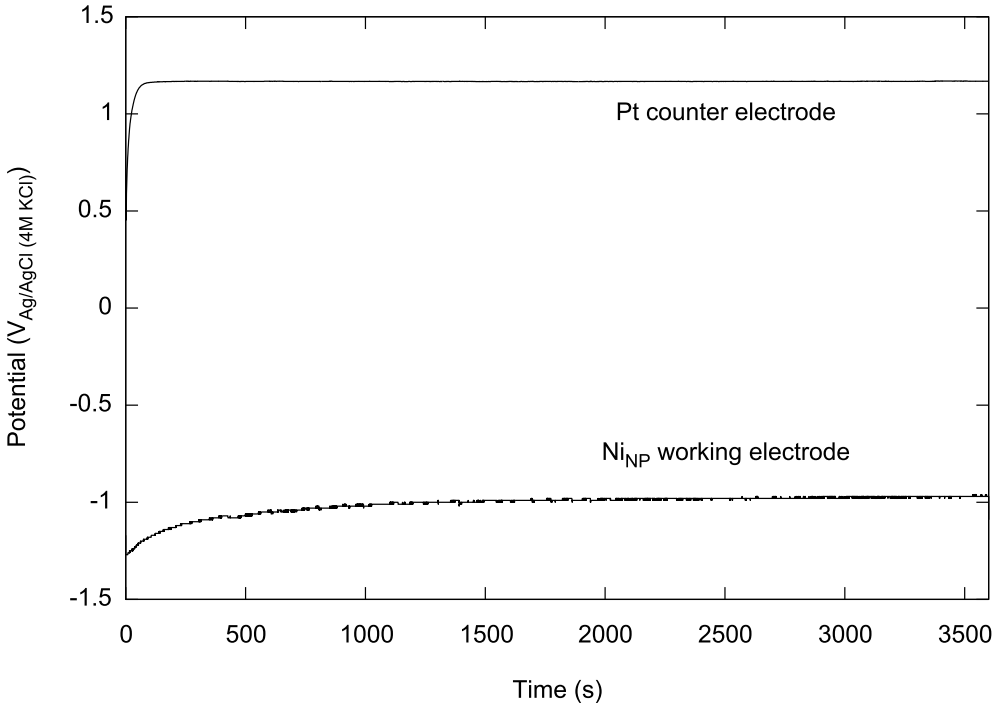

Figure 3-4 *Current profile of the traditional potentiostatic deposition of $Pt_{Tr}Ni_{NP}$ at -100 $mV_{Ag/AgCl\ (4M\ KCl)}$ in 1.2 x 10^{-4} M K_2PtCl_6/0.01 M $HClO_4$.*

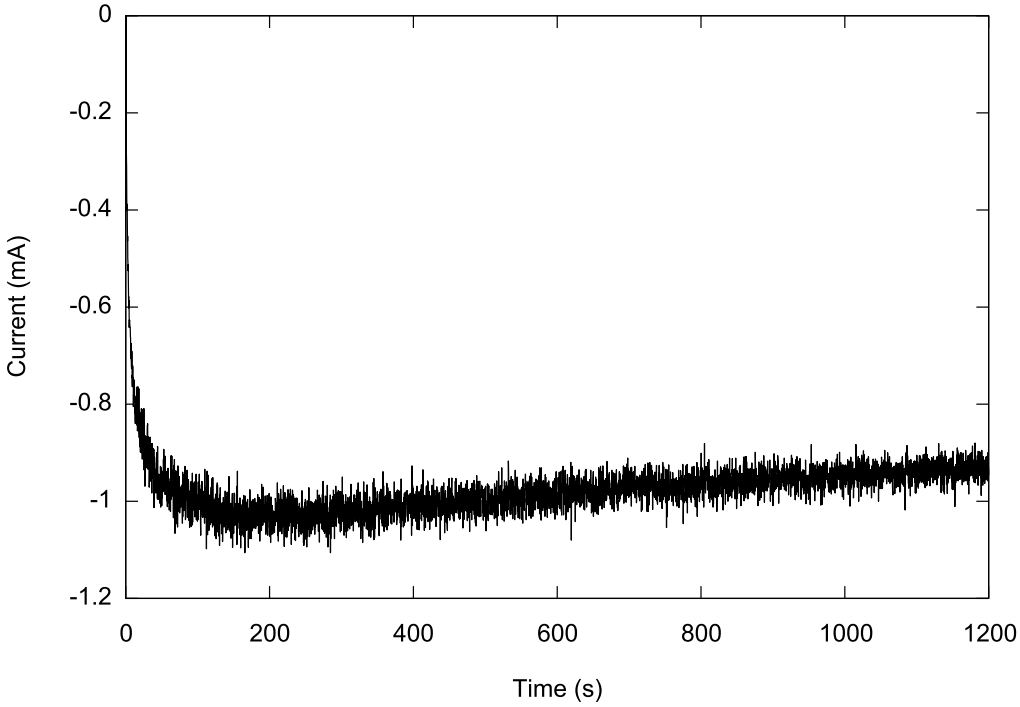

3.2.2 Microscopic and crystallographic comparison of Ni_{NP}, $Pt_{CE}Ni_{NP}$ and $Pt_{Tr}Ni_{NP}$

Figure 3-5 shows SEM images of the Ni_{NP}, $Pt_{CE}Ni_{NP}$ and $Pt_{Tr}Ni_{NP}$ catalysts. The Ni_{NP} (3-5a and 3-5d) are aligned normal to the substrate with diameters that increase with pillar height. The average pillar diameter is roughly 200 nm at the maximum height of 500 nm. The approximate number density is 15 μm^{-2}. These dimensions correspond to a roughness factor of ~ 5 in the approximation of smooth cylindrical pillars. The SEM images also show that the Ni_{NP} comprises smaller, vertically oriented and elongated pillar shaped grains. The tops of the pillars appear segmented into the tops of the grains, that is the pillars do not have perfectly smooth surfaces. Therefore, the approximate roughness factor is likely underestimated.

Figure 3-5 *Scanning electron micrographs showing cross-sectional views of (a) Ni_{NP}, (b) $Pt_{CE}Ni_{NP}$ and (c) $Pt_{Tr}Ni_{NP}$, and plan view of the same (d), (e) and (f) respectively. All scale bars represent 200 nm.*

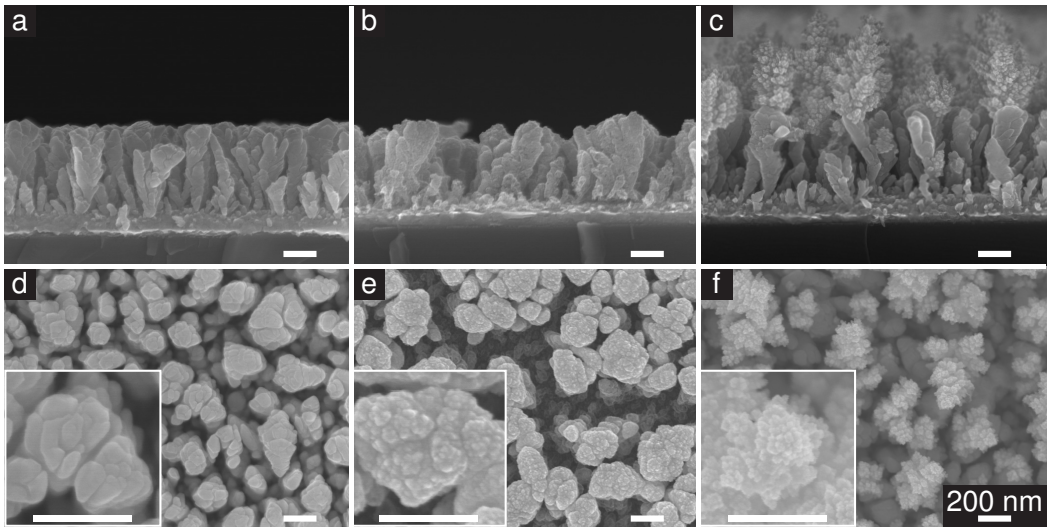

Figure 3-5b and e show the side and plan view of the Ni_{NP} after the *Pt CE deposition*. The Ni_{NP} are largely intact, and the underlying structure is visible under the Pt deposit. The Ni_{NP} do show slight wilting together in the plan view (Figure 3-5e), as is typical of GLAD films after solution processing and drying [28]. The tops and sides of the nanopillars were roughened by the *Pt CE deposition*, showing that Pt was deposited over the entire nanopillar surface. This result is consistent with the self-limiting nature of the *Pt CE deposition* we observed previously for Ni gauze and foam substrates [25,26]. We believe that the combination of the aforementioned mixed potential Pt-Ni surface, and the facile evolution of H_2 over Pt, results in a preferential deposition of Pt onto Ni until a thin layer of Pt forms on the Ni_{NP} surface.

In stark contrast, there is a distinct region of Pt growth by the traditional deposition (Figure 3-5c and f). In this case, Pt nucleation and growth occurs predominantly on top of each Ni nanopillar, as a ~ 500 nm rough, Pt extension that resembles lilac flowers. The traditional Pt deposition appears to be mass-

transport limited, that is, nucleation occurs as Pt arrives at the most exposed (top) surface of the pillars. Subsequently, the majority of growth processes occurs at the Pt deposits on the top of the pillars.

Figure 3-6 shows the X-ray diffractograms obtained from the Ni_{NP}, $Pt_{CE}Ni_{NP}$, and $Pt_{Tr}Ni_{NP}$ materials. The XRD data shows that the diffracting portion of the Ni_{NP} consists of polycrystalline Ni in the *fcc* phase. The *hcp* phase was not detected. The Scherrer Ni grain diameter (calculated from the Ni (111) peaks of 13 samples) was 35 ± 8 nm. This dimension roughly corresponds to those of the smaller, vertically oriented, and elongated column-shaped grains observed in the SEM images of the Ni_{NP} (Figure 3-5). The relative intensities of the Ni (200), (220), and (311) peaks in all three samples are less intense than those in bulk, polycrystalline Ni. Expressed differently, the relative intensities of the Ni (111) and (222) peaks are higher than those in bulk, polycrystalline Ni. These relative intensities suggest that the {111} family of planes are preferentially oriented in the GLAD Ni_{NP} samples, regardless of whether Pt has been deposited. No alloying is detectable between the Ni and Pt, as the position of the Ni peaks in Ni_{NP} is superimposable onto both of the Pt-containing samples.

Figure 3-6 *X-ray diffractograms of Ni_{NP}, $Pt_{CE}Ni_{NP}$ and $Pt_{Tr}Ni_{NP}$. Ni peaks are denoted by "x" and Pt peaks are denoted by "o".*

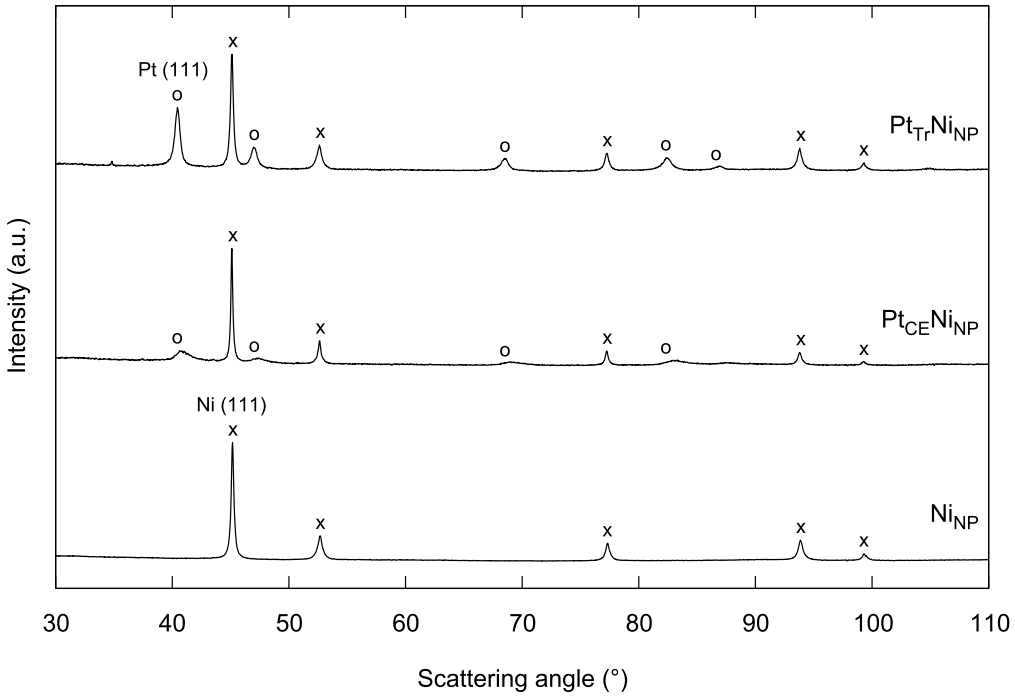

The diffractograms for both $Pt_{CE}Ni_{NP}$ and $Pt_{Tr}Ni_{NP}$ display peaks for Pt in the *fcc* phase. For the $Pt_{Tr}Ni_{NP}$ sample, the relative intensities of the Pt (200), (220) and (311) peaks are slightly less than those in bulk, polycrystalline Pt, but the (222) peak is more intense than expected. These relative intensities suggest that Pt growth proceeds with a preferential orientation of the {111} family of planes.

The relative Pt:Ni peak intensities for the $Pt_{Tr}Ni_{NP}$ sample is much higher than for the $Pt_{CE}Ni_{NP}$ sample, and the full width at half maximum is perhaps narrower, showing that the traditional deposition forms larger amounts of polycrystalline Pt than the *Pt CE deposition*. This is consistent with the results of the SEM studies (Figure 3-5) showing the conformal nature of the *Pt CE deposition*. The Scherrer Pt grain diameter (calculated from the Pt (111) peak) for the $Pt_{CE}Ni_{NP}$ samples was on average 9 ± 2 nm (3 samples), whereas for

$Pt_{Tr}Ni_{NP}$, the typical diameters were 10 ± 4 nm (5 samples). These relatively small Pt grain sizes were promising as the first aim of this study was to create deposits with relatively large surface areas.

3.2.3 Cyclic voltammetry

Figures 3-7 and 3-8 show the stabilized cyclic voltammograms (CVs) for the Ni_{NP}, $Pt_{CE}Ni_{NP}$, and $Pt_{Tr}Ni_{NP}$ materials in 1 M KOH at room temperature. The CVs in Figure 3-7 were recorded with lower (-0.1 V_{RHE}) and upper (0.4 V_{RHE}) potential limits that are typically employed for Ni in base [25,26], while the lower potential limit was increased in Figure 3-8 to minimize the effects of H_2 evolution. In both cases the CVs are normalized to the geometric area of the nanopillar film, that is, 1 cm^2.

The CV of Ni_{NP} in Figure 3-7 shows that it is substantially more active towards H_2 evolution than Ni_{black} (compare Figure 2-6). Although the origins of this difference are unknown, it is a reproducible phenomenon that likely arises from structural features, such as the high porosity, of the GLAD Ni_{NP}. On the other hand, the CVs of $Pt_{CE}Ni_{NP}$ and the $Pt_{Tr}Ni_{NP}$ are similar in shape to $Pt_{CE}Ni_{foam}$ at the same potential range (Figure 2-8). It is also apparent that both the $PtNi_{NP}$ deposits are more efficient at H_2 production than Ni_{NP} alone, with significant currents for H_2 production and hydride oxidation in the cathodic and anodic scans between -100 and 50 mV_{RHE} over $Pt_{CE}Ni_{NP}$ and $Pt_{Tr}Ni_{NP}$.

Figure 3-7 *Cyclic voltammograms of Ni_{NP}, $Pt_{CE}Ni_{NP}$ and $Pt_{Tr}Ni_{NP}$ in 1M KOH at 25°C with a scan rate of 10 mVs^{-1} at wide potential limits.*

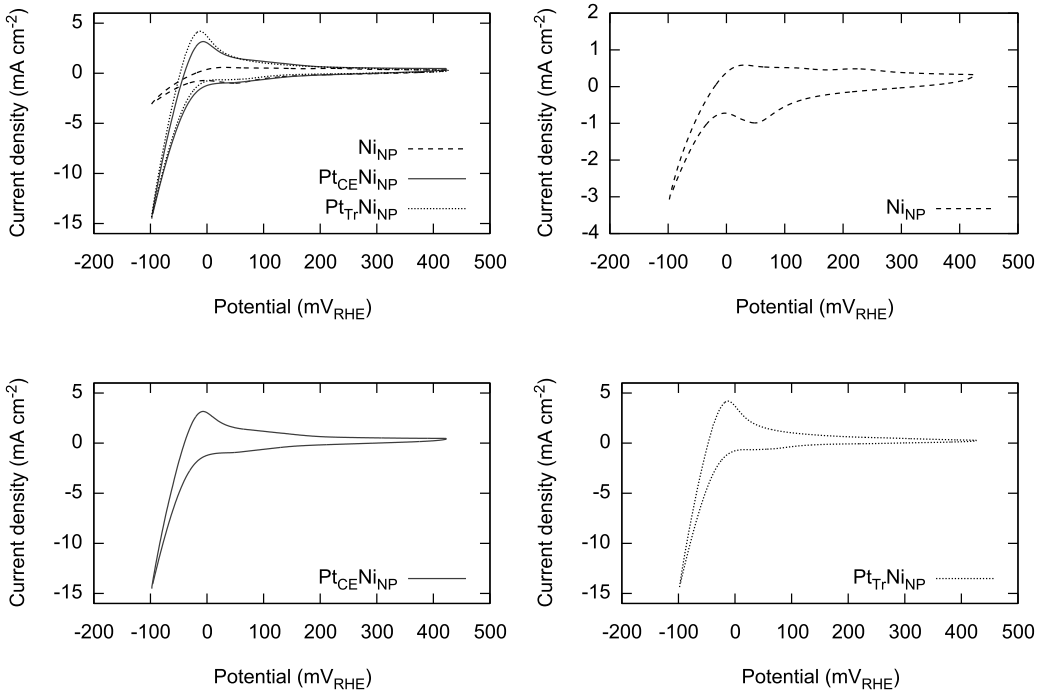

Figure 3-8 shows the resulting CVs in the narrow potential range (-0.05 to 450 mV_{RHE}). The Ni and/or NiO and/or α-$Ni(OH)_2$ reduction peak appears to be present in the cathodic scan of the Ni_{NP} CV at E_{peak} ~ 60 mV_{RHE}, but the corresponding anodic peak at ~220 mV_{RHE} is broad and not well defined, especially compared to Ni_{black} (Figure 2-6). It has been suggested that appearance of the anodic peak is connected to pre-polarization of the electrode [29,30]. For example, Seghioer *et al.* explain that a nickel hydroxide layer is hardly formed unless the surface is polarized at potentials below 0.53 V_{RHE}, the thickness of the layer (quantified by peak current) increasing with duration of the pre-treatment and with decreasing potential. We pre-polarized neither the Ni_{black} nor the Ni_{NP} electrode before performing voltammetry. However, all the cyclic voltammograms were performed below 0.53 V_{RHE} and otherwise they experienced the same treatment. Furthermore, the CV of Ni_{NP} in Figure 3-7 is

recorded at even lower initial potentials, yet the anodic peak is still suppressed. Therefore, the origins of these differences are likely structure dependent. Perhaps the Ni_{NP} are less prone to oxidation or surface passivation than Ni_{black}. This would be a desirable feature to avoid corrosion under working conditions, but not necessarily to promote bi-functional mechanisms during catalysis.

The anodic charge of the α-$Ni(OH)_2$ peak is proposed to be an estimate of the surface area of Ni electrodes where Q = 514 μC cm^{-2} [31], although previous work using destructive CO stripping experiments show that this number likely underestimates the surface area by a factor of ~ 2.6 [25]. The charge under the α-$Ni(OH)_2$ anodic peak in the CV of Ni_{NP} corresponds to a surface area of 20.5 cm^2 cm^{-2}. We consider this value to be only a tentative, lower limit to the real surface area of the Ni_{NP}.

Figure 3-8 *Cyclic voltammograms of Ni_{NP}, $Pt_{CE}Ni_{NP}$ and $Pt_{Tr}Ni_{NP}$ in 1M KOH at 25°C with a scan rate of 10 mVs^{-1} at narrow potential limits.*

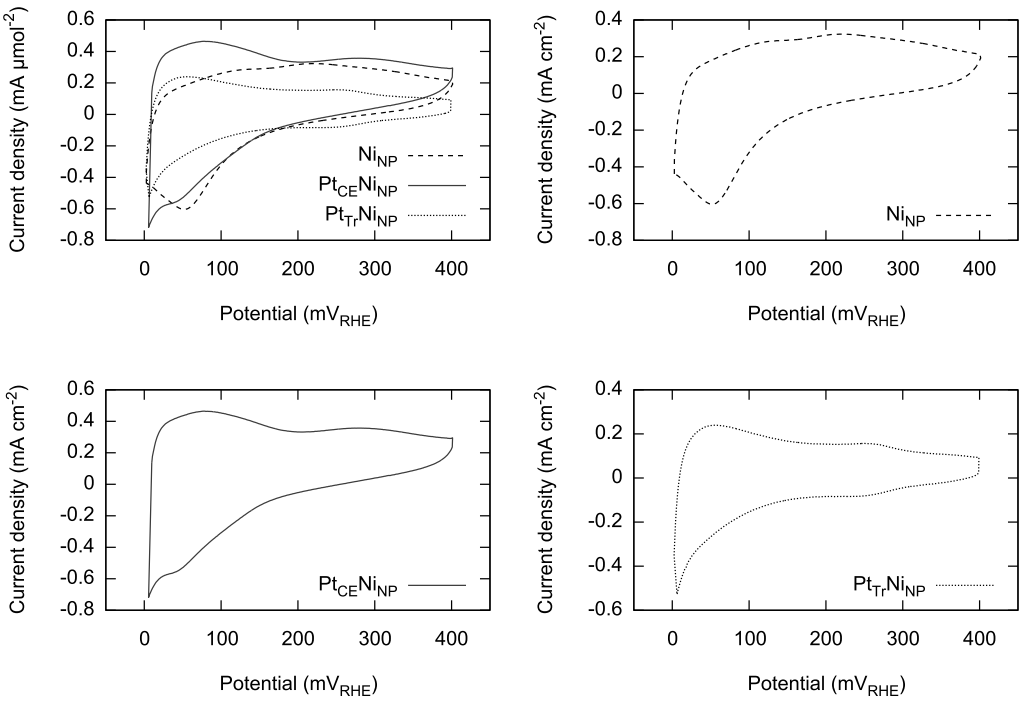

The CVs of $Pt_{CE}Ni_{NP}$, and $Pt_{Tr}Ni_{NP}$ in Figure 3-8 contain features that are associated with those of Pt_{black} (compare Figure 2-5), with the apparent electro-active surface area of the $Pt_{CE}Ni_{NP}$ being larger than $Pt_{Tr}Ni_{NP}$ and Ni_{NP}. Both CVs have features associated with hydrogen adsorption in the positive going sweeps between 0 and 400 $mV_{RHE,}$ although the peaks are much less defined than polycrystalline Pt. The peaks for oxidation of adsorbed hydrogen in the cathodic sweeps are also apparent. If we treat the CVs as polycrystalline Pt (that is, as if no Ni component present) the estimated surface areas from the charge associated with HUPD are 32.0 and 23.3 $cm^2\ cm^{-2}$ respectively for $Pt_{CE}Ni_{NP}$ and $Pt_{Tr}Ni_{NP}$ (See Equation 2-7 and assuming the charge density of Pt is 210 μC cm^{-2}).

3.2.4 Evaluation of 2-propanol electro-oxidation activity

The activity of the Ni_{NP}, $Pt_{CE}Ni_{NP}$ and $Pt_{Tr}Ni_{NP}$ catalysts towards 2-propanol oxidation in base was measured and compared to the activity of a shiny Pt foil (Pt_{foil}). Figure 3-9 shows a comparison of the sampled current voltammograms (SCVs) of the different catalysts based on their respective geometric areas. The catalysts were reduced at 0 V_{RHE} for 60 s, and then stepped to the desired potential. The steady-state currents were sampled after 15 minutes. All the samples exhibited the low-potential current maximum associated with partial 2-propanol oxidation followed by acetone inhibition (50 to 300 mV_{RHE}). It appears that the high activity of $Pt_{Tr}Ni_{NP}$ at low potentials is a summation of the activity of the Pt and Ni deposits (*vide infra*). Above 300 mV_{RHE}, the Ni_{NP} electrode was the only catalyst that did not show any activity, while the bimetallic catalysts demonstrated significantly higher activity, with the *Pt CE deposited* catalyst performing the best.

Figure 3-9 *Sampled current voltammograms of Ni_{NP}, $Pt_{CE}Ni_{NP}$, $Pt_{Tr}Ni_{NP}$ and Pt_{foil} in 1 M KOH + 1 M $(CH_3)_2CH(OH)$ at 60°C. The current densities are based on the geometric area of the catalysts (1 cm^2 for all GLAD-based catalysts and 2.7 cm^2 for the Pt_{foil}.*

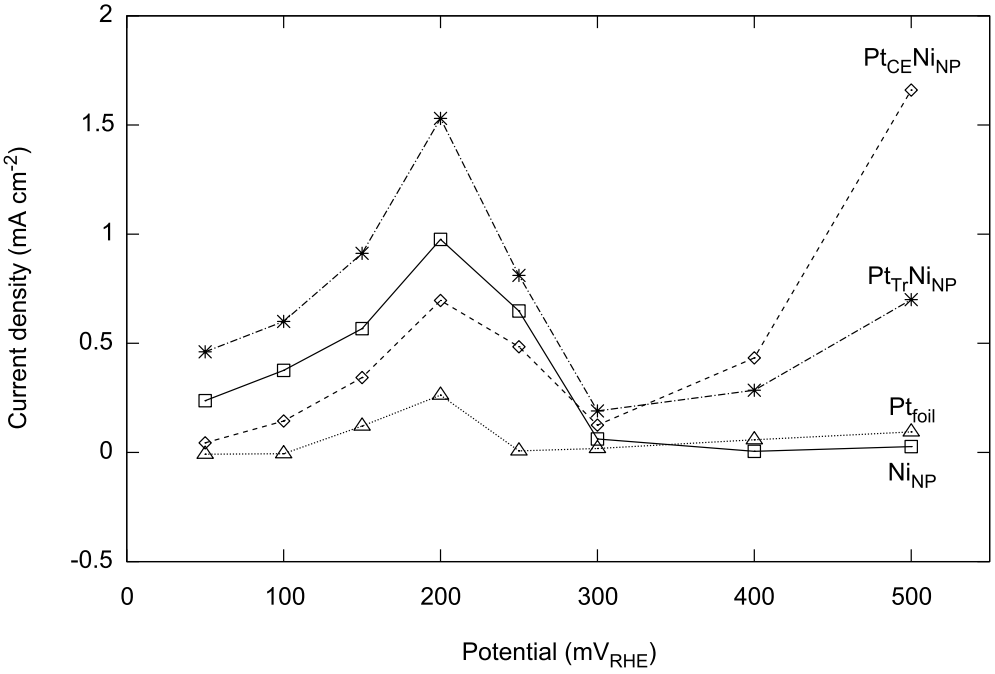

Figure 3-10 shows a comparison of the SCVs normalized by the estimated number of surface atoms. We include the activities of unsupported Pt and Pt-Ru nanoparticles (Johnson-Matthey HiSPECTM 1000 and HiSPEC 6000) [32] and $Pt_{CE}Ni_{foam}$ (Chapter 2). The number of surface atoms on the $Pt_{CE}Ni_{NP}$ and $Pt_{Tr}Ni_{NP}$ catalysts was estimated from the charge in the HUPD region of the respective cyclic voltammograms recorded in base (Figure 3-8). The nanoparticles were prepared by drop-coating 200 µL of a sonicated suspension of 2.5 mg catalyst in 2 mL triply distilled water onto a clean Pt foil followed by air drying. The calculation is shown below:

$$n_{surface\ atoms} = \frac{Q_{HUPD}}{nF} \qquad 3-1$$

where $n_{surface\ atoms}$ is the number of surface atoms

Q_{HUPD} is the charge associated with the Pt HUPD

n is the number of electrons passed during HUPD[2]

F is Faraday's constant (96485 $C \bullet mol^{-1}$)

[2] For $Pt_{CE}Ni_{NP}$

$$n_{surface\ atoms} = \frac{5.175 \times 10^{-3}\ C \times 10^{6}\ \mu mol \bullet mol^{-1}}{96485\ C \bullet mol^{-1}}$$

$$= 0.054\ \mu mol$$

For $Pt_{Tr}Ni_{NP}$

$$n_{surface\ atoms} = \frac{3.762 \times 10^{-3}\ C \times 10^{6}\ \mu mol \bullet mol^{-1}}{96485\ C \bullet mol^{-1}}$$

$$= 0.040\ \mu mol$$

The figure shows that the normalized activity of $Pt_{CE}Ni_{NP}$ was higher than both $Pt_{CE}Ni_{foam}$ and unsupported Pt nanoparticles at low and high potentials. We do note that $Pt_{CE}Ni_{NP}$ had behavior very similar to the unsupported Pt nanoparticles between 50 and 150 mV_{RHE}. On the other hand, the low-potential peak currents for the $Pt_{CE}Ni_{NP}$ and the unsupported Pt-Ru catalysts were comparable, yet the onset potential for 2-propanol oxidation was lower for the latter. Nevertheless, $Pt_{CE}Ni_{NP}$ may be more active than Pt-Ru at potentials greater than 450 mV_{RHE}. $Pt_{Tr}Ni_{NP}$ significantly more active than all the catalysts at potentials between 50 and 300 mV_{RHE}, was comparative to $Pt_{CE}Ni_{NP}$ at 300 to 400 mV_{RHE} and only achieved about 50% of the activity of $Pt_{CE}Ni_{NP}$ at 500 mV_{RHE}.

[2] The 1-electron Heyrosky reaction describes the HUPD: $H_2 + Pt = H_{ads}\text{-}Pt + H^+ + e^-$.

Figure 3-10 *Sampled current voltammograms of $Pt_{CE}Ni_{NP}$, $Pt_{Tr}Ni_{NP}$, $Pt_{CE}Ni_{foam}$, Pt nanoparticles and Pt-Ru nanoparticles in 1 M KOH + 1 M $(CH_3)_2CH(OH)$ at 60°C. The current densities are based on the estimated number of active surface atoms, 0.054, 0.040 and 0.173 µmol for $Pt_{CE}Ni_{NP}$, $Pt_{Tr}Ni_{NP}$ and $Pt_{CE}Ni_{foam}$ respectively. The values for Pt and Pt-Ru were not reported* [32].

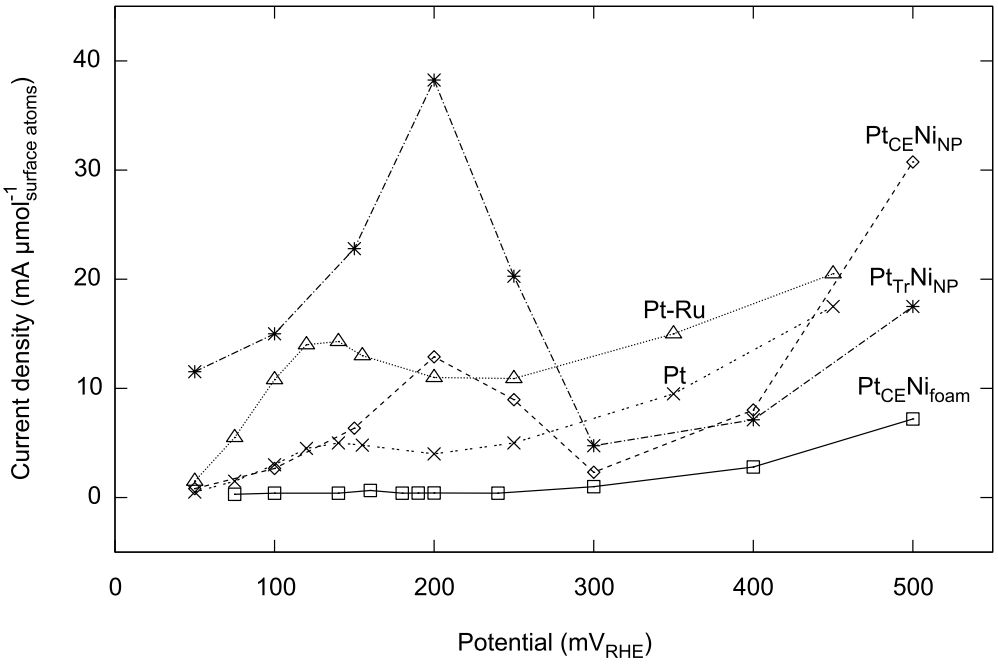

To explain the activity of Ni_{NP} at low potentials but not at high potentials, two hypotheses were tested. The first was that Ni_{NP} is not active towards 2-propanol oxidation; therefore the current density observed below 300 mV_{RHE} is only as a result of oxidation of the Ni_{NP} surface (Equation 2-4). Based on the trivial oxidation peaks in the baseline CVs of Ni_{NP} discussed earlier (Figures 3-7 and 3-8), we predicted that this assumption would be invalidated. However, to test the hypothesis, the sampled current voltammograms were collected in alcohol-free electrolyte. The results (Figure 3-11: solid line, x markers) show that the current density between 50 and 300 mV_{RHE} in the 2-propanol-free electrolyte was lower than when the alcohol was present, and comparable to that observed in the CVs. However, the current is not negligible compared to that recorded

above 300 mV_{RHE}. Thus, we postulated that the anodic current observed in the presence of 2-propanol below 300 mV_{RHE} comprises a minor surface oxidation component and major alcohol oxidation component.

The second hypothesis was that the Ni_{NP} catalyst is indeed active in the entire potential range, but the five potentiostatic experiments performed below 300 mV_{RHE} collectively oxidise the Ni_{NP} electrodes to the point of surface passivation before activity above 300 mV_{RHE} could be recorded. Hence, as a control, the data points were collected from 300 to 500 mV_{RHE} first and then from 50 to 250 mV_{RHE}. The SCV in Figure 3-11 (dashed line, □ markers) shows that there is still no oxidation activity at high potentials. In fact, the current above 300 mV_{RHE} was reductive in nature, perhaps indicating that Ni_{NP} is very effective at catalyzing proton reduction even at these potentials, a feature supported by the significant H_2 evolution current observed in its baseline cyclic voltammogram (Figure 3-8). Furthermore, the low potential current maximum is still present and the activity almost unchanged despite the electrode being polarized at higher potentials first. Thus, even polarization above 300 mV_{RHE} does not passivate the Ni_{NP} catalyst. Together, these control experiments show definitively that Ni_{NP} is active towards 2-propanol oxidation below 300 mV_{RHE}.

The origin of the activity of Ni_{NP} may be due to the structure of the nanopillars. There are reports of alcohol oxidation over oxidised Ni catalysts in alkaline solution. Ni dispersed in graphite by electro-deposition from solutions of $NiSO_4/H_2SO_4$ was found to catalyze methanol oxidation once they were converted to Ni oxide, whereas similarly prepared bulk Ni was inactive [33]. In another report, *hcp* nanocrystalline Ni with diameters of 9±2.7 nm were found to catalyze the MOR through the formation of NiOOH [34]. The oxidation of

methanol, 1-butanol and 2-butanol was found to commence over $Ni(OH)_2$ electrodes upon the formation of NiOOH on the surface [35]. This result was confirmed for methanol for a $Ni(OH)_2$ catalyst supported on a GC disk [36]. These reports suggest that an oxidised Ni surface is active towards alcohol oxidation in base. Perhaps there are more defects, lattice boundaries and low-coordination atoms on the surface of the porous Ni_{NP}. These sites are easily oxidised making the Ni_{NP} active towards 2-propanol oxidation. Further work is required to confirm this proposal. Regardless, the Ni nanopillars are likely in an oxidised state as they have been exposed to air during the experimental procedures, and this may be contributing to their observed activity.

Figure 3-11 *Sampled current voltammograms of Ni_{NP} in 1 M KOH at 25°C and 1 M KOH + 1 M $(CH_3)_2CH(OH)$ at 60°C recorded from 50 to 500 mV_{RHE} , and in 1 M KOH + 1 M $(CH_3)_2CH(OH)$ at 60°C recorded from 300 to 500 mV, then 50 to 250 mV_{RHE}.*

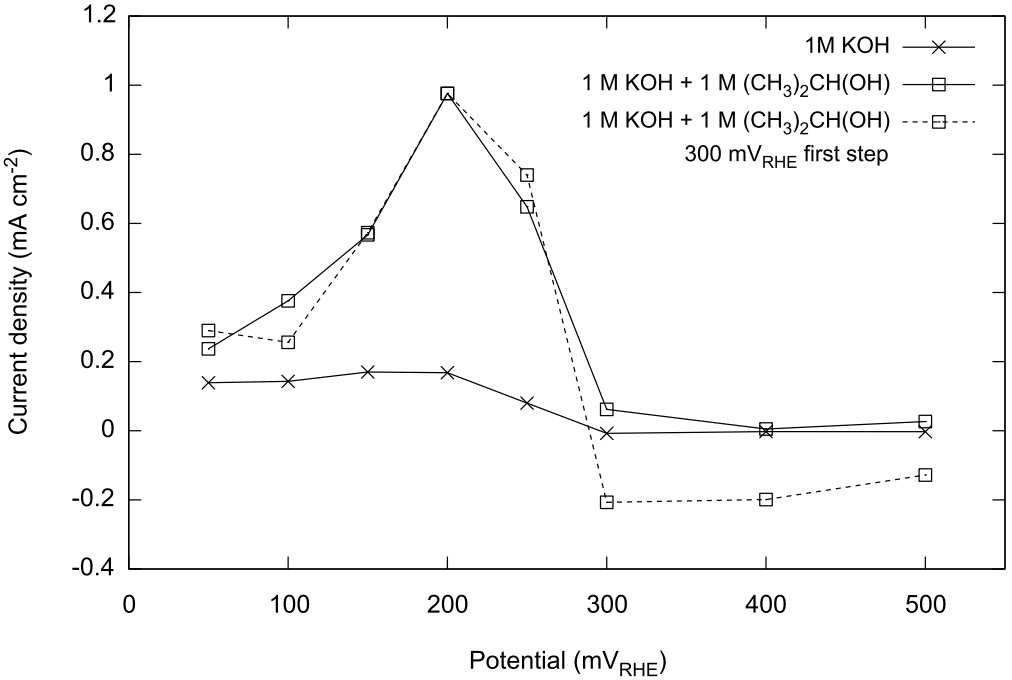

Given the performance of Ni_{NP} at low potentials, it follows that the 2-propanol oxidation current of the $Pt_{CE}Ni_{NP}$ and $Pt_{Tr}Ni_{NP}$ catalysts below 300 mV may result from the combined activity of the Pt and Ni components. The SCV for $Pt_{Tr}Ni_{NP}$ in Figure 3-9 is consistent with this statement in that below 300 mV_{RHE} this catalyst has the highest activity. Indeed, this catalyst has features most like bulk Ni_{NP} and bulk Pt based on its SEM image (Figure 3-5) so that a suggestion of combined activity of its components is reasonable. In contrast, the activity of $Pt_{CE}Ni_{NP}$ below 300 mV_{RHE} is even lower than the Ni_{NP} itself. Furthermore, the conformal coating of Pt onto the Ni substrate in $Pt_{CE}Ni_{NP}$ is very different to the well-defined structure of the $Pt_{Tr}Ni_{NP}$ catalyst. We therefore cannot separate geometric/composition effects from the effect of combined activity of the Ni and Pt components. A geometric/composition effect has been described by Yang *et al.* for MeOH oxidation over bi-metallic catalysts [37] and is well established by Gasteiger, Markovic, Ross and Cairns [38,39]. According to the literature, at least three neighbouring Pt sites in the correct crystallographic arrangement are required to activate methanol chemisorption. If this mechanism is relevant for 2-propanol, then the probability of having enough Pt sites in the correct orientation for 2-propanol adsorption is higher in $Pt_{Tr}Ni_{NP}$ where the Pt is segregated to just the top of the catalyst film. In contrast, in $Pt_{CE}Ni_{NP}$, the Pt is homogenously distributed and the likelihood of the correct arrangement for 2-propanol adsorption is less favoured.

The control experiments on Ni_{NP} showed that above 300 mV, the Ni component is not passivated, but we assume that it is in fact oxidised. We therefore propose that a bi-functional mechanism is induced in both $Pt_{CE}Ni_{NP}$ and $Pt_{Tr}Ni_{NP}$. The Pt in the $Pt_{CE}Ni_{NP}$ catalyst is conformally deposited and therefore maximizes contact with the underlying oxidised Ni_{NP} substrate, making any bi-

functional effects quite favourable. In fact, the SCV of $Pt_{CE}Ni_{NP}$ in Figure 3-10 shows that it has catalytic behavior very similar to bulk Pt (estimated by the supported Pt nanoparticles) below 150 mV_{RHE} where oxidation of the Ni_{NP} and the bi-functional mechanism is not yet maximized. In contrast, this process is expected to be less prevalent over $Pt_{Tr}Ni_{NP}$ because there is less contact between the active Pt surfaces and oxidised Ni surfaces. This accounts for its lower relative activity above 300 mV_{RHE}. However, this analysis does not rule out any possible electronic effects in either catalyst.

XPS was performed to probe any electronic effects that could contribute to the activity difference observed between $Pt_{CE}Ni_{NP}$ and $Pt_{Tr}Ni_{NP}$ catalysts. Figures 3-12 and 3-13 show the Pt 4*f* XPS spectra collected on $Pt_{CE}Ni_{NP}$ and $Pt_{Tr}Ni_{NP}$ respectively. Both spectra display a doublet of metallic Pt peaks. Similar to observations for the Ni foam supported catalysts (Figure 2-14), the $Pt_{CE}Ni_{NP}$ exhibits a Ni 3*p* shoulder at ~ 68 eV. In contrast, this feature is absent for the $Pt_{Tr}Ni_{NP}$ catalyst. This is consistent with the thick (~ 500 nm) Pt layer observed in the $Pt_{Tr}Ni_{NP}$ SEM (Figure 3-5). The XPS probe depth is only ~ 3 to 9 nm, therefore Ni was not strongly detected in this sample. Table 3-2 summarizes the peak positions of the component peaks in the XPS spectra. Compared to bulk Pt, no electronic shifts were observed for the $Pt_{CE}Ni_{NP}$ catalyst. This is consistent with the results for $Pt_{CE}Ni_{foam.}$ A statistically negligible +0.2 eV shift was observed for $Pt_{Tr}Ni_{NP}$. Therefore, both catalysts are electronically similar to Pt and to each other and no electronic effects are postulated.

Figure 3-12 *X-ray photoelectron spectroscopy of $Pt_{CE}Ni_{NP}$. Dashed lines are experimental data, solid lines are calculated fits and solid grey lines are component peaks of the calculated fits.*

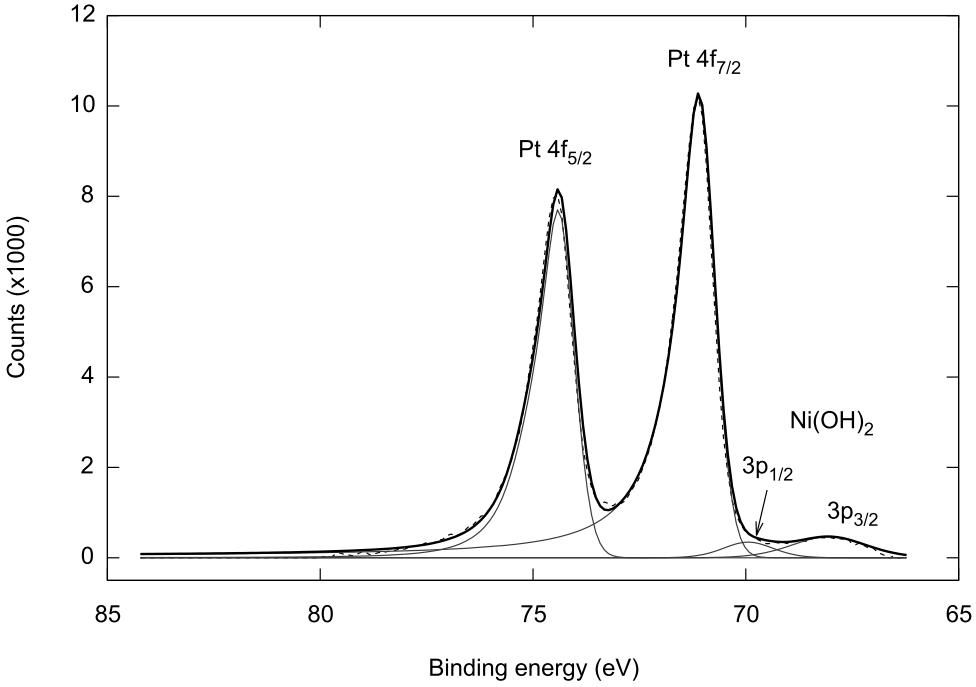

Figure 3-13 *X-ray photoelectron spectroscopy of $Pt_{Tr}Ni_{NP}$. Dashed lines are experimental data, solid lines are calculated fits and solid grey lines are component peaks of the calculated fits.*

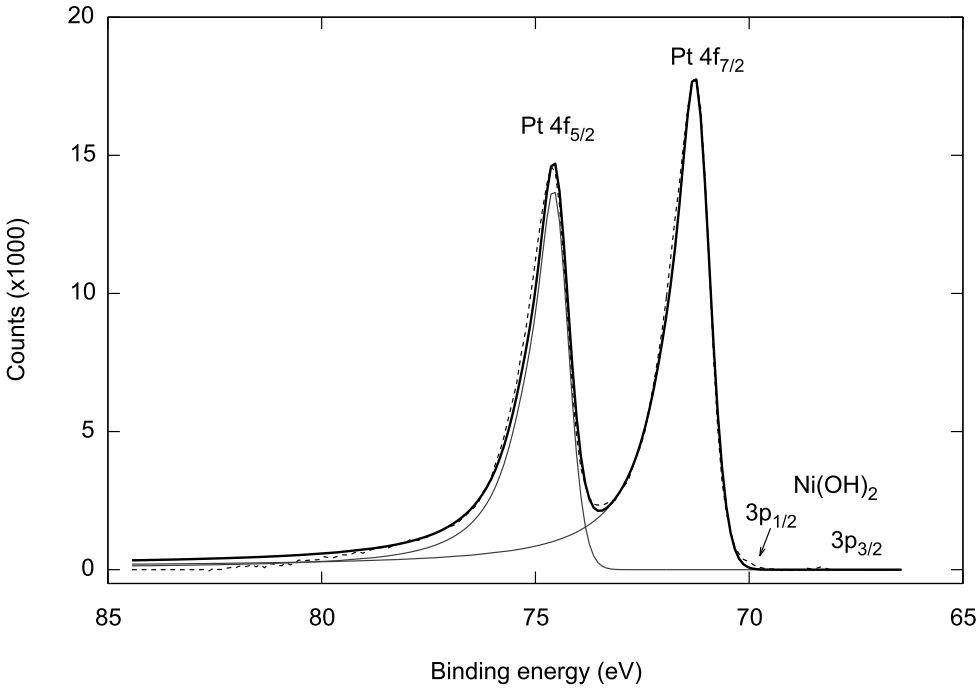

Table 3-2 *Reference and calculated binding energies and standard deviations (bracketed numbers) used in XPS analysis of the catalysts.*

Chemical state and spectral line	*Binding energy (eV)*		
	Reference	$Pt_{CE}Ni_{NP}$	$Pt_{Tr}Ni_{NP}$
Pt $4f_{7/2}$	*71.1 (0.1)*[a]	*71.1*	*71.3*
$Ni(OH)_2$ $3p_{3/2}$	*68.0 (-)*	*68.0*	-

[a] Numbers in brackets denote the standard deviation for the values in the reference column. In all other columns experimental error was ± 0.1 eV. Dashes in brackets signify that no standard deviation has been recorded as only one value has been reported.

Collectively, these analyses show that a GLAD Ni_{NP}-based catalyst with both a conformal coating of Pt and segregated regions of Pt and Ni_{NP} may be the best configuration for a highly active 2-propanol oxidation catalyst. Such a catalyst would exploit the activity of Ni_{NP} and Pt, the geometric effects in $Pt_{Tr}Ni_{NP}$ and the bi-functional effects in $Pt_{CE}Ni_{NP}$.

3.3 Conclusions

The first alcohol oxidation study over GLAD-based catalysts was investigated. To summarize, bimetallic Ni-Pt electrodes were prepared via two methods: the *Pt CE deposition* and a traditional potentiostatic deposition. Both methods were successful in incorporating Pt onto the surface of GLAD Ni_{NP} to effect an increase in electro-active surface area. Both catalysts showed superior activity towards 2-propanol oxidation in base relative to a $Pt_{CE}Ni_{foam}$, discussed in Chapter 2, and a shiny Pt_{foil} T(able 3-3). The surface atom normalized activity of $Pt_{CE}Ni_{NP}$ was higher than unsupported Pt nanoparticles at low and high potentials, while at low-potentials $Pt_{CE}Ni_{NP}$ was comparable to Pt-Ru; the normalized activity of $Pt_{Tr}Ni_{NP}$ was superior below 300 mV_{RHE}. It was demonstrated that the Ni_{NP} catalyst was also active at potentials below 300 mV_{RHE}; therefore activity enhancement at low potentials was attributed to the combined activity of the Pt and Ni components in the catalysts and/or a geometric/composition effect. At potentials above 300 mV_{RHE}, a bi-functional mechanism was suggested where $Pt_{CE}Ni_{NP}$ experienced a higher bi-functional effect than $Pt_{Tr}Ni_{NP}$. Overall, the results suggest that an optimum fuel cell catalyst made from these systems might be a combination of $Pt_{CE}Ni_{NP}$ and $Pt_{Tr}Ni_{NP}$.

Table 3-3 *Summary of the relative activity enhancements of the $Pt_{CE}Ni_{NP}$ and $Pt_{Tr}Ni_{NP}$ catalysts compared to Pt_{foil} and Johnson-Matthey Pt nanoparticle catalysts towards 2-propanol oxidation in 1M $(CH_3)_2CHOH$/1 M KOH at 60°C.*

	$Pt_{CE}Ni_{NP}$		$Pt_{Tr}Ni_{NP}$	
Potential (mV vs. RHE)	Low	High	Low	High
Enhancement compared to Pt_{foil} (mA cm^{-2})	5.8 x	7.4 x	2.7 x	17.6 x
Johnson Matthey Pt nanoparticles (mA surf. $atoms^{-1}$)	9.6 x	None	3.2 x	~ 1.4 x
Effects proposed	Ni and Pt summative activity and bi-functional	Bi-functional	Bi-functional	Geometric and bi-functional

Naturally, the next logical step is to investigate the oxygen reduction activity of these GLAD-based Ni catalysts. There is much precedent in the literature for GLAD-based oxygen reduction catalysts but no one to date has reported Ni as the base metal for such studies [10-17]. These results will be discussed in the subsequent chapter.

3.4 Experimental

3.4.1 General

The following reagents were used as received from the supplier: Nitrogen (Praxair, pre-purified), concentrated sulfuric acid (Caledon), hydrochloric acid (EMD chemicals), nitric acid (EMD chemicals), and perchloric acid (Anachemia Corporation), potassium permanganate (Fischer Scientific), 30% hydrogen peroxide (Fischer Scientific), potassium hydroxide (Caledon Laboratory Chemicals), ammonium chloride (Caledon Laboratory chemicals), 2-propanol (Fischer Scientific, ACS plus grade), ethanol (Greenfield Ethanol Incorporated) and potassium hexachloroplatinate (Aithica Chemical Corporation). The following materials were used as received from the supplier: platinum gauze (Alfa Aesar, 52 mesh woven from 0.1 mm wire, 99.9% metals basis), silicon wafers (p-type, (100), University Wafer), titanium (1 inch target, 99.95% purity), and nickel metal chunks (Cerac, Inc., 99.9% purity)

Triply distilled H_2O was used to prepare all aqueous solutions and was itself prepared by distilling a mixture of alkaline $KMnO_4$ and doubly distilled H_2O. Analytical grade reagents were used to prepare all electrolyte solutions. Electrolytes were purged with N_2 before use, and all voltammetric experiments were carried out under N_2. All glassware was rinsed with *Piranha* solution (5:1 by volume concentrated H_2SO_4 and 30% H_2O_2) followed by thorough rinsing with triply distilled H_2O, and drying in an oven at 80°C.

Electrochemical experiments were performed on either an EG&G Princeton Applied Research Potentiostat/Galvanostat Model 273 using the corresponding M270 software or a Solartron SI 1287 Electrochemical Interface controlled by CorrWare for Windows Version 2-3d software and using a

conventional three-electrode cell configuration. During electrochemical depositions, the potential of the platinum counter electrode was recorded using a Radio Shack multimeter and Scope View version 1.08 software.

Scanning electron microscopy (SEM) was performed on a Hitachi S-4800 instrument. Where side images were necessary, the samples were first cleaved before mounting to SEM stubs. X-ray diffraction (XRD) patterns were taken using an Inel diffractometer equipped with a CPS 120 detector. The diffraction patterns were recorded at room temperature using Cu Kα radiation (λ = 1.5046 Å). Reference XRD patterns were generated using Powdercell 2.3 freeware. A Kratos Analytical Axis X-ray imaging photoelectron spectrometer was used to perform X-ray photoelectron spectroscopy (XPS). XPS data was fit using CASA XPS Software File version 1.0.0.1, and the spectra were calibrated to adventitious carbon at 284.8 eV. The binding energies of the component peaks were calculated from the background-subtracted spectra using an applied Shirley background. All peaks were fit with 30% Gaussian-Lorentzian curves whereas metallic components were assigned 10 to 11% asymmetry in their higher binding energy tails. The intensity ratios of the Pt $4f_{7/2}$ and Pt $4f_{5/2}$ peaks were set to the theoretical value of 4:3 and spin-orbit coupling was 3.3 eV; the Ni $3p_{3/2}$ and $3p_{1/2}$ peaks' intensity ratio was 2:1 and separated by 1.9 eV. Reference data was retrieved from the National Institute of Standards and Technology (NIST) XPS online database [40].

Inductively coupled plasma mass spectrometry was performed on an Elan 6000 spectroscope from Perkin Elmer. Samples were prepared by dissolving the deposits in *aqua regia*, evaporating to dryness on a hot plate and making up the residue quantitatively in 0.3 M HNO_3.

3.4.2 Preparation of platinum electrodes

The platinum black electrode used as a source of platinum in the platinum counter electrode deposition (see below) consisted of a 2.5 cm x 2.5 cm platinum gauze blacked with 0.02 M K_2PtCl_6/1 M $HClO_4$. A typical blackening experiment would be performed at -0.1 V vs. Ag/AgCl (4M KCl) (Aldrich) until the observed current decayed to ~ 0 mA. The real surface area of the platinum black electrode was determined from the hydrogen under potential deposition (H_{UPD}) peak of a stabilized cyclic voltammogram recorded in 0.5 M H_2SO_4 assuming the charge associated with a monolayer of hydrides on polycrystalline Pt is 210 μC cm^{-2} [41] with 77% efficiency. Typical estimations were more than 25,000 cm^2. The counter electrode was freshly blacked after three uses in the platinum counter electrode deposition.

The platinum black electrode used as a counter electrode in voltammetry was prepared in the manner described above. The Pt foil electrode used as a working electrode for the electro-oxidation of $(CH_3)_2CH(OH)$, was 0.8 x 1.7 cm, for a total geometric area of 2.7 cm^2.

3.4.3 Preparation of glancing angle deposited nickel working electrodes

The substrate used for deposition was a glancing angle deposited nanopillar nickel film. Nanopillar Ni films were prepared by glancing angle deposition on Si substrates. Si wafers were rinsed in acetone, 2-propanol, and water before being diced into 1 cm x 2 cm pieces. The samples were placed in a high vacuum deposition chamber (Kurt J. Lesker) that was evacuated to below 0.1 mPa. A 10 nm layer of Ti was sputtered under argon flow at 75 W. The Ti layer promotes adhesion between the substrate and Ni layers. Ni was then deposited from Ni metal chunks via electron beam deposition. The flux rate was maintained at 1 nm

s^{-1} while the substrate was rotated constantly in φ at a rate of one rotation every 10 nm of film growth. A 200 nm planar layer of Ni was first deposited at a deposition angle of α = 30˚, followed by 500 nm of vertical nanopillars deposited at α = 85˚. The resulting material is denoted as Ni_{NP} herein. After deposition, a task wipe was used to define a 1 cm x 1 cm area of nanopillars for deposition of Pt. The Ni_{NP} substrates were cleaned with triply distilled water before being used as working electrodes.

3.4.4 Platinum counter electrode deposition

The electrolyte comprised 30 mL of 2.0 M NH_4Cl prepared in a glass cylinder of dimensions 10 cm x 2.5 cm inner diameter. A current of -0.1 A was applied between the Ni working electrode and the Pt black counter electrode in the presence of a Ag/AgCl (4M KCl) reference electrode for 1 hour, with magnetic stirring at 500 rpm, to afford Pt deposits on the working electrodes. The Ni_{NP} film was oriented to face the counter electrode. After deposition the working electrodes, denoted $Pt_{CE}Ni_{NP}$ herein, were gently rinsed with copious amounts of triply distilled water.

3.4.5 Traditional platinum deposition

The deposition apparatus was a glass cylinder of dimensions 10 cm x 2.5 cm inner diameter equipped with a magnetic stir bar, a Ag/AgCl (4M KCl) double junction reference electrode and a Pt counter electrode shielded in a glass tube with a 10 μm porous glass frit. The plating solution comprised 25 mL of an aqueous solution of 1.2 x 10^{-4} M K_2PtCl_6/0.01 M $HClO_4$ prepared by serial dilution. The deposition was performed by applying a potential of -0.1 V versus the reference electrode ($V_{Ag/AgCl\ (4M\ KCl)}$), with stirring at 500 rpm.

3.4.6 Electrochemical characterization

Cyclic voltammetry and chronoamperometry were performed in 1 M KOH at 25°C, or 1.0 M KOH/1.0 M $(CH_3)_2CH(OH)$ at 60°C, in which case the cell was equipped with a dry ice/acetone condenser to minimize evaporation of the $(CH_3)_2CH(OH)$. The Pt counter electrode was isolated in a glass tube with a 10 μm porous glass frit. A static reversible hydrogen electrode (RHE) was used as a reference point and all potentials are versus this reference unless otherwise stated (denoted V_{RHE}). Sampled current voltammograms were constructed by calculating the average current in the last 5 seconds of the 15-minute chronoamperometric steps, and plotting against the relevant potential. Prior to stepping to the desired potential, the working electrode was held at a constant potential of 0 V_{RHE} for 1 minute.

3.5 Bibliography

[1] M.M. Hawkeye, M.J. Brett, J. Vac. Sci. Technol. A, 25 (2007) 1317-1335.

[2] M.T. Taschuk, M.M. Hawkeye, M.J. Brett, Chapter 13 - Glancing Angle Deposition In: Peter M. Martin, (Ed), Handbook of Deposition Technologies for Films and Coatings (Third Edition), William Andrew Publishing, Boston, 2010, pp. 621-678.

[3] M.A. Summers, K. Tabunshchyk, A. Kovalenko, M.J. Brett, Photonics and Nanostructures - Fundamentals and Applications, 7 (2009) 76-84.

[4] S. Kennedy, M.J. Brett, Appl. Opt., 42 (2003) 4573-4579.

[5] J.Q. Xi, M.F. Schubert, J.K. Kim, E.F. Schubert, M. Chen, S.Y. Lin, W. Liu, J.A. Smart, Nat. Photon, 1 (2007) 176-179.

[6] J.G. Van Dijken, M.D. Fleischauer, M.J. Brett, Organic Electronics, 12 (2011) 2111-2119.

[7] N. Li, S.R. Forrest, App. Phys. Lett., 95 (2009) 123309-123311.

[8] M.D. Fleischauer, J. Li, M.J. Brett, J. Electrochem. Soc., 156 (2009) A33-A36.

[9] S.R. Jim, M.T. Taschuk, G.E. Morlock, L.W. Bezuidenhout, W. Schwak, M.J. Brett, Anal. Chem., 82 (2010) 5349-5356.

[10] W.J. Khudhayer, N.N. Kariuki, X. Wang, D.J. Myers, A.U. Shaikh, T. Karabacak, J. Electrochem. Soc., 158 (2011) B1029-B1041.

[11] W.J. Khudhayer, N. Kariuki, D.J. Myers, A.U. Shaikh, T. Karabacak, J. Electrochem. Soc., 159 (2012) B729-B736.

[12] M.D. Gasda, R. Teki, T.M. Lu, N. Koratkar, G.A. Eisman, D. Gall, J. Electrochem. Soc., 156 (2009) B614-B619.

[13] M.D. Gasda, G.A. Eisman, D. Gall, J. Electrochem. Soc., 157 (2010) B71-B76.

[14] M.D. Gasda, G.A. Eisman, D. Gall, J. Electrochem. Soc., 157 (2010) B437-B440.

[15] M.D. Gasda, G.A. Eisman, D. Gall, J. Electrochem. Soc., 157 (2010) B113-B117.

[16] A. Bonakdarpour, R.T. Tucker, M.D. Fleischauer, N.A. Beckers, M.J. Brett, D.P. Wilkinson, Electrochim. Acta, 85 (2012) 492-500.

[17] A. Bonakdarpour, M.D. Fleischauer, M.J. Brett, J.R. Dahn, Appl. Catal. A-Gen., 349 (2008) 110-115.

[18] G.C.K. Liu, C. Bums, R. Sanderson, D.A. Stevens, G. Vernstromb, R.T. Atanasoski, M.K. Debe, J.R. Dahn, ECS Transactions, 33 (2010) 153-159.

[19] M.K. Debe, A.J. Steinbach, G.D. Vernstrom, S.M. Hendricks, M.J. Kurkowski, R.T. Atanasoski, P. Kadera, D.A. Stevens, R.J. Sanderson, E. Marvel, J.R. Dahn, ECS Transactions, 33 (2010) 143-152.

[20] D.A. Stevens, R. Mehrotra, R.J. Sanderson, G.D. Vernstrom, R.T. Atanasoski, M.K. Debe, J.R. Dahn, J. Electrochem. Soc., 158 (2011) B905-B909.

[21] C.K.G. Liu, D.A. Stevens, J.C. Burns, R.J. Sanderson, G. Vernstrom, R.T. Atanasoski, M.K. Debe, J.R. Dahn, J. Electrochem. Soc., 158 (2011) B919-B926.

[22] M.K. Debe, A.J. Steinbach, G.D. Vernstrom, S.M. Hendricks, M.J. Kurkowski, R.T. Atanasoski, P. Kadera, D.A. Stevens, R.J. Sanderson, E. Marvel, J.R. Dahn, J. Electrochem. Soc., 158 (2011) B910-B918.

[23] L. Gancs, T. Kobayashi, M.K. Debe, R. Atanasoski, A. Wieckowski, Chem. Mater., 20 (2008) 2444-2454.

[24] A.M. Feltham, M. Spiro, Chem. Rev., 71 (1971) 177-193.

[25] L.N. Menard, S.H. Bergens, J. Power Sources, 194 (2009) 298-302.

[26] S.A. Francis, S.H. Bergens, J. Power Sources, 196 (2011) 7470-7480.

[27] Y. Xu, M. Shao, M. Mavrikakis, R.R. Adzic In: W. Wieckowski, M.T.M. Koper, (Eds), Fuel Cell Catalysis-A Surface Science Approach, John Wiley and Sons, New Jersey, 2009, pp. 271-315.

[28] J.K. Kwan, J.C. Sit, Nanotechnology, 21 (2010) 295301-295301.

[29] A. Seghiouer, J. Chevalet, A. Barhoun, F. Lantelme, J. Electroanal. Chem., 442 (1998) 113-123.

[30] S.A.S. Machado, L.A. Avaca, Electrochim. Acta, 39 (1994) 1385-1391.

[31] I.J. Brown, S. Sotiropoulos, J. Appl. Electrochem., 30 (2000) 107-111.

[32] M.E.P. Markiewicz, S.H. Bergens, J. Power Sources, 185 (2008) 222-225.

[33] M.A.A. Rahim, R.M.A. Hameed, M.W. Khalil, J. Power Sources, 134 (2004) 160-169.

[34] R.M.A. Tehrani, S. AbGhani, Fuel Cells, 9 (2009) 579-587.

[35] A. Kowal, S.N. Port, R.J. Nichols, Catal. Today, 38 (1997) 483-492.

[36] A.A. El-Shafei, J. Electroanal. Chem., 471 (1999) 89-95.

[37] H. Yang, C. Coutanceau, J. Léger, N. Alonso-Vante, C. Lamy, J. Electroanal. Chem., 576 (2005) 305-313.

[38] H.A. Gasteiger, N. Markovic, P.N. Ross Jr., E.J. Cairns, J. Electrochem. Soc., 141 (1994) 1795-1803.

[39] N.M. Marković, P.N. Ross Jr., Surf. Sci. Rep., 45 (2002) 117-229.

[40] C.D. Wagner, A.V. Naumkin, A. Kraut-Vass, J.W. Allison, C.J. Powell, J.R. Rumble Jr., NIST X-ray Photoelectron Spectroscopy Database, Version 3.5 (Web Version). 2003; Available at: srdata.nist.gov/xps. Accessed March 1st, 2012.

[41] B.E. Conway, H. Angerstein-Kozlowska, Acc. Chem. Res., 14 (1981) 49-56.

Chapter 4: Oxygen reduction reaction activity of Pt electro-deposits on glancing angle deposited nanopillar Ni films

4.1 Introduction

The previous chapter (Section 3-1) described the use of GLAD deposits as ORR catalysts in 3-electrode and fuel cell experiments by the Gall [1-4], Wilkinson, Dahn and Brett [5,6], and Karabacak [7,8] research groups. We also described the results of the first GLAD based Ni-Pt anode catalysts reported in the literature [9]. This new study seeks to use the combined information gleaned from these results to explore GLAD Ni-Pt materials as cathode catalysts towards efficient oxygen reduction in fuel cells.

Interest in designing highly active ORR catalysts is related to overcoming the kinetic activation losses at the cathode of fuel cells. To illustrate, the ORR has several orders of magnitude lower exchange current density[1] than the HOR over Pt in acidic solution (10^{-7} to 10^{-9} versus 10^{-3} A cm^{-2}) [10]. Yet, Pt group metals are still the most active catalysts for the ORR. Thus, to counteract the slow reaction at the cathode, high Pt loadings are required, which add significantly to the cost per fuel cell unit. ORR catalysts that maximize performance and durability while minimizing cost are therefore desirable. For example, the United States Department of Energy targets for their Hydrogen and Fuel Cells Program are total PGM (Platinum group metal) loading of less than 0.125 mg cm^{-2}, activity of 0.72 mA cm_{Pt}^{-2} or 0.44 A mg_{Pt}^{-1} at 0.9 V_{RHE} (150 kPa H_2/O_2, 80°C, 100% R.H.) and <

[1] Exchange current density reflects the intrinsic rate of electron transfer between the analyte (in this case, oxygen molecules) and the electrode. It is dependent on the identity, roughness and surface condition of the electrode, and the nature of the analyte. Also, see Section A.2.3.

40% mass activity loss after degradation protocols [11]. We note that these targets are primarily for PEMFCs towards automotive applications, but are feasible general benchmarks for AEMFCs as well.

Indeed, there are a vast number of reports of Pt-free ORR catalysts, but feel that an in-depth discussion of these is beyond the scope of this work. The interested reader is directed to the following resources: Section 4.2 and 4.3 in [12], and Section 3.2 in [10], as well as references [13] and [14] where Pt-free catalysts such as non-precious or transition metal chalcogenides, carbides, and nitrides, and metal porphrins and phthalocyanine materials are discussed.

4.1.1 Mechanism of the oxygen reduction reaction over Pt

The suggested ORR mechanism over Pt in acid is shown in Scheme 4-1 [15]. In the direct pathway (A), O_2 is reduced directly to water, whereas in the series pathway (B1 and B2) the reduction occurs via adsorbed H_2O_2, which is subsequently reduced to water. Alternatively, incomplete O_2 reduction can occur if H_2O_2 decomposes (C) or desorbs (D) before it can react further. We note that this proposal is an over-simplified representation of what is occurring. Firstly, oxygen adsorption could occur via molecular adsorption, dissociative chemisorption and/or via oxide formation. Furthermore, the mechanism is potential dependent; at high potentials (>0.5 V_{RHE}) in the presence of oxygen, the electrode surface likely exists as a mixture of Pt and PtO, while at lower potentials a clean Pt surface arises [16]. Moreover, the presence of adsorbed spectator ions (such as SO_4^{2-} from sulfuric acid electrolyte) also modifies the catalysts surface structure [17]. Thus, the mechanism in Scheme 4-1 may incorrectly presume a clean Pt metal surface. Finally, there is still debate as to the identity of the rate-determining step. It is agreed that it involves activation of

O_2, which has a significant BDE of 498 kJ mol^{-1} [18], but whether it is the first electron transfer to adsorbed oxygen, or the dissociative chemisorption of oxygen, with or without electron transfer, is still unclear [19].

Scheme 4-1 *Mechanism of the acid oxygen reduction reaction over Pt. The subscripts* sol *and* ads *indicate the species is in the bulk solution or adsorbed on the catalyst surface respectively.*

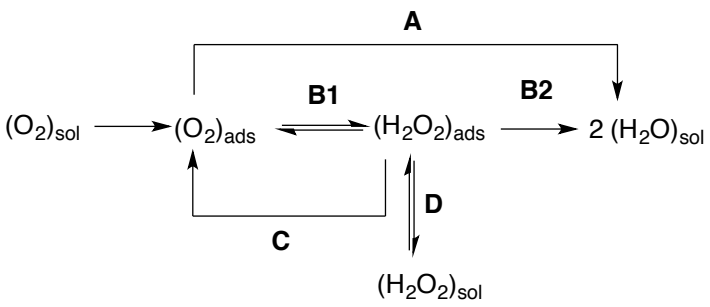

In alkaline media, two mechanisms are proposed. The first is similar to Scheme 4-1, in that they are both inner sphere, that is, occur in the inner Helmholtz layer[2] and involve all reaction intermediates remaining adsorbed on the active site until the final product is desorbed (Scheme 4-2).

Scheme 4-2 *Mechanism of the inner sphere alkaline oxygen reduction reaction over Pt. The subscript* ads *indicates the species is adsorbed on the catalyst surface.*

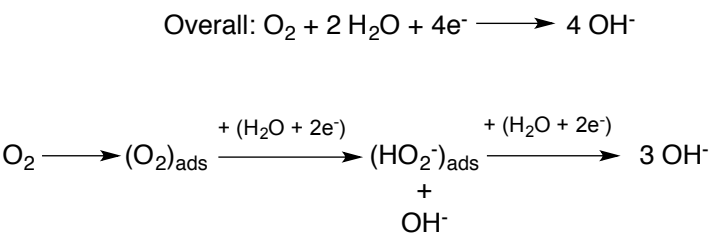

[2] In general the inner Helmholtz layer describes all the species specifically adsorbed on the electrode surface, whereas the outer Helmholtz layer comprises ions closest to the electrode surface that are not specifically adsorbed. The ions' solvation spheres are still intact and held in place only by electrostatic forces [62].

The second mechanism, proposed by Ramaswamy and Mukerjee, involves an outer sphere process that is unique to the alkaline system [19,20]. In this case the O_2 molecule is not directly adsorbed on the Pt surface, but rather is associated with a solvation sphere of water molecules (denoted $[O_2 \bullet (H_2O)_n]_{aq}$). The authors propose that, in alkaline solution, a hydrogen bond is formed between an H atom in surface adsorbed hydroxyl groups (OH_{ads}) and an O atom in a water molecule in $[O_2 \bullet (H_2O)_n]_{aq}$. This bond thus stabilizes the solvated O_2 molecule in the Outer Helmholtz layer. The first electron transfer, which occurs via tunneling, proceeds as shown in Equation 4-1a.

$$(OH)_{ads} + [O_2 \bullet (H_2O)_n]_{aq} + e^- \rightarrow (OH)_{ads} + [O_2^{\bullet -} \bullet (H_2O)_n]_{aq} \qquad 4\text{-}1a$$

Next, the radical species is desolvated and adsorbed on the catalyst surface (Equation 4-1b).

$$[O_2^{\bullet -} \bullet (H_2O)_n]_{aq} \rightarrow (O_2^{\bullet -})_{ads} + n\ H_2O \qquad 4\text{-}1b$$

A subsequent proton transfer and electron transfer produces the adsorbed peroxide species (Equations 4-1c and 4-1d), which desorbs from the electrode surface (Equation 4-1e) or reacts to form OH^- via the mechanism shown in Scheme 4-2.

$$O_2^{\bullet -}{}_{ads} + H_2O \rightarrow (HO_2^{\bullet})_{ads} + OH^- \qquad 4\text{-}1c$$

$$(HO_2^{\bullet})_{ads} + e^- \rightarrow (HO_2^-)_{ads} \qquad 4\text{-}1d$$

$$(HO_2^-)_{ads} \rightarrow (HO_2^-)_{aq} \qquad 4\text{-}1e$$

It is imperative to note that in the acidic ORR it is widely accepted that OH_{ads} from H_2O activation inhibits adsorption of molecular O_2 and other intermediates. The

same blocking effect is apparent for the alkaline ORR, but based on the above proposed mechanism, OH_{ads} also has a promoting effect on the 2-electron outer sphere reduction to peroxide.

4.1.2 Pt-based oxygen reduction reaction catalysts

For both the acid and alkaline mechanistic studies discussed in Section 4.1.1, it is apparent that the ORR activity of a Pt-based catalyst will depend on the adsorption energy of O_2, the O-O bond dissociation energy, and the binding energy of OH on the surface. Thus many efforts have been made to tailor catalyst syntheses and structures to precisely control these measures.

Early success came with alloying Pt with cheaper transition metals such as Fe, Co, Cu and Ni. For example, fundamental work by Mukerjee and co-workers has shown that PtCo alloys supported on carbon show higher ORR activity than analogous Pt/C [21]. The enhancement was credited to a combination of Pt-Pt lattice contraction (geometric effect) and increasing *d*-band vacancy in surface Pt atoms (electronic effect) (see Section 2.1 for a more detailed description of these and other effects). Combined, the result is a lower tendency to electro-adsorb O or OH on the catalyst surface and decrease the blocking effect discussed in Section 4.1.1. Toda *et al*. described similar electronic effects for PtNi and PtFe alloys [22].

Adzic and co-workers designed Pt monolayer (Pt_{ML}) catalysts supported on a multitude of intermetallic cores including Ru [23], Pd-Au [24], Ir and Re [25], NiN [26], IrNi [27], PdPb, PtPb and PdFe [28], $AuNi_{0.5}Fe$ [29], and Pd_3Co [30], with the highest ORR activity gains, compared to Pt catalysts, observed with a Pd core [24,30-32]. The unique Pt_{ML} synthesis involves the underpotential deposition

(UPD)[3] of a Cu_{ML} onto the core material in a monolayer-limited reaction, followed by the galvanic displacement of the Cu by the more noble Pt metal to give interconnected 2D nanoclusters of Pt with monoatomic height, and ultimately yield catalysts with low Pt-loading. Significantly, this synthesis was demonstrated in gram-scale quantities using a Pd [33] and a Pd_2Co core [34]. A variation of this procedure was also reported whereby a mixed-monolayer comprising Pt and late transition metals Au, Pd, Ir, Rh, Ru, Re or Os, were prepared on a Pd core with up to 20-fold increases in ORR activity compared to traditional all-Pt catalysts. The enhancement was attributed to low OH coverage on the active Pt sites due to the interaction of the underlying Pd core, and the presence of the neighbouring transition metal [35,36]. Finally, ORR studies in alkaline solution were carried out on Pt_{ML} on (111) surfaces of Au, Ag, Pd, Rh and Ir, and the (0001) surface of Ru, and nanoparticles of the same, supported on carbon [37]. The ORR kinetic currents of the materials showed a volcano-type dependency on the *d*-band center of the Pt_{ML} with the Pd(111) and Pd/C core catalysts positioned at the volcano peak.

The Strasser group has investigated dealloyed Pt intermetallic nanoparticle materials as highly active acidic ORR catalysts. Dealloying is the incomplete removal of the less noble component(s) by selective electro-dissolution from a metallic alloy precursor. Optionally, a subsequent annealing treatment results in a catalyst with an alloyed core and a Pt shell surface (*vide infra)* [38]. Initial reports described dealloyed Pt-Cu materials used in both RDE

[3] Underpotential deposition is the deposition of a metal (M1) monolayer onto a different metal substrate (M2) at a more positive potential than the Nernst potential of bulk deposition (that is, deposition of M1 onto M1 substrate). The UPD potential is thus too positive for bulk deposition to occur, and thus limited to a monolayer coverage of M1 onto M2.

and MEA experiments [39-42]. Initial activities higher than 0.6 A mg_{Pt}^{-1} and 1000 μA cm_{Pt}^{-2} at 0.9 V_{RHE} were recorded, values well beyond the DOE targets quoted in Section 4.1. Similar to Mukerjee's observations for Pt-Co alloy catalysts, the enhanced activity was attributed to compressive strain in the Pt shell which causes a shift in the electronic band structure of Pt, thereby weakening the chemisorption of oxygen-containing species [39]. Due to instability of the Pt-Cu based catalysts under fuel cell conditions, the group later performed a survey of PtM_3 (M = Cu, Co, Ni) and $PtNi_3M$ (M = Cu, Co, Fe, Cr) alloy precursors [38]. The best results (0.47 A mg_{Pt}^{-1} and 406 μA cm_{Pt}^{-2} at 0.9 V_{RHE}) were obtained from the catalyst with dealloyed near-surface composition of $Pt_{48}Ni_{48}Cu_4$ (from a $Pt_{20}Ni_{60}Cu_{20}$ precursor). The presence of Ni was found to stabilize the catalysts compared to previous PtCu-based materials and the authors again suggested that compressive strain and electronic effects between the Ni and Pt components affect the chemisorption of ORR intermediates and lower the overpotential for the reaction compared to pure Pt. The success with Ni-based alloys led the group to pursue more in-depth investigations on $PtNi_3$ and $Pt_{1-x}Ni_x$ (x = 0.14 – 1) precursor formulations [43,44]. The dealloyed $PtNi_3$ catalyst achieved 0.29 A mg_{Pt}^{-1} at 0.9 V_{RHE}, that is, 7 to 8 and 2 to 3 times higher mass activity than a heat treated Pt catalyst with similar particle size, and a commercial Pt catalyst respectively. The area-specific activity was 1491 μA cm_{Pt}^{-2}, a 2 to 3-fold and 5 to 6-fold enhancement over the same Pt catalysts. [43] The best ORR results in the $Pt_{1-x-}Ni_x$ series of nanoparticles appeared at x =0.74, after 200 dealloying potential cycles (0.06 to 1 V_{RHE}, 500 mV s^{-1}) and 4000 stability cycles (0.5 to 1 V_{RHE}, 50-100 mV s^{-1}) where kinetic current densities of 0.44 A mg_{Pt}^{-1} and 1185 μA cm_{Pt}^{-2} at 0.9 V_{RHE} were achieved [44].

Stamenkovic *et al.* have reported Pt 'skin' and Pt 'skeleton' surfaces synthesized in an ultra high vacuum (UHV) argon-filled arc-melting furnace. Annealing of a Pt-M alloy (M = Co, Ni, Fe) forms the Pt skin-type catalysts due to the thermodynamics of surface segregation [45,46]. The segregation of Pt to the surface is balanced by the depletion of Pt in the next 2 or 3 sub-layers so that the concentration profile oscillates around the bulk alloy value. On the other hand, potential cycling, or simply immersion in 0.1 M $HClO_4$ results in Pt skeleton-type materials. The acid treatment causes the instantaneous dissolution of the non-noble metal M from the near surface layers, to leave a pure Pt arrangement. In both cases, the outer Pt layers protect the inner transition metal atoms from dissolution so that their electronic and geometric influences on the surface Pt activity is preserved [47]. The highest ORR activity to date was reported for a well-defined single crystal Pt_3Ni (111) extended surface with a Pt skin [48]. The activity was 10 times higher than a Pt (111) surface and a remarkable 90 times higher than the state-of-the-art Pt/C catalyst at that time. The high performance was attributed to a positive shift in the adsorption potential of oxide species, resulting in weaker interactions between the Pt surface sites and non-reactive oxygenated species (electronic effect). Thus, the surface had an increased availability of Pt sites for O_2 adsorption. Efforts have been made to recreate the same type of structure as a nanoparticle. The group has recently reported the synthesis of such a material, but have not reported ORR activity [49,50]. The challenge remains to synthesize stable Pt skin Pt_3Ni nanoparticles with exclusively (111) facets *and* comparable activity to the analogous extended surfaces. Two issues are that annealing nanostructures, as opposed to annealing extended surfaces, can result in sintering/particle size growth/Ostwald ripening and ultimately loss of active surface area, and nanoparticle surfaces have an

abundance of corner and edge sites that preferentially adsorb inactive oxygenated species decreasing the ORR activity [51].

Publications by the Dahn group on sputtered NSTF-supported Pt-Ni ORR catalysts were discussed in Section 3-1 [52-56]. Compared to traditional thicker carbon-supported Pt catalysts, the NSTF-type electrodes have been shown to experience a smaller loss in current density as the Pt loading decreases below 0.2 mg cm^{-2}. Furthermore, unlike carbon supports, the NSTF support is non-corroding. Stamenkovic and co-workers have also reported sputtered Pt-Ni alloy catalysts supported on the dislodged whiskers of a NSTF in RDE systems [57]. The authors found that in general Pt-Ni/NSTF alloys had superior activity to Pt-Co/NSTF alloys. The most superior specific and mass activity was recorded for Pt-Ni with 55 wt.% Pt loading, that is, it was 10 and 2.5 times more active than commercial Pt/C by real surface area and mass respectively. Given the above discussion it is clear that Pt-Ni is a very attractive material for catalytic studies of the oxygen reduction reaction, and that a GLAD-based study of this material is imperative. This chapter therefore addresses preliminary studies of this nature.

For this study, we deposited the Ni_{NP} directly onto glassy carbon disk electrodes (GDE) with a geometric surface area, A_{geo} of 0.196 cm^2. After assembling into the RDE apparatus, the A_{geo} of the Ni_{NP} film is 0.126 cm^2. Two oblique deposition angles were investigated, $\alpha = 85°$ and $\alpha = 88°$. To differentiate between the Ni_{NP} prepared at the two deposition angles, the substrate is denoted as $Ni_{NP(85)}$ or $Ni_{NP(88)}$ respectively. This angle was changed to indirectly probe the effect of changing the density of, or wall-to-wall distance between, the posts. The density of the posts may have an effect on the distribution of platinum during the Pt depositions andor the mass transport of oxygen to the prepared catalyst surface. For example, a recent theoretical study by Debe suggests that for NSTF

catalysts the rate of physisorption of O_2 on the catalyst surface and therefore the observed current density for the ORR, is related to the compactness of the catalyst's surface area distribution (*i.e.* surface area per unit volume) [58].

Pt was deposited in three ways on the Ni_{NP} substrate. The first two methods were the traditional Pt deposition and the *Pt CE deposition* as described in the previous chapter. In the third method, the *Pt CE deposition* was performed twice on some substrates to afford $Pt_{CE2X}Ni_{NP}$/GC electrodes (see Experimental Section 4.4.4). Based on the mechanism of the deposition (Section 1.4.1), we presumed that if the Ni_{NP} is not fully covered by Pt during one *Pt CE deposition*, then, in the second deposition, Pt would only nucleate on those areas of exposed Ni. The objective was therefore to create a continuous coating of Pt over the base metal to protect it from the electrochemical environment. Finally, activity studies were performed in both basic and acidic media.

4.2 Results and Discussion

4.2.1 Comparison of the depositions of $Pt_{CE}Ni_{NP(85)}$/GC and $Pt_{Tr}Ni_{NP(85)}$/GC

Figure 4-1 shows the deposition profiles for the preparation of $Pt_{CE}Ni_{NP(85)}$/GC using the *Pt CE deposition* over nickel nanopillars supported on a 5 mm diameter glassy carbon disk. Compared to the deposition of $Pt_{CE}Ni_{NP(85)}$ supported on silicon wafer substrates (Figure 3-3), the Pt CE behaved similarly in that it stabilized at ~1.3 V and the potential of the $Ni_{NP(85)}$/GC WE did not exhibit a large rise from its initial potential. On the other hand, the WE potential did stabilize at a much lower voltage than that observed for silicon wafer-supported $Ni_{NP(85)}$ (~-2 V versus ~-1 V). Nevertheless, we believe that the mechanism of the deposition did not change significantly. Firstly, hydrogen evolution did occur over the WE at short times. Indeed, we had to modify the experimental apparatus because the bubbles of H_2 were trapped on the vertically aligned WE and insulated the WE from the electrolyte. The WE was tilted as shown in Figure 4-2 to allow the H_2 to escape the surface rather than collect at the surface. Secondly, Pt was detected in the $Pt_{CE}Ni_{NP(85)}$/GC deposits by ICP-MS. Three samples had an average Pt mass of 6 μg_{Pt}. This is far below the Pt mass detected in $Pt_{CE}Ni_{foam}$ (210 μg_{Pt}) (Chapter 2) and $Pt_{CE}C$ (200 μg_{Pt}) (Chapter 5). We are unsure of the reason for this discrepancy but suspect that the excessive hydrogen evolution over such a small geometric surface area WE may have slowed the rate of Pt deposition onto the $Ni_{NP(85)}$/GC so that far less Pt is deposited during the hour duration of the experiment.

Figure 4-1 *Potential profile of the electrodes during the* Pt CE deposition *of* $Pt_{CE}Ni_{NP(85)}$*/GC at – 100 mA for 1 hour in 2.0 M* NH_4Cl*. The* Ni_{NP} *were deposited directly onto a 5 mm diameter GC disk.*

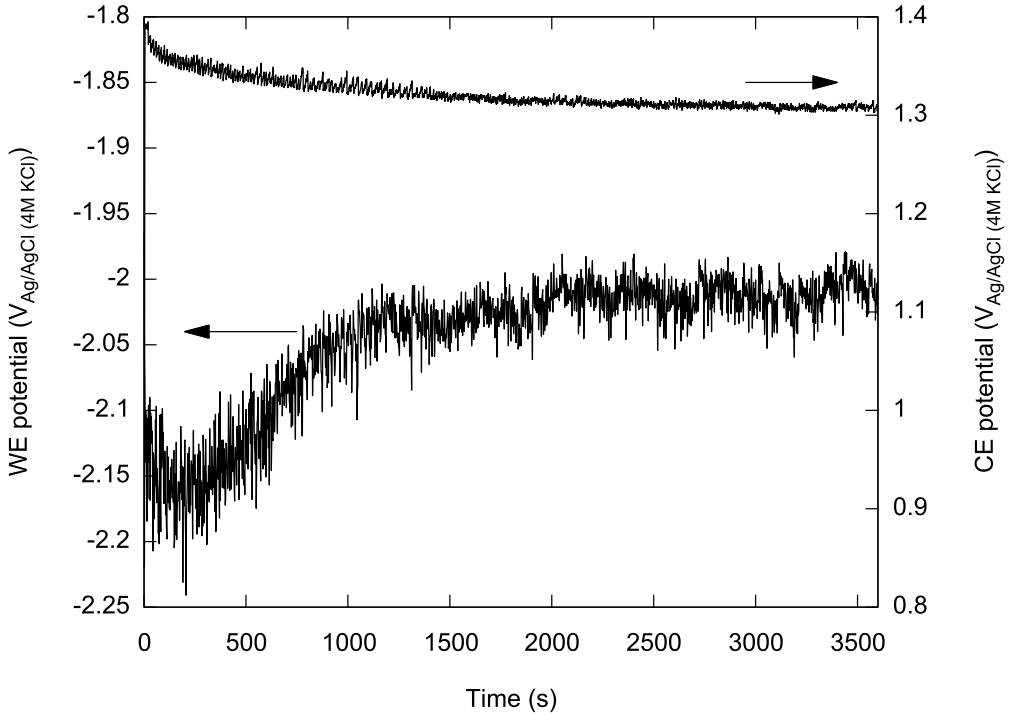

Figure 4-2 *Apparatus used for the* Pt CE deposition *on* Ni_{NP}*/GC working electrodes.*

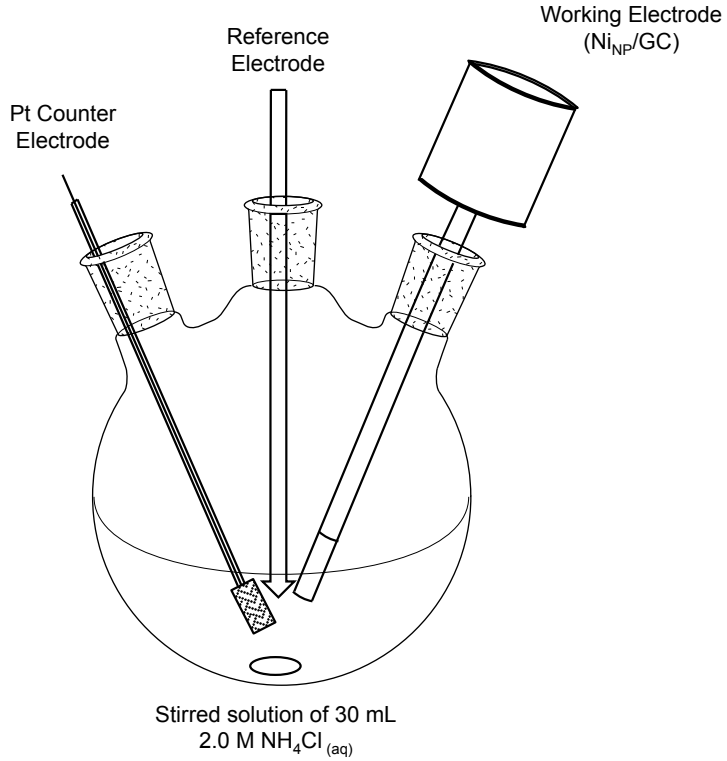

Figure 4-3 shows the deposition current profile for $Pt_{Tr}Ni_{NP(85)}$/GC. This catalyst was prepared in a stirred acidic solution of 0.12 mM K_2PtCl_6 by applying a potential of -100 mV versus the reference electrode. This potential is far below the equilibrium redox potential for the $[PtCl_6]^{2-}$/Pt couple (522 mV) [59]. Interestingly, the deposition on $Ni_{NP(85)}$/GC was quite different to that on Ni_{NP} supported on silicon wafer (Figure 3-4, reproduced as an inset in Figure 4-3.) Although the steady state current of both depositions was -1 mA cm^{-2}, the deposition on $Ni_{NP(85)}$/GC initially increased to an oxidizing current of 1.5 mA cm^{-2}. This feature was observed every time this deposition was performed. To this day we do not have a clear understanding of the origin of this phenomena but the current profile suggests that the WE undergoes some type of surface oxidation before the deposition of Pt occurs. It is also possible that Ni dissolution in the acid is occurring at this potential, which ceases either due to passivation by formation of surface oxides or by deposition of Pt.

If all of the Pt present in the electrolyte was deposited on the working electrode, we would expect the Pt mass in $Pt_{Tr}Ni_{NP(85)}$/GC to be on the order of 580 μg_{Pt}. However, for three samples, the average mass of Pt deposited according to ICP-MS data is 8.4 μg_{Pt}, on scale with the mean Pt mass of $Pt_{CE}Ni_{NP(85)}$/GC deposits. These lower than expected Pt loadings on $Ni_{NP(85)}$/GC substrates suggest a link to some nature of GC substrate limiting the mass of Pt deposition.

Figure 4-3 *Current profile of the traditional potentiostatic deposition on to GC-supported $Ni_{N(85)P}$ to create $Pt_{Tr}Ni_{NP(85)}$. Conditions are -100 $mV_{Ag/AgCl\ (4M\ KCl)}$ in 1.2 x 10^{-4} M K_2PtCl_6/0.01 M $HClO_4$ at room temperature. Inset: Current profile of the traditional potentiostatic deposition onto silicon wafer-supported $Ni_{NP(85)}$ to fabricate $Pt_{Tr}Ni_{NP(85)}$ under the same conditions.*

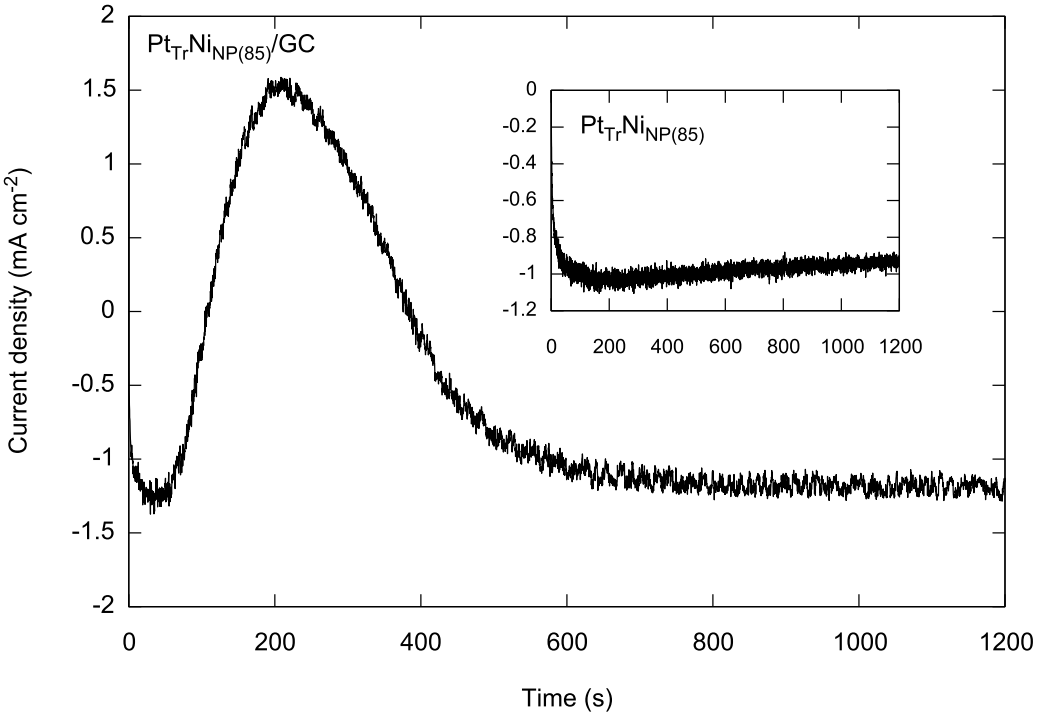

4.2.2 Microscopic comparison of $Ni_{NP(85)}$, $Pt_{CE}Ni_{NP(85)}$/GC and $Pt_{Tr}Ni_{NP(85)}$/GC

SEM images of $Pt_{CE}Ni_{NP(85)}$/GC and $Pt_{Tr}Ni_{NP(85)}$/GC are shown in Figure 4-4. As a comparison, the image of silicon wafer-supported $Ni_{NP(85)}$ is also included. The underlying $Ni_{NP(85)}$ appear largely intact, and its structure is visible under the Pt deposit. The data supports that the surface of the $Ni_{NP(85)}$ substrate has been roughened by the Pt depositions as previously observed for silicon wafer-supported substrates (Figure 3-5). However, due to the difficulty and cost associated with microtoming the reusable GC substrate, we could not obtain cross-sectional views of the deposits. Therefore, we could not directly confirm Pt

segregation to the top of the pillars in the traditional Pt deposition as previously observed for silicon substrates (Figure 3-5c). However, previous reports of Pt depositions on GLAD nanorods have suggested that Pt has the tendency to accumulate on the tips of dense nanorods during sputtering deposition [2-4,6,8].

Figure 4-4 *Scanning electron micrographs showing plan views of a) silicon wafer-supported $Ni_{NP(85)}$, b) $Pt_{CE}Ni_{NP(85)}$/GC and c) $Pt_{Tr}Ni_{NP(85)}$/GC.*

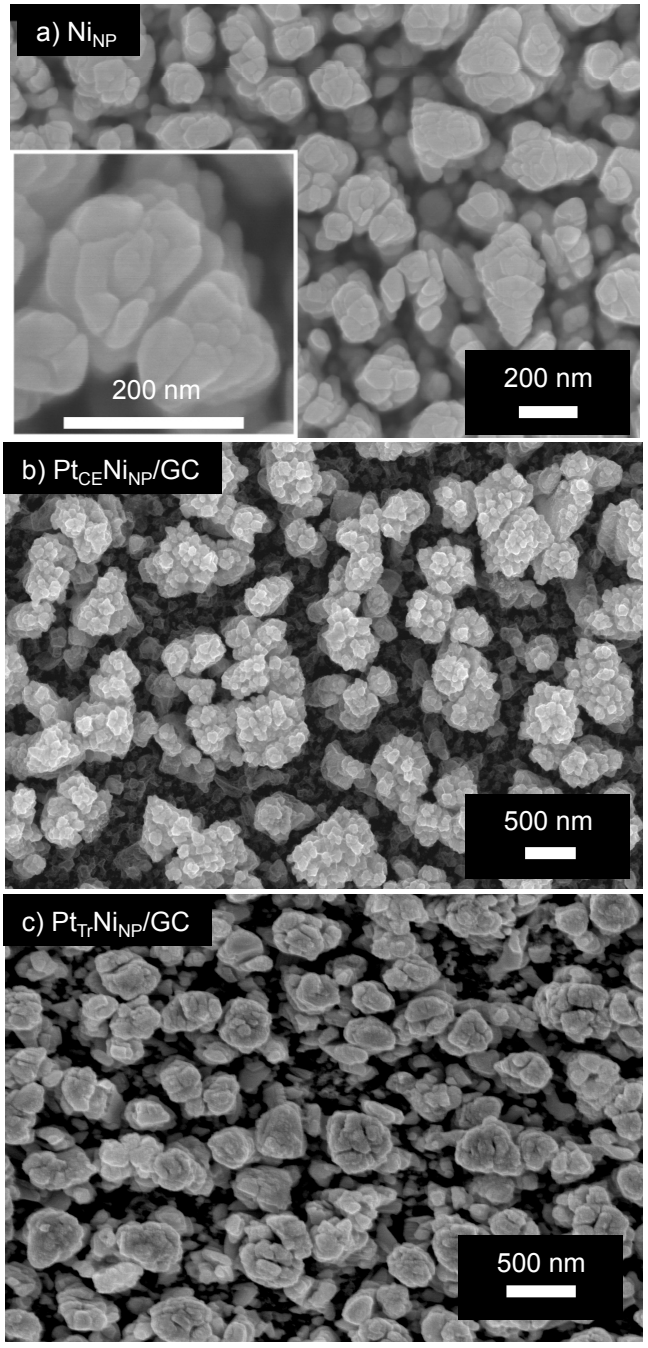

4.2.3 Cyclic voltammetry

The CV of $Ni_{NP(85)}$/GC is shown in Figure 4-5. Compared to the $Ni_{NP(85)}$ on silicon wafers, the CVs are quite similar. The latter CV showed a much larger hydrogen evolution peak because the minimum scan potential was lower in that case. Both CVs feature the Ni and/or NiO and/or α-$Ni(OH)_2$ reduction peaks at E_{peak} ~ 0.6 V_{RHE}, but the corresponding anodic peak at ~0.22 V is broad and not well defined.

Figure 4-5 *Cyclic voltammogram of $Ni_{NP(85)}$/GC in 1M KOH at 25°C with a scan rate of 10 mVs^{-1}. Inset: Cyclic voltammogram of $Ni_{NP(85)}$ supported on a silicon wafer. Both voltammograms are normalized by the geometric area of the substrates: The GC disk is 0.196 cm^2 and Si wafer is 1 cm^2.*

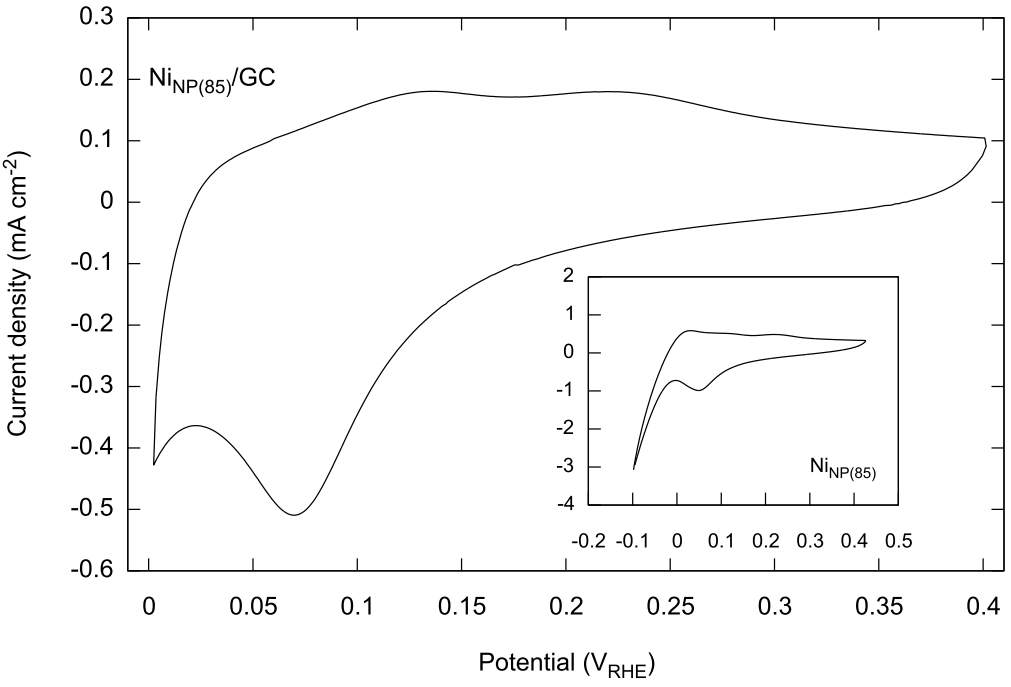

Cyclic voltammetry of the two Pt deposits confirm the successful deposition of Pt on the $Ni_{NP(85)}$/GC substrates. The CV of $Pt_{CE}Ni_{NP(85)}$/GC is shown in Figure 4-6. It displays the typical HUPD region of Pt, that is hydrogen adsorption and desorption peaks, between 0.02 and0.18 V_{RHE}, although they are

quite broad and not well-defined. Compared to the same deposit on silicon wafers (shown inset) the HUPD region has a wider potential range.

Figure 4-6 *Cyclic voltammogram of $Pt_{CE}Ni_{NP(85)}$/GC in 1M KOH at 25°C with a scan rate of 10 mVs^{-1}. Inset: Cyclic voltammogram of $Pt_{CE}Ni_{NP(85)}$ supported on a silicon wafer. Both voltammograms are normalized by the geometric area of the substrates: The GC disk is 0.196 cm^2 and Si wafer is 1 cm^2.*

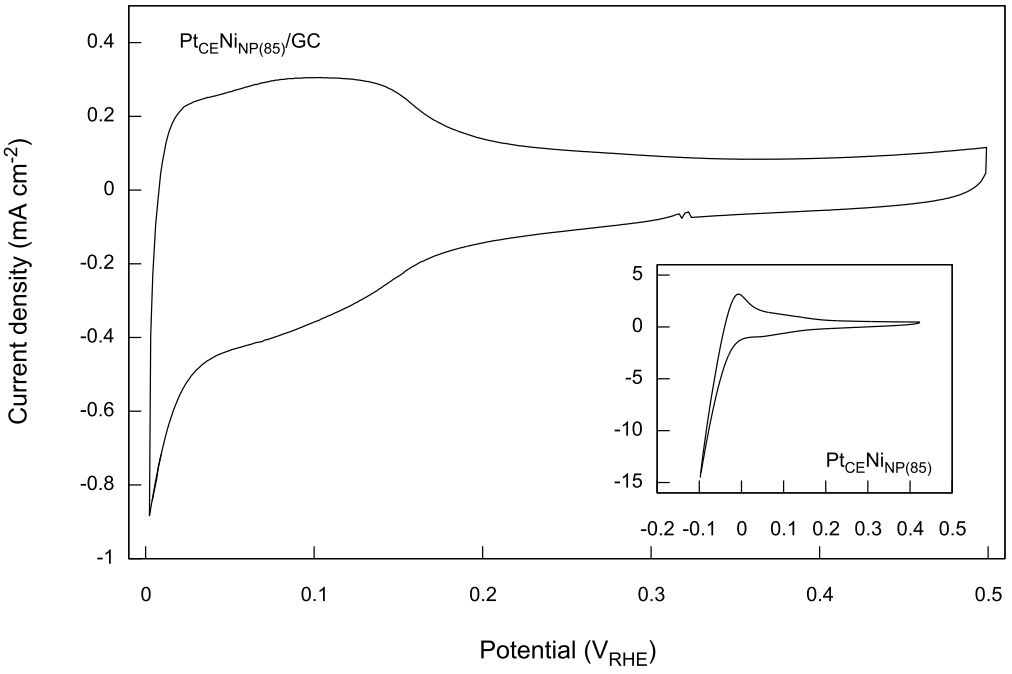

In contrast, the HUPD region of $Pt_{Tr}Ni_{NP(85)}$/GC is very well defined (Figure 4-7). Indeed the CV resembles a pure Pt surface and suggests that the Pt deposit is in fact segregated at the tips of the nanopillars. Interestingly, such a well-defined CV was not obtained on deposits on the silicon wafers (inset). The CVs of $Pt_{Tr}Ni_{NP}$ resembled those obtained with the *Pt CE deposition* shown in Figure 4-6.

Figure 4-7 *Cyclic voltammogram of $Pt_{Tr}Ni_{NP(85)}$/GC in 1M KOH at 25°C with a scan rate of 10 mVs^{-1}. Inset: Cyclic voltammogram of $Pt_{Tr}Ni_{N(85)P}$ supported on a silicon wafer. Both voltammograms are normalized by the geometric area of the substrates: The GC disk is 0.196 cm^2 and Si wafer is 1 cm^2.*

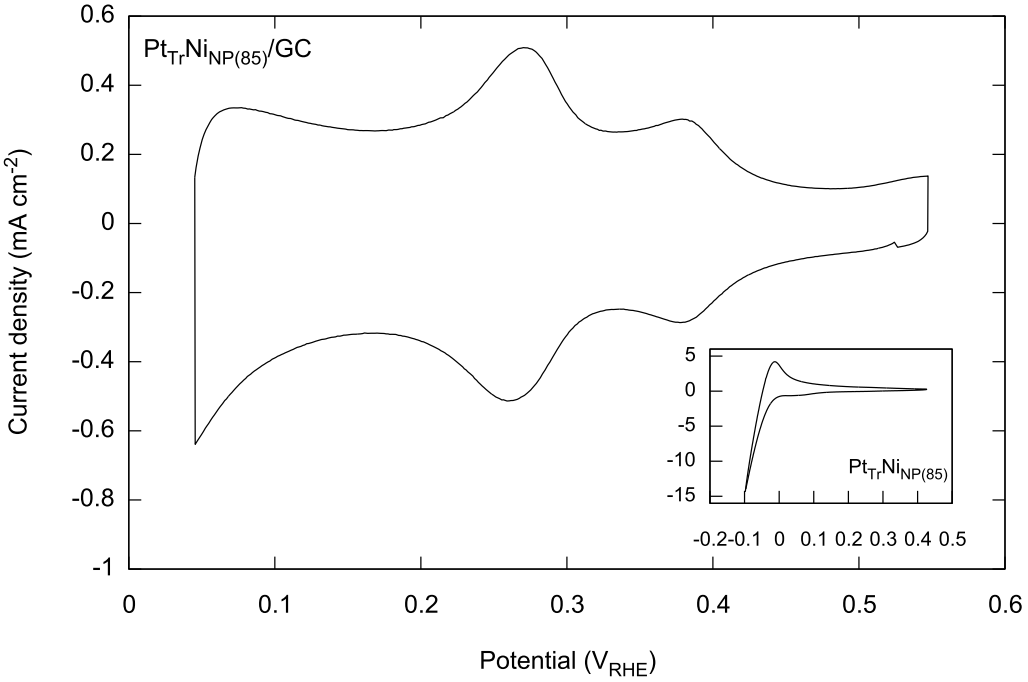

If we treat both $Pt_{CE}Ni_{NP(85)}$/GC and $Pt_{Tr}Ni_{NP(85)}$/GC as pure Pt surfaces, we can estimate the real surface area from the CVs in the above figures by using Equation 2-7 and assuming the charge density of Pt is 210 μC cm^{-2}. According to this method, the $Pt_{CE}Ni_{NP(85)}$/GC has an electro-active real surface area (ESA) of 4.4 cm^2, while $Pt_{Tr}Ni_{NP(85)}$/GC is 8.2 cm^2. However, four $Pt_{CE}Ni_{NP(85)}$/GC samples had an average ESA of 1.9 cm^2, while for seven $Pt_{Tr}Ni_{NP(85)}$/GC sample, the mean ESA was 3.7 cm^2.

4.2.4 Evaluation of oxygen reduction activity of $Pt_{CE}Ni_{NP(85)}$/GC and $Pt_{Tr}Ni_{NP(85)}$/GC

Oxygen reduction activity of $Pt_{CE}Ni_{NP(85)}$/GC and $Pt_{Tr}Ni_{NP(85)}$/GC was determined using rotating disk electrode voltammetry. These methods are discussed in detail in the Appendices. CVs in N_2-saturated and O_2-saturated 1 M KOH of the catalysts in Figure 4-8a and b show that both catalysts are active towards the ORR. The O_2 voltammograms also display the typical mixed kinetic and diffusion controlled region between 700 and 1000 mV and the diffusion-controlled region from 50 to 700 mV.

Figure 4-8 *Cyclic voltammetry of a) $Pt_{CE}Ni_{NP(85)}$/GC (4.42 μg_{Pt} and 4.4 cm^2) and b) $Pt_{Tr}Ni_{NP(85)}$/GC (8.51 μg_{Pt} and 1.9 cm^2) in nitrogen- and oxygen-saturated 1M KOH at 25°C. Scan rates were 10 mVs^{-1} and rotation rate for O_2 CV is 1000 rpm. c) Comparison of baseline-corrected oxygen reduction currents of both catalysts in the negative-going sweep.*

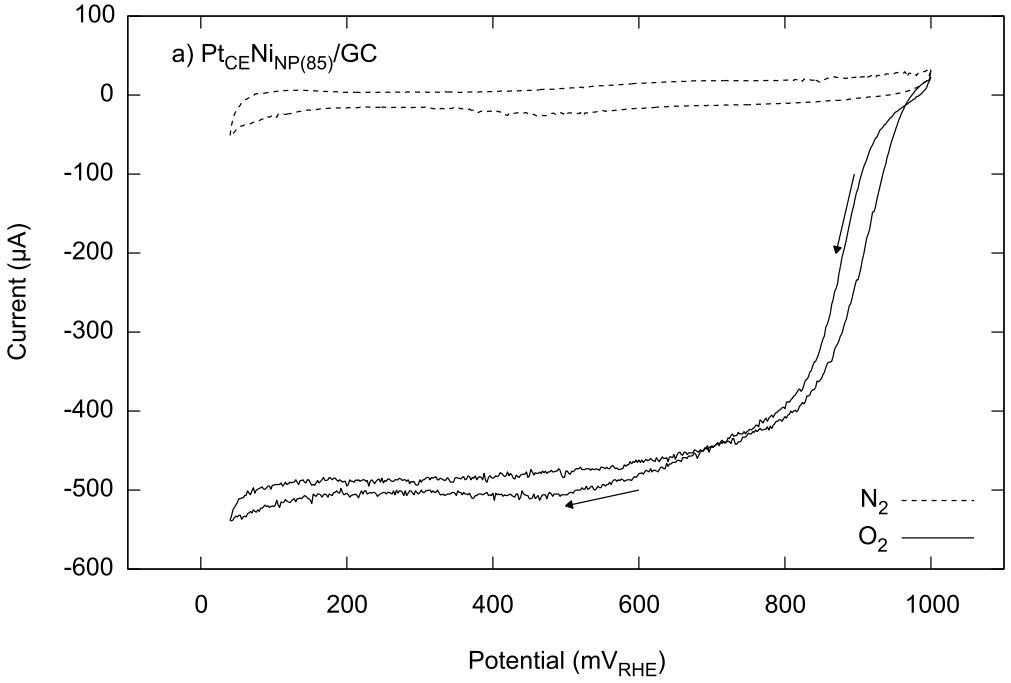

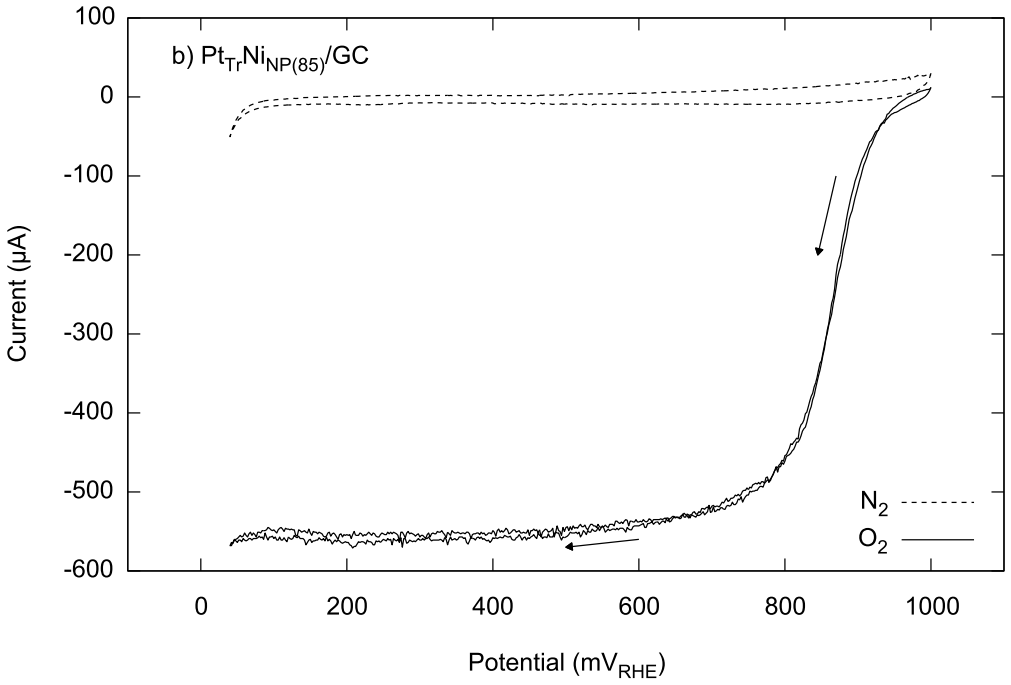

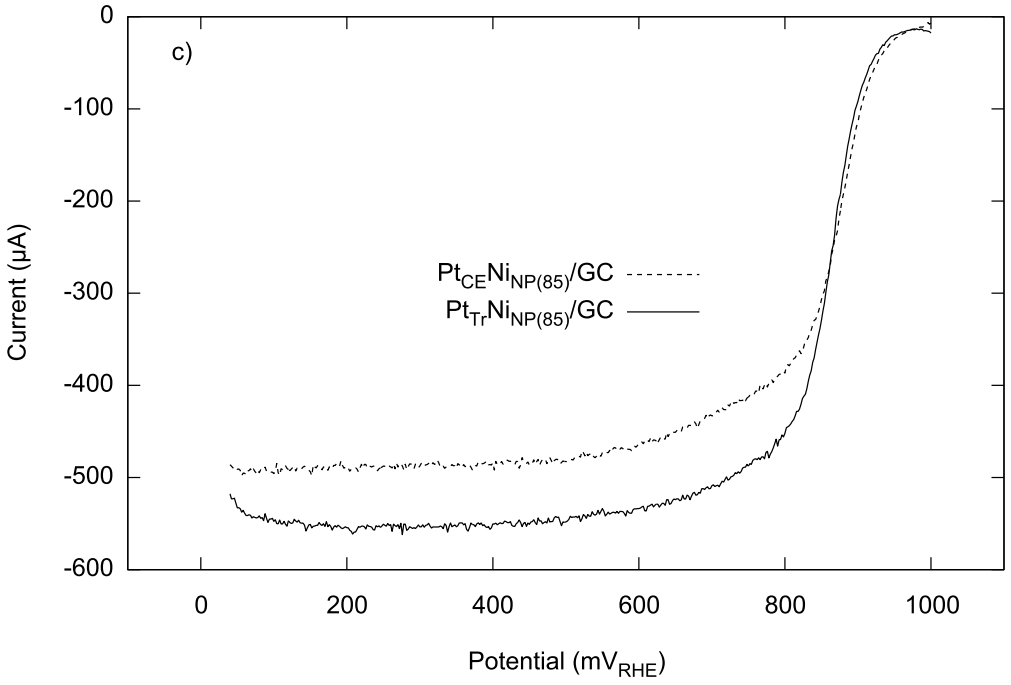

Figure 4-8c shows the baseline-corrected voltammograms for the two catalysts. Without applying a Koutecky-Levich correction (see Section A.2.3), both catalysts appear to have similar activity towards the oxygen reduction reaction. In both

cases, the onset potential was *circa* 800 mV_{RHE}. The theoretical limiting current for both catalysts should be 0.68 mA.[4] $Pt_{CE}Ni_{NP(85)}$/GC has a limiting current of 0.49 mA while $Pt_{Tr}Ni_{NP(85)}$/GC has a limiting current of 0.55 mA. Both values are within 30% of the expected value. As the limiting current depends on the geometric area of the electrode, the discrepancy may be due to the inadequate coverage of the GC disk with Pt, given that the Pt loadings are ultra-low. The Tafel plots for the two catalysts in the mixed kinetic and diffusion-limited region are shown in Figure 4-9. The currents have been normalized by the Pt ESA calculated from CVs such as those in Figures 4-6 and 4-7.

Both catalysts had an approximate Tafel slope of 60 mV dec^{-1}, that is, the slope expected for Pt ORR catalysts. As outlined in section A.2.3, we can use the Tafel plots to determine the exchange current density over the two catalysts. The exchange current density, j_0, is that at the Nernst potential for the oxygen reduction reaction, 1.229 V_{RHE}, and represents the intrinsic rate of electron transfer. The larger the magnitude of j_0, the more rapidly the reaction can occur. Both catalysts had j_0 values of -2.4 x 10^{-4} μA cm^{-2}. Therefore, on an ESA basis the two catalysts had similar activities. This is an interesting result as it suggests that the position of the underlying Ni layer does not have an effect on the Pt activity. In the $Pt_{CE}Ni_{NP(85)}$/GC catalyst, the Pt should be in intimate contact with Ni, whereas in $Pt_{Tr}Ni_{NP(85)}$/GC, the Pt is presumably segregated to the top of the Ni posts, yet the Pt activity is similar for the two structures.

[4] Based on Equation A-8, i_L = 0.68 mA for a disk with A_{geo} = 0.196 cm^2 using the following values determined for 1M NaOH, 25°C, 1 atm O_2 [63]: D_{O2} = 1.65 x 10^{-5} cm^2 s^{-1}, v = 0.011 cm^2 s^{-1} and O_2 solubility (concentration) = 8.4 x 10^{-7} mol cm^{-3}.

Figure 4-9 *Tafel plot in O_2-saturated 1M KOH at 25°C, 10 mVs^{-1} and 1000 rpm based on ESA-normalized kinetic currents for a) $Pt_{CE}Ni_{NP(85)}$/GC (4.4 cm^2) and b) $Pt_{Tr}Ni_{NP(85)}$/GC (1.9 cm^2) catalysts. Dashed double-headed arrows represent the best-fit line in the kinetic region of the Tafel plot.*

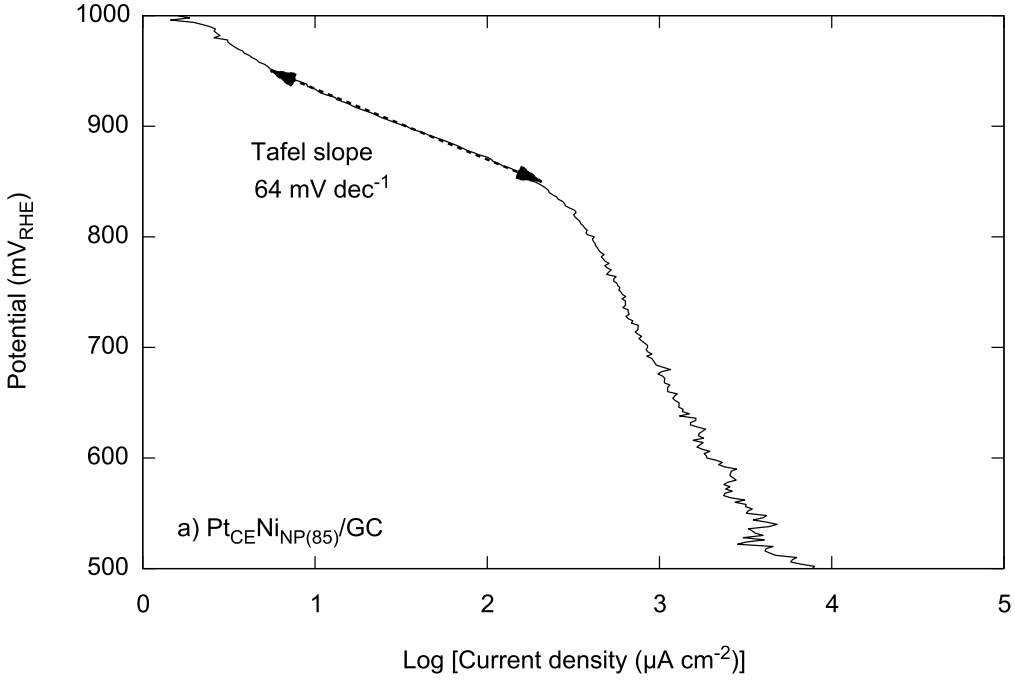

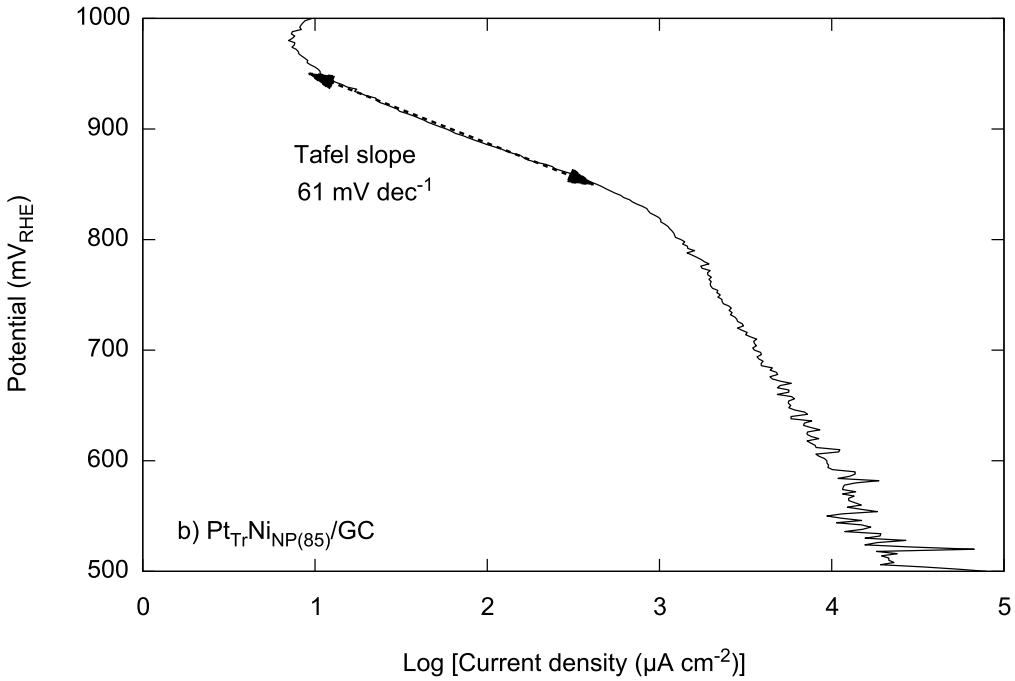

The same analysis was thus performed on the basis of the mass of Pt and ESA of the catalysts. The currents were therefore normalized by the product of each catalyst's Pt mass and estimated real surface area. The resulting Tafel plots are shown in Figure 4-10. The absolute exchange current density obtained for $Pt_{CE}Ni_{NP985)}$/GC was 5.3 x 10^{-2} mA cm^{-2} g^{-1} while the value for $Pt_{Tr}Ni_{NP(85)}$/GC was 2.8 x 10^{-2} mA cm^{-2} g^{-1}. Therefore, the $Pt_{CE}Ni_{NP(85)}$/GC appears to display a higher Pt catalyst utilization. Indeed, the specific surface area of this catalyst was ~ 1.0 cm^2 μg_{Pt}^{-1} while $Pt_{Tr}Ni_{NP(85)}$/GC had a specific surface area of only 0.22 cm^2 μg_{Pt}^{-1}. These values also reflect the tendency for the *Pt CE deposition* to produce a more conformal coating of Pt than the traditional method.

Figure 4-10 *Tafel plot in O_2-saturated 1M KOH at 25°C, 10 mVs^{-1} and 1000 rpm from kinetic currents normalized by the product of the catalysts' Pt masses and real surface areas for a) $Pt_{CE}Ni_{NP(85)}$/GC and b) $Pt_{Tr}Ni_{NP(85)}$/GC catalysts. Dashed double-headed arrows represent the best-fit line in the kinetic region of the Tafel plot.*

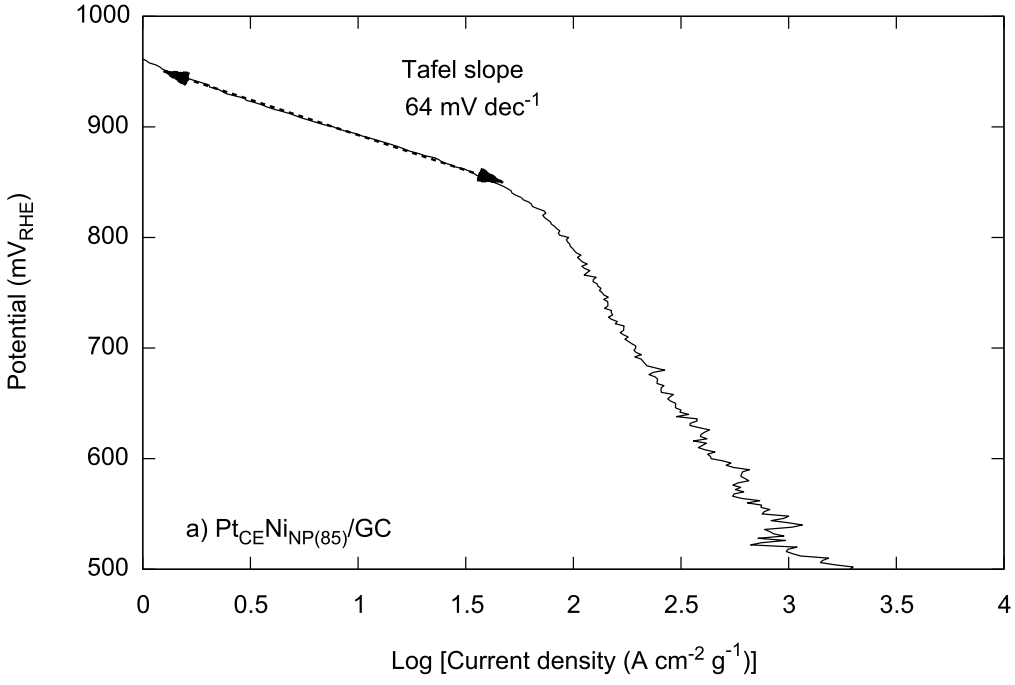

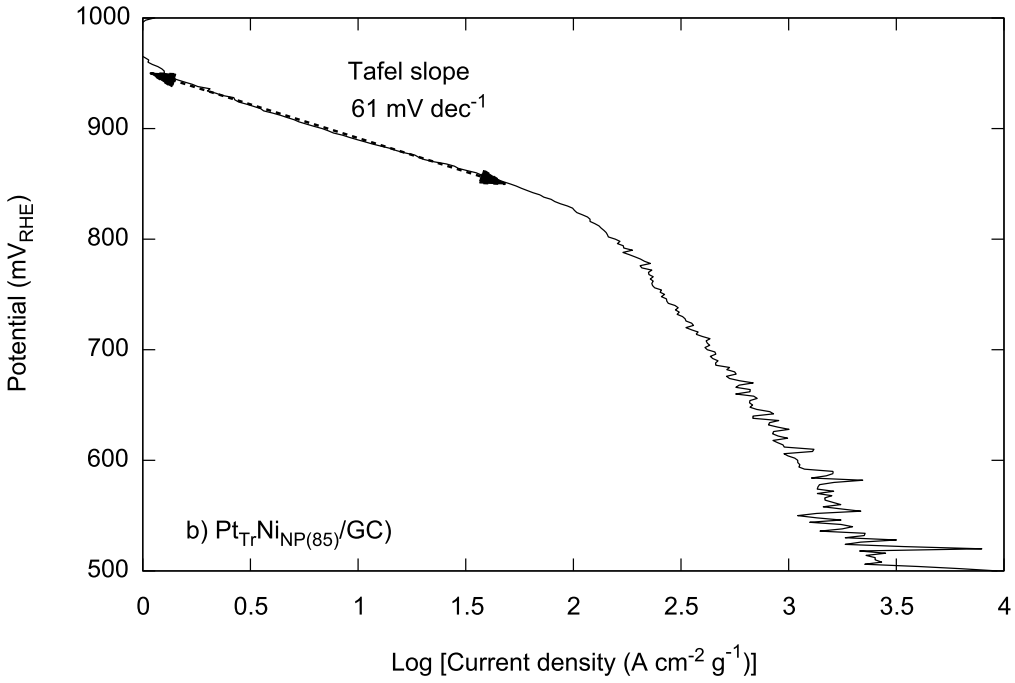

4.2.5 Deposition and characterization of $Pt_{CE2X}Ni_{NP(88)}$/GC

Based on the above results, we attempted to improve the performance of the catalyst prepared by the *Pt CE deposition* by increasing the coverage of the Ni layer with Pt. The ability to form a continuous layer of Pt over the $Ni_{NP(88)}$ underlayer would potentially protect the base metal from dissolution during activity experiments in acidic conditions. Further, we hypothesized that if we could increase the Pt loading, while keeping it low (< 250 μg), and concurrently preserve the conformal nature of the deposition, then we could increase the performance of the catalyst and any Pt-Ni interaction present. To further aid the homogeneity of the deposition, we adjusted the oblique angle of the deposition to α = 88°. The slight increase in α should widen the spacing between the posts and

possibly increase mass transport of Pt during deposition. A $Pt_{CE}Ni_{NP(88)}$/GC catalyst was also prepared at α = 88° as a comparison.

A $Pt_{CE2X}Ni_{NP(88)}$/GC catalyst was prepared by performing two successive *Pt CE depositions* on the same substrate and in the same solution, punctuated by reactivating the Pt CE by reducing its surface in a stream of hydrogen. Based on the mechanism of the deposition (Section 1.4.1), we suggest that if the $Ni_{NP(88)}$ is not fully covered by Pt during one *Pt CE deposition*, then, in the second deposition, Pt would only nucleate on those areas of exposed Ni.

Figure 4-11 shows the deposition profile of the step-wise deposition to prepare $Pt_{CE2X}Ni_{NP(88)}$/GC. The CE potential in both steps was ~1.3 V as expected, and has been omitted from the figure for clarity. The second step features a steady voltage for the duration of the deposition. It follows that the potential represents the hydrogen evolution and Pt deposition reactions, especially as it is quite close to the steady state potential in the first deposition. This result is consistent with our expectations. Pt is already present on the substrate, therefore there is no infinitesimal time before hydrogen evolution can commence and set up the mixed potential system. Though we did not characterize the Pt CE between the two steps, we believe its initial surface area did not change significantly. Besides, a typical Pt CE is used at most five times for *Pt CE depositions* before it is re-blackened without affecting reproducibility of results.

Figure 4-11 *Potential profile of the working electrodes during the* Pt CE deposition *of* $Pt_{CE2X}Ni_{NP(88)}$*/GC at – 100 mA for 1 hour in 2.0 M* NH_4Cl*. The Pt CE was removed from solution, washed with triply distilled water and dried in a stream of hydrogen before replacing in the cell and commencing the second deposition.*

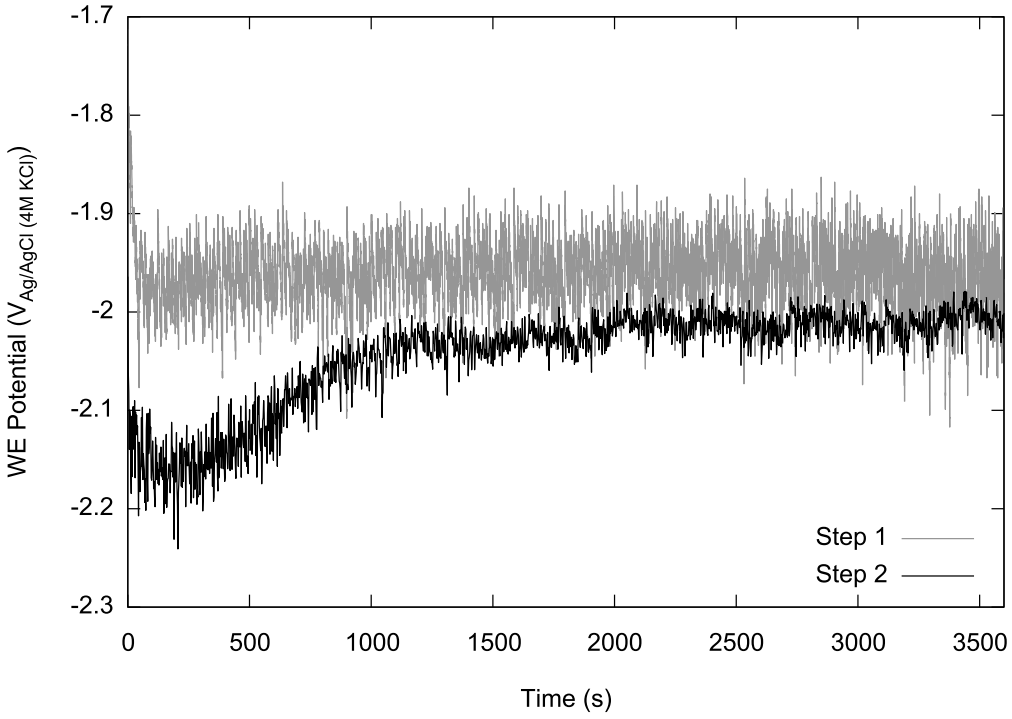

Scanning Electron Microscopy was used to compare the morphology of $Pt_{CE}Ni_{NP(88)}$/GC and $Pt_{CE2X}Ni_{NP(88)}$/GC. As a reminder, the $Ni_{NP(88)}$/GC catalyst substrates are prepared by GLAD deposition of Ni nanopillars at 88°. In contrast, the $Ni_{NP(85)}$ supported on silicon wafers were prepared by sputtering a Ti adhesion layer before the deposition of the Ni film and Ni nanopillars at α = 85°. Figure 4-12 shows the micrographs collected. Firstly, it appears that the $Pt_{CE2X}Ni_{NP(88)}$/GC has significantly more voids where nanopillars are missing. This extent of degradation was not observed for $Pt_{CE}Ni_{NP(85)}$/GC (Figure 4-4) or $Pt_{CE}Ni_{NP(88)}$/GC. The extra hour (step 2) under the conditions of the deposition may have contributed to this degradation. Secondly, the Pt deposited to form

$Pt_{CE}Ni_{NP(88)}$/GC seems to consist of more platelet-shaped particles (4-12b), while on $Pt_{CE2X}Ni_{NP(88)}$/GC the particles appear to be mostly spherical globules (4-12d). Moreover, the platelet feature of the Ni nanopillar themselves (see for example Figure 3-3d) appear completely obscured by the overlaying Pt in $Pt_{CE2X}Ni_{NP(88)}$/GC. We hoped that this continuous Pt layer would protect the base metal below and allow activity determination in acid media.

Figure 4-12 *Scanning Electron Micrographs of a) and b) $Pt_{CE}Ni_{NP(88)}$/GC and c) and d) $Pt_{CE2X}Ni_{NP(88)}$/GC at 15 kV, and 20 and 100K magnification respectively.*

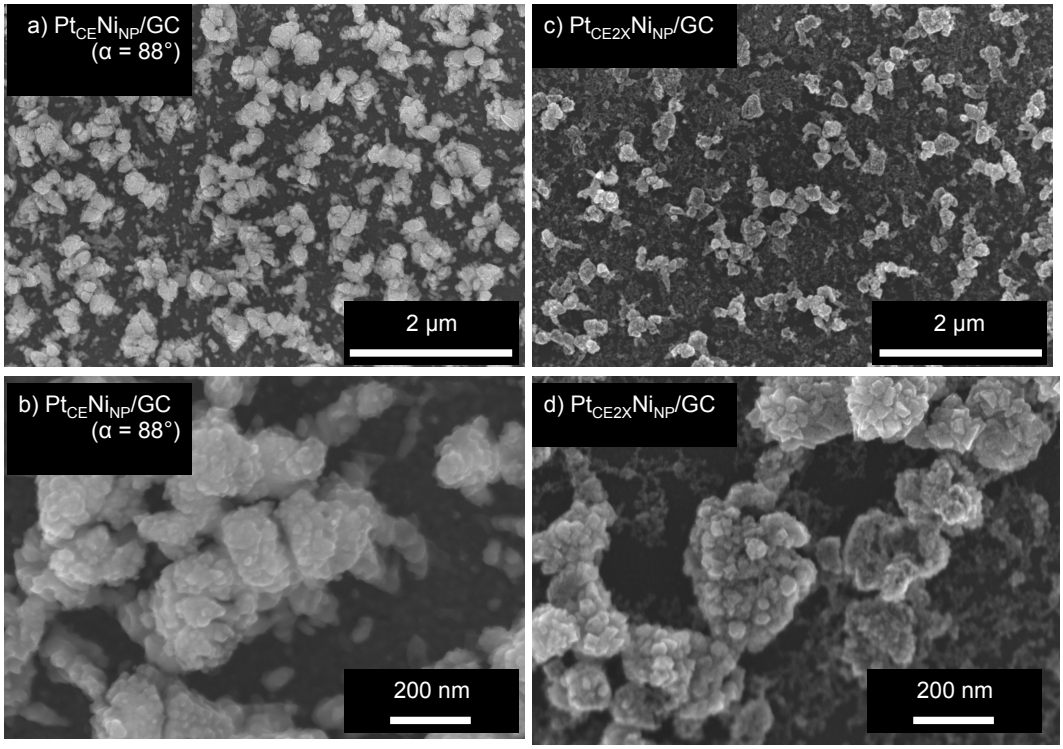

Cyclic voltammetry of $Pt_{CE}Ni_{NP(88)}$/GC and $Pt_{CE2X}Ni_{NP(88)}$/GC in 0.1 M $HClO_4$ is shown in Figure 4-13. The CVs portray typical Pt features, that is, the hydrogen region between 50 and 400 mV, the double layer region between 400 and 650 mV and the oxygen region above 650 mV. Treating the catalyst as pure polycrystalline Pt, the surface area of the catalysts based on this CV is 20.8 cm^2.

The mean surface area for such catalysts was ~15 cm^2. This is a marked improvement from the singly deposited $Pt_{CE}Ni_{NP(88)}$/GC that had an ESA of 4.7 cm^2. The mass of Pt in these deposits was on average 50 μg_{Pt} compared to 6 μg_{Pt} for $Pt_{CE}Ni_{NP(88)}$/GC. Thus, applying a second *Pt CE deposition* increased the Pt surface area and loading by factors of 3 and 8 respectively. Assuming the Pt particles are spherical, this suggests that the mean particle size has at least doubled. However, the SEM in Figure 4-12 did not confirm this feature.

Figure 4-13 *Cyclic voltammograms of $Pt_{CE}Ni_{NP(88)}$/GC and $Pt_{CE2X}Ni_{NP(88)}$/GC in 0.1M $HClO_4$ at 25°C with a scan rate of 10 mVs^{-1} at a) narrow potential range and b) wide potential range. The current is normalized by the geometric area of the GC disk, that is, 0.196 cm^2. The ESA of $Pt_{CE}Ni_{NP(88)}$/GC is 20.8 cm^2 and $Pt_{CE2X}Ni_{NP(88)}$/GC is 4.7 cm^2 from b).*

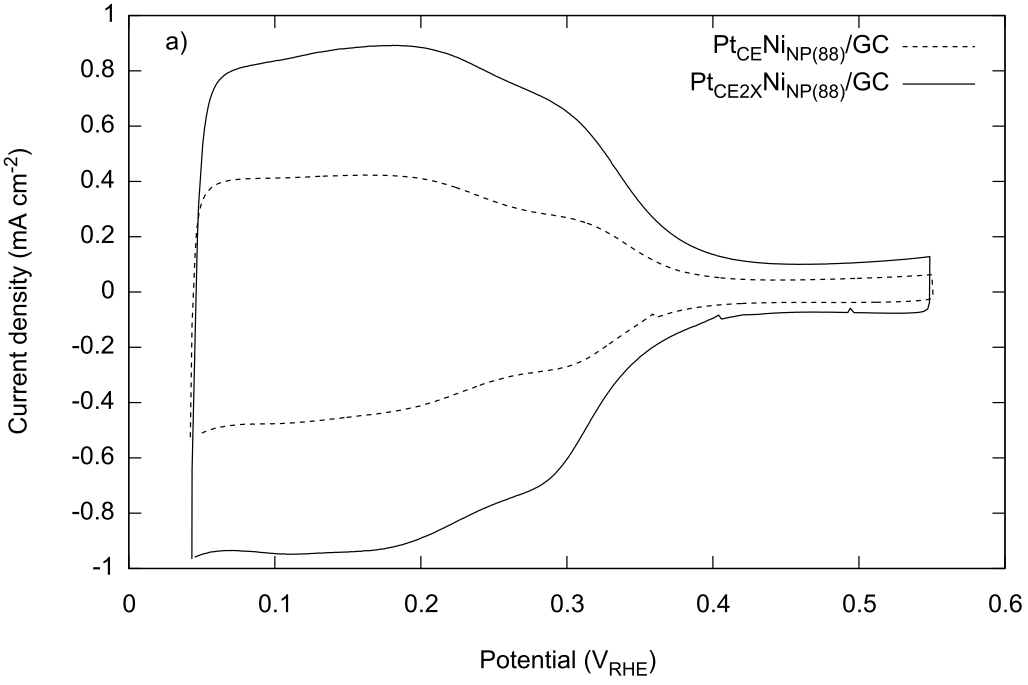

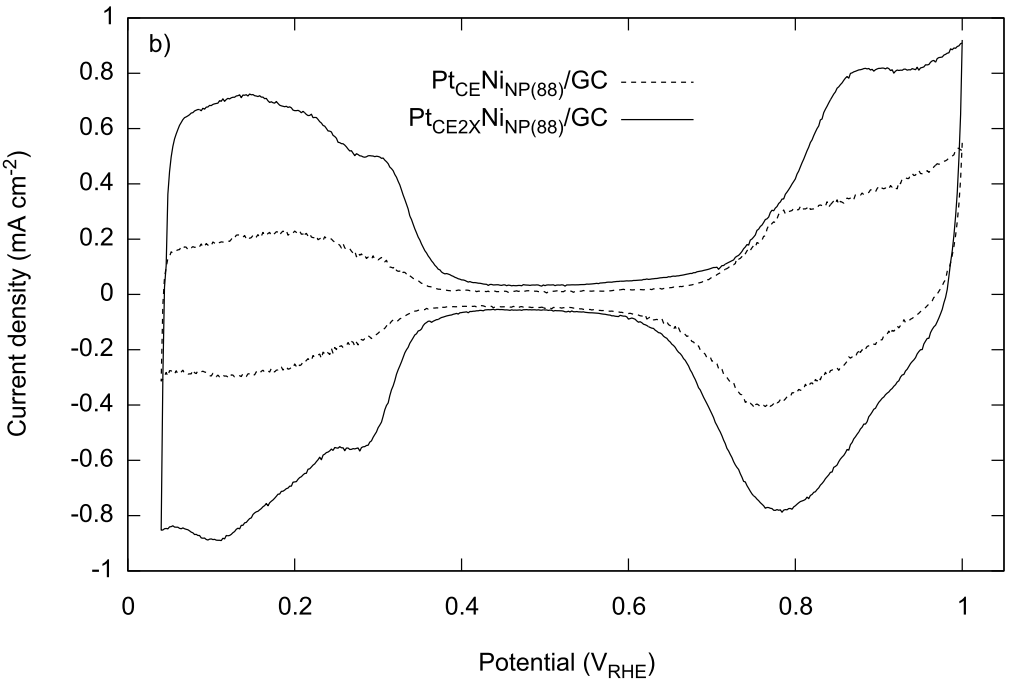

4.2.6 Oxygen reduction activity of $Pt_{CE2X}Ni_{NP(88)}$/GC

Oxygen reduction activity of $Pt_{CE}Ni_{NP(88)}$/GC and $Pt_{CE2X}Ni_{NP(88)}$/GC was determined in acidic solution with the hope that the Pt deposition would protect the underlying Ni metal from dissolution. Figure 4-14 shows the corrected currents for both catalysts in 0.1 M $HClO_4$ normalized by their real surface areas, and the associated Tafel plots based on their kinetic current densities. We note that the corrected currents in the diffusion-limited region for $Pt_{CE}Ni_{NP(88)}$/GC were quite noisy. Therefore, the Tafel analyses for both catalysts are performed in a more limited range of 0.9 to 1 V, which is still within 10 and 80% of the limiting currents.

Figure 4-14 *a) Corrected voltammograms for $Pt_{CE}Ni_{NP(88)}$/GC and $Pt_{C2XE}Ni_{NP(88)}$/GC in 0.1 M $HClO_4$ normalized by catalyst ESA. Baseline CVs were performed at 25°C and 10 mVs^{-1}. Oxygen CVs were performed at 25°C and 1000 and 1600 rpm respectively. ESA of $Pt_{CE}Ni_{NP(88)}$/GC is 4.7 cm^2 and $Pt_{CE}Ni_{NP(88)}$/GC is 20.8 cm^2. b)Tafel plot for $Pt_{CE}Ni_{NP(88)}$/GC in O_2-saturated 0.1 M $HClO_4$ and c) Tafel plot for $Pt_{CE}Ni_{NP(88)}$/GC in O_2-saturated 0.1 M $HClO_4$. Dashed double-headed arrows in Tafel plots represent the best-fit line in the kinetic region of the Tafel plot.*

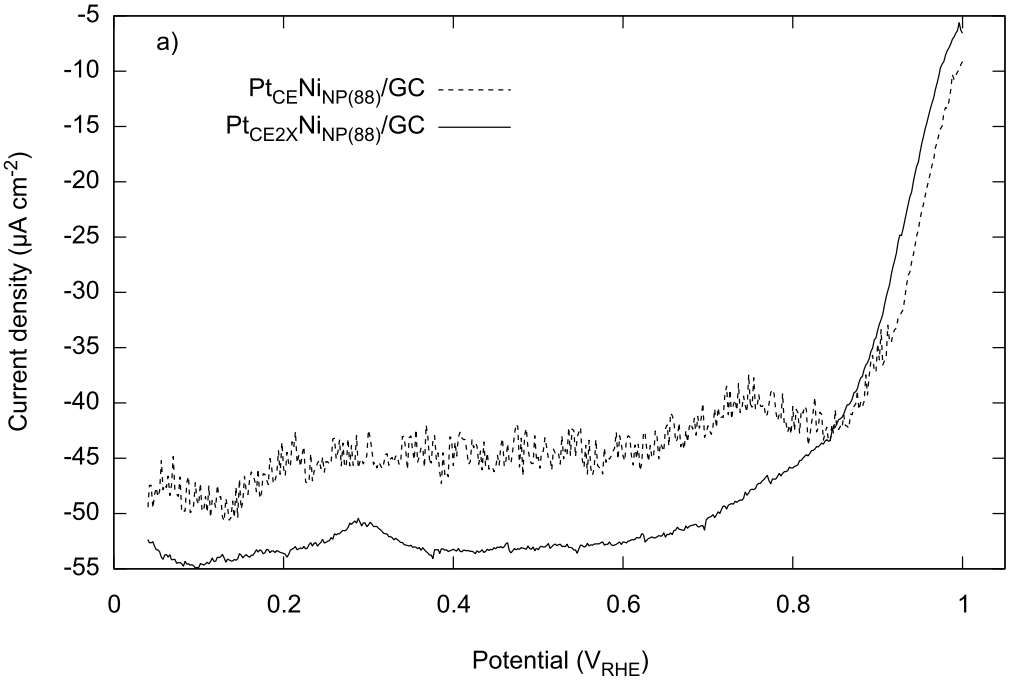

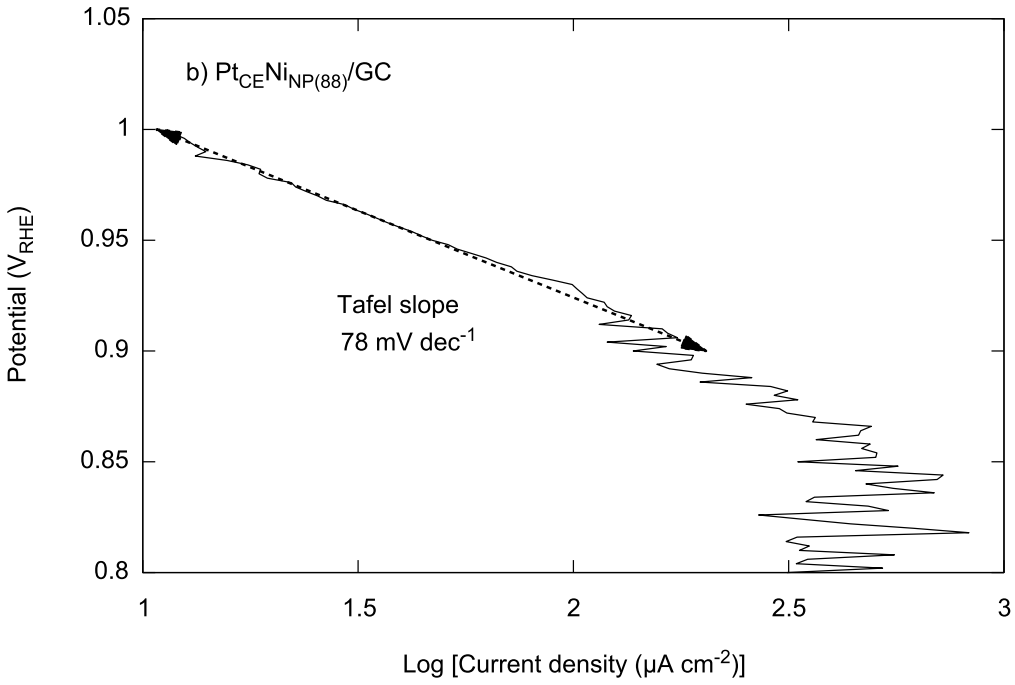

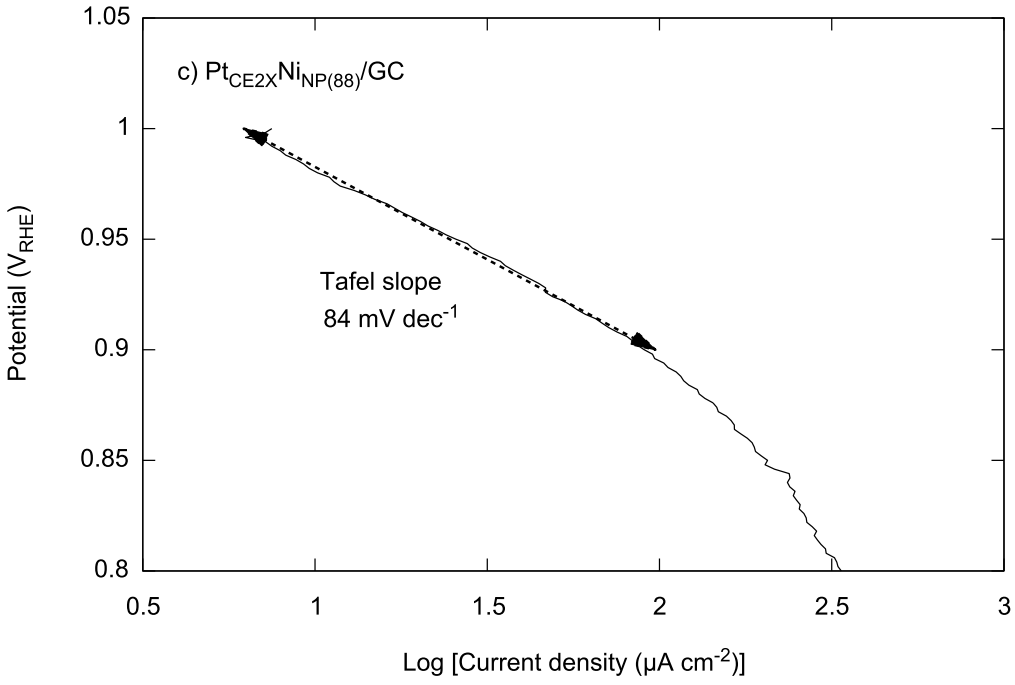

The onset potential for both catalysts was ~ 1 V, higher than that observed for either $Pt_{CE}Ni_{NP(85)}$/GC or $Pt_{Tr}Ni_{NP(85)}$/GC in 1 M KOH (~ 0.8 V). The activation of the acidic ORR is therefore quite facile over the two catalysts supported on

Ni_{NP}(88). However, the Tafel slopes of the two catalysts were larger than that observed in alkaline media for either $Pt_{CE}Ni_{NP(85)}$/GC or $Pt_{Tr}Ni_{NP(85)}$/GC, indicating a more sluggish reaction. We used the Tafel plots to determine the exchange current density over the two catalysts as well. $Pt_{CE}Ni_{NP(88)}$/GC had a j_0 value of -1.2 x 10^{-2} μA cm^{-2}, while $Pt_{CE2X}Ni_{NP(88)}$/GC had a j_0 value of -1.1 x 10^{-2} μA cm^{-2}. The two values are quite close, but also are two orders of magnitude higher than that observed for both $Pt_{CE}Ni_{NP(85)}$/GC and $Pt_{Tr}Ni_{NP(85)}$/GC (-2.4 x 10^{-4} μA cm^{-2}). Thus, the intrinsic rate of charge transfer seems to be higher over $Pt_{CE}Ni_{NP(88)}$/GC and $Pt_{CE2X}Ni_{NP(88)}$/GC. It should be noted, however, that these are rough estimations given the large errors associated with extrapolating across several orders of magnitude to determine the exchange current density.

Finally, we found that the ESA of $Pt_{CE2X}Ni_{NP(88)}$/GC exhibited a decrease in ESA ranging from 9 to 26% after acidic ORR activity testing. Perhaps, some Pt loss by dissolution occurred in the acidic solution or there may have been some aggregation or agglomeration of Pt under these conditions. A consistent decrease is also observed for $Pt_{Tr}Ni_{NP(85)}$/GC after *basic* ORR testing with values ranging from 20 to 40 %. We believe that in the case of $Pt_{Tr}Ni_{NP(85)}$/GC, Pt and/or Ni dissolution via corrosion may be occurring although did not expect the exposed Ni_{NP} in this catalyst to be susceptible to dissolution in base. Another possibility therfore is agglomeration of the Pt particles. Moreover, we note that data for ORR activity in acid could not be collected for $Pt_{Tr}Ni_{NP(85)}$/GC due to its instability on acid.

Interestingly, $Pt_{CE}Ni_{NP(88)}$/GC displayed a 100% increase in ESA after ORR activity testing in acid. We suspect that some surface restructuring may have taken place. It is possible that the $Ni_{NP(88)}$ underlayer is less protected from acid corrosion in this catalyst and that some of the surface Ni has dissolved

leaving a Pt skeleton-like structure with higher surface area due to the voids left by the base metal. The SEM of the pristine catalyst certainly did show more regions where the underlying Ni layer may have been more exposed than in the $Pt_{CE2X}Ni_{NP(88)}$/GC where most of the pillars were covered with thick globules of Pt. Figure 4-15 shows the change in the cyclic voltammograms for $Pt_{Tr}Ni_{NP(85)}$/GC, $Pt_{CE}Ni_{NP(88)}$/GC and $Pt_{CE2X}Ni_{NP(88)}$/GC after ORR activity determinations.

FIGURE 4-15 *Cyclic voltammograms of a) $Pt_{CE}Ni_{NP(88)}$/GC, b) $Pt_{Tr}Ni_{NP(85)}$/GC and c) $Pt_{CE2X}Ni_{NP(88)}$/GC in 1M KOH before and after ORR activity testing in 0.1 M $HClO_4$, 1M KOH and 0.1 M $HClO_4$ respectively.*

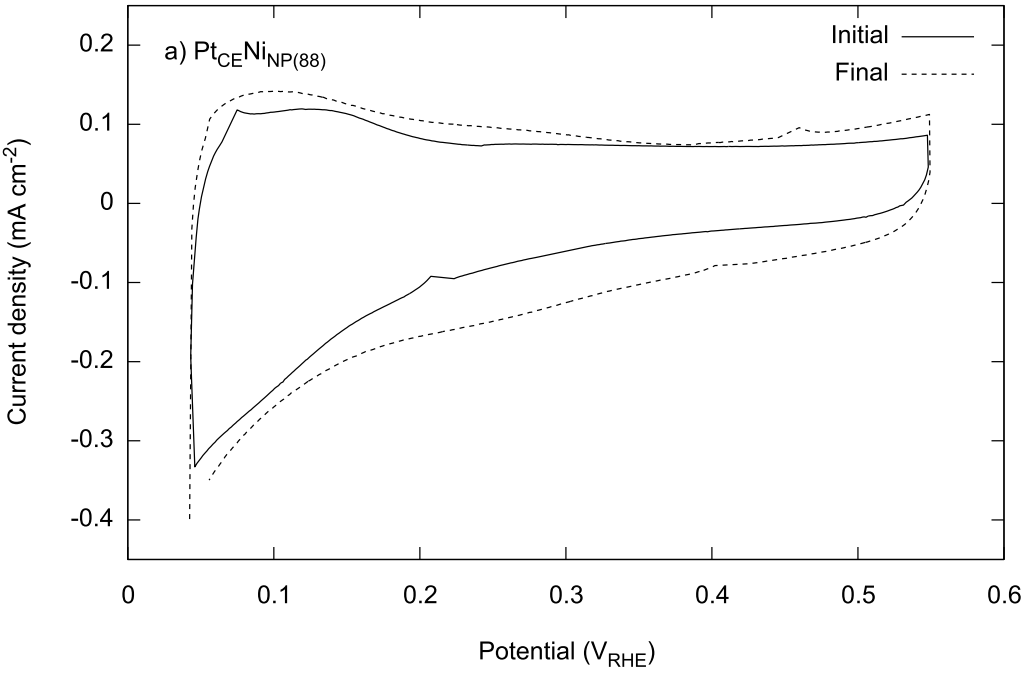

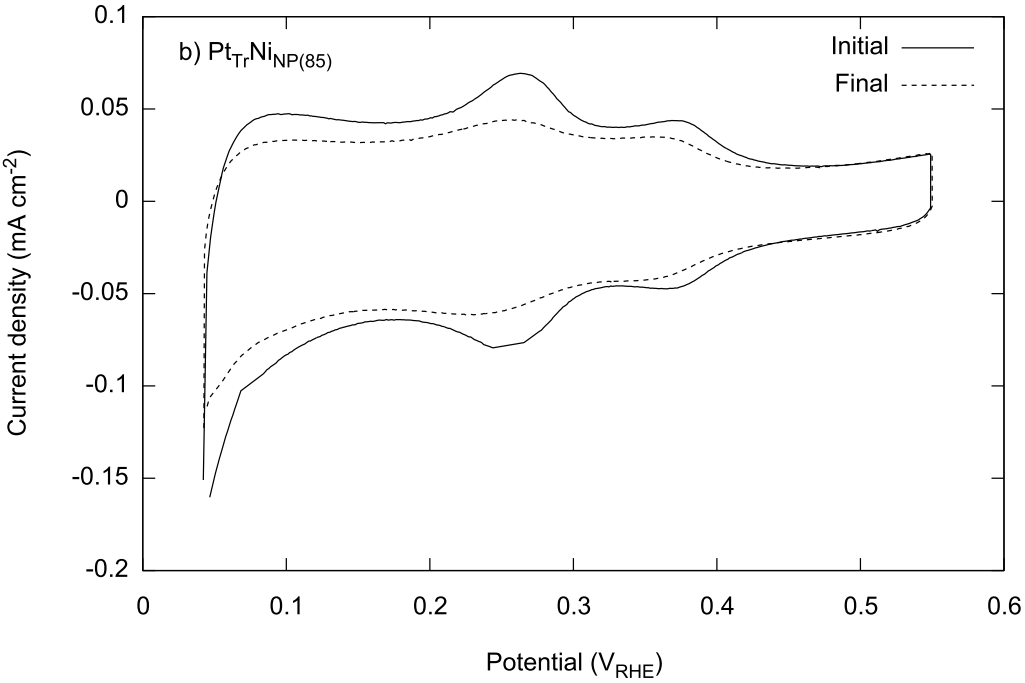

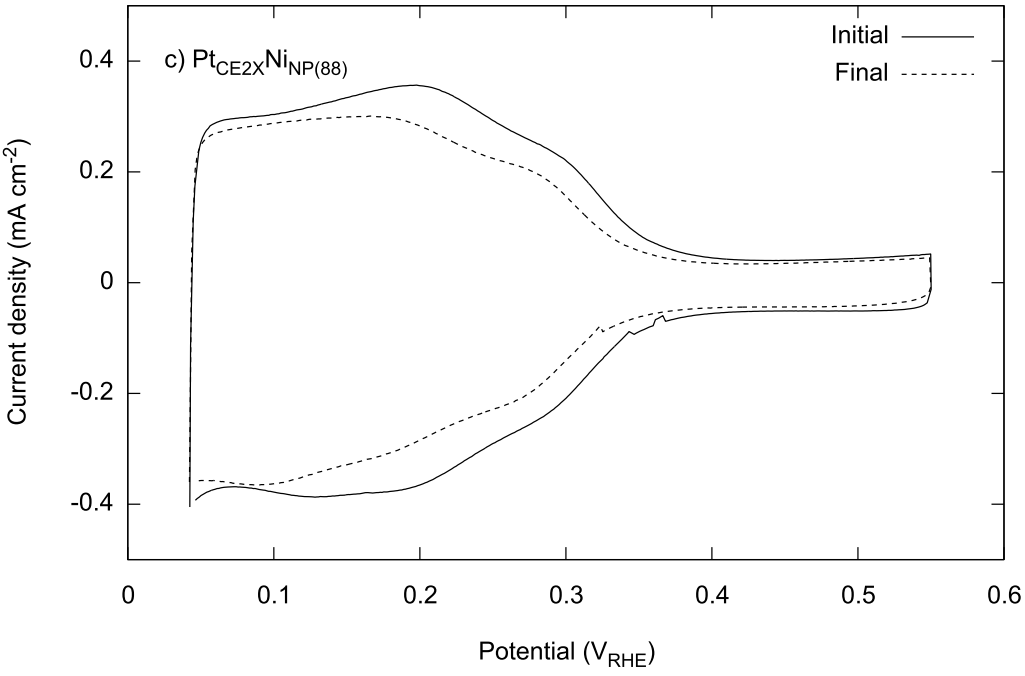

Although directly analogous data collected under the same experimental conditions are not available, an effort is made to compare our catalysts to the best in the literature. Table 4-1 shows a comparison of our catalysts with selected

reported catalyst systems. Our catalysts are superior in terms of specific surface area, especially the $Pt_{CE}Ni_{NP(85)}$/GC. The values indicate that the Pt is well dispersed especially in the case of the catalysts prepared by the *Pt CE deposition.* However, there is room for optimization of our catalysts, especially in terms of current density on a surface-area specific scale.

Table 4-1 *Oxygen reduction reactivity and surface area related characteristics of state-of-the-art and GLAD-based catalysts.*

Catalyst	*Specific surface area ($cm^2\ mg_{Pt}^{-1}$)*	*Real surface area (cm^2)*	*Kinetic current density @0.9 V ($mA\ cm^{-2}$)*	*Reference*
Pt/NSTF [a]	80	6.15	4.0 [e]	[60]
400 nm GLAD Pt nanorods [b]	670	4.22	1.2 [f]	[7]
SAD Pt/Cr nanorods [c]	160	1.25	0.89 [g]	[8]
Pt_3Ni [d]	-	-	3.6 [h]	[48]
Pt/C (ETEK 10 wt. %)	43	1.0	0.03 [I]	This work (Chapter 5)
$Pt_{CE}Ni_{NP}$/GC	1000	4.4	0.19 [J]	This work
$Pt_{Tr}Ni_{NP}$/GC	220	1.9	0.17	This work
$Pt_{CE2X}Ni_{NP}$/GC	300	15	0.03	This work

[a] Pt deposited on NSTF substrate.

[b] GLAD Pt deposited at α = 85° onto GC disks.

[c] SAD (Small angle deposition) Pt deposited at α = 30° on GLAD Cr nanorods.

[d] Pt_3Ni (111) extended surface sputtered in UHV conditions.

[e] 0.1 M $HClO_4$, 1600 rpm, 60°C, 20 mV s^{-1}, kinetic current density at 0.85 V.

[f] 0.1 M $HClO_4$, 1600 rpm, 20°C, 10 mV s^{-1}.

[g] 0.1 M $HClO_4$, 1600 rpm, 20°C, 20 mV s^{-1}.

[h] 0.1 M $HClO_4$, 1600 rpm, 60°C. Scan rate and real surface area were not reported.

[I] 1 M KOH, 1500 rpm, 25°C, 10 mV s^{-1}.

[j] 1 M KOH, 1000 rpm, 25°C, 10 mV s^{-1}.

4.3 Conclusion

The *Pt CE deposition* was used to prepare oxygen reduction catalysts. Pt was deposited on Ni_{NP}/GC supports via both a single and a double *Pt CE deposition* and compared to traditionally deposited Pt from an aqueous acidic solution of Pt salt. The resulting deposits, $Pt_{Tr}Ni_{NP(85)}$/GC, $Pt_{CE}Ni_{NP(85)}$/GC, $Pt_{CE}Ni_{NP(88)}$/GC and $Pt_{CE2X}Ni_{NP(88)}$/GC all showed activity towards oxygen reduction. In particular, $Pt_{CE}Ni_{NP(88)}$/GC and $Pt_{CE2X}Ni_{NP(88)}$/GC showed the highest onset potential for the reaction at *circa* 1 V, and the highest exchange current densities, on the order of 10^{-2} μA cm^{-2}. The Tafel slopes of $Pt_{Tr}Ni_{NP(85)}$/GC and $Pt_{CE}Ni_{NP(85)}$/GC were similar to Pt (60 mV s^{-1}). The Tafel slopes for $Pt_{CE}Ni_{NP(88)}$/GC and $Pt_{CE2X}Ni_{NP(88)}$/GC were slightly higher at 74 and 84 mV s^{-1} respectively indicating slow reaction kinetics. In all cases, the surface area of the deposits increased with Pt deposition, and interestingly, the ESA of $Pt_{CE}Ni_{NP(85)}$/GC and $Pt_{CE}Ni_{NP(88)}$/GC increases after ORR activity determination in base and acid respectively. In the first case, this is likely due to extensive surface reorganization of the catalyst. In the latter case, it is likely that combined with surface reorganization, some of the surface Ni has dissolved leaving a Pt skeleton-like structure with higher surface area. Compared to similar and state-of-the-art catalysts reported in the literature, our catalysts perform fairly and with optimization of deposition conditions and ORR methods, there is room for improvement.

4.4 Experimental

4.4.1 General

The following reagents were used as received from the supplier: Nitrogen (Praxair, pre-purified), oxygen (Praxair, pre-purified), concentrated sulfuric acid (Caledon), hydrochloric acid (EMD chemicals), nitric acid (EMD chemicals), and perchloric acid (Anachemia Corporation), potassium permanganate (Fischer Scientific), 30% hydrogen peroxide (Fischer Scientific), potassium hydroxide (Caledon Laboratory Chemicals), ammonium chloride (Caledon Laboratory chemicals), ethanol (Greenfield Ethanol Incorporated) and potassium hexachloroplatinate (Aithica Chemical Corporation). The following materials were used as received from the supplier: platinum gauze (Alfa Aesar, 52 mesh woven from 0.1 mm wire, 99.9% metals basis), silicon wafers (p-type, (100), University Wafer), glassy carbon disks (Pine Research Instrumentation, 5 mm outer diameter x 4 mm thick, mirror polished), titanium (1 inch target, 99.95% purity), and nickel metal chunks (Cerac, Inc., 99.9% purity).

Triply distilled H_2O was used to prepare all aqueous solutions and was itself prepared by distilling a mixture of alkaline $KMnO_4$ and doubly distilled H_2O. Analytical grade reagents were used to prepare all electrolyte solutions. Electrolytes were purged with N_2 before use, and all voltammetric experiments were carried out under N_2 unless otherwise specified. All glassware was rinsed with *Piranha* solution (5:1 by volume concentrated H_2SO_4 and 30% H_2O_2) followed by thorough rinsing with triply distilled H_2O, and drying in an oven at 80°C.

Electrochemical experiments were performed on either an EG&G Princeton Applied Research Potentiostat/Galvanostat Model 273 using the

corresponding M270 software or a Solartron SI 1287 Electrochemical Interface controlled by CorrWare for Windows Version 2-3d software. During electrochemical depositions, the potential of the platinum counter electrode was recorded using a Radio Shack multimeter and Scope View version 1.08 software. Rotating ring disk electrode (RRDE) experiments were performed using a Pine Research Instrumentation Modulated Speed Rotator, RRDE shaft, and E5TQ series ChangeDisk RRDE tip.

Scanning electron microscopy (SEM) was performed on a Hitachi S-4800 instrument. Where side images were necessary, the samples were first cleaved before mounting to SEM stubs. Inductively coupled plasma mass spectrometry was performed on an Elan 6000 spectroscope from Perkin Elmer. Samples were prepared by dissolving the deposits in *aqua regia*, evaporating to dryness on a hot plate and making up the residue quantitatively in 0.3 M HNO_3.

4.4.2 Preparation of platinum electrodes

The platinum black electrode used as a source of platinum in the platinum counter electrode deposition (see below) consisted of a 2.5 cm x 2.5 cm platinum gauze blacked with 0.02 M K_2PtCl_6/1 M $HClO_4$. A typical blackening experiment would be performed at -0.1 V vs. Ag/AgCl (4M KCl) (Aldrich) until the observed current decayed to ~ 0 mA. The real surface area of the platinum black electrode was determined from the hydrogen under potential deposition (H_{UPD}) peak of a stabilized cyclic voltammogram recorded in 0.5 M H_2SO_4 assuming the charge associated with a monolayer of hydrides on polycrystalline Pt is 210 μC cm^{-2} [61] with 77% efficiency. Typical estimations were more than 4,000 cm^2. The counter electrode was freshly blacked after three uses in the platinum counter electrode

deposition. The platinum black electrode used as a counter electrode in voltammetry was prepared in the manner described above.

4.4.3 Preparation of glancing angle deposited nickel working electrodes

The glassy carbon (GC) disks were polished with a Pine Research Instrumentation polishing kit (5, 0.3 and/or 0.05 μm alumina slurry and nylon or rayon microcloth) and cleaned with acetone, 2-propanol and water before being placed in the high vacuum deposition chamber (Kurt J. Lesker). The deposition chamber was evacuated to below 0.1 mP and Ni was deposited from Ni metal chunks via electron beam deposition. The flux rate was maintained at 1 nm s^{-1} while the substrates were rotated constantly in φ at a rate of one rotation every 10 nm of film growth. The 500 nm vertical nanopillars were deposited at α = 85 or 88˚.

Alternatively, 1 cm x 2 cm pieces of Si wafers were used as deposition substrates and treated in the same manner. The deposition chamber was evacuated to below 0.1 mPa and a 10 nm layer of Ti was sputtered under argon flow at 75 W. The Ti layer promotes adhesion between the Si substrate and Ni layers. Ni was then deposited from Ni metal chunks via electron beam deposition. The flux rate was maintained at 1 nm s^{-1} while the substrates were rotated constantly in φ at a rate of one rotation every 10 nm of film growth. A 200 nm planar layer of Ni was first deposited at a deposition angle of α = 30˚, followed by 500 nm of vertical nanopillars deposited at α = 85 and 88˚ to give $Ni_{NP(85)}$/GC and $Ni_{NP(88)}$/GC respectively.

In the case of the Si substrates, a task wipe was used to define a 1 cm x 1 cm area of nanopillars for deposition of Pt. In the case of GC substrates, the disk was loaded into the RRDE tip using a homemade hands-free mounting tool

where only the outer 0.5 mm area of the film is removed to leave 0.126 cm^2 active area of nanopillars. In both cases, the Ni_{NP} working electrodes were cleaned with triply distilled water before being used as working electrodes. Herein, deposits on Si and on GC are differentiated by the suffix "/GC" for the latter.

4.4.4 Platinum counter electrode deposition

The electrolyte comprised 30 mL of 2.0 M NH_4Cl prepared in a glass cylinder of dimensions 10 cm x 2.5 cm inner diameter (Si-based substrates) or a 3-neck 100 mL round bottom flask (GC-based substrates) set up as shown in Figure 4-2. In the latter case, the WE could not be vertically aligned for two reasons: i) hydrogen bubbles formed during the *Pt CE deposition* become trapped on the WE, and ii) the stir bar causes a vortex to form directly below the WE. Contact between the electrode and the electrolyte is prevented in both cases. When the WE was positioned on an angle the hydrogen bubbles could escape from the surface.

Before deposition, the Pt counter electrode was washed in triply distilled water and dried in a stream of hydrogen to reduce its surface. A current of -0.1 A was applied between the Ni_{NP} working electrode and the Pt black counter electrode in the presence of a Ag/AgCl (4M KCl) reference electrode for 1 hour, with magnetic stirring at 500 rpm, to afford Pt deposits on the working electrodes. After deposition, the $Pt_{CE}Ni_{NP}$ or $Pt_{CE}Ni_{NP}$/GC WE was gently rinsed with copious amounts of triply distilled water.

For double Pt counter electrode depositions, the procedure was repeated in the same deposition solution for a second time. The Pt counter electrode was removed from the solution after the first deposition, washed in triply distilled

water, dried in a stream of hydrogen, and replaced into the cell before commencing the second deposition. The electrodes in this case are referred to as $Pt_{CE2X}Ni_{NP}$/GC.

4.4.5 Traditional platinum deposition

The deposition apparatus for Si-based substrates was a glass cylinder of dimensions 10 cm x 2.5 cm inner diameter equipped with a magnetic stir bar, a Ag/AgCl (4M KCl) double junction reference electrode and a Pt counter electrode shielded in a glass tube with a 10 μm porous glass frit. For GC-based substrates the deposition was carried out using a 100 mL 3-neck round bottom flask instead of the glass cylinder. The plating solution comprised 25 mL of an aqueous solution of 1.2 x 10^{-4} M K_2PtCl_6 in 0.01 M $HClO_4$, prepared by serial dilution. The deposition was performed by applying a potential of -0.1 V versus the reference electrode, with magnetic stirring at 500 rpm.

4.4.6 Electrochemical methods

Cyclic voltammetry was performed using a conventional three-electrode cell configuration. The Pt counter electrode was isolated in a glass tube with a 10 μm porous glass frit. A static reversible hydrogen electrode (RHE) was used as a reference point and all potentials are versus this reference unless otherwise stated. The electrolyte was either 1 M KOH or 0.1 M $HClO_4$ at 25°C. Hydrodynamic voltammetry, to determine oxygen reduction reaction activity, was performed at 60°C in O_2-saturated electrolytes obtained by bubbling O_2 through the solution for 30 minutes. O_2 was also flushed over the solution during the measurements. Scan and rotation rates were between 5 and 20 mV s^{-1}, and 400 to 2000 rpm respectively, and are specified in the relevant text herein.

4.5 Bibliography

[1] M.D. Gasda, R. Teki, T.M. Lu, N. Koratkar, G.A. Eisman, D. Gall, J. Electrochem. Soc., 156 (2009) B614-B619.

[2] M.D. Gasda, G.A. Eisman, D. Gall, J. Electrochem. Soc., 157 (2010) B437-B440.

[3] M.D. Gasda, G.A. Eisman, D. Gall, J. Electrochem. Soc., 157 (2010) B113-B117.

[4] M.D. Gasda, G.A. Eisman, D. Gall, J. Electrochem. Soc., 157 (2010) B71-B76.

[5] A. Bonakdarpour, R.T. Tucker, M.D. Fleischauer, N.A. Beckers, M.J. Brett, D.P. Wilkinson, Electrochim. Acta, 85 (2012) 492-500.

[6] A. Bonakdarpour, M.D. Fleischauer, M.J. Brett, J.R. Dahn, Appl. Catal. A-Gen., 349 (2008) 110-115.

[7] W.J. Khudhayer, N.N. Kariuki, X. Wang, D.J. Myers, A.U. Shaikh, T. Karabacak, J. Electrochem. Soc., 158 (2011) B1029-B1041.

[8] W.J. Khudhayer, N. Kariuki, D.J. Myers, A.U. Shaikh, T. Karabacak, J. Electrochem. Soc., 159 (2012) B729-B736.

[9] S.A. Francis, R.T. Tucker, M.J. Brett, S.H. Bergens, J. Power Sources, 222 (2013) 533-541.

[10] A. Brouzgou, S.Q. Song, P. Tsiakaras, App. Cat. B-Environ., 127 (2012) 371-388.

[11] M.K. Debe, A.J. Steinbach, S.M. Hendricks, M.J. Kurkowski, G.D. Vernstrom, A.E. Hester, et al. DOE Hydrogen and Fuel Cells Program Fiscal Year 2012 Annual Progress Report. Available at: http://www.hydrogen.energy.gov/pdfs/progress12/v_d_1_debe_2012.pdf. Accessed June 19th, 2013.

[12] A. Rabis, P. Rodriguez, T.J. Schmidt, ACS Catalysis, 2 (2012) 864-890.

[13] N. Alonso-Vante, ChemPhysChem, 11 (2010) 2732-2744.

[14] H.A. Gasteiger, S.S. Kocha, B. Sompalli, F.T. Wagner, App. Cat. B-Environ., 56 (2005) 9-35.

[15] N.M. Marković, P.N. Ross Jr., Surf. Sci. Rep., 45 (2002) 117-229.

[16] M.T.M. Koper, Fuel Cell Catalysis: A Surface Science Approach, (2009).

[17] N.M. Markovic, H.A. Gasteiger, P.N. Ross Jr., J.Phys.Chem., 99 (1995) 3411-3415.

[18] Luo Y. Bond Dissociation Energies in CRC Handbook of Chemistry and Physics. 93rd Ed., 2012-2013; Available at: www.hbcpnetbase.com. Accessed May 7th, 2013.

[19] N. Ramaswamy, S. Mukerjee, J. Phys. Chem. C, 115 (2011) 18015-18026.

[20] N. Ramaswamy, S. Mukerjee, Advances in Physical Chemistry, 2012 (2012).

[21] S. Mukerjee, S. Srinivasan, M.P. Soriaga, J. Electrochem. Soc., 142 (1995) 1409-1422.

[22] T. Toda, H. Igarashi, H. Uchida, M. Watanabe, J. Electrochem. Soc., 146 (1999) 3750-3756.

[23] L. Yang, M.B. Vukmirovic, D. Su, K. Sasaki, J.A. Herron, M. Mavrikakis, S. Liao, R.R. Adzic, J. Phys. Chem. C, 117 (2013) 1748-1753.

[24] Y. Zhang, C. Ma, Y. Zhu, R. Si, Y. Cai, J.X. Wang, R.R. Adzic, Catal. Today, 202 (2013) 50-54.

[25] H.I. Karan, K. Sasaki, K. Kuttiyiel, C.A. Farberow, M. Mavrikakis, R.R. Adzic, ACS Catalysis, 2 (2012) 817-824.

[26] K.A. Kuttiyiel, K. Sasaki, Y. Choi, D. Su, P. Liu, R.R. Adzic, Nano Letters, 12 (2012) 6266-6271.

[27] K.A. Kuttiyiel, K. Sasaki, Y. Choi, D. Su, P. Liu, R.R. Adzic, Energy and Environmental Science, 5 (2012) 5297-5304.

[28] T. Ghosh, M.B. Vukmirovic, F.J. DiSalvo, R.R. Adzic, J. Am. Chem. Soc., 132 (2010) 906-907.

[29] K. Gong, D. Su, R.R. Adzic, J. Am. Chem. Soc., 132 (2010) 14364-14366.

[30] J.X. Wang, H. Inada, L. Wu, Y. Zhu, Y. Choi, P. Liu, W.P. Zhou, R.R. Adzic, J. Am. Chem. Soc., 131 (2009) 17298-17302.

[31] S.T. Bliznakov, M.B. Vukmirovic, L. Yang, E.A. Sutter, R.R. Adzic, J. Electrochem. Soc., 159 (2012) F501-F506.

[32] C. Koenigsmann, A.C. Santulli, K. Gong, M.B. Vukmirovic, W.P. Zhou, E. Sutter, S.S. Wong, R.R. Adzic, J. Am. Chem. Soc., 133 (2011) 9783-9795.

[33] K. Sasaki, J.X. Wang, H. Naohara, N. Marinkovic, K. More, H. Inada, R.R. Adzic, Electrochim. Acta, 55 (2010) 2645-2652.

[34] W.P. Zhou, K. Sasaki, D. Su, Y. Zhu, J.X. Wang, R.R. Adzic, J. Phys. Chem. C, 114 (2010) 8950-8957.

[35] A.U. Nilekar, Y. Xu, J. Zhang, M.B. Vukmirovic, K. Sasaki, R.R. Adzic, M. Mavrikakis, Top. Catal., 46 (2007) 276-284.

[36] M.B. Vukmirovic, J. Zhang, K. Sasaki, A.U. Nilekar, F. Uribe, M. Mavrikakis, R.R. Adzic, Electrochim. Acta, 52 (2007) 2257-2263.

[37] F.H.B. Lima, J. Zhang, M.H. Shao, K. Sasaki, M.B. Vukmirovic, E.A. Ticianelli, R.R. Adzic, J. Phys. Chem. C, 111 (2007) 404-410.

[38] P. Mani, R. Srivastava, P. Strasser, J. Power Sources, 196 (2011) 666-673.

[39] P. Strasser, S. Koh, J. Anniyev, J. Greeley, K. More, C. Yu, Z. Liu, S. Kaya, D. Nordlund, H. Ogasawara, M.F. Toney, A. Nilsson, Nat. Chem., 2 (2010) 454-460.

[40] R. Srivastava, P. Mani, N. Hahn, P. Strasser, Angew. Chem. Int. Edit., 46 (2007) 8988-8991.

[41] P. Mani, R. Srivastava, C. Yu, P. Strasser, ECS Transactions, 11 (2007) 933-939.

[42] S. Koh, P. Strasser, J. Am. Chem. Soc., 129 (2007) 12624-12625.

[43] F. Hasché, M. Oezaslan, P. Strasser, J. Electrochem. Soc., 159 (2012) B24-B33.

[44] S. Rudi, X. Tuaev, P. Strasser, Electrocatal., 3 (2012) 265-273.

[45] V. Stamenković, T.J. Schmidt, P.N. Ross, N.M. Marković, J. Phys. Chem. B, 106 (2002) 11970-11979.

[46] V. Stamenkovic, T.J. Schmidt, P.N. Ross, N.M. Markovic, J. Electroanal. Chem., 554-555 (2003) 191-199.

[47] V.R. Stamenkovic, B.S. Mun, K.J.J. Mayrhofer, P.N. Ross, N.M. Markovic, J. Am. Chem. Soc., 128 (2006) 8813-8819.

[48] V.R. Stamenkovic, B. Fowler, B.S. Mun, G. Wang, P.N. Ross, C.A. Lucas, N.M. Markovic, Science, 315 (2007) 493-497.

[49] B. Fowler, C.A. Lucas, A. Omer, G. Wang, V.R. Stamenkovic, N.M. Markovic,Electrochim. Acta, 53 (2008) 6076-6080.

[50] D.F. Van Der Vliet, C. Wang, D. Li, A.P. Paulikas, J. Greeley, R.B. Rankin, D. Strmcnik, D. Tripkovic, N.M. Markovic, V.R. Stamenkovic, Angew. Chem. Int. Ed., 51 (2012) 3139-3142.

[51] C. Wang, M. Chi, D. Li, D. Strmcnik, D. Van Der Vliet, G. Wang, V. Komanicky, K. Chang, A.P. Paulikas, D. Tripkovic, J. Pearson, K.L. More, N.M. Markovic, V.R. Stamenkovic, J. Am. Chem. Soc., 133 (2011) 14396-14403.

[52] G.C.K. Liu, C. Bums, R. Sanderson, D.A. Stevens, G. Vernstromb, R.T. Atanasoski, M.K. Debe, J.R. Dahn, ECS Transactions, 33 (2010) 153-159.

[53] M.K. Debe, A.J. Steinbach, G.D. Vernstrom, S.M. Hendricks, M.J. Kurkowski, R.T. Atanasoski, P. Kadera, D.A. Stevens, R.J. Sanderson, E. Marvel, J.R. Dahn, ECS Transactions, 33 (2010) 143-152.

[54] D.A. Stevens, R. Mehrotra, R.J. Sanderson, G.D. Vernstrom, R.T. Atanasoski, M.K. Debe, J.R. Dahn, J. Electrochem. Soc., 158 (2011) B905-B909.

[55] C.K.G. Liu, D.A. Stevens, J.C. Burns, R.J. Sanderson, G. Vernstrom, R.T. Atanasoski, M.K. Debe, J.R. Dahn, J. Electrochem. Soc., 158 (2011) B919-B926.

[56] M.K. Debe, A.J. Steinbach, G.D. Vernstrom, S.M. Hendricks, M.J. Kurkowski, R.T. Atanasoski, P. Kadera, D.A. Stevens, R.J. Sanderson, E. Marvel, J.R. Dahn, J. Electrochem. Soc., 158 (2011) B910-B918.

[57] D. Van Der Vliet, C. Wang, M. Debe, R. Atanasoski, N.M. Markovic, V.R. Stamenkovic,Electrochim. Acta, 56 (2011) 8695-8699.

[58] M.K. Debe, J. Electrochem. Soc., 159 (2012) B53-B66.

[59] G. Lu, G. Zangari, Electrochim. Acta 51 (2006) 2531-2538.

[60] K.J.J. Mayrhofer, D. Strmcnik, B.B. Blizanac, V. Stamenkovic, M. Arenz, N.M. Markovic, Electrochim. Acta, 53 (2008) 3181-3188.

[61] B.E. Conway, H. Angerstein-Kozlowska, Acc. Chem. Res., 14 (1981) 49-56.

[62] A. Doménech-Carbó, Solid State Electr., (2013) 1-2.

[63] C. Paliteiro, A. Hamnett, J.B. Goodenough, Journal of Electroanalytical Chemistry and Interfacial Electrochemistry, 233 (1987) 147-159.

Chapter 5: Preparation, characterization and oxygen reduction reaction electrocatalytic activity on Vulcan carbon-supported Pt nanoparticles: First application of the Pt counter electrode deposition onto particulate substrates[1]

5.1 Introduction

Up to this point, the WE substrates used for the *Pt CE deposition* were rigid heterogeneous materials. We were therefore interested in expanding the utility of this method to accommodate homogenous particulate substrates such as Vulcan carbon. Our aim is to use the *Pt CE deposition* to prepare a Pt/C oxygen reduction catalyst powder with low Pt-loading and uniform dispersion of Pt on the carbon. This would be a proof-of-concept study. The ramifications of this experiment being successful are wide-ranging as we could envision using highly specialized carbon substrates [1,2] such as carbon nanotubes [3-11], carbon aerogels [12-18], activated carbons [19-27], carbon cryogels [28,29], nanoporous carbon [30-35], or mesoporous carbon [36-55], for example. Further, nanostructured substrates do not have to be limited to carbon materials. We foresee that once the substrate is conductive and stable under the deposition conditions, it can be employed.

[1] *A version of this chapter has been presented in poster form at the 95th Canadian Chemistry Conference and Exhibition, May 2012, Calgary, AB.*

However, some logistic difficulties have to be considered. First, every particle of the carbon powder substrate has to experience the deposition current, and be exposed to the solvated Pt, to ensure a uniform deposition would occur. Therefore, packing the carbon powder into a rigid pellet would not be a viable option; the carbon particles in the interior of the pellet would not be exposed to the solution. Furthermore, deposition directly onto the film on the disk would not be a large-scale synthesis, thus only being suitable for 3-electrode experiments and not fuel cell membrane electrode assembly preparation. We were therefore inspired by reports from Adzic and co-workers describing gram-scale synthesis of Pt monolayer (Pt_{ML}) shell: Pd/C or Pd_2O/C core nanoparticle catalysts [56,57].

The Adzic Pt_{ML} catalysts were described in Section 4.1.2. Similar to our proposed experiment, Pt in solution was deposited onto a particulate substrate and the Pt was deposited in a self-limiting manner. Specifically, the unique synthesis involves the underpotential deposition (UPD) of a Cu_{ML} onto the core material in a monolayer-limited reaction, followed by the galvanic displacement of the Cu by the more noble Pt metal. As a reminder, UPD is the deposition of a metal on a foreign metal substrate at a more positive potential than that required for bulk deposition. The galvanic displacement step that follows UPD is spontaneous and irreversible, and described by Equation 5-1 [58]:

$$M^0 + \left(\frac{m}{z}\right)P^{z+} \rightarrow M^{m+} + \left(\frac{m}{z}\right)P^0 \qquad 5\text{-}1$$

where M^0 is the metal adatom comprising the UPD layer

M^{m+} is the metal cation in solution obtained after the UPD metal adatom M has been oxidised

P^0 is a more nobel metal atom than M being electrolessly deposited

P^{z+} is the nobel metal cation with positive charge z+ and valence z

The driving force of this reaction is that the equilibrium potential of metal P and its solvated cations is more positive than the equilibrium potential of the metal UPD layer. In the case where M = Cu, P = Pt and z = 2, the exchange is limited to monolayer coverage as Cu oxidation supplies 2 electrons per adatom to Pt^{2+} for a 1:1 ratio of Cu to Pt.

Some of the earliest reports described the synthesis directly onto a thin film of the core material supported on a glassy carbon electrode [59-62]. The scale-up synthesis employed a new electrochemical cell comprising a Ti cylinder (14 cm diameter) that doubles as a WE. The internal surface of the cylinder was lined with RuO_2 for corrosion resistance. The carbon-supported core materials were placed on the bottom of the cell along with the reference electrode and counter electrode (behind a glass frit), both supported by polystyrene floats. The Cu UPD experiment was performed with occasional stirring to disperse the particles in the electrolyte and to allow them to make contact with the Ti/RuO_2 WE, thereby facilitating formation of the Cu_{ML} on the core material surfaces. The Ti/RuO_2 therefore acted as a current distributor to the homogenous substrate.

With this experimental setup as inspiration, we designed an electrochemical cell as shown in Figure 5-1. The cell consisted of a glass cylinder with inner diameter of 2.5 cm, equipped with a Teflon cup. The base of the cup was equipped with a shiny nickel foil disk with a handle of Ni wire enclosed in glass. This disk was the WE/current distributor. The carbon powder and aqueous NH_4Cl was thus added to the cup and the Pt blacked CE and the reference electrode were clamped into place in the solution above the disk. We proposed that any carbon in contact with the disk during the deposition would experience the same voltage as the disk, facilitating Pt nucleation on the carbon surface. A particular Pt-nucleated carbon particle can encounter the Ni disk several times

during the deposition. However, excessive Pt growth should be controlled by hydrogen evolution occurring on the nucleated Pt. Thus, we expect a uniform deposition of Pt on the carbon. We further hypothesized that the total surface area of the carbon particles, being significantly higher than that of the shiny disk, would allow preferential nucleation on the former. The magnetic stir bar in this setup was omitted to prevent dislodging of the connecting cables to the Ni disk handle by the continuous stirring motion. Instead, we depended on hydrogen evolution over the Pt deposit to agitate the powder during the deposition.

Figure 5-1 *Illustration representing the experimental cell used for the* Pt CE deposition *on Vulcan carbon. Within dashed lines are expanded views of the processes occurring during the deposition.*

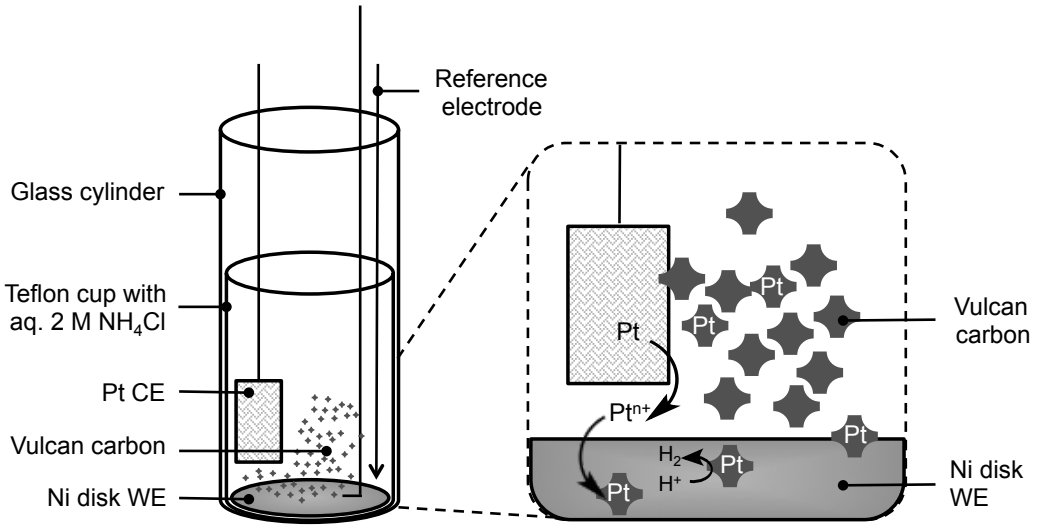

The Pt/C powder prepared by the modified *Pt CE deposition* is referred to as $Pt_{CE}C$ herein. The $Pt_{CE}C$ catalyst was characterized by voltammetry, X-ray diffraction, Transmission electron microscopy and Inductively coupled plasma-Mass Spectrometry. The powder was then used to prepare a series of catalyst

inks that were cast as thin-films on glassy carbon disks [63]. The rotating disk electrode method was used to evaluate its oxygen reduction activity.

5.2 Results and Discussion

5.2.1 Comparison of the depositions of $Pt_{CE}C$, Ni–$Pt_{CE}Ni_{gauze}$, Ni–$Pt_{CE}Ni_{foam}$, and $Pt_{CE}Ni_{foam}$

Figure 5-2 shows the voltage response of the Pt CE and Ni disk/carbon powder WE during the preparation of $Pt_{CE}C$ using 50 mg XC-72R Vulcan carbon. Compared to the deposition on Ni_{gauze} and Ni_{foam} (Figure 2-3), and Ni_{NP} (Figure 3-3) the Pt CE behaved similarly, stabilizing at short times to a voltage of E_{CE} ~ 1.4 V_{SHE}. In contrast, the potential response of the Ni disk (or carbon powder), E_{WE}, was mainly similar to that for the Ni_{NP}. Recall that the foam electrodes both show longer times before the rise in WE potential. We had ascribed this to either the higher real surface area of the foam and/or a longer induction period for Pt deposition on the foam. The Ni disk/carbon powder did not have a long induction period as the rise in E_{WE} began at very short times, spanning between 250 and 500 seconds. Moreover, the steady state potential of the Ni disk/carbon powder WE was much lower (~ -1 V) than either Ni–$Pt_{CE}Ni_{gauze}$, Ni–$Pt_{CE}Ni_{foam}$, or $Pt_{CE}Ni_{foam}$. We suggest that this is because H_2 evolution occurred mainly on the Pt nucleated on the carbon particles and not on the Ni disk itself. Thus, the WE potential did not rise as much as expected. Moreover, when the Ni disk was removed from the deposition cell, rinsed with triply distilled water, and immersed in aqueous 30 % H_2O_2, we did not observe O_2 evolution, indication that no or negligible amounts of Pt were deposited on the disk.

FIGURE 5-2 *Potential profile of the electrodes during the* Pt CE deposition *of $Pt_{CE}C$ at -100 mA for 1 hour in 2.0 M NH_4Cl.*

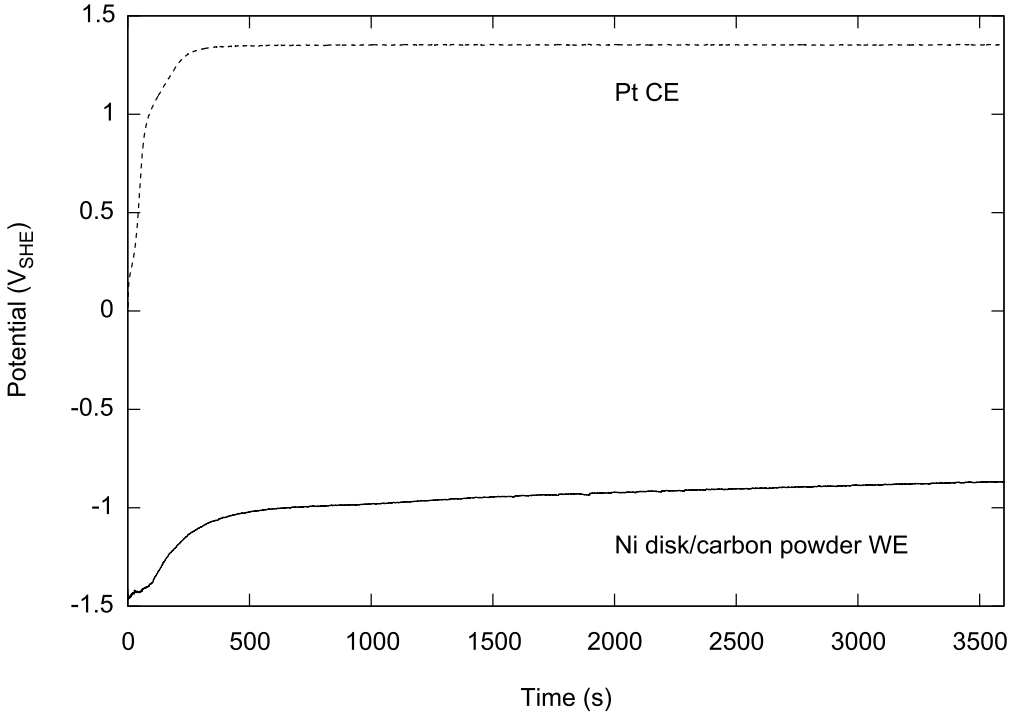

5.2.2 Characterization of $Pt_{CE}C$

After deposition, the $Pt_{CE}C$ was isolated from the solution via a series of centrifugation steps, washed three times with triply distilled water and dried under vacuum overnight. X-ray diffractograms were collected on the dry catalyst. These are shown in Figure 5-3. We note that the large broad features between 30 and 50° are typical of the Vulcan carbon support. Peaks at approximately 40, 47, 68, 82 and 87° were indexed to the Pt *fcc* crystal planes (111, 200, 220, 311 and 222 respectively) [64], supporting the presence of Pt. This result was also supported by selected area electron diffraction (SAED) as shown in Figure 5-4.

Figure 5-3 *X-ray diffractogram of $Pt_{CE}C$ and polycrystalline fcc Pt reference peaks.*

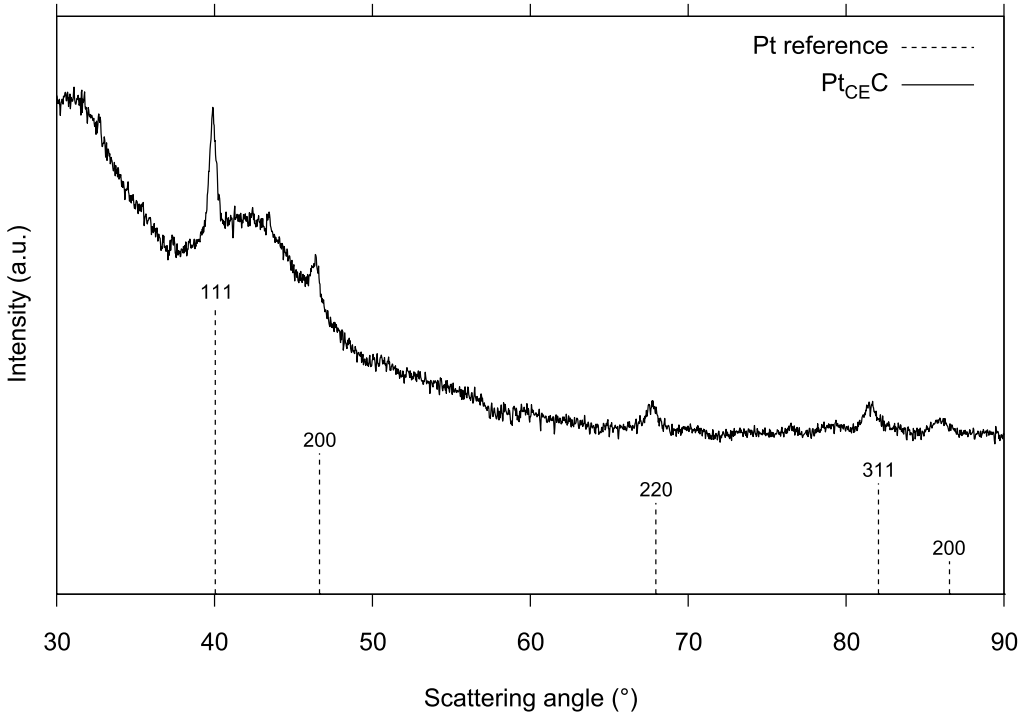

Figure 5-4 *TEM image of $Pt_{CE}C$ showing the Pt particle (circled) on which SAED was performed. Guides for the eye show the indices for polycrystalline fcc Pt. HV = 200 kV; Camera length = 1m.*

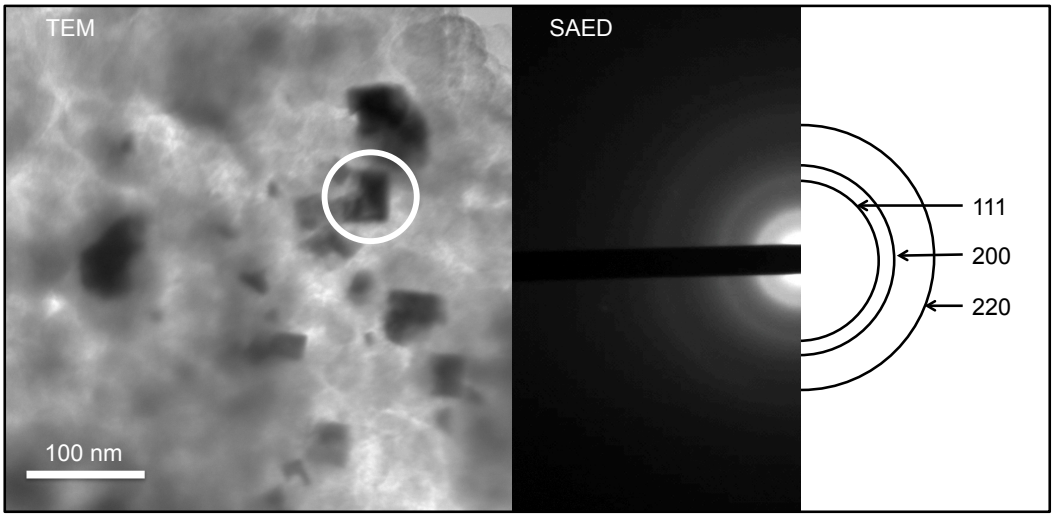

Transmission electron micrographs of the dry $Pt_{CE}C$ show a conformal distribution in regions where Pt was detected (Figure 5-5a to c). We do note, however, that there were many more regions where there was no Pt observed on the carbon powder (for example, Figure 5-5d). Regardless, ICP-MS showed that the average amount of Pt in the catalyst was 4 wt. % or 0.2 mg_{Pt} in the 50 mg sample of carbon. This is on scale with the mass of Pt in the analogous preparation of $Pt_{CE}Ni_{foam}$ (0.23 mg_{Pt}). Combined with the hydrogen peroxide test on the Ni disk above, these results suggest that most or all of the solvated Pt is being deposited on the carbon. Scherrer analysis using the Pt (111) peak from the diffractogram in Figure 5-3 gave the average Pt crystallite size of 18 nm. On the other hand, based on manual TEM analysis, the Pt particle size was 13±3 nm (Figure 5-7e).

Cyclic voltammetry was performed on thin films of $Pt_{CE}C$. The catalyst ink was prepared by sonicating 2 mg of the prepared catalyst powder with 1.6 and 0.4 mL of H_2O and $(CH_3)_2CH(OH)$ respectively, and 20 µL of 5 wt. % Nafion solution. 10 µL of this mixture was cast onto a glassy carbon disk electrode to give an approximate Pt loading of 40 ng_{Pt}. CVs in both acid and base are shown in Figure 5-6. In acid (5-6a), hydrogen evolution was quite pronounced as shown by the large reduction current at -0.05 V_{RHE}. The hydrogen desorption peak at ~ 0.05 V in the positive going sweep is also indicative of the Pt present in the catalyst ink. However, peaks for platinum oxide and hydroxide formation and the corresponding reduction peaks were suppressed in acid. On the other hand, CVs in base (5-6b) showed suppression of the hydrogen adsorption/desorption peaks between -0.05 and 0.3 V, while peaks associated with oxidation of Pt (0.9 and 1.4 V) were visible. The reduction peak of oxides/hydroxides on the Pt surface at ~

0.65 V was well defined. Together, the CVs in basic and acidic media support the presence of electrochemically active Pt surfaces in the catalyst.

Figure 5-5 (*a) to (d) Sample transmission electron micrographs of $Pt_{CE}C$ collected at 200 kV high voltage and 40,000x direct magnification. Scale bars in all cases are 100 nm. No Pt was detected in image (d). (e) Histogram showing particle distribution size based on manual TEM analysis.*

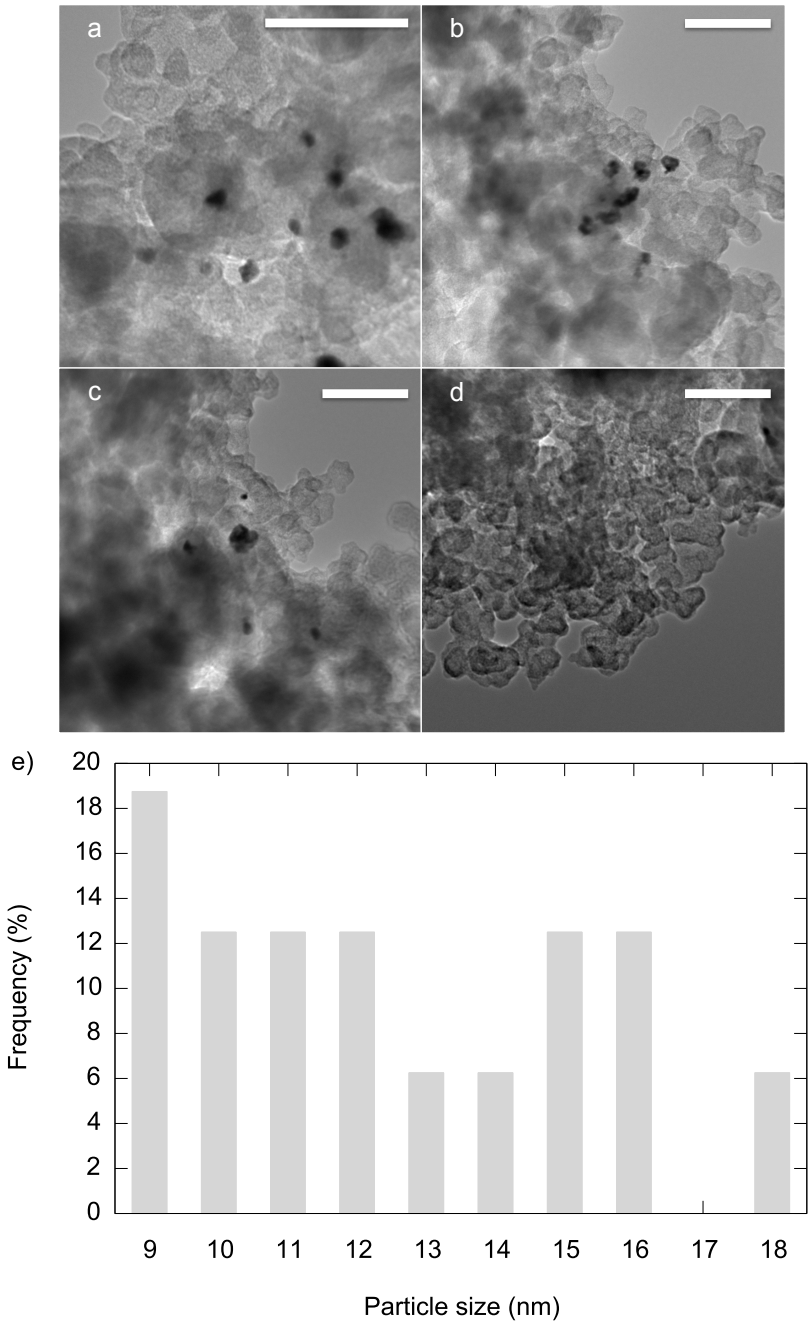

Figure 5-6 *Cyclic voltammograms of $Pt_{CE}C$ in a) 0.5 M H_2SO_4 and b) 1M KOH at 25°C with a scan rate of 10 mVs^{-1}.*

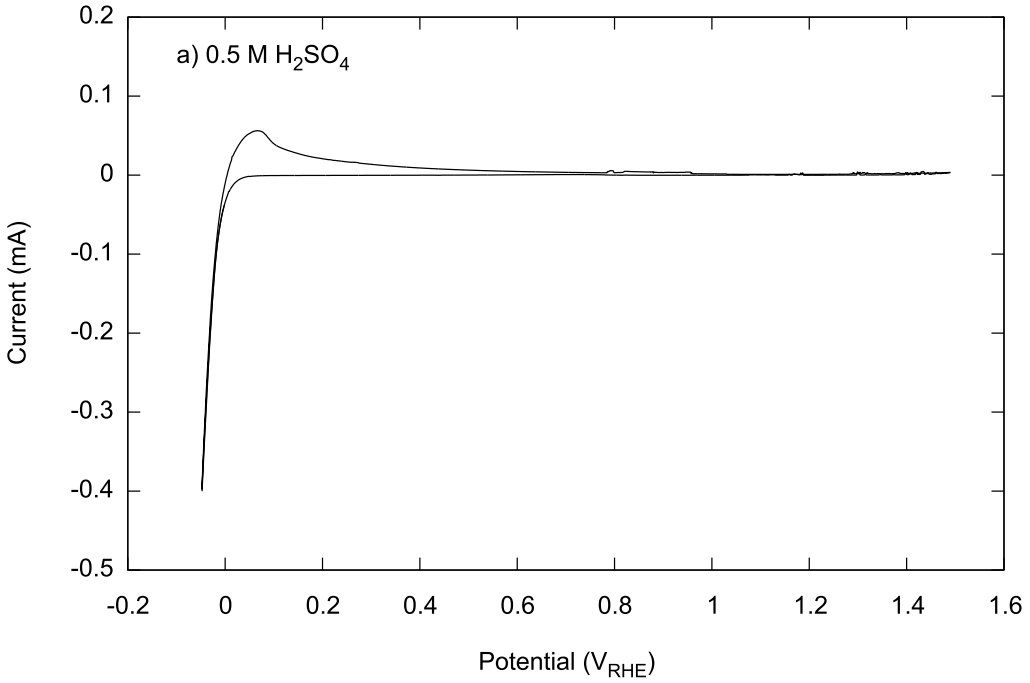

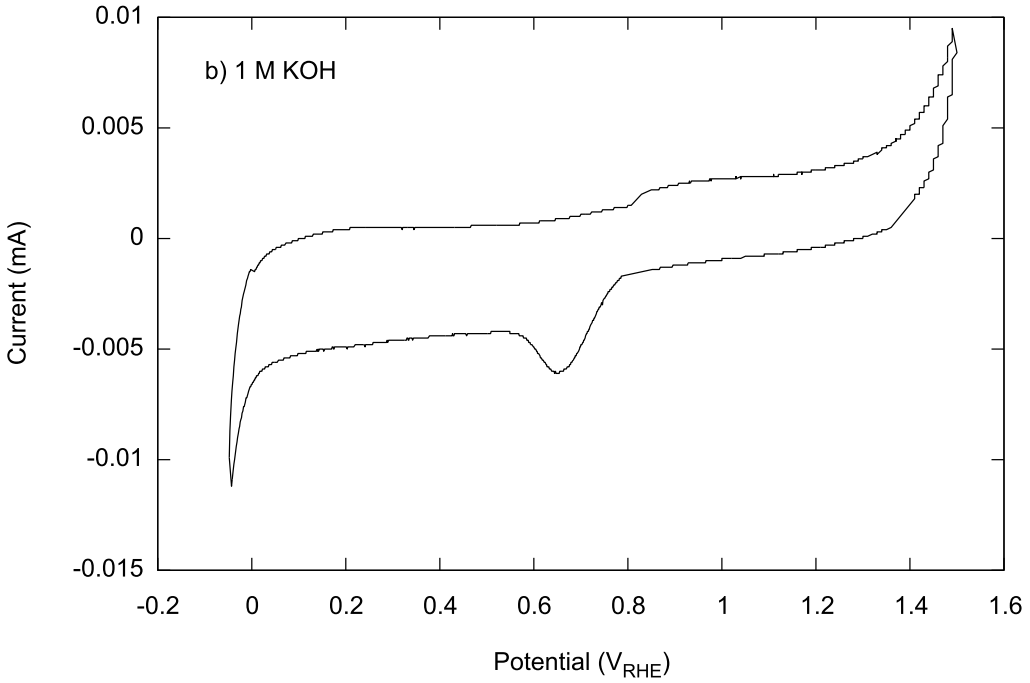

5.2.3 Oxygen reduction activity of $Pt_{CE}C$

Oxygen reduction activity of $Pt_{CE}C$ was determined using thin film rotating disk electrode voltammetry. These methods are described in more detail in Chapter 7 (Appendices). In this case, the thin film was prepared by casting 10 µL of the sonicated catalyst ink mixture (2.3 mg of the catalyst powder and 1 mL triply distilled H_2O) onto a 0.196 cm^2 GC electrode to give an approximate Pt loading of 0.92 μg_{Pt}. The ink was allowed to air dry, covered with 8 µL of 0.2 wt.% Nafion and dried in an oven at 80°C for 1 min before use. CVs of the catalyst in N_2-saturated and O_2-saturated 1M KOH are shown in Figure 5-7. We could not estimate the electrochemically active surface area of the Pt in the film from the baseline N_2 CV in Figure 5-6 or the CVs in Figure 5-7 because of the suppressed H_{UPD} region. Instead, we have calculated an estimated surface area using Equation 5-2 and assuming the Pt particles are spherical.

$$\text{Total surface area, } A_{tot} = \frac{3\, m_{tot}}{\rho\, r} \qquad 5\text{-}2$$

where m_{tot} is the total mass of Pt in the film

ρ is the density of Pt, 21.45 g cm^{-3}

r is the mean particle radius

The total mass of Pt in the thin film used for ORR activity was 0.92 μg_{Pt}. Given that the Pt particles are 13 nm in diameter (from TEM), the estimated Pt surface area is 0.20 cm^2 and the specific surface area is 22 $m^2\, g^{-1}$.

Figure 5-7 *Cyclic voltammetry of $Pt_{CE}C$ in nitrogen and oxygen saturated 1M KOH at 25°C. Scan rates were 10 mVs^{-1} and rotation rate for O_2 CV is 1500 rpm. The estimated Pt loading and surface area is 0.92 μg_{Pt} and 0.20 cm^2 respectively.*

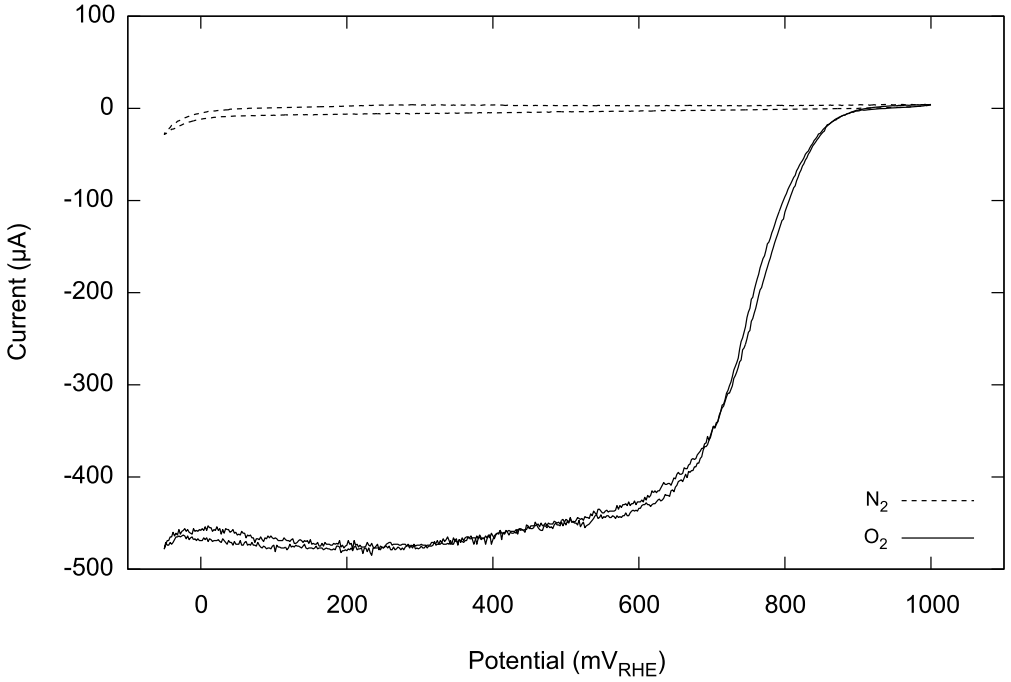

The baseline-corrected current densities of $Pt_{CE}C$ are shown in Figure 5-8 (negative going sweep). As a comparison, we have also included data for a commercially available E-TEK 10 wt. % Pt/C catalyst film. For $Pt_{CE}C$, the limiting current, 0.47 mA, was within 30% of the theoretical value expected.[2] For 10 wt. % Pt/C, the limiting current (0.13 mA) had a much larger deviation of about 80%. The deviations from the theoretical value for Pt supported on porous carbons is typically attributed to the high capacitance of the carbon supports in the double layer region (as observed in the base CV in Figure 5-6b for $Pt_{CE}C$) [63]. Comparing the two catalysts, we find that the onset potential of the ORR over $Pt_{CE}C$ (~900 mV) was lower than the commercial catalyst (~990 mV).

[2] Based on Equation A-8, i_L = 0.68 mA for a 0.196 cm^2 disk using the following values determined for 1M NaOH, 25°C, 1 atm O_2 [69]: D_{O2} = 1.65 x 10^{-5} $cm^2\,s^{-1}$, v = 0.011 $cm^2\,s^{-1}$ and O_2 solubility (concentration) = 8.4 x 10^{-7} mol cm^{-3}.

Figure 5-8 *Baseline-corrected oxygen reduction currents for $Pt_{CE}C$ and commercial 10 wt. % Pt/C catalysts in oxygen saturated 1M KOH at 25°C. Scan rates were 10 mVs^{-1} and rotation is 1500 rpm. The estimated Pt loading and surface area is 0.92 µg and 0.20 cm^2 for $Pt_{CE}C$, and 2.3 µg and 1.0 cm^2 for Pt/C. The surface area of Pt/C, 1.0 cm^2, was determined using Equation 5-1, given that the mean particle size is 6 nm* [65].

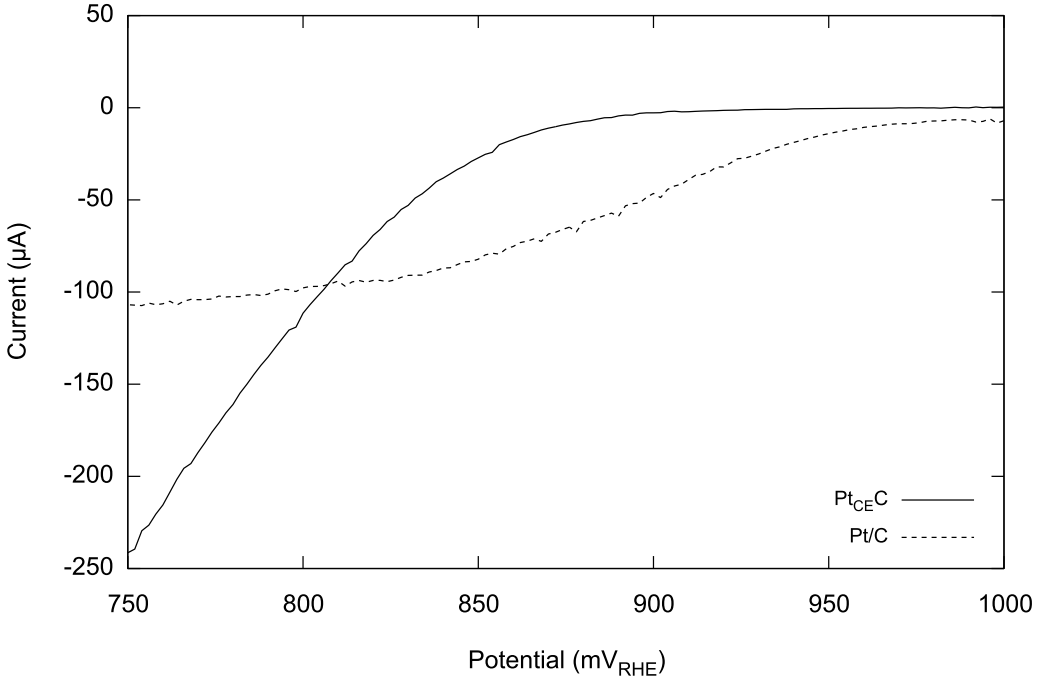

The mass transport-corrected kinetic current densities of the catalysts were calculated using the Koutecky-Levich equation (Equation A-9'). Tafel plots are shown in Figure 5-10. Despite having a higher onset potential for the ORR, the commercial catalyst had a steeper Tafel slope (84 mV dec^{-1} for 10 wt. % Pt/C *versus* 55 mV dec^{-1} for $Pt_{CE}C$). In other words, the overpotential for the ORR increases more slowly with current density over $Pt_{CE}C$, indicating a higher catalytic efficiency. For polycrystalline Pt, the expected Tafel slope in this potential region is close to 60 mV dec^{-1} [66].[3] It is thus possible that there is some

[3] At more negative potentials, 120 mV dec^{-1} is expected, as the surface changes from Pt-like to Pt oxide-like.

contribution from the carbon support in the ORR over our catalyst that has affected the observed Tafel slope. It is well known that in alkaline solution, carbon is active towards oxygen reduction [67].

The best fit line in the kinetic region, shown by the dashed double-headed arrows in Figure 5-9, is governed by the Tafel equation, Equation A-10. We can therefore extrapolate to the apparent exchange current densities for both catalysts. The exchange current density, j_0, is that at the Nernst potential for the oxygen reduction reaction, 1.229 V_{RHE}, and represents the intrinsic rate of electron transfer. The larger the magnitude of i_0, the more rapidly the reaction can occur. For the commercial catalyst, j_0, is 1.1 x 10^{-2} μA cm^{-2}. The j_0 of the $Pt_{CE}C$ catalyst is much smaller at 1.7 x 10^{-5} μA cm^{-2}. We note that there is a large error associated with this calculation as we have extrapolated over several orders of magnitude. However, we do acknowledge that there is much room for optimization of our catalyst especially in terms of Pt particle size and specific surface area. In principle, both of these parameters can be affected by the choice of deposition substrate.

Figure 5-9 *Tafel plot in O_2-saturated 1M KOH at 25°C, 10 mVs^{-1} and 1500 rpm for a) $Pt_{CE}C$ and b) 10 wt. % Pt/C catalysts. Dashed double-headed arrows represent the best-fit line in the kinetic region of the Tafel plot.*

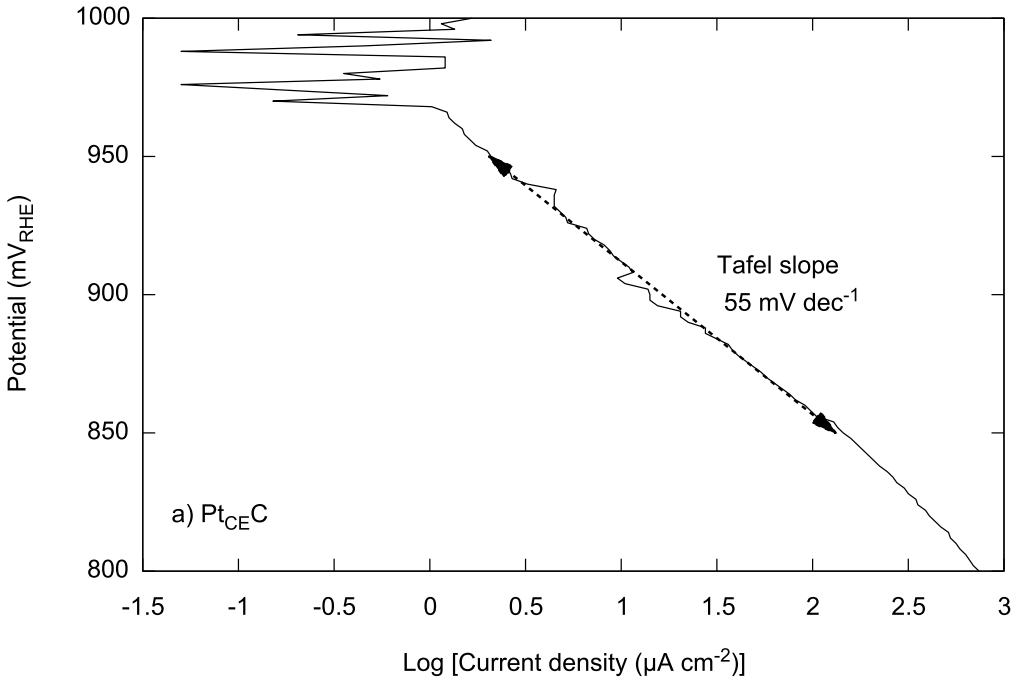

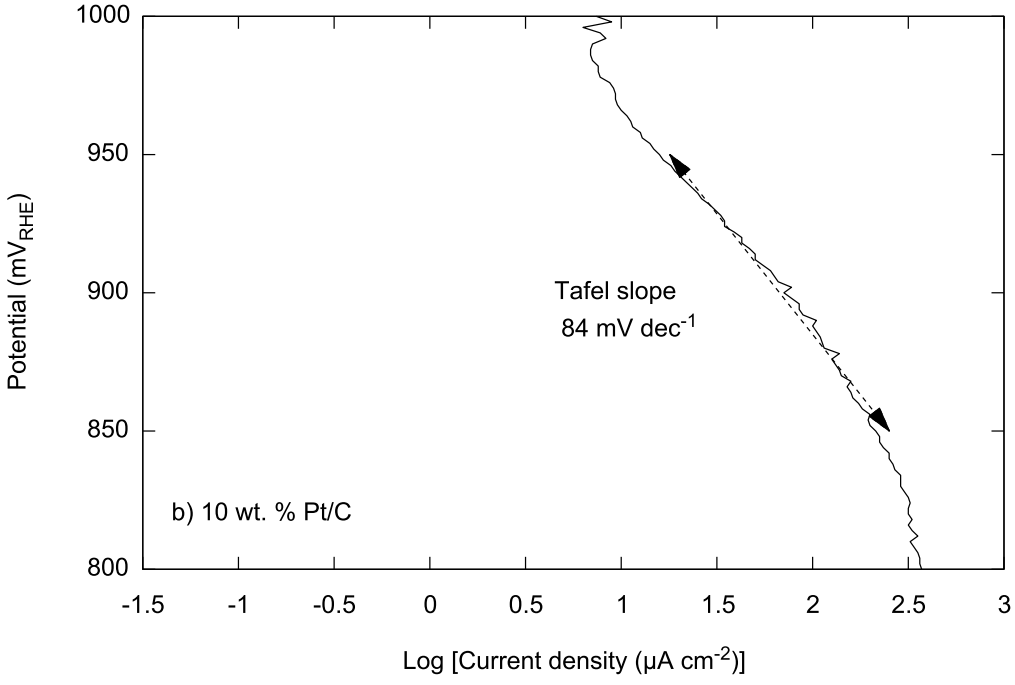

Finally, the oxygen reduction activity was determined by constructing sampled current voltammograms (SCVs). This is analogous to the determination of 2-propanol oxidation activity described in Chapters 2 and 3. We believe that the steady state current obtained using this method is more indicative of the conditions in a fuel cell run at a constant cell voltage. Moreover, we could also gain qualitative information regarding the tolerance of the catalyst to the build-up of adsorbates.

The thin film of catalyst supported on the GC disk was rotated at 1500 rpm in N_2- and O_2-saturated 1M KOH at 25°C and potentiostated at 1 V_{RHE} for 2 min prior to each 10 minute potential step. Figure 5-10 shows the raw and normalized sampled current voltammograms. The corresponding Tafel plots of $Pt_{CE}C$ are also included. The Tafel slope in this case is 91 mV dec^{-1} indicating that $Pt_{CE}C$ is less efficient under steady state conditions than dynamic conditions. This change in slope may be due to the build-up of inactive adsorbates, or change in the surface from a Pt-like to Pt oxide-like composition, during the time-scale of the potentiostatic experiment.

Figure 5-10 *Mixed and kinetic regions of sampled current voltammograms of $Pt_{CE}C$ collected at 25°C, 10 mVs^{-1} and 1500 rpm: a) Raw currents in N_2- and O_2-saturated 1M KOH, b) surface area normalized kinetic currents and c) corresponding Tafel plots d) mass-normalized kinetic currents and e) corresponding Tafel plots.*

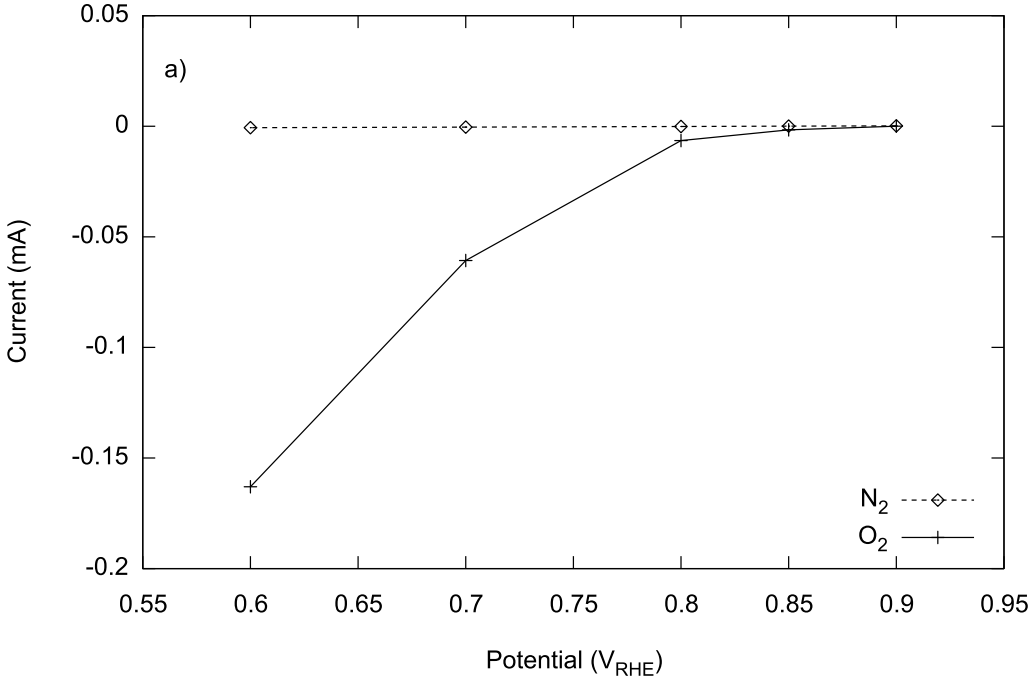

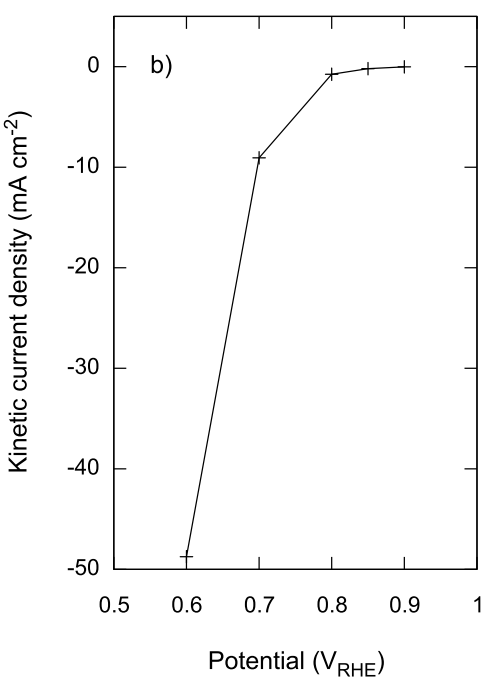

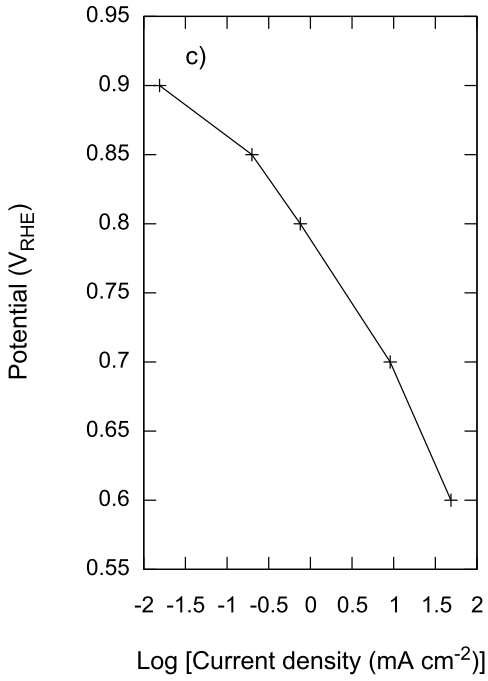

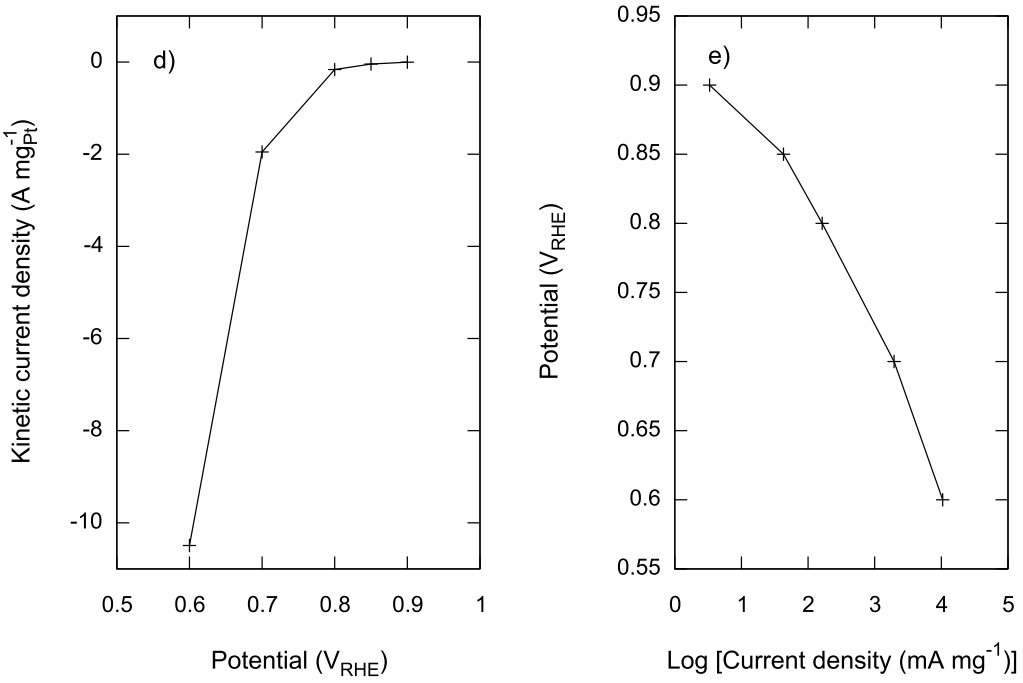

Overall, $Pt_{CE}C$ prepared using the *Pt CE deposition* is active towards the alkaline oxygen reduction reaction.

5.3 Conclusions

A carbon-supported Pt catalyst, $Pt_{CE}C$, was prepared using the *Pt CE deposition*. This was the first example of the application of this method using homogenous substrates. XRD, SAED and ICP-MS experiments confirmed the presence of Pt in the deposit. Further, from ICP-MS the mass of Pt deposited, ~0.2 mg, is congruent with the mass of Pt deposited by this method on heterogeneous substrates. XRD and TEM analysis show that the Pt particle size is between 10 and 18 nm. Finally, the catalyst showed activity towards the oxygen reduction reaction in alkaline aqueous solution. With optimization of the support, we foresee the *Pt CE deposition* having wide application towards the preparation of low-Pt loading catalysts with high dispersion of Pt on the support.

5.4 Experimental

5.4.1 General

The following reagents were used as received from the supplier: Nitrogen (Praxair, pre-purified), argon (Praxair, pre-purified), oxygen (Praxair, pre-purified), concentrated sulfuric acid (Caledon), hydrochloric acid (EMD chemicals), and nitric acid (EMD chemicals), chlorotrimethylsilane (Aldrich), potassium permanganate (Fischer Scientific), 30% hydrogen peroxide (Fischer Scientific), perfluorosulfonic acid-PTFE copolymer (Nafion) (Alfa Aesar, 5% w/w), potassium hydroxide (Caledon Laboratory Chemicals), ammonium chloride (Caledon Laboratory chemicals), and potassium hexachloroplatinate (Aithica Chemical Corporation). The following materials were used as received from the supplier: platinum gauze (Alfa Aesar, 52 mesh woven from 0.1 mm wire, 99.9% metals basis), nickel foil (Alfa Aesar, 0.5 mm thick, annealed, 99.5% metals basis), carbon powder (ElectroChem Inc., EC-C-Vulcan XC-72R), and glassy carbon disks (Pine Research Instrumentation, 5 mm outer diameter x 4 mm thick, mirror polished).

Triply distilled H_2O was used to prepare all aqueous solutions and was itself prepared by distilling a mixture of alkaline $KMnO_4$ and doubly distilled H_2O. Analytical grade reagents were used to prepare all electrolyte solutions. Electrolytes were purged with N_2 before use, and all voltammetric experiments were carried out under N_2 unless otherwise specified. All glassware was rinsed with *Piranha* solution (5:1 by volume concentrated H_2SO_4 and 30% H_2O_2) followed by thorough rinsing with triply distilled H_2O, and drying in an oven at 80°C.

Electrochemical experiments were performed on either an EG&G Princeton Applied Research Potentiostat/Galvanostat Model 273 using the corresponding M270 software or a Solartron SI 1287 Electrochemical Interface controlled by CorrWare for Windows Version 2-3d software. During electrochemical depositions, the potential of the platinum counter electrode was recorded using a Radio Shack multimeter and Scope View version 1.08 software. Rotating ring disk electrode (RRDE) experiments were performed using a Pine Research Instrumentation Modulated Speed Rotator, RRDE shaft, and E5TQ series ChangeDisk RRDE tip.

Transmission electron microscopy (TEM) and selected area electron diffraction (SAED) was performed on a JEOL 2010 instrument operation at 200 kV. TEM samples were prepared by sonicating a suspension of the powder catalyst in ethanol, and drop-coating onto a carbon grid (Ted Pella, Inc.). X-ray diffraction (XRD) patterns were taken using an Inel diffractometer equipped with a CPS 120 detector. The diffraction patterns were recorded at room temperature using Cu Kα radiation (λ = 1.5046 Å). Reference XRD patterns were generated using Powdercell 2.3 freeware.

Inductively coupled plasma mass spectrometry was carried out on an Elan 6000 spectroscope from Perkin Elmer. Samples were prepared by dissolving the deposits in *aqua regia*, evaporating to dryness on a hot plate and making up the residue quantitatively in 0.3 M HNO_3.

5.4.2 Preparation of platinum electrodes

The platinum black electrode used as a source of platinum in the platinum counter electrode deposition (see below) consisted of a 2.5 cm x 2.5 cm platinum gauze blacked with 0.02 M K_2PtCl_6/1 M $HClO_4$. A typical blackening experiment

would be performed at -0.1 V vs. Ag/AgCl (4M KCl) (Aldrich) until the observed current decayed to ~ 0 mA. The real surface area of the platinum black electrode was determined from the hydrogen under potential deposition (H_{UPD}) peak of a stabilized cyclic voltammogram recorded in 0.5 M H_2SO_4 assuming the charge associated with a monolayer of hydrides on polycrystalline Pt is 210 μC cm^{-2} [68] with 77% efficiency. Typical estimations were more than 4,000 cm^2. The counter electrode was freshly blacked after three uses in the platinum counter electrode deposition. The platinum black electrode used as a counter electrode in voltammetry was prepared in the manner described above.

5.4.3 Platinum counter electrode deposition

The deposition apparatus consisted of a glass cylinder of dimensions 10 cm x 2.5 cm inner diameter. The internal surface of the cylinder was silanized before use employing the following procedure. The cylinder was fitted with a rubber septum secured with copper wire, and evacuated and back filled with argon four times. 5 mL of $(CH_3)_3SiCl$ was added to the cylinder under argon via a gastight syringe. The contents were then warmed to 40°C for 1 hour. The excess $(CH_3)_3SiCl$ was removed under vacuum and the vessel dried in a desiccator overnight.

The working electrode was a Ni foil disk with a diameter of 2.2 cm. A 15 cm Ni wire handle was spot-welded to the edge of the disk and oriented perpendicular to the plane of the disk. The disk was placed at the bottom of the cylinder, and 50 mg carbon powder was carefully placed on the center of the disk. 10 mL of 2.0 M NH_4Cl was then added to the vessel carefully so as to avoid excessive dispersion of the carbon powder. The Pt counter electrode was washed in triply distilled water and dried in a stream of hydrogen to reduce its surface before placing into the deposition solution. The Ag/AgCl (4M KCl)

reference electrode was also rinsed with triply distilled water and positioned closed to the center of the Ni disk. A current of -0.1 A was applied between the Ni working electrode and the Pt black counter electrode for 1 hour. After deposition, the electrolyte with suspended catalyst (denoted $Pt_{CE}C$ herein) was collected and centrifuged to collect the powder. The powder was then washed and centrifuged 3 times with triply distilled water, discarding the washings each time. Lastly, the powder was dried under high vacuum overnight. The isolated catalyst powder is referred to as $Pt_{CE}C$ herein.

5.4.4 Electrochemical methods

The working electrode was prepared as described presently. A mixture of 2 mg of the catalyst powder, 1.6 mL of triply distilled H_2O, 0.4 mL of $(CH_3)_2CH(OH)$ and 20 µL of 5% w/w Nafion was prepared in a ½ dram vial, shaken vigorously and sonicated for 25 minutes. 10 µL of the resulting suspension was then cast as a thin film onto the surface of a pre-polished GC disk. The film was allowed to air dry before use in electrochemical experiments. Other ink preparations are explicitly stated in the text *vide supra*.

Cyclic voltammetry was performed using a conventional three-electrode cell configuration. The Pt counter electrode was isolated in a glass tube with a 10 µm porous glass frit. A static reversible hydrogen electrode (RHE) was used as a reference point and all potentials are versus this reference unless otherwise stated (denoted V_{RHE}). The electrolyte was 1 M KOH or 0.5 M H_2SO_4 at 25°C.

Rotating disk voltammetry and potentiostatic experiments were used to determine oxygen reduction reaction activity. These experiments were performed at 25°C in O_2-saturated electrolytes obtained by bubbling O_2 through the solution for 30 minutes. O_2 was also flushed over the solution during the measurements.

The working electrode was rotated at 1500 rpm. For cyclic voltammetry, the scan rate was 10 mV s^{-1}. For potentiostatic experiments, the electrode was stepped to potentials between 1 and 0 V_{RHE} for 20 minutes punctuated by 2 minute potential steps at 1 V to bring the catalyst surface back to its initial condition. Sampled current voltammograms were then constructed by calculating the average current in the last 5 seconds of the potential steps, applying a Koutecky-Levich correction (see section A.2.3), and plotting against the relevant potential.

5.5 Bibliography

[1] E. Antolini, App. Cat. B-Environ., 88 (2009) 1-24.

[2] A.L. Dicks, J. Power Sources, 156 (2006) 128-141.

[3] K. Lee, J. Zhang, H. Wang, D.P. Wilkinson, J. Appl. Electrochem., 36 (2006) 507-522.

[4] Y. Mu, H. Liang, J. Hu, L. Jiang, L. Wan, J. Phys. Chem. B., 109 (2005) 22212-22216.

[5] G. Girishkumar, K. Vinodgopal, P.V. Kamat, J. Phys. Chem. B., 108 (2004) 19960-19966.

[6] K. Gong, F. Du, Z. Xia, M. Durstock, L. Dai, Science, 323 (2009) 760-764.

[7] W. Li, C. Liang, W. Zhou, J. Qiu, Z. Zhou, G. Sun, Q. Xin, J. Phys. Chem. B., 107 (2003) 6292-6299.

[8] Z. Liu, X. Lin, J.Y. Lee, W. Zhang, M. Han, L.M. Gan, Langmuir, 18 (2002) 4054-4060.

[9] B. Seger, P.V. Kamat, J. Phys. Chem. C, 113 (2009) 7990-7995.

[10] C. Wang, M. Waje, X. Wang, J.M. Tang, R.C. Haddon, Y. Yan, Nano Letters, 4 (2004) 345-348.

[11] Y. Xing, J. Phys. Chem. B., 108 (2004) 19255-19259.

[12] E. Guilminot, F. Fischer, M. Chatenet, A. Rigacci, S. Berthon-Fabry, P. Achard, E. Chainet, J. Power Sources, 166 (2007) 104-111.

[13] N. Job, J. Marie, S. Lambert, S. Berthon-Fabry, P. Achard, Energy Conversion and Management, 49 (2008) 2461-2470.

[14] H.J. Kim, W.I. Kim, T.J. Park, H.S. Park, D.J. Suh, Carbon, 46 (2008) 1393-1400.

[15] J. Marie, S. Berthon-Fabry, P. Achard, M. Chatenet, A. Pradourat, E. Chainet, J. Non Cryst. Solids, 350 (2004) 88-96.

[16] J. Marie, S. Berthon-Fabry, M. Chatenet, E. Chainet, R. Pirard, N. Cornet, P. Achard, J. Appl. Electrochem., 37 (2007) 147-153.

[17] J. Marie, R. Chenitz, M. Chatenet, S. Berthon-Fabry, N. Cornet, P. Achard, J. Power Sources, 190 (2009) 423-434.

[18] S. Wei, D. Wu, X. Shang, R. Fu, Energy and Fuels, 23 (2009) 908-911.

[19] J. Maruyama, I. Abe, J. Power Sources, 148 (2005) 1-8.

[20] A. Guha, W. Lu, T.A. Zawodzinski Jr., D.A. Schiraldi, Carbon, 45 (2007) 1506-1517.

[21] J.J. Niu, J.N. Wang, Electrochim. Acta, 53 (2008) 8058-8063.

[22] H.X. Huang, S.X. Chen, C. Yuan, J. Power Sources, 175 (2008) 166-174.

[23] A. Guha, T.A. Zawodzinski Jr., D.A. Schiraldi, J. Power Sources, 172 (2007) 530-541.

[24] A.Ö. Yazaydin, I. Eroglu, E. Han, L. Türker, Chem. Eng. Commun., 190 (2003) 976-985.

[25] J. Maruyama, I. Abe, J. Electrochem. Soc., 153 (2006) A1181-A1185.

[26] J. Maruyama, K.I. Sumino, M. Kawaguchi, I. Abe, Carbon, 42 (2004) 3115-3121.

[27] J. Maruyama, I. Abe, Electrochim. Acta, 48 (2003) 1443-1450.

[28] B. Babic, V. Radmilovic, N. Krstajic, B. Kaludjerovic, Materials Science Forum, 518 (2006) 283-288.

[29] B.M. Babic, B.V. Kaluderovic, L.M. Vracar, V. Radmilovic, N.V. Krstajic, Journal of the Serbian Chemical Society, 72 (2007) 773-785.

[30] S.H. Joo, S.J. Choi, I. Oh, J. Kwak, Z. Liu, O. Terasaki, R. Ryoo, Nature, 412 (2001) 169-172.

[31] P. Kim, H. Kim, J.B. Joo, W. Kim, I.K. Song, J. Yi, J. Power Sources, 145 (2005) 139-146.

[32] R. Rajagopalan, J. Coronado, H.C. Foley, A. Vannice, Materials Research Society Symposium - Proceedings, 756 (2003) 371-377.

[33] R. Rajagopalan, A. Ponnaiyan, P.J. Mankidy, A.W. Brooks, B. Yi, H.C. Foley, Chem. Comm., 10 (2004) 2498-2499.

[34] S. Thiele, T. Fürstenhaupt, D. Banham, T. Hutzenlaub, V. Birss, C. Ziegler, R. Zengerle, J. Power Sources, 228 (2013) 185-192.

[35] A. Vinu, Top. Catal., 53 (2010) 291-296.

[36] E.P. Ambrosio, M.A. Dumitrescu, C. Francia, C. Gerbaldi, P. Spinelli, Fuel Cells, 9 (2009) 197-200.

[37] E.P. Ambrosio, C. Francia, C. Gerbaldi, N. Penazzi, P. Spinelli, M. Manzoli, G. Ghiotti, J. Appl. Electrochem., 38 (2008) 1019-1027.

[38] E.P. Ambrosio, C. Francia, M. Manzoli, N. Penazzi, P. Spinelli, Int. J. Hydrogen Energy, 33 (2008) 3142-3145.

[39] D. Banham, F. Feng, T. Fürstenhaupt, K. Pei, S. Ye, V. Birss, J. Power Sources, 196 (2011) 5438-5445.

[40] L. Calvillo, V. Celorrio, R. Moliner, M.J. Lázaro, Mater. Chem. Phys., 127 (2011) 335-341.

[41] L. Calvillo, M. Gangeri, S. Perathoner, G. Centi, R. Moliner, M.J. Lázaro, Int. J. Hydrogen Energy, 36 (2011) 9805-9814.

[42] L. Calvillo, M.J. Lázaro, E. García-Bordejé, R. Moliner, P.L. Cabot, I. Esparbé, E. Pastor, J.J. Quintana, J. Power Sources, 169 (2007) 59-64.

[43] W.C. Choi, S.I. Woo, M.K. Jeon, J.M. Sohn, M.R. Kim, H.J. Jeon, Adv. Mater., 17 (2005) 446-451.

[44] G. Gupta, D.A. Slanac, P. Kumar, J.D. Wiggins-Camacho, J. Kim, R. Ryoo, K.J. Stevenson, K.P. Johnston, J. Phys. Chem. C, 114 (2010) 10796-10805.

[45] J.B. Joo, P. Kim, W. Kim, J. Yi, Journal of Electroceramics, 17 (2006) 713-718.

[46] S.H. Joo, K. Kwon, D.J. You, C. Pak, H. Chang, J.M. Kim, Electrochim. Acta, 54 (2009) 5746-5753.

[47] S.H. Joo, H.I. Lee, D.J. You, K. Kwon, J.H. Kim, Y.S. Choi, M. Kang, J.M. Kim, C. Pak, H. Chang, D. Seung, Carbon, 46 (2008) 2034-2045.

[48] S.H. Joo, C. Pak, D.J. You, S.-. Lee, H.I. Lee, J.M. Kim, H. Chang, D. Seung, Electrochim. Acta, 52 (2006) 1618-1626.

[49] H.T. Kim, D.J. You, H.K. Yoon, S.H. Joo, C. Pak, H. Chang, I.-. Song, J. Power Sources, 180 (2008) 724-732.

[50] S.H. Liu, C.C. Chiang, M.T. Wu, S.B. Liu, Int. J. Hydrogen Energy, 35 (2010) 8149-8154.

[51] P.V. Shanahan, L. Xu, C. Liang, M. Waje, S. Dai, Y.S. Yan, J. Power Sources, 185 (2008) 423-427.

[52] Z.P. Sun, X.G. Zhang, Y.Y. Liang, H. Tong, R.L. Xue, S.D. Yang, H.L. Li, J. Electroanal. Chem., 633 (2009) 1-6.

[53] S. Vengatesan, H.J. Kim, S.K. Kim, I.H. Oh, S.Y. Lee, E. Cho, H.Y. Ha, T.H. Lim, Electrochim. Acta, 54 (2008) 856-861.

[54] Z. Wen, J. Liu, J. Li, Adv. Mater., 20 (2008) 743-747.

[55] J. Zeng, F. Su, J.Y. Lee, X.S. Zhao, J. Chen, X. Jiang, J. Mater. Sci., 42 (2007) 7191-7197.

[56] K. Sasaki, J.X. Wang, H. Naohara, N. Marinkovic, K. More, H. Inada, R.R. Adzic, Electrochim. Acta, 55 (2010) 2645-2652.

[57] W.P. Zhou, K. Sasaki, D. Su, Y. Zhu, J.X. Wang, R.R. Adzic, J. Phys. Chem. C, 114 (2010) 8950-8957.

[58] S.R. Brankovic, J.X. Wang, R.R. Adžić, Surf. Sci., 474 (2001) L173-L179.

[59] K. Sasaki, Y. Mo, J.X. Wang, M. Balasubramanian, F. Uribe, J. McBreen, R.R. Adzic, Electrochim. Acta, 48 (2003) 3841-3849.

[60] A.U. Nilekar, Y. Xu, J. Zhang, M.B. Vukmirovic, K. Sasaki, R.R. Adzic, M. Mavrikakis, Top. Catal., 46 (2007) 276-284.

[61] J.X. Wang, H. Inada, L. Wu, Y. Zhu, Y. Choi, P. Liu, W.-. Zhou, R.R. Adzic, J. Am. Chem. Soc., 131 (2009) 17298-17302.

[62] T. Ghosh, M.B. Vukmirovic, F.J. DiSalvo, R.R. Adzic, J. Am. Chem. Soc., 132 (2010) 906-907.

[63] K.J.J. Mayrhofer, D. Strmcnik, B.B. Blizanac, V. Stamenkovic, M. Arenz, N.M. Markovic, Electrochim. Acta, 53 (2008) 3181-3188.

[64] P. Villars, K. Cenzual, Pearson's Crystal Data - Crystal Structure Database for Inorganic Compounds, ASM International, Materials Park, OH; release 2010/11.

[65] A. Bayrakçeken, A. Smirnova, U. Kitkamthorn, M. Aindow, L. Türker, İ. Eroğlu, C. Erkey, J. Power Sources, 179 (2008) 532-540.

[66] T.J. Schmidt, V. Stamenkovic, P.N. Ross Jr., N.M. Markovic, Physical Chemistry Chemical Physics, 5 (2003) 400-406.

[67] E. Yeager, J. Mol. Cat., 38 (1986) 5-25.

[68] B.E. Conway, H. Angerstein-Kozlowska, Acc. Chem. Res., 14 (1981) 49-56.

[69] C. Paliteiro, A. Hamnett, J.B. Goodenough, Journal of Electroanalytical Chemistry and Interfacial Electrochemistry, 233 (1987) 147-159.

Chapter 6: Conclusions and final remarks

This dissertation described the use of the *Pt CE deposition* to prepare a variety of nickel- and carbon-supported platinum catalysts. To summarize, we have prepared eight new catalysts for 2-propanol oxidation or oxygen reduction: $Pt_{CE}Ni_{foam}$, Ni-$Pt_{CE}Ni_{foam}$, $Pt_{CE}Ni_{NP}$, $Pt_{Tr}Ni_{NP}$, $Pt_{CE}Ni_{NP}$/GC, $Pt_{Tr}Ni_{NP}$/GC, $Pt_{CE2X}Ni_{NP}$/GC and $Pt_{CE}C$. The catalysts were fully characterized by electrochemical, microscopic and spectroscopic techniques including voltammetry, SEM, TEM, SAED, ICP-MS, XRD and XPS. $Pt_{CE}Ni_{foam}$, Ni-$Pt_{CE}Ni_{foam}$, $Pt_{CE}Ni_{NP}$, $Pt_{Tr}Ni_{NP}$, $Pt_{CE}Ni_{NP}$/GC were investigated for their 2-propanol oxidation activity. $Pt_{CE}Ni_{NP}$/GC, $Pt_{Tr}Ni_{NP}$/GC, $Pt_{CE2X}Ni_{NP}$/GC and $Pt_{CE}C$ were evaluated for oxygen reduction activity. Attempts to explain any connection between catalyst structure or properties and catalytic activity were made. Finally, the catalysts were compared to state-of-the-art commercial catalysts. The following commentary summarizes the main findings of each study and suggested recommendations for future work.

6.1 General findings

In general, the results of these studies indicate that the mechanism of the *Pt CE deposition* is substrate-independent. Specifically, for all substrates, hydrogen evolution was observed at early times, the Pt was uniformly deposited, and the mass of Pt was low (<250 μg). Minor changes in the working electrode potential profiles on each substrate were observed. However, these discrepancies did not affect the ultimate structure of the catalysts. In every case the catalysts were active with low Pt-loadings. The structure of solvated Pt

remains a mystery. Current available technology does not lend itself to characterization of the Pt species *in situ.* Yet, this may not necessarily be a high value result.

6.2 Low Pt-loading Ni-Pt and Pt deposits on Ni: Preparation, activity and investigation of electronic properties

This initial study on foam-based catalysts, $Pt_{CE}Ni_{foam}$ and Ni-$Pt_{CE}Ni_{foam}$, set out to determine the microscopic and electronic characteristics of catalysts prepared by *the Pt CE deposition*. This is the first report in the literature discussing and providing evidence for the possible effects (bi-functional, electronic and geometric) at play in Ni-Pt 2-propanol oxidation catalysis. The most significant results to emerge from this study are that $Pt_{CE}Ni_{foam}$ and Ni-$Pt_{CE}Ni_{foam}$ were markedly more active than Pt_{black} at potentials above 250 mV. At 500 mV, Ni-$Pt_{CE}Ni_{foam}$ was 5 times more active than Ni-$Pt_{CE}Ni_{gauze}$ and 9 times more active than Pt_{black}. Moreover, $Pt_{CE}Ni_{foam}$ was 20 times more active than Ni-$Pt_{CE}Ni_{gauze}$ and a remarkable 38 times more active than Pt_{black}. The observed activity at potentials between 50 and 250 mV_{RHE} were therefore attributed to slight electronic effects in the Ni–$Pt_{CE}Ni_{foam}$ catalysts. We believe that the enhanced activity at potentials > 250 mV for Ni–$Pt_{CE}Ni_{foam}$ was a combination of electronic and bi-functional effects and for $Pt_{CE}Ni_{foam}$ a combination of geometric and bi-functional effects. Our findings add substantially to the body of work on 2-propanol systems, as well as Ni-Pt electro-catalysts. Many of the reports that specifically discuss electronic effects in Ni-Pt catalysts lack rigor in their data analyses and interpretations. Often, poor choice of XPS calibration scales and fitting methods result in conclusions that fit the predictions of authors rather than reflect reality. That being said, great efforts were made to set a good foundation

for subsequent studies in terms of thorough data collection and careful analysis methods.

6.3 Structural and activity comparison of self-limiting versus traditional Pt electro-deposits on glancing angle deposited nanopillar Ni films

The second study compared a conventional platinum deposition with the *Pt CE electrode deposition* on nickel nanopillar films prepared by Glancing Angle Deposition (GLAD). This work is the first alcohol oxidation study reported on GLAD-based systems. The deposits prepared via our method were more active towards 2-propanol oxidation than both traditionally prepared deposits and commercially available state-of-the-art unsupported platinum nanoparticles. Of particular significance was the similar activity of $Pt_{CE}Ni_{NP}$ and carbon–supported Pt-Ru. In the simplest terms, the replacement of the noble metal Ru with base metal Ni without loss in activity represents a significant cost reduction. Furthermore, the discovery that the Ni_{NP} substrate itself was active toward 2-propanol oxidation in base was noteworthy. The catalytic properties of the Ni_{NP} definitely warrant further study. Specifically, it would be interesting to perform a comparative Atomic Force Microscopy study on the pristine and used substrate to investigate its surface topography before and after use. The results of this study could allude to the source of activity. The scope of alcohols that could be oxidised can also be explored.

6.4 Oxygen reduction reaction activity of Pt electro-deposits on glancing angle deposited nanopillar Ni films

The third study, oxygen reduction over $Pt_{Tr}Ni_{NP}$/GC, $Pt_{CE}Ni_{NP}$/GC and $Pt_{CE2X}Ni_{NP}$/GC, contributes to existing knowledge of ORR activity over GLAD-based structures. Noteworthy is the discovery that a double *Pt CE deposition* can be used to prepare a more protective Pt layer over Ni. The Ni underlayer did not seem to have any beneficial effects except those related to dispersion of the Pt on its rough, porous surface. This was reflected in the specific surface area of $Pt_{Tr}Ni_{NP(85)}$/GC, $Pt_{CE}Ni_{NP(85)}$/GC and $Pt_{CE2X}Ni_{NP(88)}$/GC being several orders of magnitude higher than several state-of-the-art catalysts, including other GLAD-based catalysts. However, our catalysts have room for optimization. For example, the oblique deposition angle could be modified and/or the number of, or duration of, the *Pt CE depositions* could be adjusted. In the former case, the spacing of the pillars (dependent on the deposition angle) may have a significant effect on the mass transport of reactants to the catalysts surface. On the other hand, the duration or number of *Pt CE depositions* will affect the mass of Pt deposited and possibly coverage of Pt on the substrate surface. An interesting study would involve electrochemical degradation testing of the $Pt_{CE2X}Ni_{NP(88)}$/GC. The extent of protection of the Ni underlayer could be evaluated by potential cycling at high potentials (up to 1.2 V) punctuated by surface area measurements by CV. The degradation could also be monitored by SEM and XRD analyses.

As this study stands, there is still the unanswered question of what processes are occurring during the traditional Pt deposition. The origin of the oxidation current at early times can be determined by control experiments. For example, the deposition can be performed without the Pt salt in the electrolyte to determine if the current reflects oxidation of the Ni_{NP} surface, although we do not know if the presence of dissolved or initially nucleated Pt could affect the surface oxidation.

Finally, it is worth trying to deposit the Ni_{NP} directly onto a fuel cell membrane, followed by modified *Pt CE deposition* to deposit Pt onto just the Ni regions. Alternatively, the Ni_{NP} can be transferred via a decal into a membrane electrode assembly, and the cell tested for performance and stability.

6.5 Preparation, characterization and oxygen reduction reaction electrocatalytic activity on Vulcan carbon-supported Pt nanoparticles: First application of the Pt counter electrode deposition onto particulate substrates.

The final study described the modification of the *Pt CE deposition* to accommodate particulate substrates. As a proof of concept, we deposited platinum onto Vulcan carbon to fabricate a carbon-supported platinum catalyst that was microscopically and electrochemically characterized and tested for oxygen reduction. The deposition was successful in terms of the mass and dispersion of Pt detected on the carbon powder. A definite yet ironic improvement would be to increase the loading of Pt on the carbon as many regions of carbon contained no Pt particles. It would be interesting to extend the time of the *Pt CE deposition* to determine whether more Pt could nucleate on the carbon powder. In the same vein, multiple depositions could be performed to possibly increase the weight percent of Pt on carbon ultimately, similar to that observed for $Pt_{CE2X}Ni_{NP(88)}$/GC catalysts in the Chapter 4. From an experimental standpoint, a more suitable cell could be machined. For example, a shiny nickel cylinder may provide more contact area for the particulate substrate. Furthermore, a suspended overhead stirrer could be used if the conventional stir bar causes excessive signal noise.

One of the most promising future studies, however, would be the use of highly functionalized particulate substrates instead of Vulcan carbon. These substrates could be tailored for the particular reaction, or to allow high dispersion of the Pt during deposition. Furthermore, if a highly active recipe is found, the catalyst can be pressed into a membrane and tested in fuel cell experiments. This would be the ultimate goal of this investigation. As a final note, the catalysts created via this method do not have to be limited to fuel cell reactions so that the scope of this work can be broadened significantly.

6.6 Summary

Altogether, the utility of the *Pt CE deposition* has been demonstrated by this work. The deposition was used to prepare a variety of Pt-based catalysts with interesting electrochemical and physical properties. There are still a number of approaches that can be taken, whether through investigation of unknown factors in this work, or by preparing and screening various novel catalysts for various electrochemical reactions.

Appendices [1-5]

A.1 Diffusion Limited Current

Faraday's Law (Equation A-1) describes the proportional relationship between the concentration of an electrolyte at an electrode surface and the observed current during electrolysis. Fick's First Law of Diffusion (Equation A-2) states that the diffusive flux of the analyte is directly proportional to the steepness of the concentration gradient. When these two expressions are combined, a general equation for the diffusion limited current, i_L, can be obtained:

Faraday's law: $Q = nF = it$ A-1

where Q is the total charge passed in C

n is the number of moles of electrons

F is Faraday's constant 96485 C mol^{-1}

i is current in A

t is time in s

Fick's first law of diffusion: $J = -D \frac{\partial C}{\partial x}$ A-2

where J is the flux of analyte in mol cm^{-2} s^{-1}

D is the analyte's diffusion coefficient in cm^2 s^{-1}

C is the concentration of the analyte in mol cm^{-3}

x is the distance from the electrode surface in cm

Diffusion limited current: $i_L = nFAD\frac{\partial C}{\partial x}$ A-3

where n is the number of electrons in the half reaction of the analyte

A is the geometric electrode area in cm^2

Equation A-3 governs all diffusion limited voltammetry techniques including potential step, potential sweep and hydrodynamic voltammetry, the only

difference in the techniques being how the concentration gradient is generated and sustained.

A.1.1 Potential Step

In potential step methods such as chronoamperometry, the electrode is stepped to a potential from some initial potential where negligible current flows. The experiment is performed in quiet solution and the initial and step potentials are chosen to enclose the formal Nernst potential, E^0, of the analyte. When the step potential is more negative than E^0, the analyte is reduced. If it is more positive, the analyte is oxidised. When the potential step is applied, the analyte is consumed, thus depleting its concentration at the electrode surface to essentially zero. A very large concentration gradient is therefore generated, resulting in a large current immediately following the potential step. Over time, the concentration gradient relaxes slowly as the *diffusion layer*[1] grows. The decay of current over time is described by the *Cottrell equation* and illustrated in Figure A-1b:

$$\text{Cottrell equation: } i(t) = nFAC\left(\frac{D}{\pi t}\right)^{\frac{1}{2}} \qquad \text{A-4}$$

[1] The diffusion layer is defined as the region adjacent to the electrode surface where the analyte concentrations are different from their value in the bulk solution.

Figure A-1 *a) Potential step and b) current transient expected for chronoamperometry experiments.*

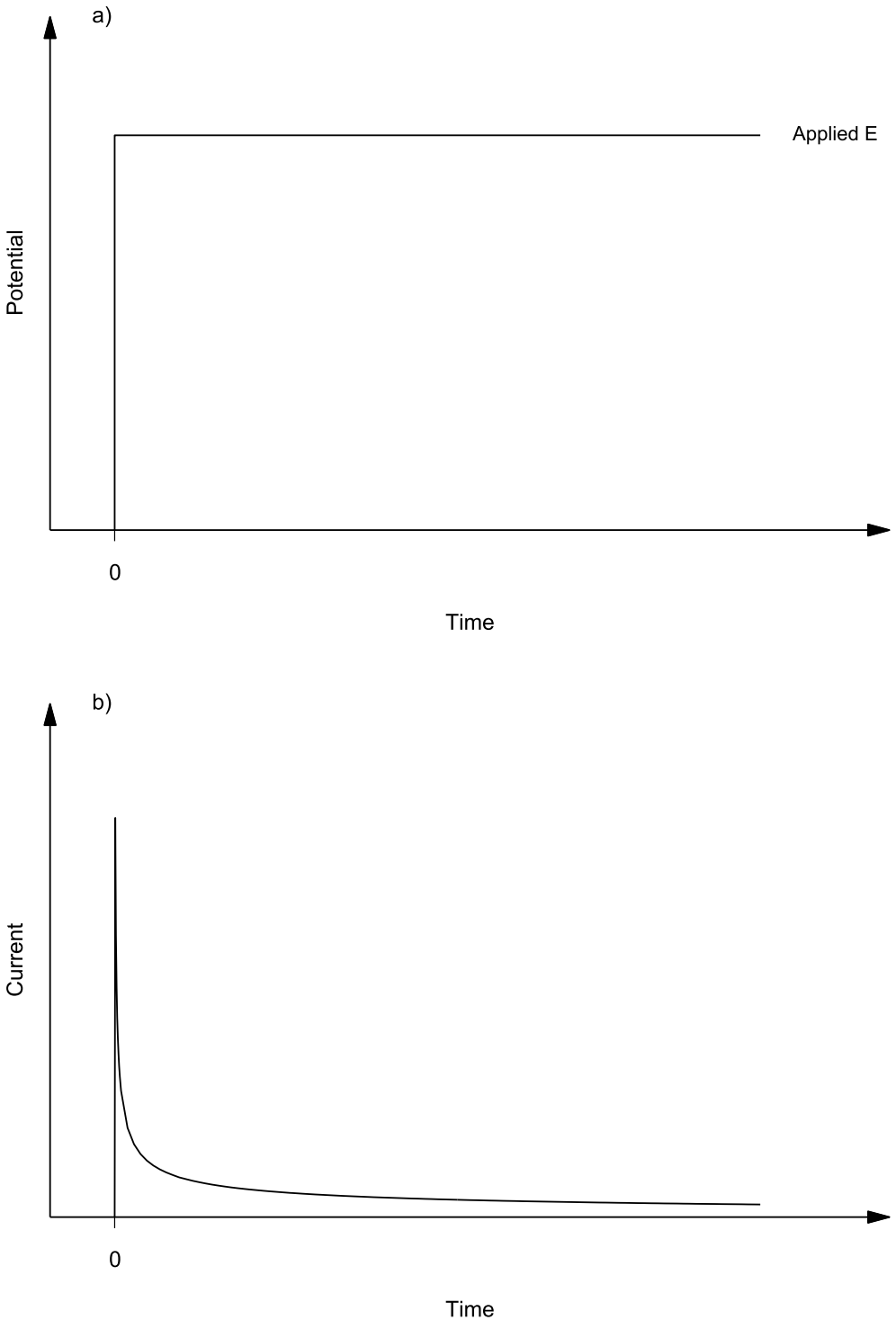

A.1.2 Potential sweep

Potential sweep methods, such as cyclic or linear sweep voltammetry involve scanning the potential at a constant rate from an initial potential to a final potential beyond the formal potential of the analyte. Similar to potential step experiments, the experiment is carried out in quiet solution. When scanning towards more negative potentials, the analyte is reduced; moving towards more positive potentials, the analyte is oxidised. Cyclic voltammetry is identical to linear sweep voltammetry except that the scan direction is reversed after the initial sweep to return the analyte to its original form. In both cases, the analyte is consumed as the potential approaches and passes its formal potential, thus generating a concentration gradient. The current increase is not as sudden as in the potential step method, but as the potential moves past E^0, the surface concentration of analyte drops to nearly zero so that mass transport is at its maximum rate and then declines as the analyte concentration depletes. The peak current, i_p, of the transient is defined by the *Randle-Sevcik equation*:

$$\text{Randles} - \text{Sevcik equation: } i_p = 0.4463\ nFAC\left(\frac{nF\nu D}{RT}\right)^{\frac{1}{2}} \qquad \text{A-5}$$

where ν is the scan rate in V s^{-1}

R is the universal gas constant, 8.314 J mol^{-1} K^{-1}

T is the temperature in K

Figure A-2 *a) Potential sweep and b) linear sweep voltammogram during linear sweep voltammetry and c) potential sweep and d) cyclic voltammogram in cyclic voltammetry.*

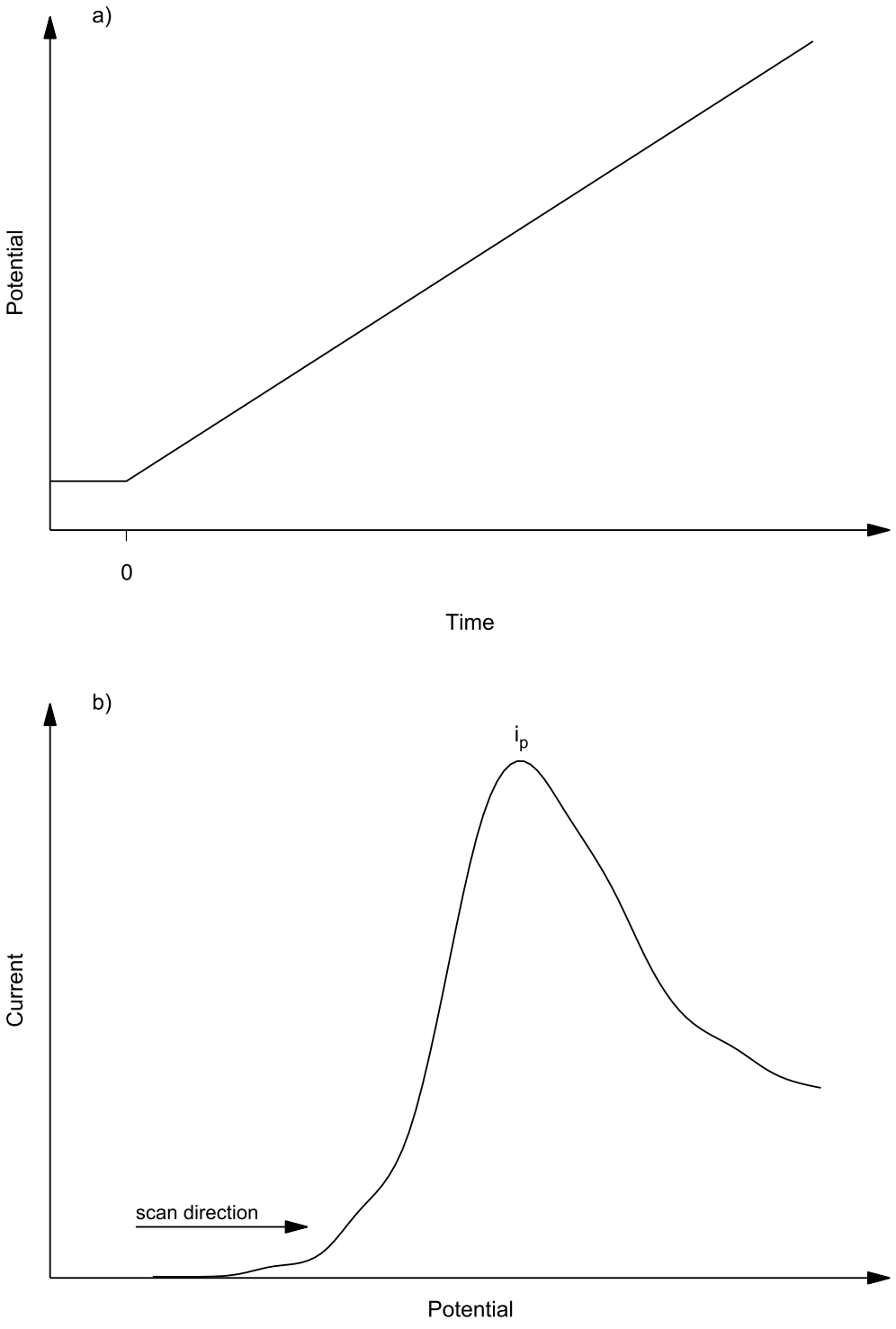

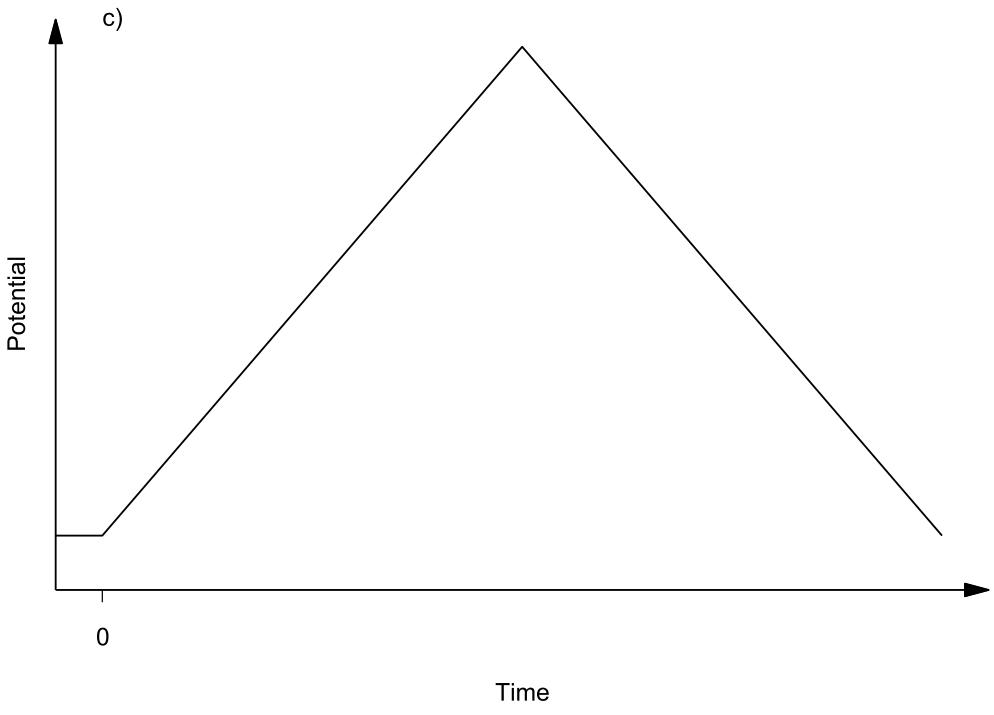
c)
Potential
0
Time

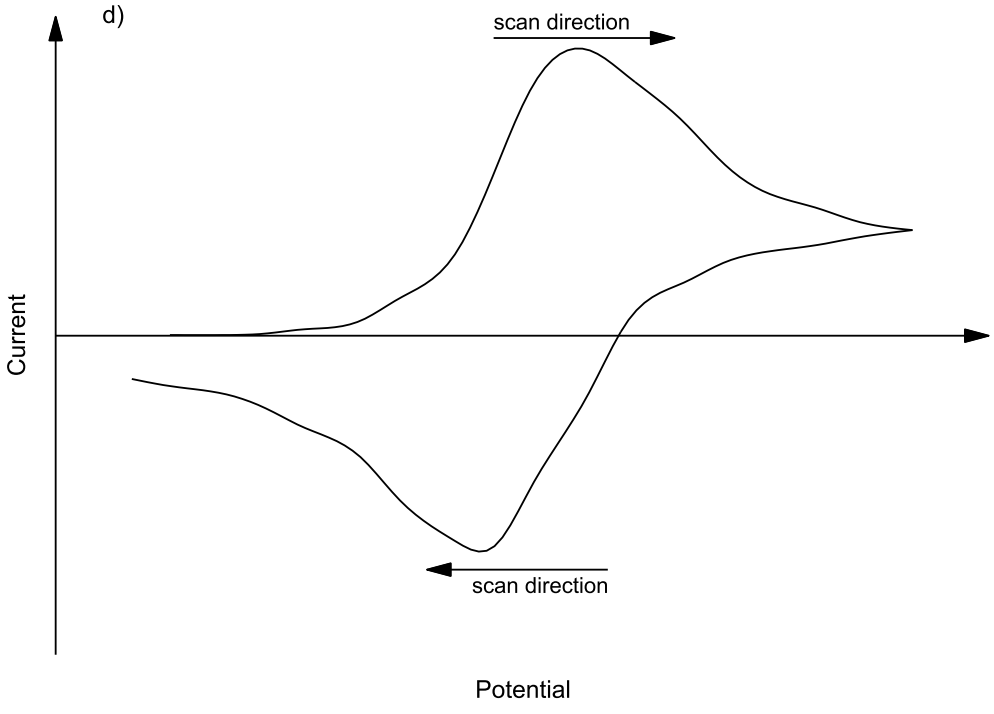
d)
scan direction
Current
scan direction
Potential

A.1.3 Hydrodynamic voltammetry

In hydrodynamic voltammetry, such as rotating disk voltammetry, the electrode is rotated in a controlled manner to induce forced convection of the analyte to the electrode surface. The stirring of the electrode ensures the bulk of the solution remains homogenous, however, a thin layer of solution directly adjacent to the electrode surface clings to the electrode and rotates with it. This thin layer, also known as the *hydrodynamic boundary layer*, has a fixed-width described by Equation A-6.

$$\text{Hydrodynamic boundary layer}: \ \delta_H = 3.6\left(\frac{v}{\omega}\right)^{\frac{1}{2}} \qquad \text{A-6}$$

where v is the kinematic viscosity of the solution in $cm^2\ s^{-1}$

ω is the rotation rate in rad s^{-1}

Although net movement of the analyte to the electrode surface is via mainly convection and diffusion, the analyte mainly travels through the hydrodynamic boundary layer by diffusion. In fact, final movement of the analyte to the electrode surface is essentially only via diffusion through the diffusion layer, which is even thinner than the hydrodynamic boundary layer.[2] The diffusion layer thickness is given by:

$$\text{Diffusion layer thickness}: \ \delta_F \cong 1.61\, D^{\frac{1}{3}} v^{\frac{1}{6}} \omega^{\frac{-1}{2}} \qquad \text{A-7}$$

The concentration gradient at the electrode is therefore kept constant with time because the diffusion layer is of fixed width, and because the concentration on the far side of the diffusion layer is controlled by the rotation rate of the electrode. When the potential is scanned past E^0, the current climbs to a maximum or diffusion-limited current. The current profile is therefore shaped like a symmetric-

[2] For a typical value of D (e.g. 10^{-5} $cm^2\ s^{-1}$, δ_F is 5% of δ_H.

sigmoid centered about E^0 (Figure A-3). This limiting current corresponds to the steepest concentration gradient that can be achieved at that rotation rate. It is defined as the difference between the foot of the wave to the plateau according to the *Levich equation*:

Levich equation: $i_L = 0.620\ nFA\ D^{\frac{2}{3}} v^{\frac{-1}{6}} \omega^{\frac{1}{2}} C$ A-8

Figure A-3 *Ideal sigmoidal voltammogram obtained via hydrodynamic voltammetry for a reduction half reaction. The potential is scanned toward more negative potentials.*

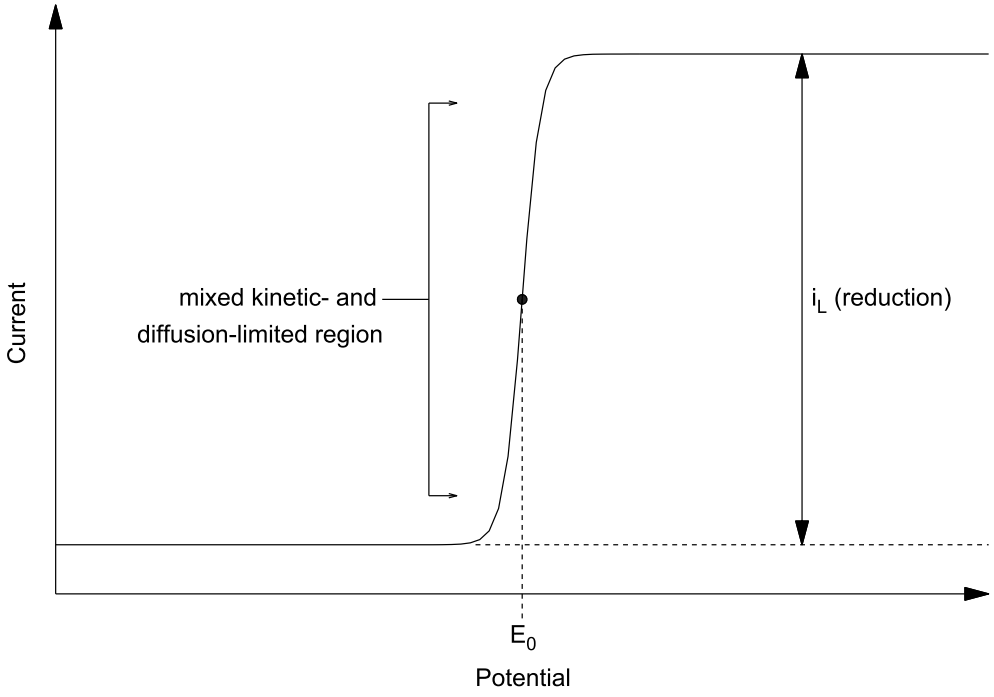

A.2 Rotating disk voltammetry: Application to Oxygen Reduction Reaction

A.2.1 Levich study

A Levich study is the collection of a series of voltammograms over various rotation rates. For a half reaction that is controlled only by mass transport to the electrode surface, the limiting current of a voltammogram should increase with the square root of the rotation rate.

1. Obtain voltammograms for the reaction at various values of ω (rotation rates).

Figure A-4 *Voltammograms at different rotation rates for a reduction reaction investigated by hydrodynamic voltammetry. E_1 is a potential in the limiting region and E_2 is a potential in the mixed region. The potential is scanned towards more negative potentials*

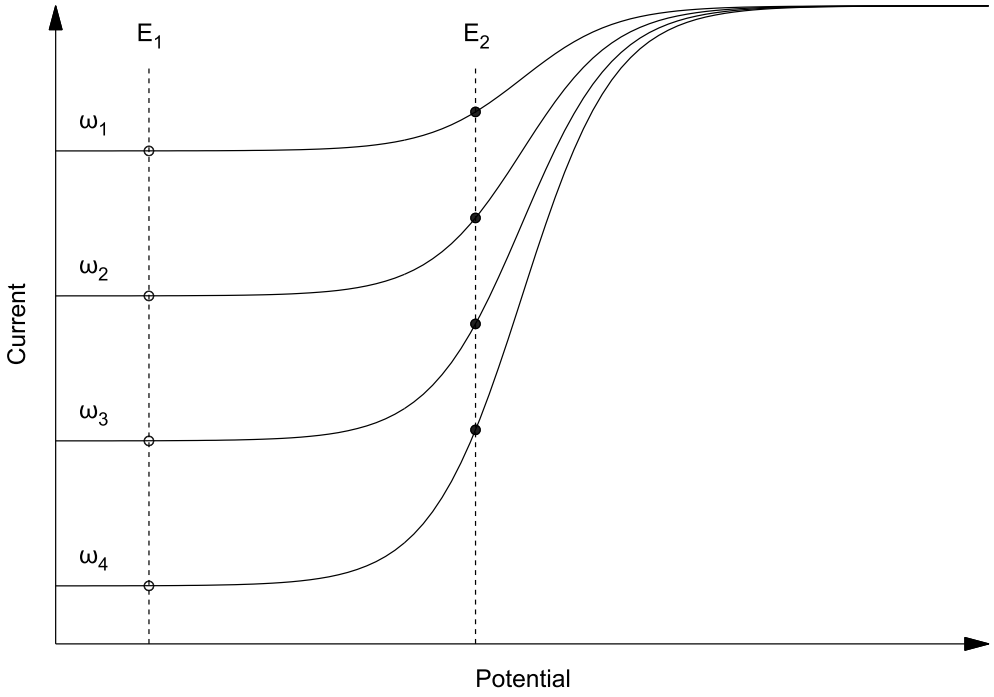

2. Choose current values at particular potentials (shown by the dashed lines in Figure A-4) for all of the corrected voltammograms in step 1 and plot the current versus the square root of the rotation rate. This is known as a

Levich plot and steps 1 and 2 can be repeated at any potential to get a series of linear Levich plots with intercepts at 0.

Figure A-5 *Levich plot created from the data in Figure A-4.*

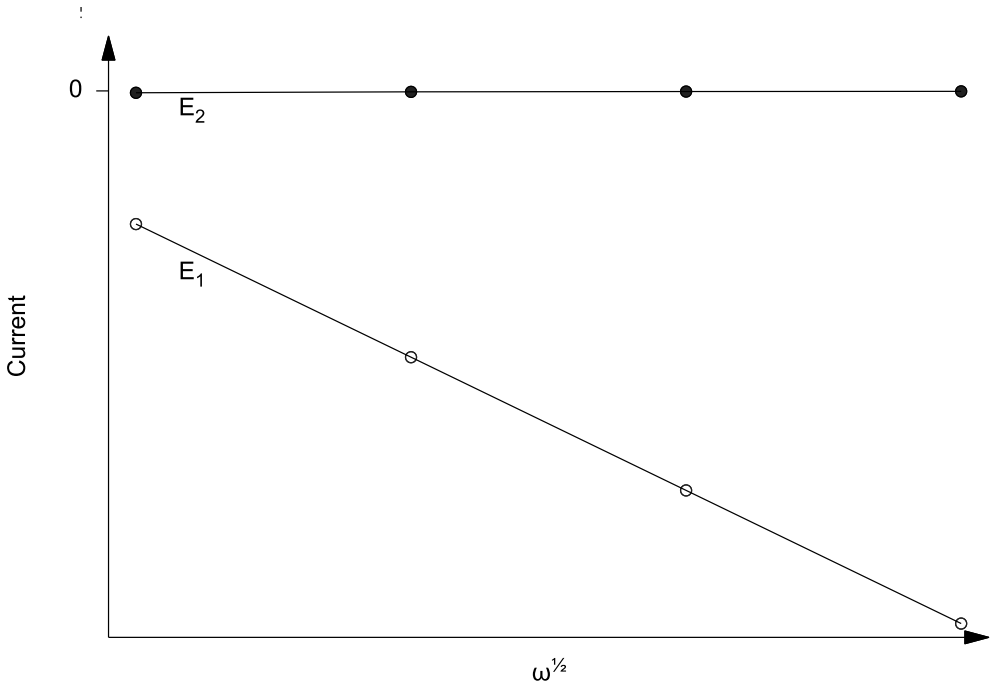

If a Levich plot at a potential in the limiting current region has a non-zero intercept, the half reaction is likely limited by slow kinetics and a Koutecky-Levich study is more appropriate.

A.2.2 Koutecky-Levich study

The rate of oxygen electro-reduction, even over Pt catalysts, is slow. Because of the slow kinetics of oxygen reduction, voltammograms obtained with rotating disk experiments have a distorted sigmoidal shape as the limiting current plateau is shifted away from the formal potential, E^0 (see Figure A-6). Therefore, a large

overpotential must be applied to the electrode to obtain data in the diffusion-limited region.

Figure A-6 *Comparison of the hydrodynamic voltammogram for half reactions that are limited and not limited by kinetics.*

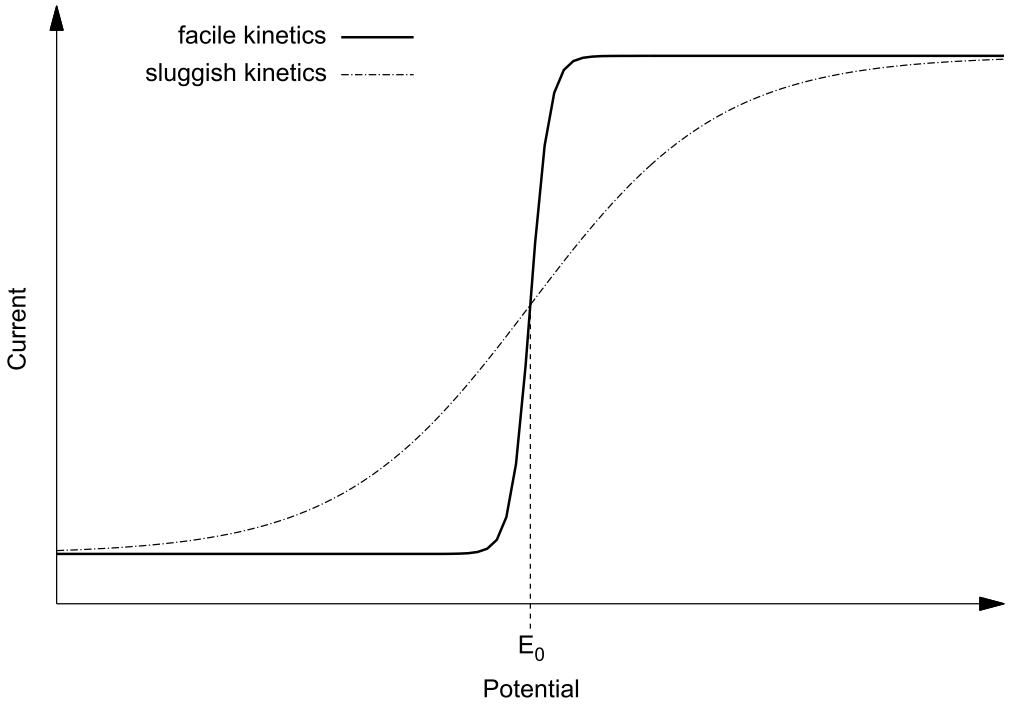

However, kinetic parameters can be determined from the mixed region of the voltammogram by performing a *Koutecky-Levich study* instead of a Levich study. The Koutecky-Levich study differs from the Levich study in that the potentials chosen in step 2 above are only in the limiting current region of the voltammograms. The Levich plot in this case is thus specified as a Koutecky-Levich plot. The linear region of this plot is governed by the Koutecky-Levich equation:

$$\text{Koutecky-Levich equation: } \frac{1}{i_{obs}} = \frac{1}{i_k} + \left(\frac{1}{0.620\ nFAD^{\frac{2}{3}}v^{\frac{-1}{6}}C}\right)\omega^{\frac{-1}{2}} \qquad \text{A-9}$$

$$= \frac{1}{i_k} + \frac{1}{i_L}$$

where i_{obs} is the experimentally observed current

i_k is kinetic current

Unlike the Levich plot, the intercept of the Koutecky-Levich plot is non-zero and is equal to the reciprocal of the kinetic current, that is, the current in the absence of mass transport limitations at a particular overpotential.

A.2.3 Koutecky-Levich corrections and Tafel plots

For ORR studies, Equation A-9 is often used to calculate kinetic currents from experimentally observed currents. In the literature, this method is referred to as applying a Koutecky-Levich correction. To minimize calculation errors, kinetic data should only be extracted for observed currents between 10 and 80 % of i_L (the mixed kinetic and transport region shown in Figure A-3). The kinetic currents obtained can then be used indirectly to determine the *exchange current density* of the reaction at a particular rotation rate. The exchange current reflects the intrinsic rate of electron transfer between the analyte (in this case, oxygen molecules) and the electrode. It is dependent on the identity, roughness and surface condition of the electrode, and the nature of the analyte. Moreover i_0 is proportional to the standard rate constant, thus an idea of the intrinsic rate of charge transfer can be determined.[3]

[3] The methods for determining the standard rate constant from values of exchange current densities are beyond the scope of this work.

1. Convert experimentally observed corrected currents to kinetic currents using the Koutecky-Levich equation (Equation A-9'). Note that i_k is not dependent on the rotation rate as the ω term cancels out. This is congruent with the argument that the kinetic currents are derived by eliminating mass transport effects.

$$\text{Koutecky} - \text{Levich correction: } i_k = \frac{i_L \bullet i_{obs}}{(i_L - i_{obs})} \qquad \text{A-9'}$$

2. Plot the logarithm of the kinetic current versus the potential. This is known as a Tafel plot. The linear region of the Tafel plot is defined by Equation A-10. (Note that it is a matter of preference to plot potential versus the logarithm of the kinetic current instead, as we have done. See for example Figure 4-9. This is because the convention for ORR catalysis is to describe the Tafel slope in units of mV per decade of current.)

$$\text{Tafel equation: } \log i_k = \frac{-\alpha nFE}{2.3RT} + \log i_0 \qquad \text{A-10}$$

where α is the transfer coefficient and describes the fraction of the applied potential that favours the reduction

i_0 is the exchange current

Typically, the transfer coefficient is assigned a value of 0.5. Tafel behavior only holds when the current from the opposing half reaction (in this case oxidation) is less than 10% of the observed current. In the case of oxygen reduction, the reaction is so slow that the large overpotentials required to derive this data ensure that Tafel behavior is supported.

A.3 Bibliography

[1] Educator's Reference Guide for Electrochemistry from Pine Instrument Company Grove City, Pennsylvania Feb 2000, http://www.pineinst.com/echem/files/lmcbp-prof1.pdf Last accessed Aug 15th 2013.

[2] Modulated Speed Rotator User Manual Pine Research Instrumentation 2012 http://www.pineinst.com/echem/files/lmmsrce.pdf Last accessed Aug 15th 2013.

[3] A.J. Bard, L.R. Faulkner, Electrochemical methods Fundamentals and applications, 2nd Ed., Wiley, New Jersey, 2001.

[4] K.J.J. Mayrhofer, D. Strmcnik, B.B. Blizanac, V. Stamenkovic, M. Arenz, N. M. Markovic, Electrochim. Acta 53 (2008) 3181-3188.

[5] G. Kear, F.C. Walsh, Corrosion and Materials 30 (2005) S-1 – S-4.